AN ABSTRACT OF THE THESIS OF

Peter C. Fetzer for the degree of Master of Science in Civil Engineering presented on March 18, 2013.

Title: Behavior of Open Grid Steel Bridge Decks Under Service and Fatigue Loads

Abstract approved: _____

Christopher C. Higgins

Open grid steel bridge decks have been in use for nearly a century. These open grid decks provide an economical and lightweight alternative to traditional reinforced concrete decks. As the transportation infrastructure continues to deteriorate, open grid decks can be used as a cost effective way to rehabilitate structurally deficient bridges. Open grid decks weigh less than conventional reinforced concrete decks and reduce the dead load on a bridge superstructure, thereby increasing the live load capacity. While modern bridge design specifications have evolved to LRFD principles, present design methods for open grid decks are mostly empirical and based on historic practice and performance. Further, fatigue limit states in practice tends to be controlled by cracking in the weak direction, for which no design provisions currently exist. A comprehensive research program was developed to address these issues. The results provide a better understanding of grid deck behavior, and will improve detailing and design provisions.

© Copyright by Peter C. Fetzer

March 18, 2013

All Rights Reserved

BEHAVIOR OF OPEN GRID STEEL BRIDGE DECKS UNDER SERVICE AND FATIGUE LOADS

by

Peter C. Fetzer

A THESIS

submitted to

Oregon State University

in partial fulfillment of

the requirements for the

degree of

Master of Science

Presented March 18, 2013

Commencement June 2013

Master of Science thesis of Peter C. Fetzer presented on March 18, 2013.

APPROVED:

Major Professor, representing Civil Engineering

Head of the School of Civil and Construction Engineering

Dean of the Graduate School

I understand that my thesis will become part of the permanent collection of Oregon State University libraries. My signature below authorizes release of my thesis to any reader upon request.

Peter C. Fetzer, Author

ACKNOWLEDGEMENTS

I would like to thank Dr. Christopher Higgins for his guidance and assistance given throughout the course of this research project, the Bridge Grid Flooring Manufacturers Association for funding the project, my committee members Dr. Michael Scott, Dr. John Gambatese, and Dr. Andrew Meigs. I would also like to thank Mark Kaczinski of The D.S. Brown Company and Gene Gilmore of Bailey Bridges Inc. for technical assistance regarding their respective bridge deck designs; Dr. O. Tugrul Turan for developing the finite element model and design equation scripts; Michael Dyson for assistance in the laboratory. I would also like to thank my family for their encouragement and support.

CONTRIBUTION OF AUTHORS

The funding proposal for experimental testing was written by Dr. Christopher Higgins and Dr. O. Tugrul Turan.

TABLE OF CONTENTS

TABLE OF CONTENTS (Continued)

Page

TABLE OF CONTENTS (Continued)

Page

LIST OF FIGURES

LIST OF FIGURES (Continued)

Figure Page

LIST OF FIGURES (Continued)

Figure Page

LIST OF FIGURES (Continued)

Figure Page

LIST OF FIGURES (Continued)

Figure Page

LIST OF TABLES

LIST OF TABLES (Continued)

Table Page

LIST OF APPENDIX FIGURES

Figure Page

LIST OF APPENDIX FIGURES (Continued)

Figure Page

LIST OF APPENDIX FIGURES (Continued)

Figure Page

LIST OF APPENDIX TABLES

LIST OF APPENDIX TABLES (Continued)

BEHAVIOR OF OPEN GRID STEEL BRIDGE DECKS UNDER SERVICE AND FATIGUE LOADS

1 INTRODUCTION

Since the early 1900s, open grid steel bridge decks have provided an economical and lightweight alternative to traditional reinforced concrete decks. Their light weight reduces the dead load on a bridge superstructure, which also makes them a viable option for bridge rehabilitation with evolving and increasing live load demands. While modern bridge design specifications continue to evolve, the design methodology with respect to open grid steel bridge decks has not changed significantly over time. Current design methodology for open grid decks is based on empirical formulas and historic practice. Open grid decking is inherently highly orthotropic, with a large variation in stiffness dependent on the orthogonal direction. An extensive experimental program funded by the Bridge Grid Flooring Manufacturers Association (BGFMA) was undertaken in order to develop a better understanding of load distribution and fatigue behavior of open grid decks. Behavior of individual components of open grid deck was investigated, as well as system behavior. Major objectives of this research project included developing AASHTO LRFD equations for service and strength design moments by testing different configurations of welded and riveted bridge decks. Objectives also include the evaluation of standard and alternative weld details, categorization of fatigue performance for weak-direction bending, and fatigue life predictions of welded open grid decks.

2 OVERVIEW

The experimental program consisted of several different types of tests, described in detail in Chapter 4. Firstly, flexural and torsional stiffness parameters were established experimentally from open each grid deck specimen. These parameters were necessary to apply a finite element analytical model.

Next, full scale system tests were performed which involved simple and continuous span configurations subjected to patch loads. Load distribution, deflections, and weak direction stresses were quantified based on transverse and parallel tire patch orientation. Tire patch load distribution was examined at various locations on the open grid decks, and locations of maximum strong- and weak-direction moment were determined in order to develop strength design equations for the AASHTO LRFD Bridge Design Specifications. Absolute stress ranges in cross bars based on tire patch location were examined in order to predict service and fatigue life. An alternate deck-to-stringer connection detail (concrete fill, opposed to shim-and-weld) was designed, constructed and tested. Strong-direction negative moment was investigated over continuous supports, followed by strong-direction negative moment fatigue testing.

Subcomponent fatigue tests were run based on full scale test results. These tests isolated weak-direction fatigue behavior. Performance of different weld details was measured for each type of welded open grid provided. The different weld details were tested and placed in specific fatigue detail categories.

Finally, based on experimental data and analytical model results, equations were developed to replace strip-width design provisions in the current AASHTO-LRFD Bridge Design

Specification in order to better characterize the orthotropic behavior of open grid decks. Design moment equations were developed in order to design for strength as well as predict fatigue life based on orthotropic properties of any given open grid deck, for any span length.

3 LITERATURE REVIEW

A review of the technical literature was conducted. A number of previous studies were identified that related to open grid steel bridge deck, those of which are described in this section.

3.1 Orthotropic Plate Theory

Timoshenko *et al.* [1959] describes orthotropic thin plates as having different elastic properties in three different planes while making three assumptions:

1) There is no deformation in the middle plane of the plate. This plane remains neutral during bending.
2) Points of the plate lying initially on a normal-to-the-middle plane of the plate remain on the normal-to-the-middle surface of the plate after bending.
3) The normal stresses in the direction transverse to the plate can be disregarded.

The general differential equation for bending and twisting moments of an orthotropic thin plate can be written as [Timoshenko and Woinowski-Krieger 1959]:

$$D_x \frac{\partial^4 w}{\partial x^4} + 2H \frac{\partial^4 w}{\partial x^2 y^2} + D_y \frac{\partial^4 w}{\partial y^4} = q(x, y); H = D_1 + 2D_{xy} \quad [3.1]$$

$$M_x = -\left(D_x \frac{\partial^2 w}{\partial x^2} + D_1 \frac{\partial^2 w}{\partial y^2} \right) \quad [3.2]$$

$$M_y = -\left(D_x \frac{\partial^2 w}{\partial y^2} + D_1 \frac{\partial^2 w}{\partial x^2} \right) \quad [3.3]$$

$$M_{xy} = 2D_{xy} \frac{\partial^2 w}{\partial x \partial y} \quad [3.4]$$

where D_x = flexural rigidity in the strong direction; D_y = flexural rigidity in the weak direction; D_1 = torsional rigidity contribution from the strong- and weak-direction rigidities; D_{xy} = torsional rigidity; H = sum of the torsional rigidity contribution from the strong- and weak-direction rigidities (D_1) and torsional rigidity (D_{xy}); $w(x, y)$ = vertical plate deflection in the Cartesian coordinate system and $q(x, y)$ = applied transverse load in the Cartesian coordinate system [Higgins, Turan, Connor, and Liu 2011]. Higgins *et al*. [2011] also states that 'H' is dependent on the torsional rigidity of the plate and three cases for 'H' correspond to different cases of orthotropy. Specifically, for open grid decks

$$H < \sqrt{D_x D_y} \qquad [3.5]$$

where the solution has imaginary roots that correspond to relatively torsionally soft, flexurally stiff decks. In order to create a unified method of analysis for all cases of orthotropy, the following equation was considered:

$$H = \alpha \sqrt{D_x D_y} \qquad [3.6]$$

where α can be varied depending on the case of orthotropy. However, the general moment equations developed may not be suitable for open grid decks. Firstly, the general equations are based on an infinitely wide plate simply supported on two edges. While open grid decks can be modeled with simple supports on two edges, the other two edges are free. Also, weak-direction moments may control design for fatigue of welded open grid decks, and weak-direction equations were not proposed in the literature. Higgins *et al.* [2011] conducted finite element analyses using ABAQUS 6.8-2. Python scripts were used to incrementally move design truck and design tandem tire patch configurations across the deck surface. Strong and weak-direction moment equations for main bars parallel and

transverse to traffic flow were developed based on the analyses for a range of stiffness ratios (D), span lengths, and α values.

3.2 Experimental Testing

GangaRao [1988] completed an experimental program to test open grid decks under static and fatigue loads. Performance was evaluated based on several factors, including main bar spacing, orientation of main bars with respect to traffic direction, and change in stiffness after fatigue testing. GangaRao stated that the most significant factor with respect to fatigue life is main bar spacing, with better fatigue performance from welded open grid decks with a closer main bar spacing. All fatigue cracks were located on the cross bar, close to the main and cross bar intersections. In an attempt to quantify residual stresses in the welded decks from the welding process, strain gages were mounted on the deck and the weld joint was removed. Alleviation of residual stresses was measured to be as high as 27 ksi from the removal of welded joints. It was also noted that higher residual stresses were measured as main bar spacing decreased. Diagonal grid decks had lower residual stresses than rectangular decks. Lower residual stresses were observed in galvanized decks, due to residual stress relief caused by the galvanization process, thus producing a longer fatigue life. GangaRao concluded that the welded grid deck system could be classified under Category E of the AASHTO specifications. Testing of riveted open grid panels produced no fatigue cracks, which GangaRao attributes to the inherent lack of high residual stress concentrations in riveted open grid panels.

Baker [1991] conducted experiments to determine bending and twisting stiffness properties in the three different planes of an orthotropic plate described by Timoshenko et al [1959]. Four grid deck specimens were tested for this report. The stiffness tests performed by

Baker are similar to the stiffness tests performed in this research project. A line load was placed across a simply supported width of deck in order to measure bending stiffness in each orthogonal direction. To measure twisting stiffness, the square specimens were held at three corners and incrementally loaded at one corner, where load versus displacement was measured. An assortment of concrete-filled steel grid decks were tested with line loads and point loads. Additionally, the bending and twisting stiffnesses were used as input parameters for a finite difference model. This model produced deflections comparable to experimental deflections (within 15%) for concrete filled grid decks subjected to line and concentrated loads.

Huang *et al.* [2002] performed experimental testing of open grid decks to compare with current AASHTO predicted effective widths for open grid decks, orthotropic plate theory and a three-dimensional finite element model. Diagonal and rectangular open grid configurations were tested. Three diagonal decks were tested: a conventionally welded deck, one with reduced welds, and one with a 2.5 in. cross bar as opposed to a then-conventional 2 in. cross bar. The reduced welds were smaller puddle welds which were chosen to minimize cost of manufacturing as well as reducing stiffness, which was predicted as a cause of puddle weld cracking. The reduced welds cracked during testing, while the standard welds remained intact. The specimen with 2 in. cross bars had a lower transverse stiffness than the one with 2.5 in. cross bars, and thus distributed the load across a smaller effective width than the 2.5 in. cross bars. The AASHTO effective widths for all panels were conservative for all specimens tested. A three-dimensional analytical model using open grid deck component geometries was created in ANSYS and calculated strains agreed closely with experimental results. Calculated deflections did not, they were much larger experimentally, which could be due to unmeasured support displacements which can

be significant. Additionally, orthotropic thin plate theory was used to compare with the experimental results and the finite element model, results did not correlate well.

3.3 Alternative Deck-To-Stringer Attachment Details

For riveted open grid panels, Apperson *et al.* [2010] proposed alternate deck-to-stringer attachments for riveted open grid decks. Fatigue tests were performed to investigate crack initiation and propagation over continuous supports. Fatigue cracks initiated at the fillet weld attaching the main bearing bars of the open grid deck to the supporting structure. As a result, two new details were proposed to replace the industry standard practice of welding main bearing bars to the supporting structure. In these two details, welds were moved to a location of low stress reversal (or eliminated altogether) and fasteners were used to attach the deck to the stringers. These alternate attachment details are not practical for welded open grid panels given the geometry of the main bearing bars, so a deck-to-stringer attachment detail was developed comparable to those discussed by Gilmore [1987]. A cast-in-place concrete connection detail using shear studs to connect the open grid deck and the stringer would produce composite action between the open grid deck and the superstructure. In addition, residual stresses caused by pinning and welding the open grid deck directly to the superstructure would be eliminated. Gilmore also suggests that the concrete cover provides protection for the stringer flanges, which may be susceptible to corrosion when open grid decks are used. Experiments by Higgins *et al.* [2001] showed that shear studs in concrete filled grid decks provide sufficient continuity between the bridge deck and supporting stringer well above service level loads, and that shear connector failure is not the controlling failure mode.

Based on a review of related literature, there are gaps in understanding of the orthotropic behavior of open grid deck components on an individual and system level. Also, performance of a proposed alternative deck-to-stringer attachment details has not previously been tested for open grid decks. Additionally, no reliable method of predicting fatigue life currently exists.

4 EXPERIMENTAL PROGRAM

An experimental program was developed to address issues described in the proposal to the BGFMA. These issues are outlined in Chapter 2. While all testing procedures were similar for all the open grid decks tested, each test was modified to accommodate the different types of open grid deck. Firstly, the four types of open grid decks are described in detail. Next, the experimental setups and grid deck instrumentation are discussed. Lastly, procedures for stiffness, load distribution, an alternate connection detail, strong-direction negative moment fatigue, and weak-direction fatigue tests are discussed.

4.1 Open Grid Bridge Deck Specimens

Open grid bridge deck consists of a grillage of steel components that are connected at intersections of the elements. The different components that comprise welded and riveted open grid decks are shown in Figs. 4.1 and 4.2, respectively. Open grid decks may or may not have diagonal bars and the main, supplemental, and cross bar sizes and spacing can vary. Four types of open grid bridge decks were studied in this test program. They were provided by members of BGFMA and were fabricated using the same materials and procedures used for decks supplied to owners for construction. Two types of welded open grid decks were shipped from The L.B. Foster Company, OH and two types of riveted open grid decks were shipped from Bailey Bridges Inc., AL. To distinguish between the different deck types and connection details, a naming convention was developed as shown in Fig. 4.3.

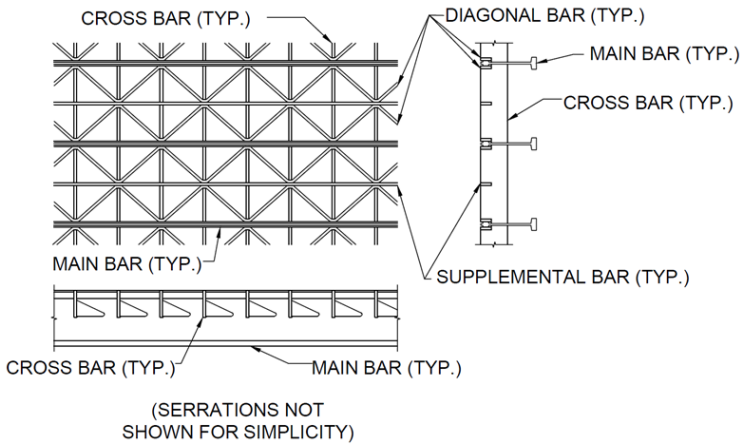

Figure 4.1: Welded open grid deck components (diagonal bar shown) (original detail provided by the BGFMA)

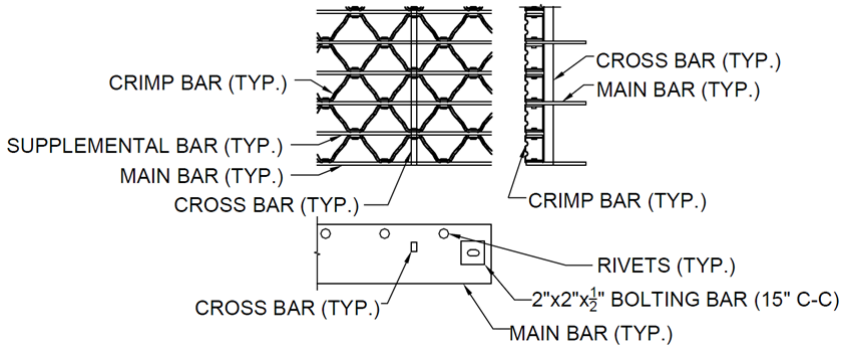

Figure 4.2: Riveted open grid deck components (original detail provided by the BGFMA)

Figure 4.3: Naming convention for welded open grid deck specimens

4.1.1 Welded Diagonal Open Grid Deck

Three (3) separate welded diagonal open grid deck specimens (one large and two small) were tested. Each specimen had different weld details joining the main and supplemental bars. The large specimen, 7.5DIAG2.5TYP1, was fabricated using a conventional industry standard puddle weld detail, (weld type 1) at every intersection. The two smaller specimens were fabricated using alternate weld details, labeled Type 2 and Type 3. The 7.5DIAG2.5TYP2 specimen weld detail consisted of a fillet weld in two opposing quadrants at every intersection, and puddle welds at each intersection of diagonal bars. The 7.5DIAG2.5TYP3 specimen was comprised of fillet welds in all quadrants, and puddle welds at every intersection. Figures 4.4 and 4.5 show configurations for all three diagonal welded open grid specimens, as well as the bar sizes and spacing. Figures 4.6 to 4.8 show the Types 1, 2 and 3 weld details, respectively.

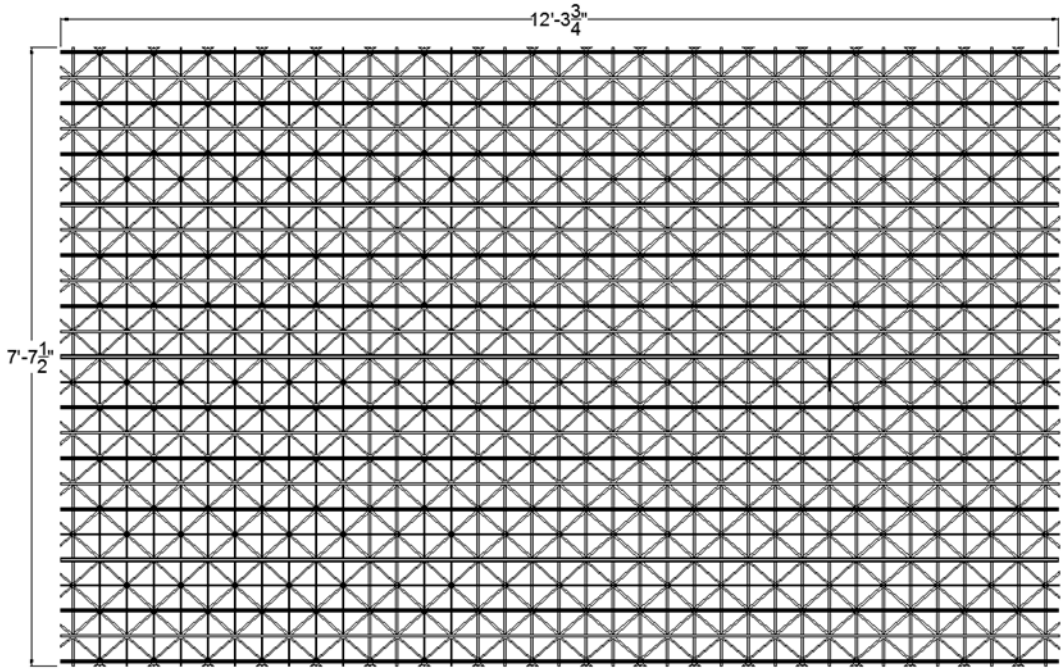

Figure 4.4: 7.5DIAG2.5TYP1 configuration

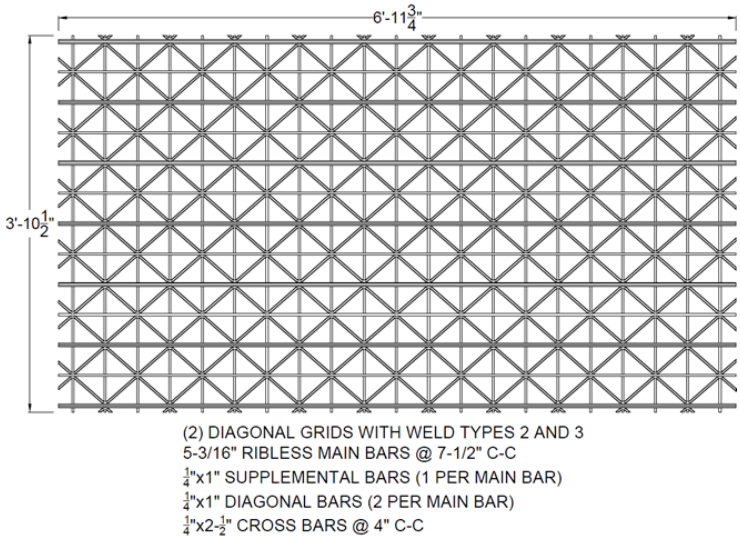

Figure 4.5: 7.5DIAG2.5TYP2 & 7.5DIAG2.5TYP3 configurations

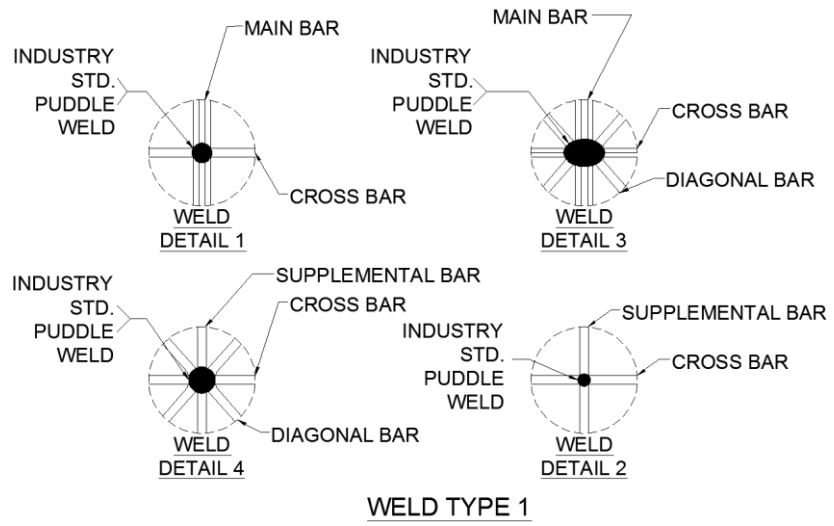

Figure 4.6: Type 1 weld detail (original detail provided by the BGFMA)

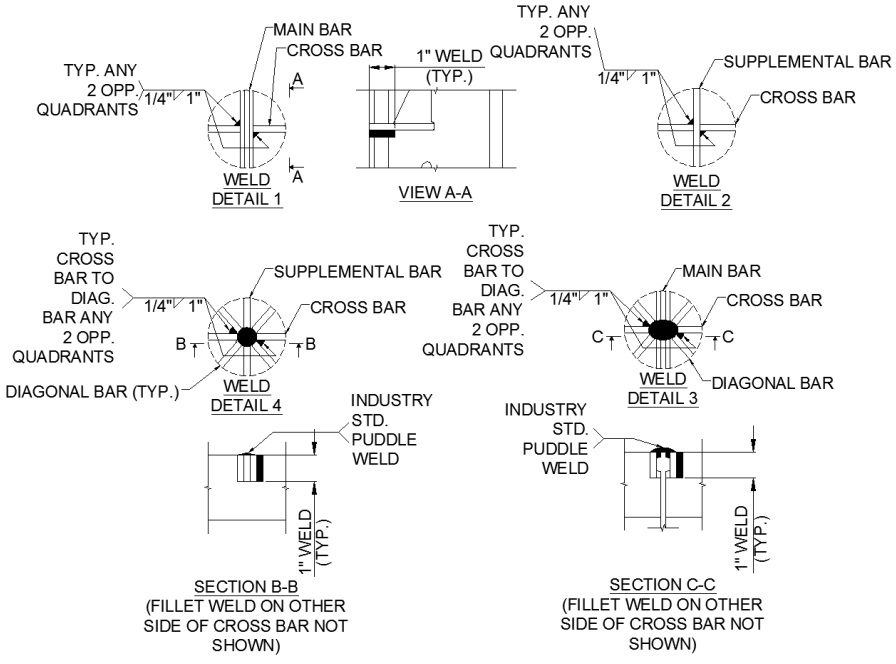

Figure 4.7: Type 2 weld detail (original detail provided by the BGFMA)

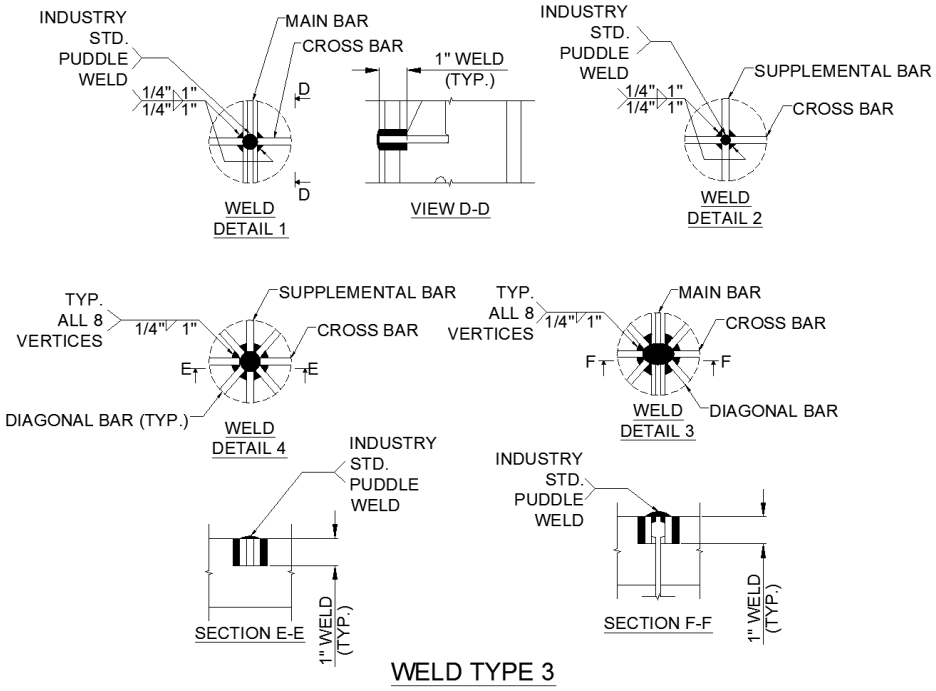

Figure 4.8: Type 3 weld detail (original detail provided by the BGFMA)

4.1.2 Welded Rectangular Open Grid Deck

Three (3) separate welded rectangular open grid bridge deck specimens were tested. The large specimen, 4.0RECT2.5TYP4 was fabricated with a conventional puddle weld at every intersection (Type 4). The two smaller specimens were fabricated using alternate weld details (Type 5 and 6). The 4.0RECT2.5TYP5 specimen contained fillet welds in two opposing quadrants at each intersection. No puddle welds were used in this specimen. The 4.0RECT2.5TYP6 specimen contained fillet welds in all quadrants, and puddle welds at every intersection. Figures 4.9 and 4.10 show configurations for all three specimens, as well as bar sizes and spacing. Figures 4.11 to 4.13 show the Type 4, 5 and 6 weld details, respectively.

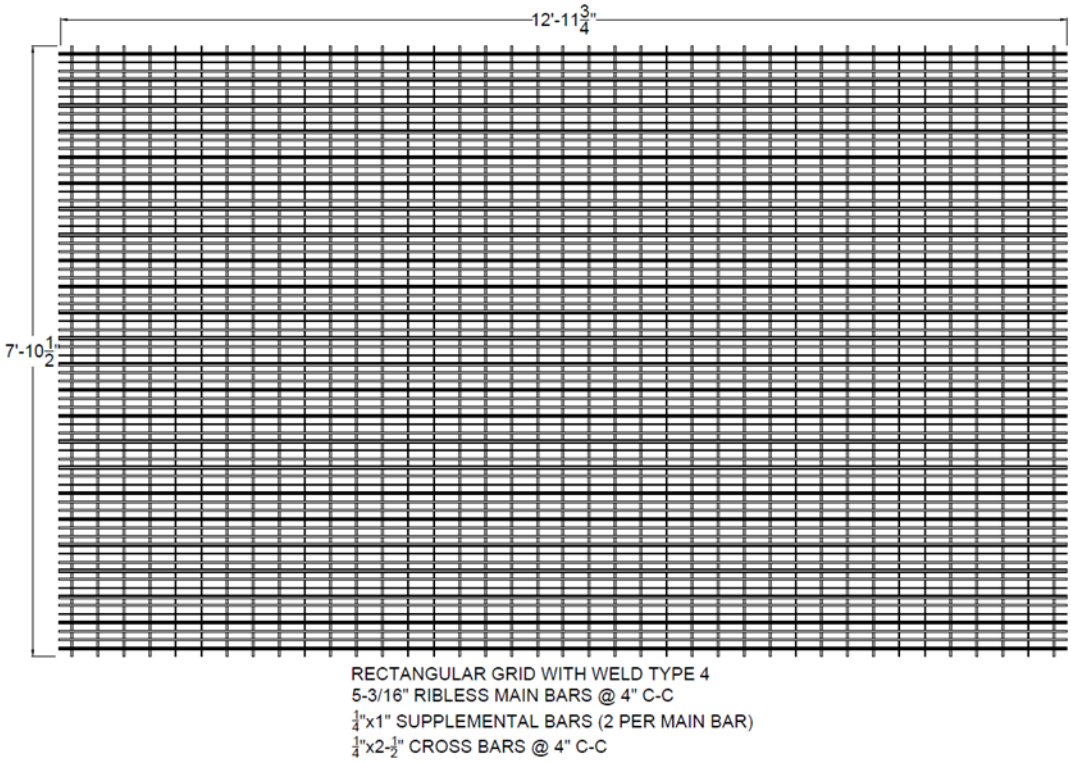

Figure 4.9: 4.0RECT2.5TYP4 configuration

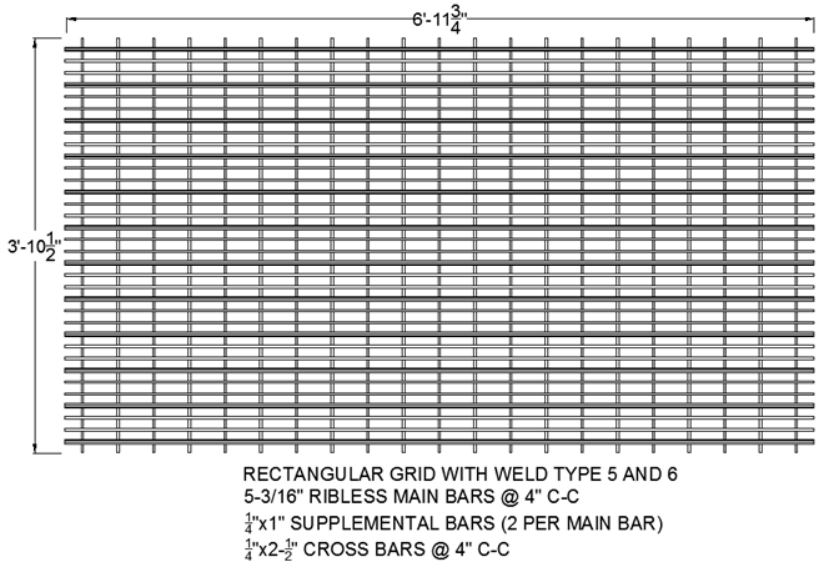

Figure 4.10: 4.0RECT2.5TYP5 and 4.0RECT2.5TYP6 configurations

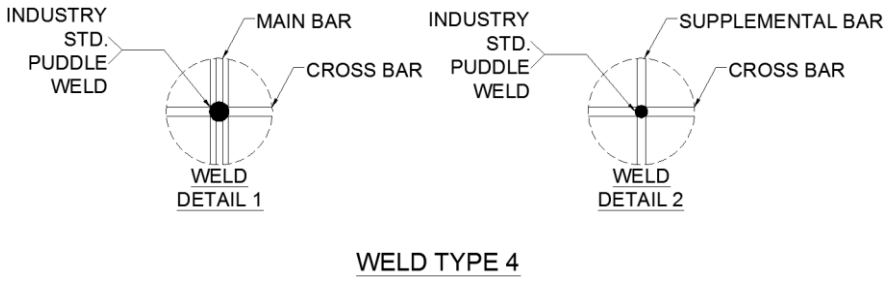

Figure 4.11: Type 4 weld detail (original detail provided by the BGFMA)

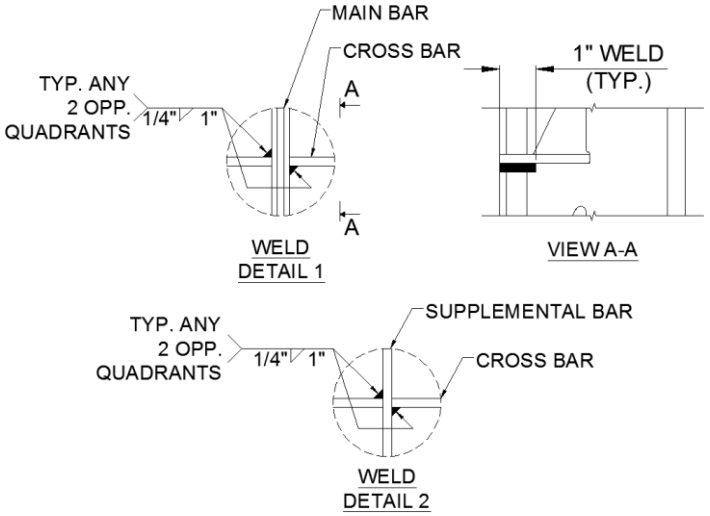

Figure 4.12: Type 5 weld detail (original detail provided by the BGFMA)

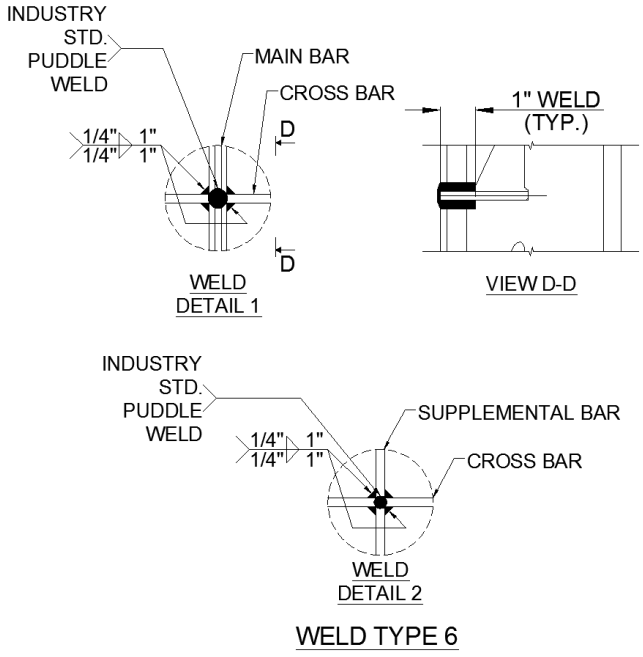

Figure 4.13: Type 6 weld detail (original detail provided by the BGFMA)

4.1.3 Riveted Open Grid Deck

Two (2) configurations of riveted open grid deck were tested: lightweight and heavyweight. Each configuration consisted of two nearly identical panels; the only difference being spacers located on the outside main bars on one of the panels, with bolt holes on the outside main bars on the other specimen, to permit connection of the adjacent panels. The lightweight riveted open grid bridge deck specimen is referred to as 37-R-L-5x¼. The two panels allowed investigation of the load transfer across the bolted connection. Figure 4.14 shows the basic configuration for each of the 37-R-L-5x¼ specimens. Figure 4.15 shows the bolting detail. The second riveted specimen was a heavy duty deck that also consisted of two panels. These specimens are referred to as 37-

R-5x¼, and their configuration is shown in Fig. 4.16. The connection between panels for these specimens was identical to that for the lightweight riveted open grid specimen.

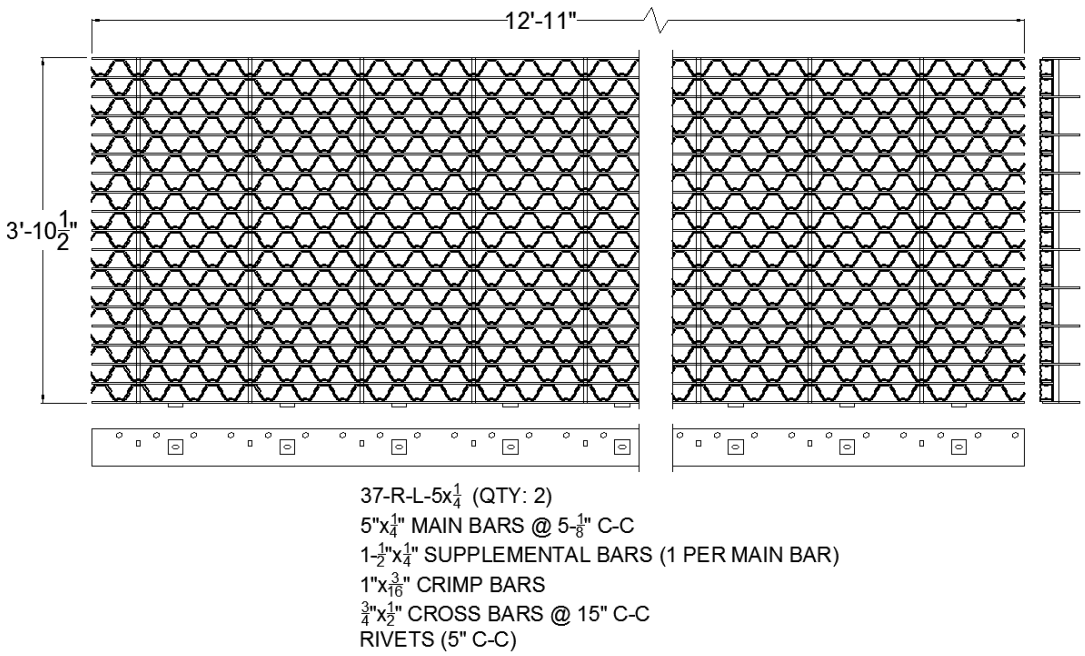

Figure 4.14: 37-R-L-5x¼ lightweight riveted open grid panel configuration

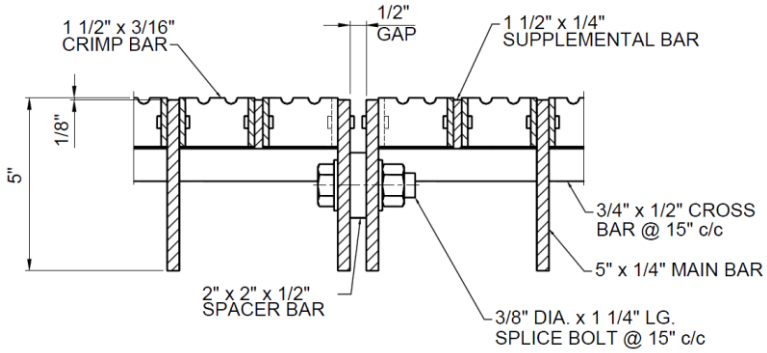

Figure 4.15: Lightweight riveted open grid deck bolting detail (original detail provided by the BGFMA)

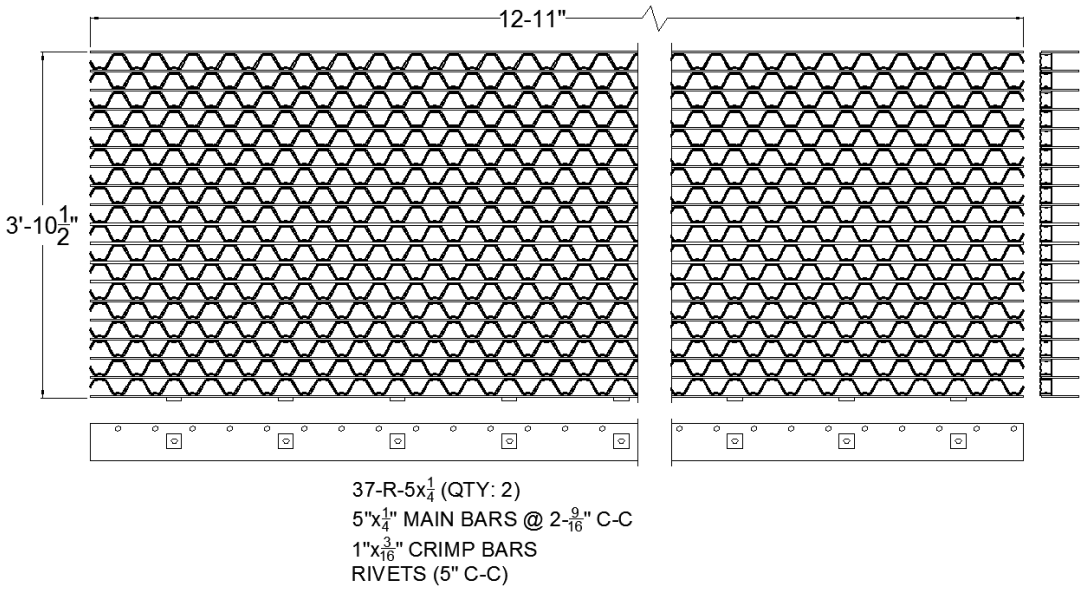

Figure 4.16: 37-R-5x¼ heavy duty riveted open grid panel configuration

4.2 Test Setups

The open grid deck specimens were instrumented and tested in the Structural Engineering Research Laboratory at Oregon State University. Three separate experimental setups were used for the different tests. The primary setup (Fig. 4.17) consisted of a large steel frame equipped with a 110 kip servo-hydraulic actuator, which was operated in either load or displacement control, depending on the test. This setup was used for flexural stiffness tests, as well as load distribution and strong- and weak-direction negative moment fatigue tests. The second test setup (Fig. 4.18) consisted of a large steel frame equipped with a 55 kip servo-hydraulic actuator, which was operated in load control. This setup was used exclusively to run subcomponent weak-direction fatigue tests. The third set-up (Fig. 4.19) was used exclusively for twisting stiffness tests. For all test setups, data was collected using a high speed, multi-channel 16-bit data acquisition system. Data acquisition and storage was controlled using commercially available software.

Figure 4.17: Test setup 1 for stiffness and load distribution tests

Figure 4.18: Test setup 2 used for subcomponent fatigue tests

Figure 4.19: Test setup 3 used for torsional stiffness tests

4.3 Instrumentation Plan

The instrumentation plan was developed to measure uniaxial strain in the individual grid deck components for the various tests. Strain gages designated as CEA-06-062UW-120 were placed on main bars, cross bars, supplemental bars, and diagonal bars. The strain gage is a general purpose strain gage manufactured by Micro-Measurements. Strain gages designated as EA-06-125BT-120 were used on the narrow riveted deck crimp bars.

Because strain gages are used in this work to measure and project strain profiles through the open grid elements, the effect of web punch-outs and serrations on the sensor measurements was of interest. In particular, it was not known if the gage length of the strain gage would be influenced by the punch-outs. Therefore, at the start of the experimental program, long gage (two inch long grid length) strain gages (N2A-06-20CBW-120) were used to compare with the small gage (approximately 3/32 inch grid length) strain gages (CEA-06-062UW-120) on the top rib of main bars (Fig. 4.20). Because of the varying cross-section over the length of the punch-out, it was thought that the longer gage length strain gage would better average the strain to more effectively identify the neutral axis in the main bars. Strain gages were mounted on the top rib, centered between cross bars. The web punch-outs in the welded deck main bars are located 4 in. on center (Fig. 4.21) and therefore the strain gages are over the punch-out. The specimen was subject to a line load (during two one-way bending stiffness tests) and the measured strains for both types of strain gages at a symmetrical location were similar as seen in Figs. B.4 and B.8 and Tables B.3 and B.7. This demonstrated that the small gage length CEA-06-062UW-120 gages were adequate to identify the neutral axis in the main bars even in the presence of the punch-outs.

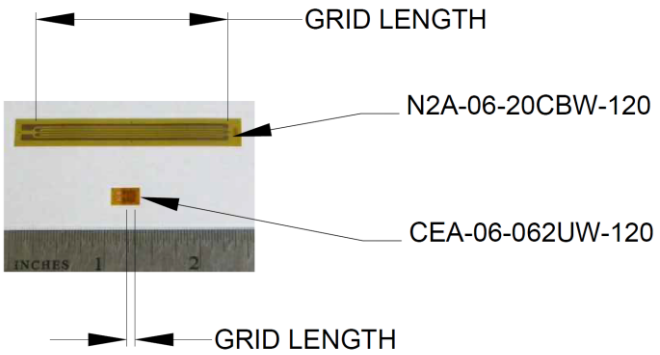

Figure 4.20: Strain gage grid lengths

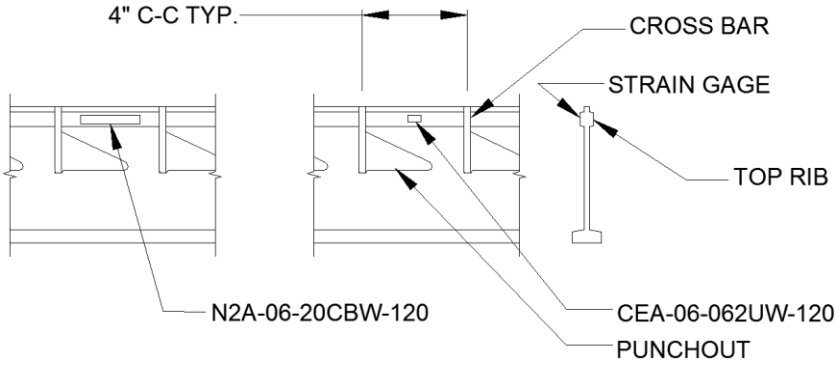

Figure 4.21: Main bar section with punch-out

In addition to strain gages, displacement sensors were placed under and on top of the deck to measure the deck deformations relative to the laboratory strong floor. The applied actuator load was measured by a load cell that was placed in the load train. Fully detailed instrumentation plans for each of the open grid specimens are found in Appendix B and C, for stiffness and load distribution tests, respectively.

4.4 Stiffness Tests

Three stiffness tests were conducted for each open grid deck type. To perform these tests, the specimens were subjected to one-way bending in each of the orthogonal directions and also deck twisting. One-way bending stiffness measured in the direction of the main bars is referred to as D_x, or the strong-direction stiffness. One-way bending measured in the direction of the cross bars is referred to as D_y, or the weak-direction stiffness. Twisting is referred to as D_{xy}, or the torsional stiffness. These parameters are used in subsequent finite element models, analytical expressions, and to compare with design moments prescribed in the AASHTO LRFD Bridge Specification [2007].

For the 7.5DIAG2.5TYP1 and 4.0RECT2.5TYP4 configurations, full system tests were completed prior to cutting the panels to the same size as the other four welded panels in order to determine stiffness properties. Load distribution tests were conducted on the two types of riveted deck panels, prior to cutting the decks to conduct the respective stiffness test.

The D_x and D_y tests were performed on simple spans by placing the specimens on two continuous roller supports. Two W12x120 beams were used to rigidly support the panels under the continuous support. For D_x tests, the main bars rested on 2 in. diameter mild steel round bar stock. For D_y tests, the cross bars rested on continuous L3x3x-½ mild steel angles. Shims were used at the supports to ensure uniform contact of all bars on the roller/angle supports. A W12x120 spreader beam was used to apply a uniform load over the width of the panels. Two 1 x ½ in. rectangular mild steel bars were placed between the spreader beam and open grid deck panels to create a four-point loading condition on the panel to represent a uniform load applied across the entire width of the deck. The stiff

loading beam produced one-way curvatures and this allows the stiffness of the deck in the bending direction to be determined. All panels were initially loaded until transverse curvatures were no longer measured. These transverse curvatures at low load levels occur because the deck is not perfectly flat due to the inevitable residual stresses and fit-up tolerances required at fabrication. Typical D_x and D_y tests are shown in Figs. 4.22 and 4.23, respectively. Figure 4.24 shows a typical test configuration. Table 4.1 shows the span configurations of all D_x and D_y tests.

Figure 4.22: Typical D_x test

Figure 4.23: Typical D_y test

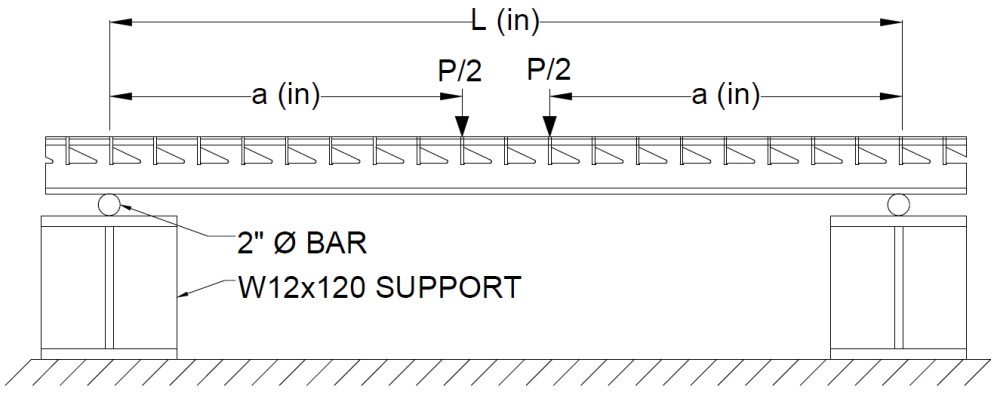

Figure 4.24: Typical D_x and D_y test configuration (D_x shown)

Table 4.1: D_x and D_y test configurations

Panel	Test Type	Load Range (P, in kips)	Span Length L (in)	Shear Span a (in)
7.5DIAG2.5TYP1	D_x	20-40	60	26
	D_y	12-17	37.5	15
7.5DIAG2.5TYP2	D_x	10-30	72	32
	D_y	10-15	37.5	15
7.5DIAG2.5TYP3	D_x	10-40	72	32
	D_y	10-15	37.5	15
4.0RECT2.5TYP4	D_x	30-35	72	32
	D_y	8-12	40	18
4.0RECT2.5TYP5	D_x	25-55	72	32
	D_y	5-15	40	18
4.0RECT2.5TYP6	D_x	20-40	72	32
	D_y	5-15	40	18
37-R-L-5x¼	D_x	10-15	96	45
	D_y	2-6	37.5	16.1875
37-R-5x¼	D_x	10-15	96	45
	D_y	1-2	37.5	16.1875

To determine the strong and weak-direction stiffnesses the applied load and corresponding deck deflections was required. The strong-direction stiffness (D_x) was computed as:

$$D_x = EI_x \qquad [4.1]$$

where E is Young's elastic modulus (taken as 29,000 ksi) and I_x is the moment of inertia per unit width of deck (in^4/ft). D_x and D_y (EI_x and EI_y, respectively) values were calculated by back-solving for EI from the static four-point load-deflection equation for an equivalent beam. This is possible because the line-load condition produced with a very stiff spreader beam imposes one-way bending and the deck is forced to act like a beam. The maximum deflection of a beam under four-point bending is calculated as:

$$\Delta_{max} = \frac{Pa}{48EI}(3L^2 - 4a^2) \quad [4.2]$$

where P is equal to one half of the applied load; Δ_{max}= measured deflection at midspan; E = elastic modulus; and all other variables are illustrated in Fig. 4.24. Rearranging Eqn. 4.2 allows calculation of the EI stiffness of the deck as:

$$EI = \frac{Pa}{48\Delta_{max}}(3L^2 - 4a^2) \quad [4.3]$$

Here I can be taken as I_x or I_y depending on the direction of bending considered. Once EI_x and EI_y are determined, they are divided by the effective deck width, and the final dimensions are k-in^2/ft.

Linearly variable differential transformers (LVDT's) were used to measure support displacements. String potentiometer displacement sensors were used to measure midspan displacements of the deck across the entire deck width. A typical displacement sensor setup for D_x and D_y tests is shown in Appendix B.

In order to measure the twisting stiffness (D_{xy}), each panel was cut to a square dimension. A typical D_{xy} test is shown in Fig. 4.19. Three corners of each specimen were pin-supported. The unsupported corner was loaded. Loading was performed by placing six steel square plates of known weight on the unsupported corner. Load versus displacement was measured in six increments (for each added plate) at the free corner. D_{xy} was calculated as:

$$D_{xy} = \frac{P}{\Delta}\frac{L^2}{4} \quad [4.4]$$

where P = applied load at the unsupported corner; Δ = displacement at unsupported corner; and L = length of square dimension (shown in Table 4.2). Panel sizes varied based on main bar center-to-center spacing in order to support main bars on pins at the corners. Strain gages were not used for D_{xy} tests. LVDT displacement sensors were placed at each pinned corner to measure support displacements, and a string potentiometer displacement sensor was used to measure deflection at the free corner.

Table 4.2: D_{xy} test configurations

Panel	Test Type	L (in) x L (in)
7.5DIAG2.5TYP1	D_{xy}	45x45
7.5DIAG2.5TYP2	D_{xy}	45x45
7.5DIAG2.5TYP3	D_{xy}	45x45
4.0RECT2.5TYP4	D_{xy}	44x44
4.0RECT2.5TYP5	D_{xy}	44x44
4.0RECT2.5TYP6	D_{xy}	44x44
37-R-L-5x¼	D_{xy}	46.125x46.125
37-R-5x¼	D_{xy}	46.125x46.125

4.5 Panel Test Setups for Full-Scale System Testing

System level tests were conducted to investigate several performance criteria for open grid decks. System level tests were conducted on two welded panels (specimens 7.5DIAG2.5TYP1 and 4.0RECT2.5TYP4) and also on the two types of riveted open grid decks.

The full-size panels were tested using an experimental set-up that was constructed to allow the panel and actuator locations to be moved with relative ease. The W12x120 beams used as rigid bridge stringers were mounted to three MC12x50 steel channels. Hydraulic jacks were mounted to the channels in order to raise and lower the entire setup enabling

placement of rollers beneath the channels. This allowed for the setup to move north and south along the strong floor beneath the test frame and hydraulic actuator. The hydraulic actuator was mounted to rollers which rested on the crossbeam of the test frame. This allowed for efficient patch load testing of any location along the entire length and width of the open grid panels. Patch loading was applied through stiffened steel load beams measuring 10 x 20 in. to simulate tire contact area. Slight differences in the elevation of puddle welds on the deck caused unrealistic localized stresses in individual grid deck components if the stiffened steel load beam and open grid panel were put in direct contact. In order to ensure uniform loading over the 10 x 20 in. patch area, a 10 x 20 x ½ in. thick elastomeric pad was placed between the stiffened beams and open grid panel. Patch load tests were performed on multiple span lengths, for simple and continuous span conditions, as well as free and fixed boundary conditions. Patch loads were oriented in both the parallel and transverse to main bar directions, with respect to direction of traffic over the open grid decks. While the full test matrices for each open grid specimens are located in Appendix B, the following subsections provide a summary of each system deck test.

4.5.1 7.5DIAG2.5TYP1 Tests

One-quarter of the full-size panel was heavily instrumented with surface mounted strain gages and displacement sensors. Strain gages were mounted along one half of the width of the open grid panel. Two sets of strain gages and displacement sensors were mounted along the entire width of the deck in order to enable superposition of load effects. An 8 ft simple span was tested first, as shown in Fig. 4.25. Next, continuous configurations with the grid panel spanning over a center stringer was used to investigate negative moment. Three span lengths (4 ft, 5 ft, and 6 ft) were tested using the continuous 2-span condition.

Strain gages were mounted to the bottom surface of main bars at midspan for each span length, as well as quarter-span locations for the 5 ft span (shown in the instrumentation plan in Appendix C). The open grid panel was subjected to a variety of patch load configurations (shown in Appendix C). The open grid panel was supported by continuous roller supports at the ends. If loading only one span, the panel would lift off the far support. In order to represent more realistic field conditions, the open grid deck at the far support was held down to produce continuity. Tests were run with the far support held down in order to obtain a realistic negative moment over the center support. A roller was placed directly above the roller that the panel rested on. A stiffened beam was centered over the roller and bolted to the test setup, as seen in Fig. 4.26.

Figure 4.25: Simply supported 8 ft span with axle load parallel to main bars

Figure 4.26: Pinned condition for far support of continuous span tests

Standard practice for open grid deck installation involves welding main bars to the stringers on the bridge superstructure. To accommodate construction tolerances and open grid deck fabrication tolerances, decks are typically clamped down in order to weld main bars to stringers. In addition to superstructure tolerances, longitudinal and transverse curvatures in open grid decks (produced by the fabrication and hot-dipping galvanization processes) can produce lock-in stresses when connection the deck to the superstructure. In order to eliminate welding the panel to the stringers during installation, an alternate attachment detail was developed. The attachment detail involves using shear studs and filling concrete over the stringer flange. A sacrificial ½ in. plate was bolted to the center stringer of a 2-span continuous span, and concrete was poured flush to the top of the open grid panel. In order to create composite action between the open grid deck and stringer, ¾ in. headed shear studs spaced at 15 in. on center were welded to the sacrificial plate (Fig.

4.27) along the entire width of the open grid deck. Plywood forms, held in place with timber wedges were used to hold the concrete across an 8 in. width over the sacrificial stringer plate (Fig. 4.28). Spray foam was used to fill gaps between formwork and open grid components. A concrete mix with a maximum aggregate size of 3/8 in. and target 28 day strength of 4,500 psi was chosen. A concrete strength of 4,890 psi was attained at 28 days. Figure 4.29 shows concrete placed flush to the top of the open grid panel. Stresses induced by pinning and welding are avoided because the concrete flows under gaps between main bars and the stringer flange.

Figure 4.27: Sacrificial plate with ¾" headed shear studs, bolted to stringer

Figure 4.28: Formwork for concrete pour

Figure 4.29 Concrete poured flush to top of open grid panel

A maximum clear span of 5.1 ft is recommended by the BGFMA for specimen 7.5DIAG2.5TYP1. Supports were placed 5 ft on center for final fatigue tests. Maximum negative moment stresses are induced by patch loads placed at midspan on either side of the continuous center support, with tire patches oriented transverse to main bars at the free

edge. A service level axle load of 32 kips multiplied by an impact factor of 1.33 gives an axle load of 42.6 kips. A typical truck axle patch spacing of 6 ft was reduced to a 5 ft axle (see Fig. 4.30) in order to produce the same stress levels in the spans when negative moment fatigue was investigated. This reduced patch spacing allowed the axle load to be set at 38.2 kips to produce the service level negative moment over the support. The open grid panel was loaded 10 times to this service axle load prior to beginning cyclic fatigue loading.

In order to categorize fatigue of the open grid deck at the location of maximum negative moment, stresses had to be projected to the weld intersection at the top of the grid deck at the center of the middle support. Strain gages were mounted at several locations along the bottom flange of the main bars. Also, strain gages were mounted on the top rib of the outer main bar, located 6 in. from the center of the support. Another strain gage was mounted on the top rib, 2 in. from the center of the support (see Fig. 4.31). Static tests were performed to identify the strain profile along the length of the deck. Linear extrapolation of measured strains was used to determine the load range necessary to fatigue the panel at a targeted fatigue stress range of 25 ksi at the top of the deck. The measured strain profile along the top fiber of the outer main bar is shown in Fig. 4.32. These strains are shown normalized to the maximum strain projected at the top fiber of the open grid deck at the support centerline. Strains at the top fiber were projected using the experimentally determined neutral axis of the outer main bar. The 25 ksi stress range corresponded to an approximate 20 kip load range for the 5 ft axle patch spacing and span configuration. Coincidentally, this 20 kip load range also produced midspan deflections of $l/800$ for the deck in the same configuration.

Figure 4.30: 5 ft axle, negative moment fatigue setup

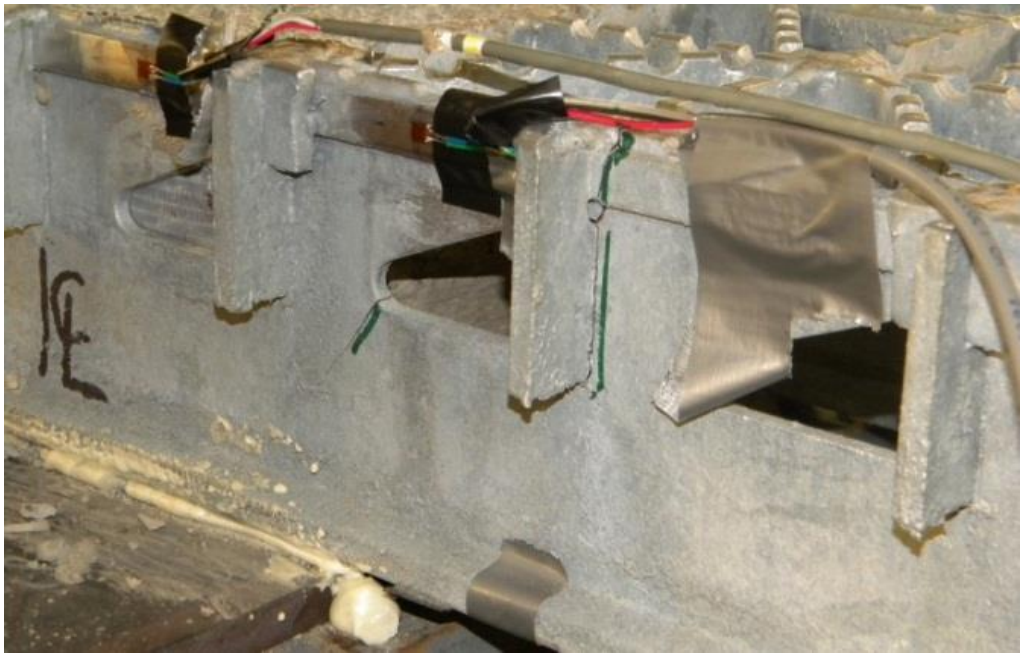

Figure 4.31: Strain gages mounted on outer main bar

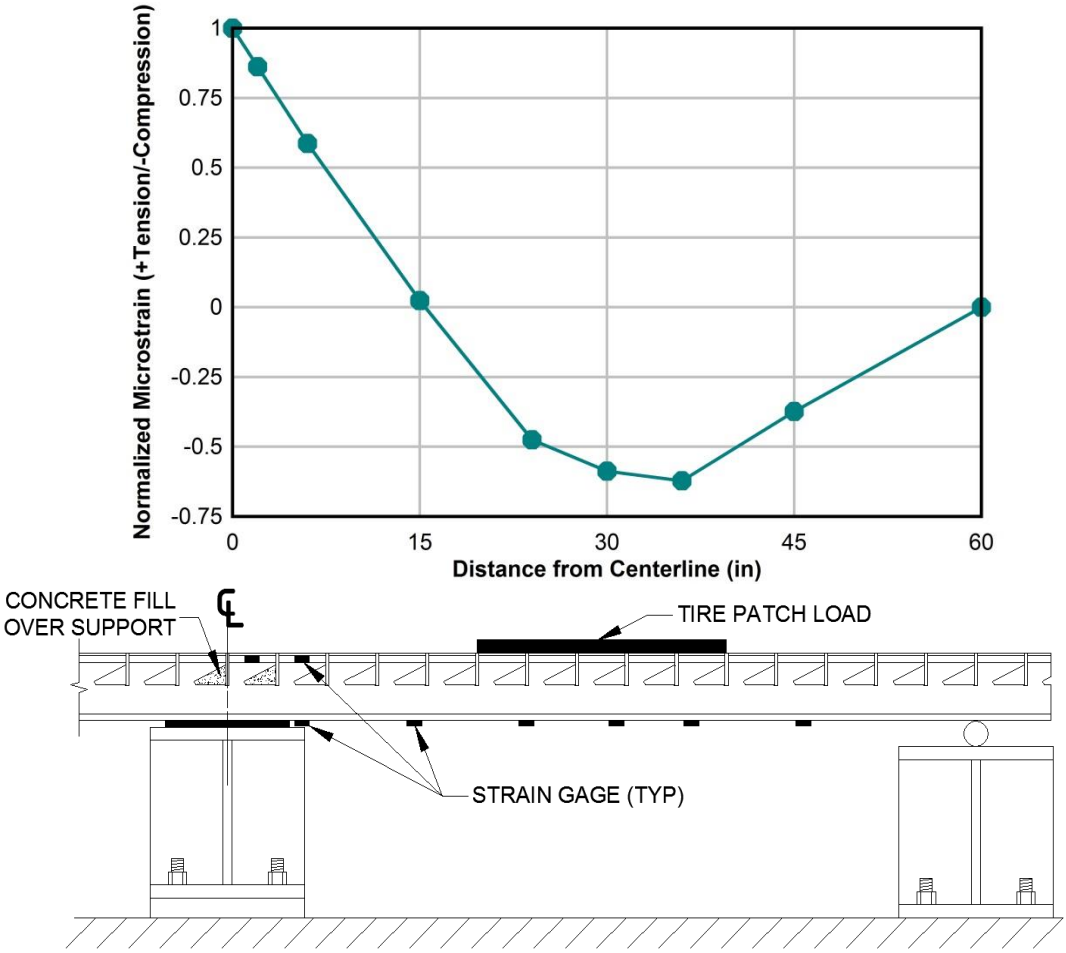

Figure 4.32: Strain at top fiber of outer main bar

The deck stiffness was measured before and during cyclic fatigue testing. Cyclic testing was performed using load control of the servo-hydraulic actuator to produce a load range of 4 to 24 kips. A minimum load of 4 kips was chosen in order to keep the actuator in constant contact with the open grid deck to prevent "walking" of the actuator or patch loads. Cyclic testing was performed at 1 Hz, and data were collected once per hour (every 3600 cycles) in order to monitor changes in stress of the individual open grid deck components. After 10,000 cycles, and each subsequent 100,000 cycles, the displacement

sensors were reattached and 10 cycles of service level load (38.2 kips) were applied to the specimen to measure the deck stiffness.

After one million cycles, no cracking or change in stiffness was observed. The load range was increased to 33 kips (approximately 3.5 to 36.5 kip range) for a targeted stress range of 40 ksi. The speed of testing was decreased to 0.5 Hz (1800 cycles per hour) and data were collected once every 30 minutes. Two cracks in the main bars were observed at 1.03 million cycles. A change in stiffness was also measured at 1.05 million cycles. Widespread cracking and sufficiently large deflection tripped an automatic shut-off switch at 1.086 million cycles. The load range was reduced back to 20 kips to allow for slower propagation of cracking in main bars and cross bars. Stiffness changes at the service level loading were measured at 1.1 million cycles, and each subsequent 100,000 cycles. Testing was stopped at 1.35 million cycles when the open grid panel exhibited extensive cracking in the main and cross bars.

4.5.2 4.0RECT2.5TYP4 Tests

Load distribution tests were run on the full size rectangular open grid panel. Two 2-span continuous configurations with 4 ft and 6 ft spans were tested. Once again, half of the width of one span was heavily instrumented (see Fig. 4.33). Strain gages were mounted on the bottom flange of every main bar and on the midspan cross bar between every main bar of the open grid deck (as opposed to every other main bar as was done on the diagonal open grid panel), and displacement sensors were attached to every main bar in order to develop a more accurate strain and deflection profile. Considering the maximum clear span recommended by the BGFMA is 6.3 ft, most of the tests were performed on the 6 ft span. Single tire patch loads were used throughout the entire testing program for the panel.

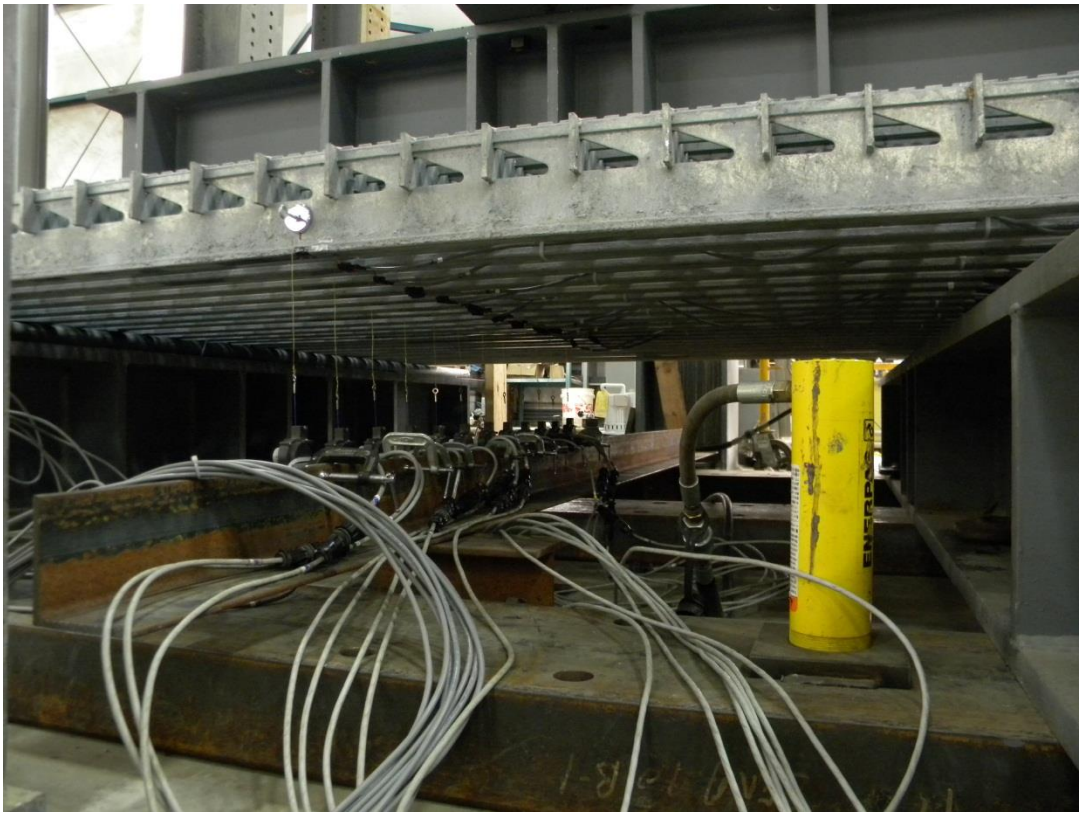

Figure 4.33: Strain gages and displacement sensors on specimen 4.0RECT2.5TYP4

4.5.3 37-R-L-5¼ Tests

Load distribution tests were first run on specimen 37-R-L-5x¼. Because of the 20 in. width of the tire patch, BGFMA's maximum recommended span lengths (which varied between 1.65 ft to 2.35 ft depending on the span configuration, load conditions, and deflection criteria) may not produce Euler-Bernoulli flexural curvatures necessary to compare the panel to available analytical models, so a 4 ft span was used for 24 of 26 tests performed. Two tests were performed on a 2 ft span. Strain gages were mounted on the bottom surface of each main bar at midspan and top surface of main bars at the center support. Strain gages were once again mounted on one half of the width of the open grid

panel, while displacement sensors were attached to each main bar along the entire width at midspan.

Next, the second 37-R-L-5¼ panel was bolted to the first panel. Strain gages were located at the bottom surface of main bars of the second panel in order to measure composite action between adjacent bolted panels. Figure 4.34 shows a typical connection detail, which are spaced at 15 in. on center along the length of the open grid deck. A design detail of the bolted connection is shown in Figure 4.15.

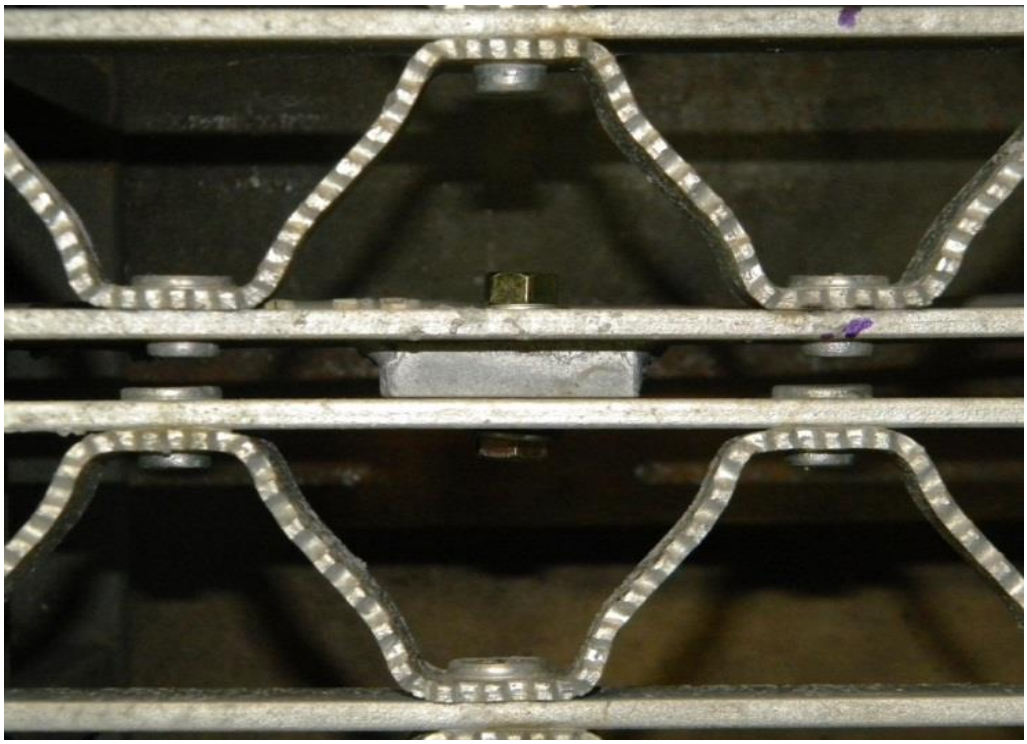

Figure 4.34: Bolted connection of adjacent riveted open grid deck panels

4.5.4 37-R-5¼ Tests

Experimental procedures for specimen 37-R-5¼ were similar to those performed on specimen 37-R-L-5¼. Strain gages and displacement sensors were placed on every other

main bar as opposed to every main bar. Strain gages were mounted on one half of the width of the panel, while displacement sensors spanned the entire width at midspan. An identical panel was bolted to the main panel in order to investigate composite action of two adjacent panels.

A 2-span continuous span configuration with support spacing of 4 ft was used for the 24 tests performed. Additionally, five tests were performed with supports spaced at 3 ft.

4.6 Subcomponent Fatigue Tests

Subcomponent fatigue tests were performed in order to categorize fatigue life of the six different weld types provided and considered for the open grid decks. The test setup shown in Fig. 4.18 was designed to test two subcomponent specimens at a time. Each specimen consisted of three cross bars, resulting in an effective width of one foot in the weak direction. Two (2) 1-½ in. mild steel square bars were welded to outermost main bars of the specimens, and steel rollers were used to load the specimens in a four point loading condition (shown in Fig. 4.35). The steel rollers were attached to a stiffened wide flange spreader beam, which was attached to the 55 kip servo-hydraulic actuator. A four point loading condition was used in order to create a constant stress region across a greater number of welds. Strain gages were placed on the bottom of all three cross bars in the constant stress region. A fourth strain gage was mounted on the side of one cross bar on each specimen in order to determine the neutral axis. This allowed the stress to be projected to the weld intersection where a strain gage could not be placed. For the final two weld types tested (Type 1 and 4 on specimens 7.5DIAG2.5TYP1 and 4.0RECT2.5TYP4, respectively), only two strain gages were mounted on each specimen. These strain gages were placed on the same cross bar in order to identify the neutral axis.

Cross bar stress ranges were consistent across all three cross bars of a particular specimen in all prior tests, so two strain gages were deemed sufficient for later tests. All specimens were monitored continuously during testing, with a maximum of 5,000 cycles between inspections.

A target stress range of 30 ksi at the top of the weld intersection was chosen for cyclic fatigue tests. After two million cycles, no cracking was visible in the first two specimens. Fatigue cracks were not produced because the top of the weld detail was stressed in compression and the bottom of the detail is very close to the neutral axis. After analyzing data from the full scale system tests, reversals of curvature were observed in the cross bars adjacent to the tire patch loads. This reversal places the top of the weld locations on cross bar intersections in tension. This reversal of curvature is likely to produce fatigue at the welded intersections on the cross bars, and thus the experimental setup was modified for this and all subsequent subcomponent fatigue tests. Details of the modified diagonal and rectangular subcomponent specimen setup can be seen in Fig. 4.36. The rollers attached to the spreader beam and support beam were moved out to the edges of the specimens, and the 1-½ in. steel square bars were welded to inner main bars. This new loading condition created a constant moment region with tension at the top of the bars at the welded intersections. Cyclic fatigue loading was restarted, and cracking was observed at 25,000 cycles. Crack locations and extents were marked and monitored closely until 40,000 cycles. At 40,000 cycles, the gap created by the 1-½ in. steel square bars closed up under loading (shown in Fig. 4.37) and the specimens were considered failed because of significant deflections, extensive cracking and loss of stiffness.

Based on this initial specimen, a Category E fatigue detail was assumed for the welded intersections in the cross bar direction. A target N (number of stress range cycles) of at least 100,000 cycles was desired in order to produce cracks in the welds. Based on the failure of the first two specimens, a stress range of 20 ksi was used for the remaining 22 specimens. Load ranges were adjusted as necessary in order to accelerate fatigue tests where needed. These adjustments were typically made for the second pair of specimens (specimens 3 and 4) for a particular weld type where stress projections from neutral axis measurements may not accurately portray stresses induced on the welds, caused by punch-outs for main, diagonal, and supplemental bars. Specimens 1 and 2 of open grid type 4.0RECT2.5TYP5 were subjected to a higher load range after no cracks were observed after 400,000 cycles. The higher load range used was based on the experimentally measured I_y relative to that for specimen 4.0RECT2.5TYP6. Table 4.3 shows load ranges for all subcomponent specimens. Projected stress ranges and normalized fatigue life based on weak direction stiffness tests for each weld type are discussed the proceeding results section. It should be noted that load amplitude should be multiplied by two to get the applied load range. Additionally, the total number of cycles in Table 4.3 represents total number of cycles applied to each specimen at the specified load amplitude, not the number of cycles until first cracking was observed in the individual bars.

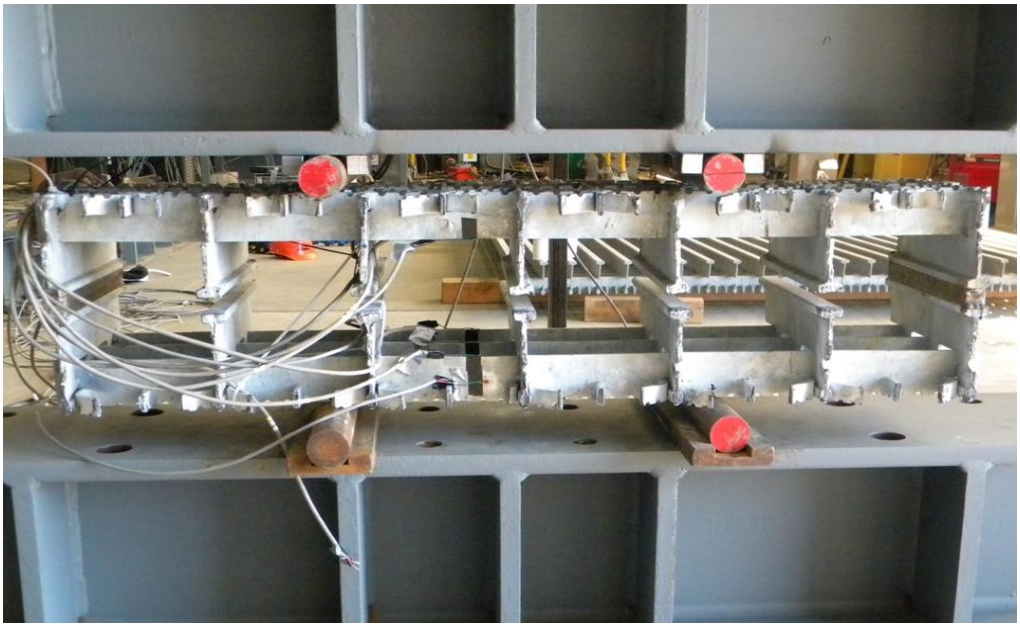

Figure 4.35: Initial subcomponent test setup

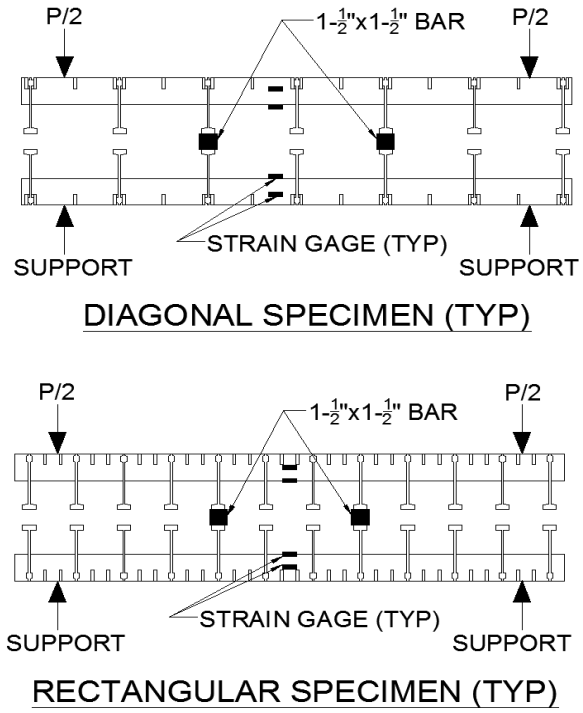

Figure 4.36: Modified subcomponent setups for diagonal and rectangular specimens

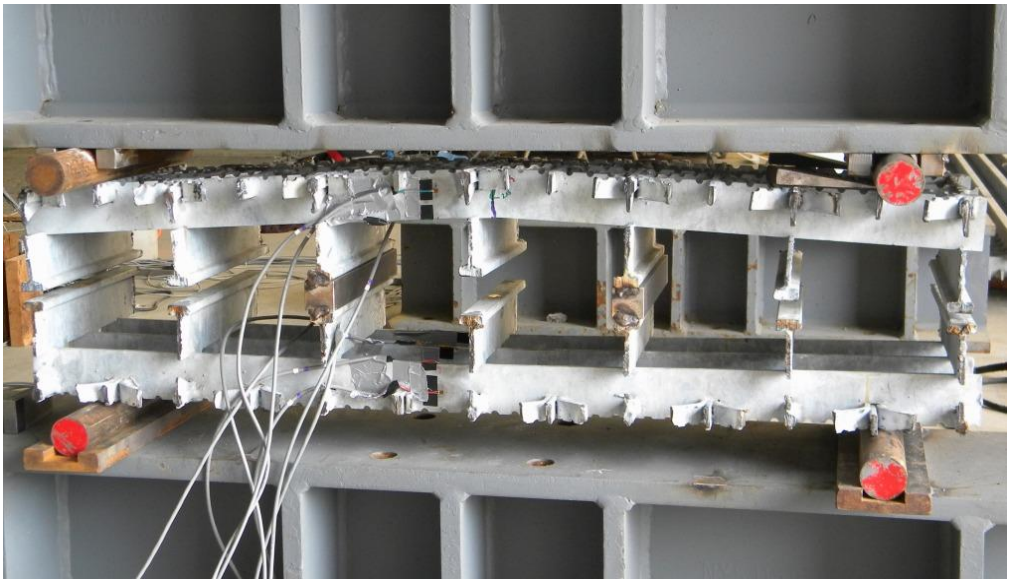

Figure 4.37: Failed subcomponent specimens

Table 4.3: Subcomponent fatigue test matrix

Specimen Type	Specimen #	Load Amplitude (kips)	Total # of cycles
7.5DIAG2.5TYP1	1	1.2	70,000
	2	1.2	70,000
	3	0.875	180,000
	4	0.875	180,000
7.5DIAG2.5TYP2	1	1.2	140,000
	2	1.2	140,000
	3	1.1	150,000
	4	1.1	150,000
7.5DIAG2.5TYP3	1	1.7	40,000[a]
	2	1.7	40,000[a]
	3	1.3	300,000
	4	1.3	300,000
4.0RECT2.5TYP4	1	0.65	35,000
		0.875	90,000
	2	0.65	35,000
		0.875	90,000
	3	0.875	70,000
	4	0.875	70,000
4.0RECT2.5TYP5	1	0.45	400,000
		0.875	156,000
	2	0.45	400,000
		0.875	240,000
	3	0.875	122,000
	4	0.875	155,000
4.0RECT2.5TYP6	1	1.2	460,000
	2	1.2	600,000
	3	1.2	520,000
	4	1.2	520,000

[a] Subjected to 2 million compression fatigue cycles before typical tension fatigue

5 EXPERIMENTAL RESULTS

5.1 Stiffness Tests

Experimental results for each of the strong-, weak-, and torsional-direction stiffness tests are reported in the following sections.

5.1.1 Strong Direction Stiffness (D_x) Results

The strong-direction stiffness (D_x) was established for each specimen in the test program. To develop D_x, firstly the strong-direction moment of inertia (I_{xs}) was determined for each of the deck panels. The stiffness was computed at incrementally increasing applied load amplitudes. There was a variation in the stiffness observed at the low load amplitudes due to the geometric imperfections inherent in the deck panels. As the load increased, the decks bending became more uniform across the width and the stiffness values became stable. Once the stiffness became stable, an average value was determined, as shown in Fig. 5.1 for specimen 7.5DIAG2.5TYP2. Stiffnesses for all specimens were determined in this manner.

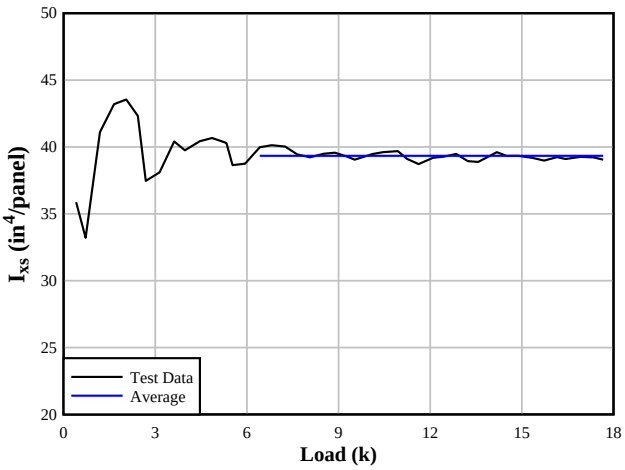

Figure 5.1: Development of I_{xs} values

For analytical orthotropic plate formulations necessary for design, the stiffness must be determined per unit width of deck. Therefore, an effective width for each tested panel must be considered. An example cross-section is shown in Fig. 5.2 to visually demonstrate the effective width. For the welded diagonal and riveted decks, the effective width was taken as the distance between the two outer-most bars plus one-half of the bar spacing (the bar spacing includes supplemental bars, if applicable) added onto the edges. For welded rectangular decks, the effective width is taken as the distance between the two outer-most bars plus the bar spacing (including supplemental bars, 1-1/3 in. in this case) added on the edges. The effective widths of the specimens are shown in Table 5.1. I_{xs} is the total moment of inertia of the entire effective width of the specimen. The resulting I_x and D_x are also shown in per-foot widths in Table 5.1. Section properties for the weak direction (D_y) were developed in the same manner for tests shown in the proceeding section.

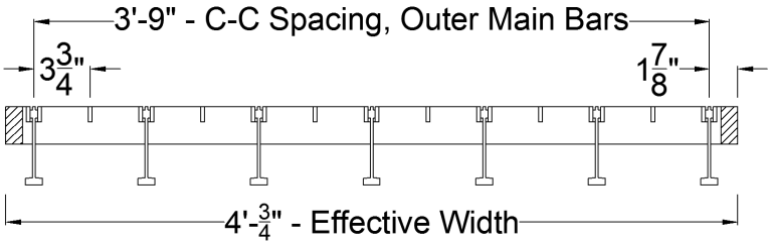

Figure 5.2: Example of effective width for a tested panel

Table 5.1: Strong-direction stiffness values for specimens

Specimen	I_{xs} (in^4/spec)	Effective Width (ft)	I_x (in^4/ft)	D_x (k-in^2/ft)
7.5DIAG2.5TYP1	36.93	4.063	9.091	263,647
7.5DIAG2.5TYP2	39.34	4.063	9.684	280,839
7.5DIAG2.5TYP3	40.14	4.063	9.881	286,561
4.0RECT2.5TYP4	83.56	3.889	21.487	623,110
4.0RECT2.5TYP5	71.63	3.889	18.419	534,154
4.0RECT2.5TYP6	82.95	3.889	21.330	618,567
37-R-L-5x1/4	37.80	4.057	9.316	270,167
37-R-5x1/4	58.08	4.057	14.316	415,169

Diagonal bar strains for the three diagonal welded panels had variable results for each specimen (the strain data is shown in tables in Appendix B). Small variations in the top-of-deck elevations for different components resulted in non-uniform loading of the diagonal bars, therefore the contribution to torsional resistance (given the direction of their span) by the diagonal bars was not quantified.

Considering the entire panel contribution, the distance between the bottom fiber and the neutral axis locations, y_b, was determined by rearranging the following equation:

$$\sigma_i = \frac{M_i y_b}{I_{xs}} \qquad [5.1]$$

where σ_i = average measured main bar bottom fiber stress from D_x test data for each specimen; M_i = static moment from particular load condition for each specimen; and I_{xs} = moment of inertia for each specimen (from Table 5.1).

Neutral axis locations are shown in Table 5.2. The neutral axis, y_b, and σ_i (the measured tensile stress at bottom of main bar shown as negative) were then used in conjunction with stresses measured on supplemental bars in order to investigate the degree of composite

action provided by the supplemental bars. The present method used in BGFMA's section property calculations assumes a 50% contribution of supplemental and diagonal bars to the moment of inertia in their respective orthogonal directions.

Table 5.2: Neutral axis and supplemental bar composite contribution to strong direction

Specimen	I_{xs} (in^4/spec)	$\mu\epsilon_i$ (in/in)	σ_i (ksi)	M_i (k-in)	y_b (in)	Supplemental Bar % Composite
7.5DIAG2.5TYP1	36.93	-238	-6.9	130	1.96	87
7.5DIAG2.5TYP2	39.34	-311	-9.0	160	2.22	90
7.5DIAG2.5TYP3	40.14	-314	-9.1	160	2.28	89
4.0RECT2.5TYP4	83.56	-166	-4.8	160	2.52	--
4.0RECT2.5TYP5	71.63	-181	-5.3	160	2.35	63
4.0RECT2.5TYP6	82.95	-172	-5.0	160	2.59	70
37-R-L-5x1/4	37.80	-709	-20.6	225	3.45	81
37-R-5x1/4	58.08	-400	-11.6	225	2.99	N/A

The experimentally determined moment of inertia and resulting neutral axis were then compared with theoretical section properties calculated by the BGFMA. These section properties were developed considering a cross-section profile containing a punch-out. The punch-out section used is illustrated in Fig. 5.3. Serrations along the top of the main bar are not shown in Fig. 5.3, but are accounted for in the section properties calculated by the BGFMA, located in Table 5.3. Serrations are also taken into account for the supplemental and diagonal bars. Supplemental bars are assumed to be 50% effective for diagonal and rectangular welded open grid decks. For diagonal welded open grid decks, diagonal bar contribution is assumed to be the same as supplemental bar contribution.

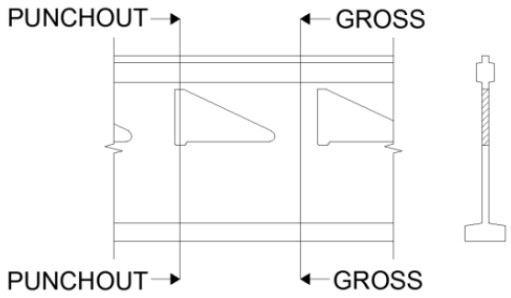

Figure 5.3: Gross and punch-out section profiles

For riveted decks, punch-outs for rivets are neglected in section geometry. A 50% crimp bar contribution is assumed by the BGFMA for both riveted open grid specimens. Comparison of experimental results with the theoretical calculations assuming 50% contribution of crimp bars was sufficiently conservative for design. For the 37-R-L-5x¼ specimen, the supplemental bar is assumed to be 100% effective.

Table 5.3: Comparison of theoretical and experimental I_x

Specimen	BGFMA Calculated I_x (in^4/ft)	Actual I_x (in^4/ft)	% Difference
7.5DIAG2.5TYP1	9.68	9.09	-6.1
7.5DIAG2.5TYP2		9.68	0.0
7.5DIAG2.5TYP3		9.88	2.1
4.0RECT2.5TYP4	16.48	21.49	30.4
4.0RECT2.5TYP5		18.42	11.8
4.0RECT2.5TYP6		21.33	29.4
37-R-L-5x1/4	9.44	9.32	-1.3
37-R-5x1/4	14.13	14.32	1.3

5.1.2 Weak Direction stiffness (D_y) Results

Results for D_y tests were developed in a similar manner to D_x tests, and are shown in Table 5.4. The number of cross bars multiplied by the center-to-center spacing of cross bars for

welded open grid specimens and center to center spacing of crimp bars on the riveted open grid panels were used to develop effective widths for I_{ys}.

Table 5.4: Weak-direction stiffness values for specimens

Specimen	I_{ys} (in^4/spec)	Effective Width (ft)	I_y (in^4/ft)	D_y (k-in^2/ft)
7.5DIAG2.5TYP1	5.7094	6.000	0.9516	27,596
7.5DIAG2.5TYP2	6.7691	7.000	0.9670	28,043
7.5DIAG2.5TYP3	6.9638	7.000	0.9948	28,850
4.0RECT2.5TYP4	5.8996	6.667	0.8849	25,663
4.0RECT2.5TYP5	4.4332	7.000	0.6333	18,366
4.0RECT2.5TYP6	6.2315	7.000	0.8902	25,816
37-R-L-5x1/4	0.6016	3.961	0.1519	4,404
37-R-5x1/4	0.1290	3.961	0.0326	944

Next, the neutral axis for each welded open grid specimen was determined using experimental moment of inertia and strains measured at the bottom of cross bars ($\mu\epsilon_i$), as shown in Table 5.5.

Table 5.5: Weak-direction neutral axis summary for welded open grid specimens

Specimen	I_{ys} (in^4/spec)	$\mu\epsilon_i$ (in/in)	σ_i (ksi)	M_i (k-in)	y_b (in)
7.5DIAG2.5TYP1	5.7094	-552	-16.0	75	1.22
7.5DIAG2.5TYP2	6.7691	-514	-14.9	75	1.34
7.5DIAG2.5TYP3	6.9638	-515	-14.9	75	1.39
4.0RECT2.5TYP4	5.8996	-648	-18.8	90	1.23
4.0RECT2.5TYP5	4.4332	-777	-22.5	90	1.11
4.0RECT2.5TYP6	6.2315	-592	-17.2	90	1.19

Table 5.6 displays I_y data for the six welded open grid specimens. BGFMA calculated section properties account for serrations; however they do not account for punch-outs in the cross bars. These punch-outs are cut into the cross bars in order to fit the continuous main, diagonal, and supplemental bars into the cross bars. Weak direction stiffness varied

for the three different rectangular specimens, which can be attributed to a greater number of punch-outs for main and supplemental bars. Specimen 4.0RECT2.5TYP5 exhibited significantly less stiffness than the other rectangular specimens. This can be attributed to the nature of the type 5 weld, which contains fillet welds in opposite quadrants of the component intersection. The gap between the punch-out and the main/supplemental bar for the type 5 weld (illustrated in Fig. 5.4) does not exist in other weld types, where puddle welds join the gap between the punch-out.

Table 5.6: Comparison of Theoretical and Experimental I_y

Specimen	BGFMA Calculated I_y (in^4/ft)	Actual I_y (in^4/ft)	% Difference
7.5DIAG2.5TYP1	0.977	0.952	-2.6
7.5DIAG2.5TYP2		0.967	-1.0
7.5DIAG2.5TYP3		0.995	1.8
4.0RECT2.5TYP4	0.977	0.885	-9.4
4.0RECT2.5TYP5		0.633	-35.2
4.0RECT2.5TYP6		0.890	-8.9

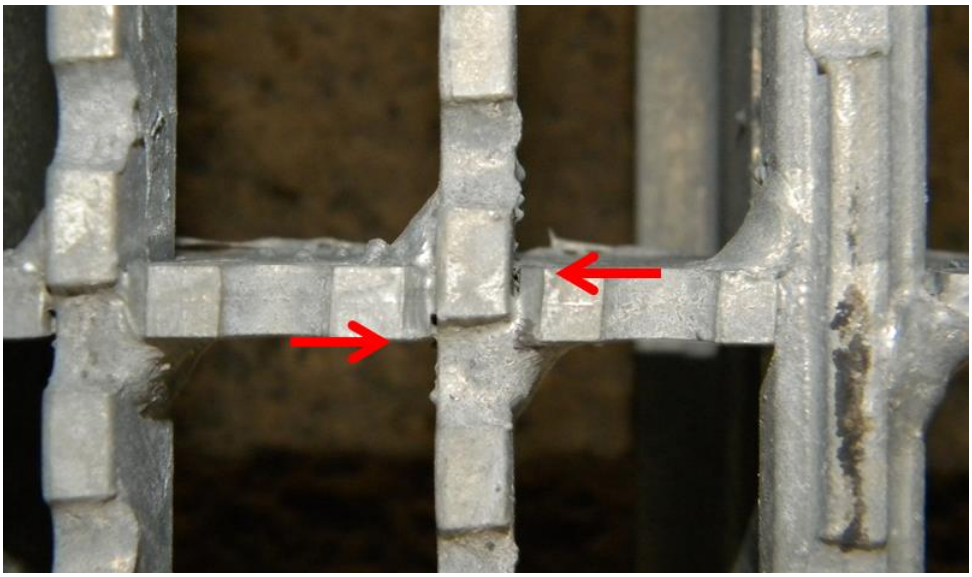

Figure 5.4: Gaps in type 5 weld

5.1.3 Twisting stiffness (D_{xy}) Results

Results for D_{xy} tests are shown in Table 5.7. Load versus displacement for each specimen was linearly curve-fit, and Eqn. 4.4 was used to determine D_{xy} for each specimen. Specimens 37-R-L-5x¼ and 37-R-5x¼ exhibited relatively high torsional resistance that could have time dependent properties after installation. Under repeated loadings, mechanical wear could reduce the friction at the rivet-bar interfaces, consequently reducing the twisting stiffness over time.

Table 5.7: Measured twisting stiffness

Specimen	Load/Displacement (k/in)	D_{xy} (k-in^2/ft)	I_{xy} (in^4/ft)
7.5DIAG2.5TYP1	0.214	1,298	0.045
7.5DIAG2.5TYP2	0.221	1,340	0.046
7.5DIAG2.5TYP3	0.208	1,263	0.044
4.0RECT2.5TYP4	0.200	1,162	0.040
4.0RECT2.5TYP5	0.218	1,267	0.044
4.0RECT2.5TYP6	0.239	1,389	0.048
37-R-L-5x1/4	0.236	1,503	0.052
37-R-5x1/4	0.287	1,834	0.063

5.2 Load Distribution on System Level, Full-Size Open Grid Panels

Several patch load tests were performed for the four different open grid configurations. Strain and displacement data for each test are reported in test matrices in Appendix C. For each open grid type, several different tests were conducted, with different patch orientations, span lengths, and boundary conditions (simply supported and pinned). Several patch locations were tested in order to simulate a truck axle driving over the width of each panel. Reversal of curvature in cross bars was identified during patch load testing of the open grid decks. This is the likely source of weak-direction fatigue.

5.2.1 Weak-Direction Strains from Patch Loads

Patch loads oriented transverse to main bars produced greater strains in both cross bars and main bars than patch loads oriented parallel to main bars. Therefore, patch loads oriented transverse to traffic were marched incrementally from the edge of the panel to the middle of the panel at midspan on the four open grid panels. Superposition was used to project strains on the untested half of the width of the panel. Additionally, the two riveted open grid panels were loaded incrementally from edge to edge. Although maximum span length recommendations dictated by the BGFMA for riveted panels eliminate concern over fatigue and significant curvatures in the weak direction, incremental patch load testing was performed to investigate the strain in the crimp bars and to permit comparisons with finite element model predictions, as discussed in the proceeding chapter.

For specimen 7.5DIAG2.5TYP1, 78 patch load tests were performed on several span lengths and support conditions. Seven more tests (tests 79-85) were performed to recreate a truck axle traveling across the deck to produce the worst weak-direction stresses. Figure

5.5 shows the plan view of the tests, with span length and support conditions. A 5 ft axle was used with two patch loads at midspan of each span. Each patch in all figures represents a 10 kip load (i.e. 20 kip axle). Detailed side views of tests 79-85 are shown in Fig. 5.6. The patch load was placed at the edge of the panel, and then centered over each main bar (spaced at 7.5 in. on center) for one half of the width of the deck. Centering the patch over one main bar produces the highest local weak-direction strain. C55.1-C55.7 represents strain gages mounted on cross bars at midspan. M55.1-M55.7 represents strain gages mounted in the strong direction on main bars at midspan and will be discussed in the following section. Hollow symbols used in Fig. 5.6 indicate a location where data was interpolated from adjacent strain gages, and do not represent actual measured strain. Figure 5.7 displays strain/stress distribution from tests 79-85. Negative values of strain represent tension at the bottom of the cross bar at midspan. Figure 5.8 shows a range of values measured by each strain gage for different patch locations. Additionally, the absolute maximum strain/stress range is shown in Fig. 5.8 for each individual strain gage. Using y_b (Table 5.5) derived from stiffness tests we can project the stress to the weld at the top of the cross bar for each strain gage location, as shown in Table 5.8. Tensile stress ranges at both the bottom and top of the cross bars are displayed as positive values. Location C55.3 is the critical location for the maximum stress range on the midspan cross bar. Figure 5.9 displays the influence of strain/stress at location C55.3, with a line that shows projected strain/stress at the top of the cross bar. This location undergoes more than one cycle of tensile stresses (i.e. fatigue) due to reversal of curvature as the truck moves over the width of the panel. Stress/strain approaching zero as truck moves away from the critical location is not shown, but assumed when the patch reaches a point further than the effective load width created by the patch.

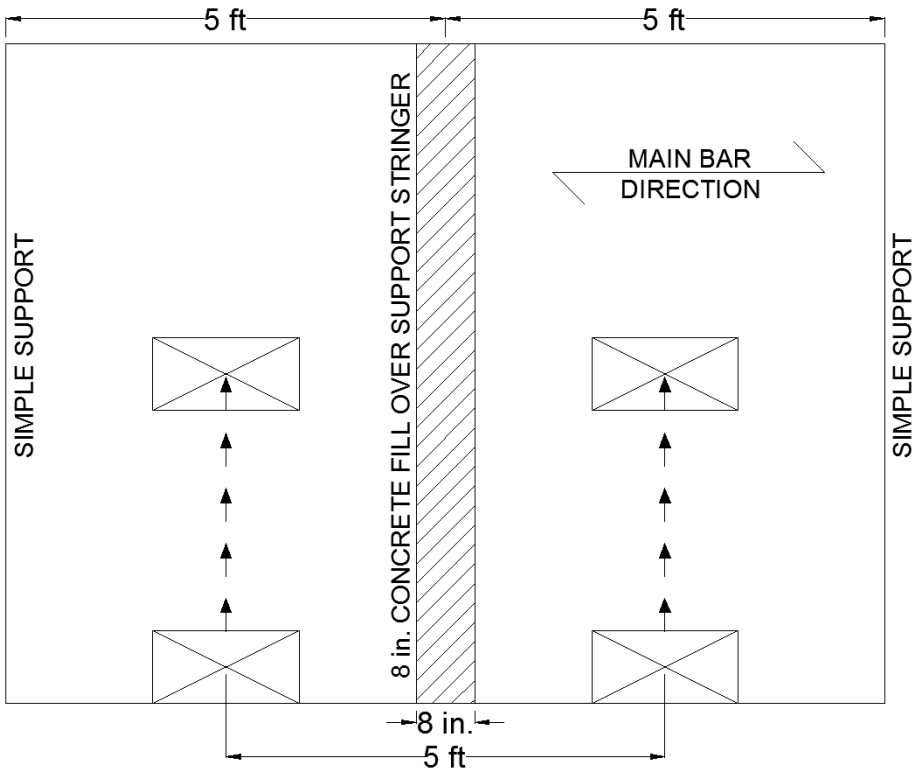

Figure 5.5: Plan view of 7.5DIAG2.5TYP1 setup to investigate weak direction stress

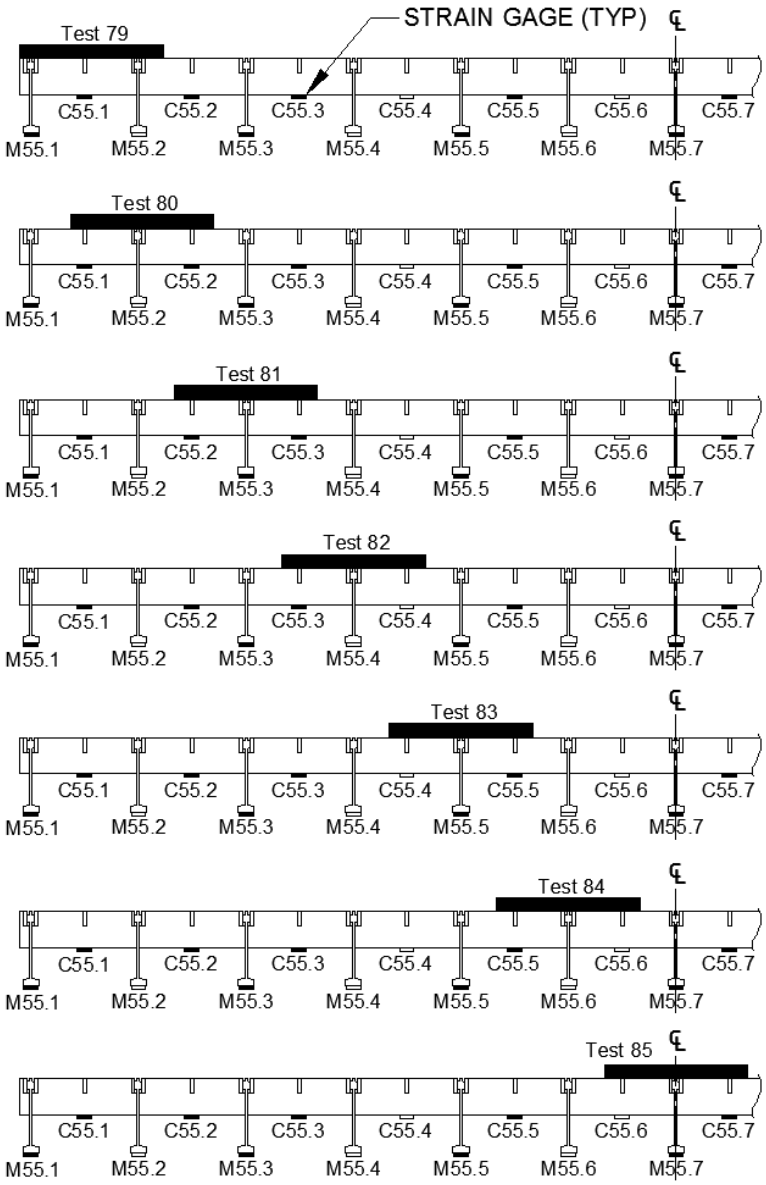

Figure 5.6: Section view at midspan for tests 79-85

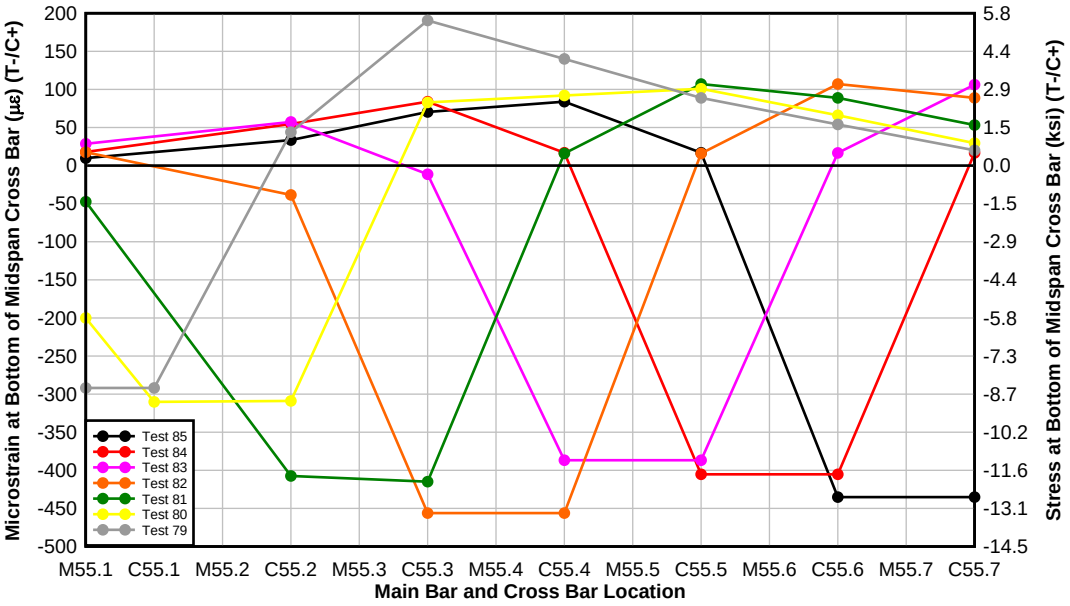

Figure 5.7: Distribution of cross bar stress for each patch location, tests 79-85

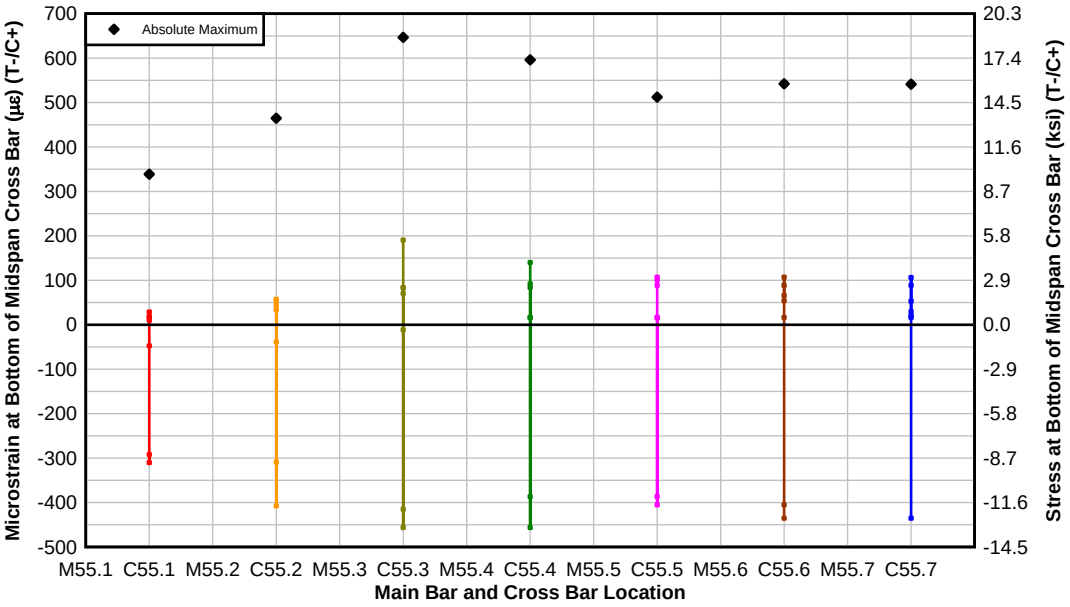

Figure 5.8: Maximum and minimum strains at each gage location, and absolute maximum strains, tests 79-85

Table 5.8: Strain/stress range on cross bar located at midspan as tire patch moves across Specimen 7.5DIAG2.5TYP1 for main bars oriented transverse to traffic

Strain Gage Location	Bottom of Crossbar		Top of Crossbar/Weld
	Strain Range (με)	Stress Range (ksi)	Stress Range (ksi)
C55.1	339	9.8	10.3
C55.2	465	13.5	14.1
C55.3	647	18.8	19.7
C55.4	596	17.3	18.1
C55.5	512	14.9	15.6
C55.6	542	15.7	16.5
C55.7	541	15.7	16.5

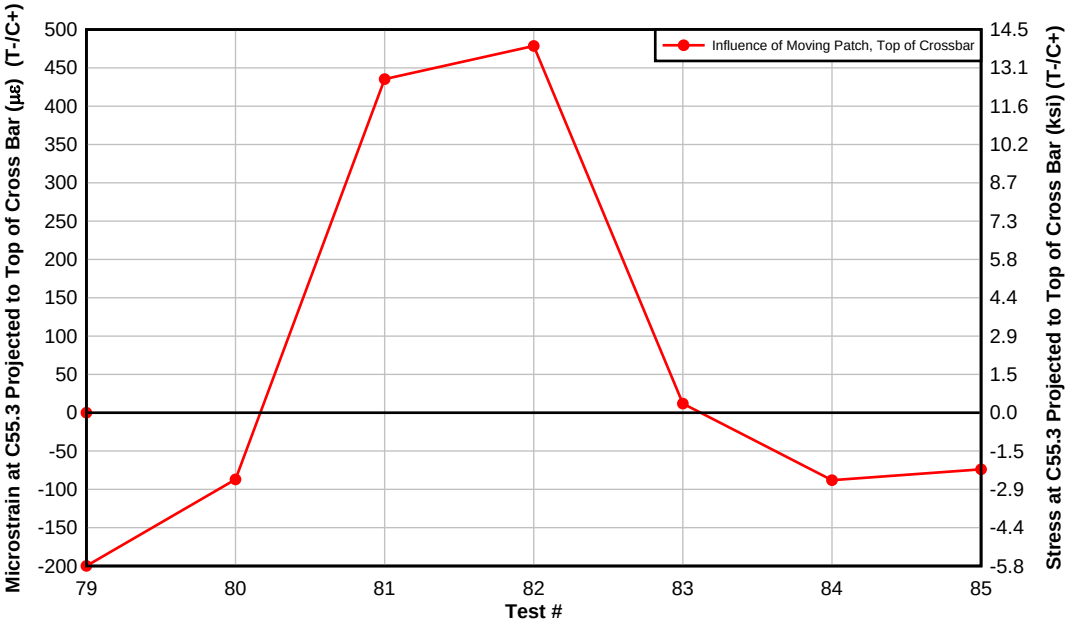

Figure 5.9: Influence of moving patch load at C55.3 projected to top of cross bar

The moving patch load was repeated for specimen 4.0RECT2.5TYP4, although only a single patch load was used for these tests. Figures 5.10 and 5.11 display the setup and test matrix for tests 92-113. The panel was tested at a 6 ft span, which is slightly less than the maximum recommended span length set by the BGFMA for this particular panel. A strain gage was located on the midspan cross bar between every main bar for the half of deck subjected to patch loading. The patch load was moved along one-half the width of the

panel at midspan at a 2 in. increment. Figure 5.12 displays strain/stress distribution from tests 92-113. Negative values of strain/stress represent tension at the bottom of the cross bar at midspan. Figure 5.13 shows a range of values measured by each strain gage for different patch locations. Additionally, the absolute maximum strain/stress range is shown in Fig. 5.13 for each individual strain gage. Again, using y_b (Table 5.5) derived from stiffness tests we can project the stress to the weld at the top of the cross bar for each strain gage location, as shown in Table 5.9. Tensile stress ranges at both the bottom and top of the cross bars are displayed as positive values. The strain gage at C5 was determined to be the location of maximum stress range in the midspan cross bar, and the influence of the moving patch load is displayed in Fig. 5.14.

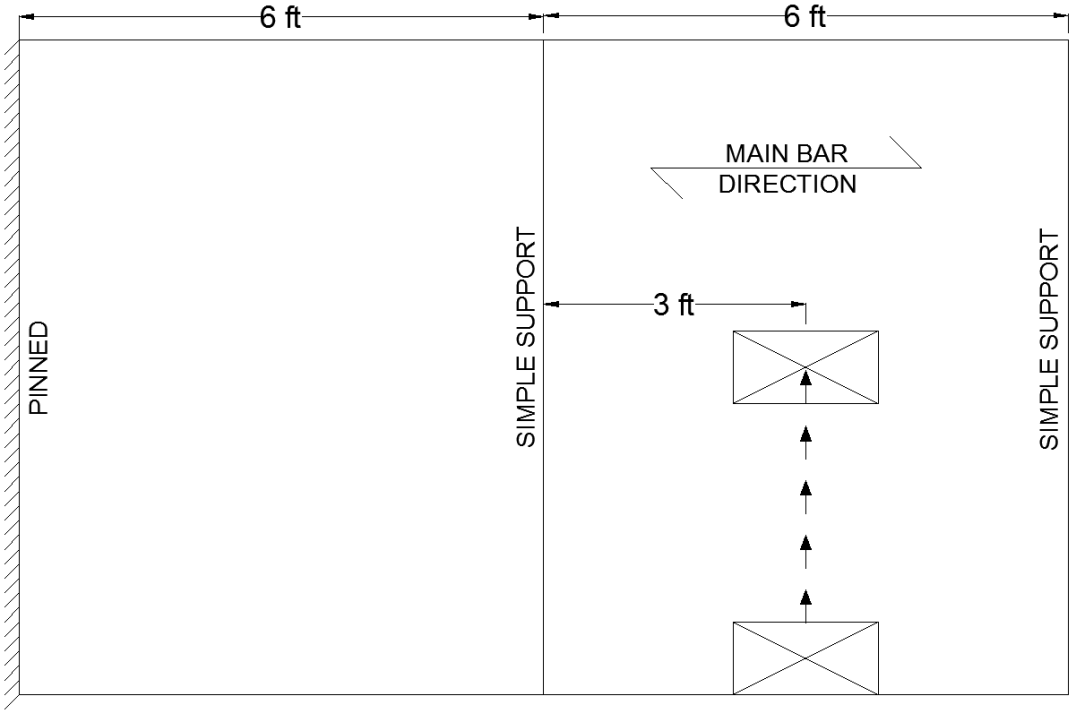

Figure 5.10: Plan view of specimen 4.0RECT2.5TYP4 setup to investigate weak direction stress

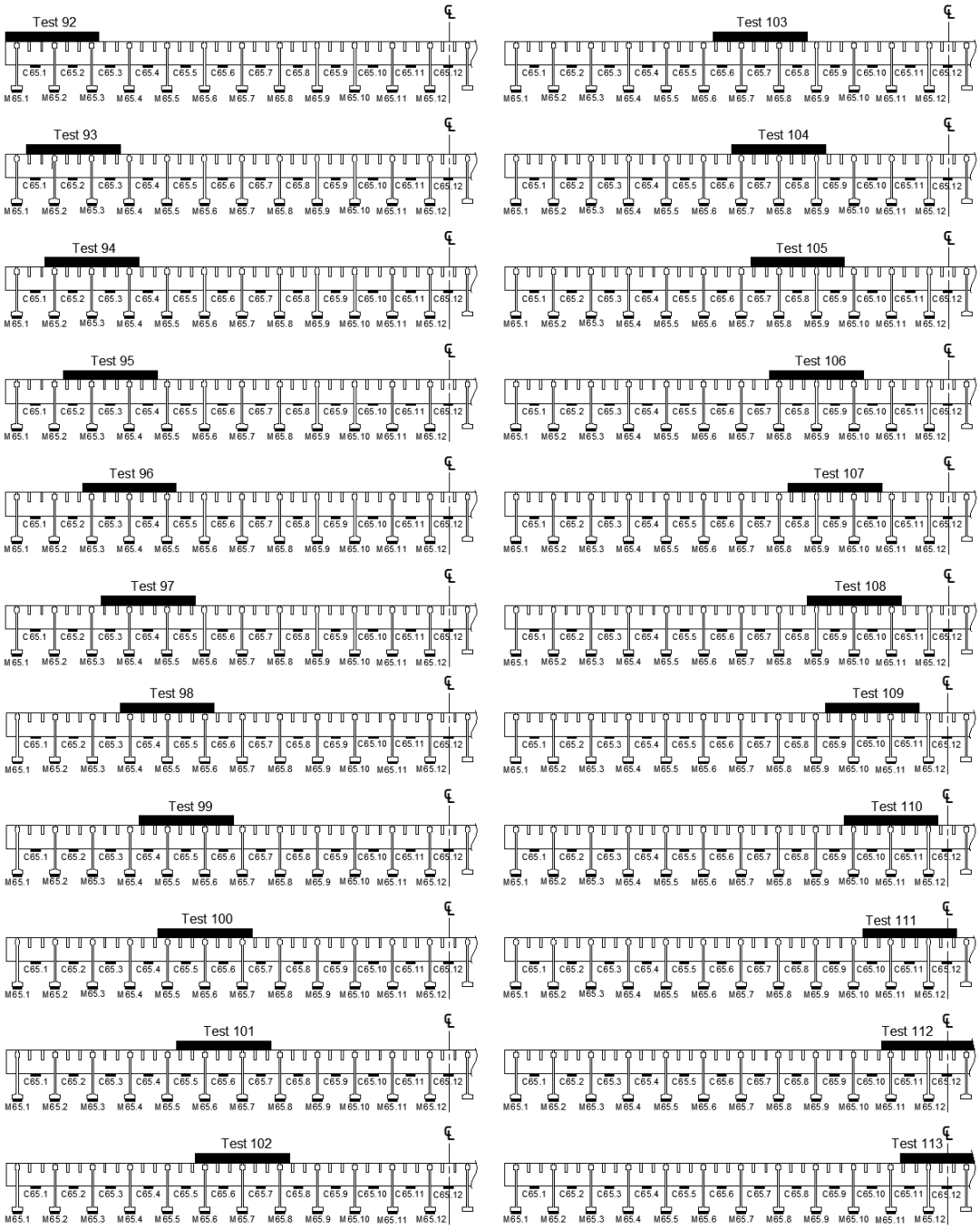

Figure 5.11: Section view at midspan for tests 92-113

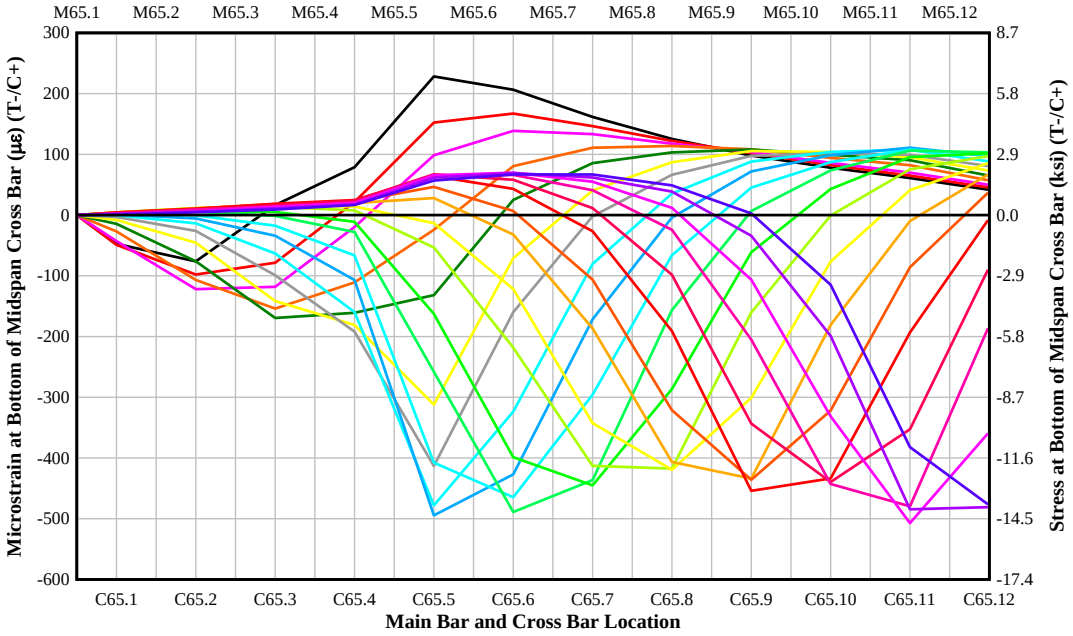

Figure 5.12: Distribution of cross bar stress for each patch location, tests 92-113

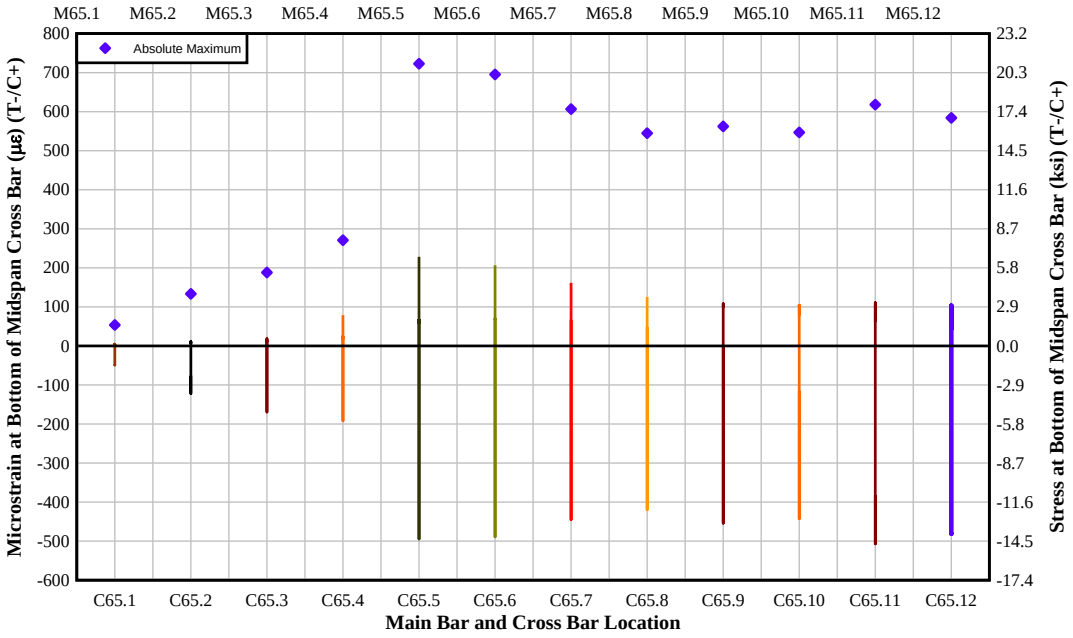

Figure 5.13: Maximum and minimum strains at each gage location, and absolute maximum strains, tests 92-113

Table 5.9: Strain/stress range on cross bar located at midspan as tire patch moves across Specimen 4.0RECT2.5TYP4 for main bars oriented transverse to traffic

Strain Gage Location	Bottom of Crossbar		Top of Crossbar/Weld
	Strain Range (με)	Stress Range (ksi)	Stress Range (ksi)
C65.1	54	1.6	1.6
C65.2	133	3.9	4.0
C65.3	188	5.5	5.6
C65.4	271	7.9	8.1
C65.5	723	21.0	21.6
C65.6	695	20.2	20.8
C65.7	607	17.6	18.2
C65.8	545	15.8	16.3
C65.9	562	16.3	16.8
C65.10	547	15.9	16.4
C65.11	618	17.9	18.5
C65.12	584	16.9	17.5

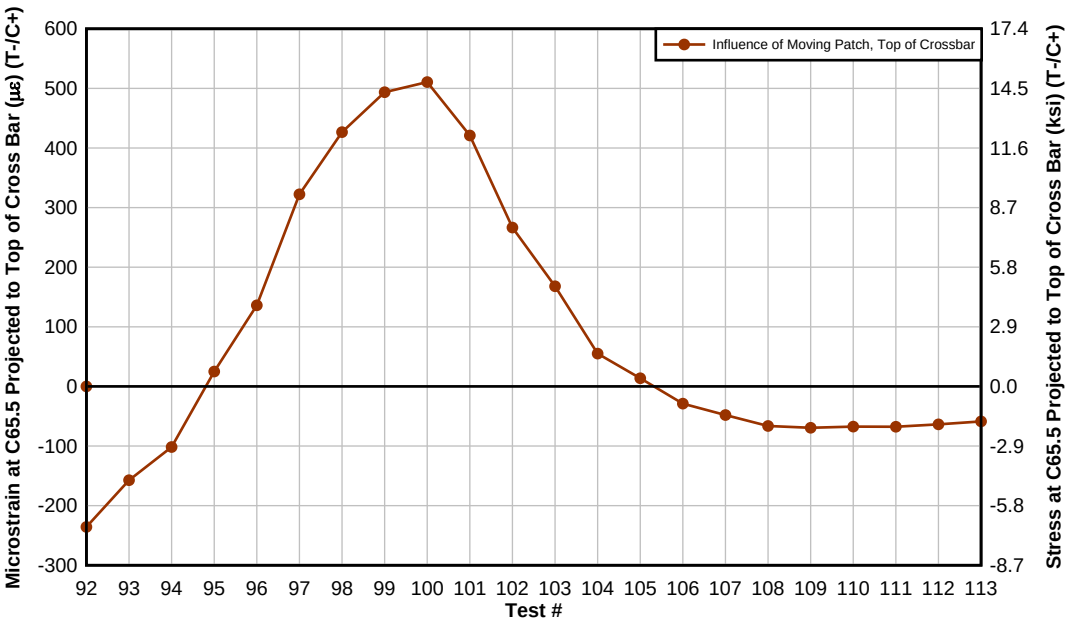

Figure 5.14: Influence of moving patch load at C65.5 projected to top of cross bar

5.2.2 Influence of Span Length on Strains in Classical Loading Conditions

In order to understand the strong direction behavior of open grid decks with respect to varying span lengths and patch orientation, specimen 7.5DIAG2.5TYP1 was tested with three different span lengths, with support conditions held constant. Testing various span lengths allows investigation of the maximum strong- and weak-direction stresses between span length values prescribed in design tables by the BGFMA. Figure 5.15 shows the plan view of the test configuration. Four tests for each span length (where L =4 ft, 5 ft, and 6 ft) were compared. Tire patches were placed at the centerline of the width ($y = w/2$), and at the free edge of the panel, oriented transverse and parallel to main bars.

Figure 5.16 shows strong-direction strain distribution in main bars at midspan from the free edge of the panel to the centerline of the width ($y = 0$ to $y = w/2$). Individual lines of data are not shown in the legend, those based on patch orientation. Center-line and edge patch load strains are also displayed in Fig. 5.16. While main bar strain magnitudes increase with increasing span length for each of the four loading conditions, strain distribution is similar. For a given span length, main bar strains are higher at the edge due to a transversely oriented tire patch in relation to a patch oriented parallel to main bars. This relationship is opposite for a patch load at the center-line of the width, with parallel oriented patch loads inducing a higher main bar strain. The patch load is in contact with more main bars in the parallel orientation at the centerline, which results in lower stresses than a transverse patch. However, a patch oriented parallel to main bars at midspan acts more like a point load than a transverse oriented patch, which acts more-so as a uniform load along the span of the main bars. Given a proportionally short span length in relation

to the 20 in. patch load along the main bar, coupled with sufficiently high weak direction stiffness, and a parallel patch orientation produces higher main bar strains.

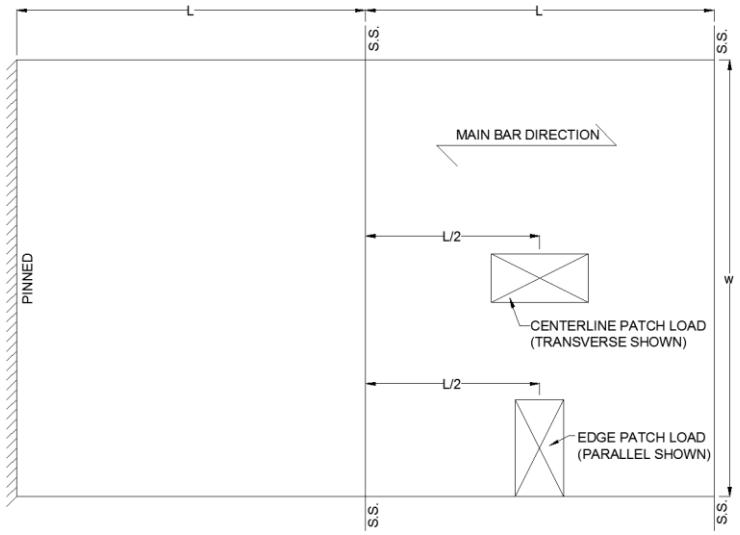

Figure 5.15: Test configuration for classic loading conditions for varying span lengths

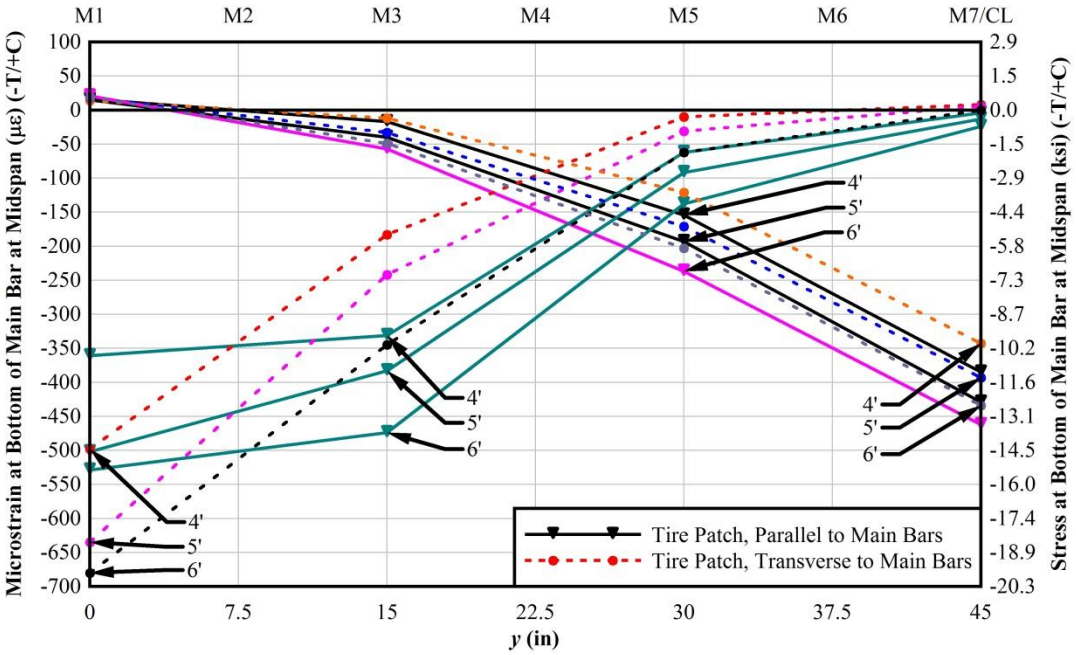

Figure 5.16: Strain/stress in main bar for varying span lengths

Weak-direction stress and strain for varying span lengths are shown in Fig. 5.17 and quantified in Table 5.10. For parallel and transverse tire patches at the centerline of the width, strain gages were located at on the bottom of closest cross bar beneath the center of the patch for each span length tested. For the transverse patch at the edge, strain gage readings were taken from the cross bar that corresponds with midspan of the 5 ft span. While the strain gage reading at C55.3 (observed as the critical location for the weak direction tensile stress) is only a true midspan reading for the 5 ft span, the transverse patch covers a 20 in. length along the span in which the cross bar is still located underneath for the 4 ft and 6 ft spans. Tensile stresses for the parallel and transverse patch at the centerline are shown, while compressive stresses are shown for the transverse patch at the edge for each respective span length.

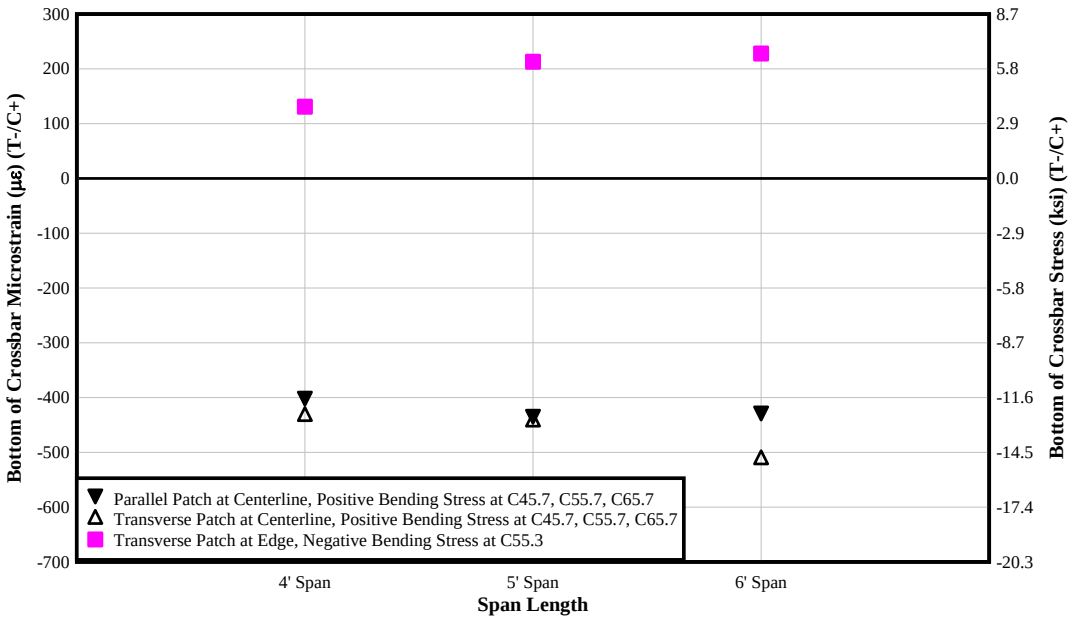

Figure 5.17: Cross bar strain/stress for varying span lengths

Table 5.10: Cross bar microstrain for varying span lengths and patch load orientations

Patch Location	Orientation	Span Length (ft)	Strain Gage	Microstrain, Bottom of Crossbar (+C/-T)
Centerline	Parallel	4	C45.7	-406
Centerline	Parallel	5	C55.7	-439
Centerline	Parallel	6	C65.7	-433
Centerline	Transverse	4	C45.7	-434
Centerline	Transverse	5	C55.7	-444
Centerline	Transverse	6	C65.7	-513
Edge	Transverse	4	C55.3	131
Edge	Transverse	5	C55.3	213
Edge	Transverse	6	C55.3	228

5.2.3 Fatigue of 7.5DIAG2.5TYP1 panel

Specimen 7.5DIAG2.5TYP1 was investigated for strong- and weak-direction fatigue. The configuration from test 79 (see Figs. 5.5 and 5.6) was used for this test. Over the negative support, fatigue was induced at the free edge of the panel. Figure 5.18 shows a plan and side view of the area of the specimen subject to fatigue cracking. After one million cycles at a projected stress range of 25 ksi at the top of the main bar at the center support, there was no cracking or change in stiffness observed. The target stress range was increased to 40 ksi in order to accelerate fatigue. After 30,000 cycles, the outer main bar cracked. The crack is located at a cross bar punch-out through the top rib on the north span, shown in Fig. 5.19. The crack continued through the punch-out, through the web, and finally through the bottom flange. At 1,086,000 cycles, significant cracking in the outer main bar on the south span was observed (Fig. 5.20), as well as cracking in the adjacent inner main bar. The stress range was then decreased to the original 25 ksi range, however due to significant amount of cracking and loss of stiffness in the outer two main bars, a 25 ksi

stress range was no longer observed in the outer main bar over the center support. Stresses were redistributed to other components. The largest stress range increase was observed to be in the cross bars underneath the tire patch contact area. As the main bars under the contact area of the tire patch continue to crack and lose stiffness, the cantilever action of the cross bars increases and a stress concentration is produced at the intact main bar adjacent to the two cracked main bars. Cracking is seen in the weak direction at the weld intersection of these cross bars, shown in Fig. 5.21. Crack mapping is shown in Appendix D. Testing was stopped at 1,350,000 cycles when the setup became too unstable due to excessive deflections and rotations caused by significant cracking of main bars and cross bars.

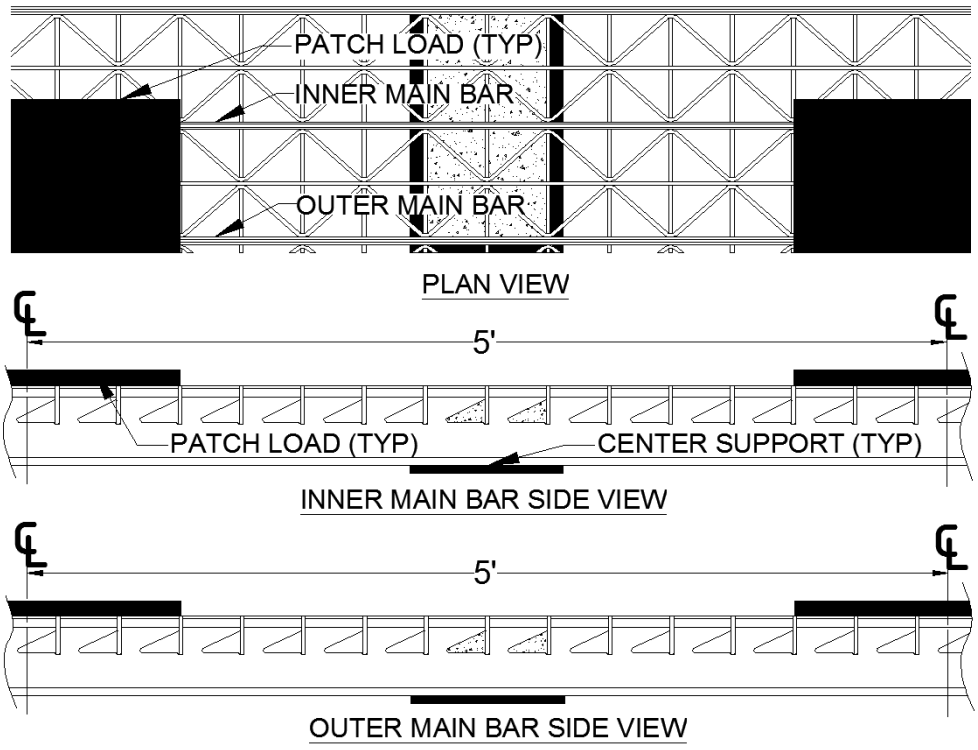

Figure 5.18: Plan and side view of critical area for fatigue cracking

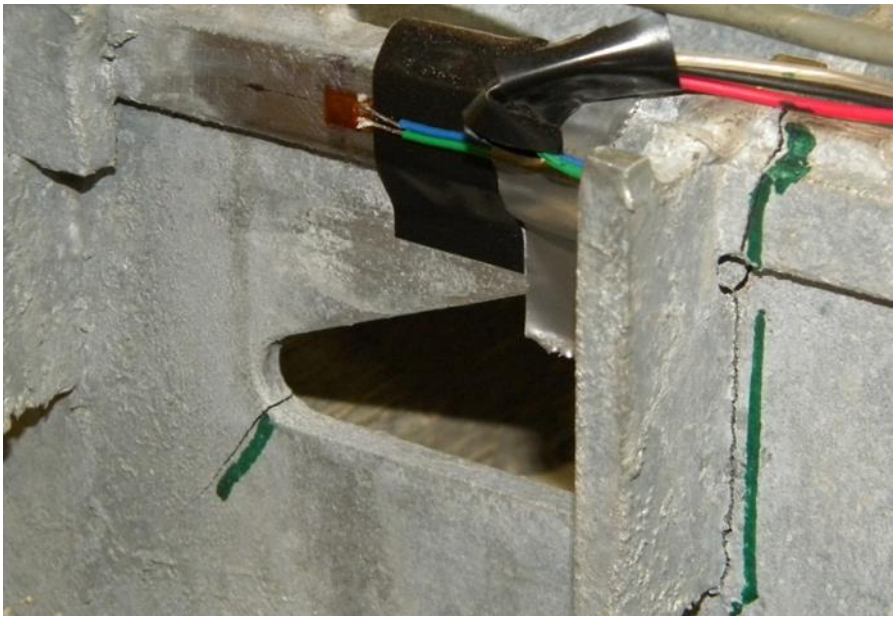

Figure 5.19: Cracking in outer main bar, north span

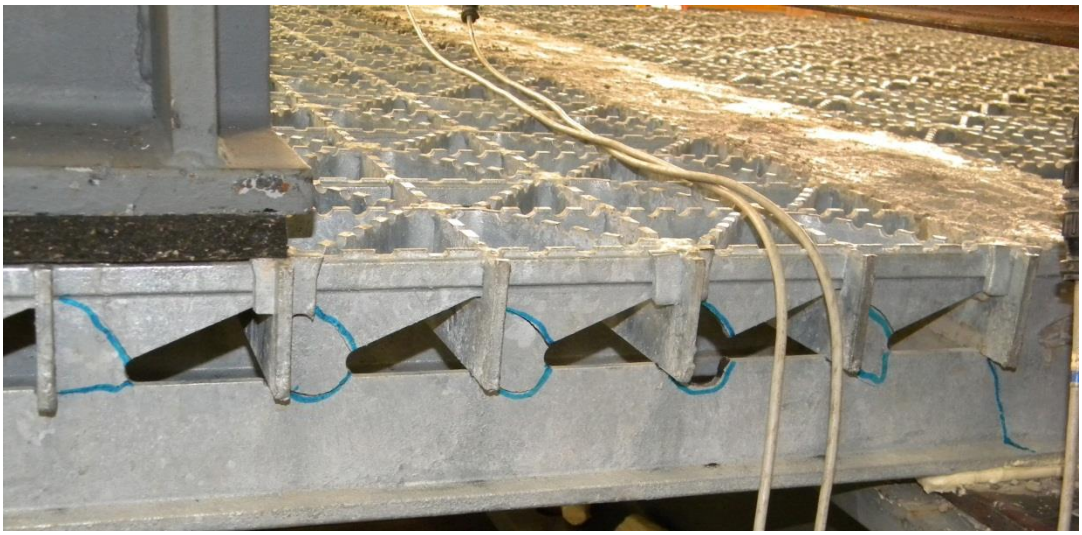

Figure 5.20: Cracking in outer main bar, south span

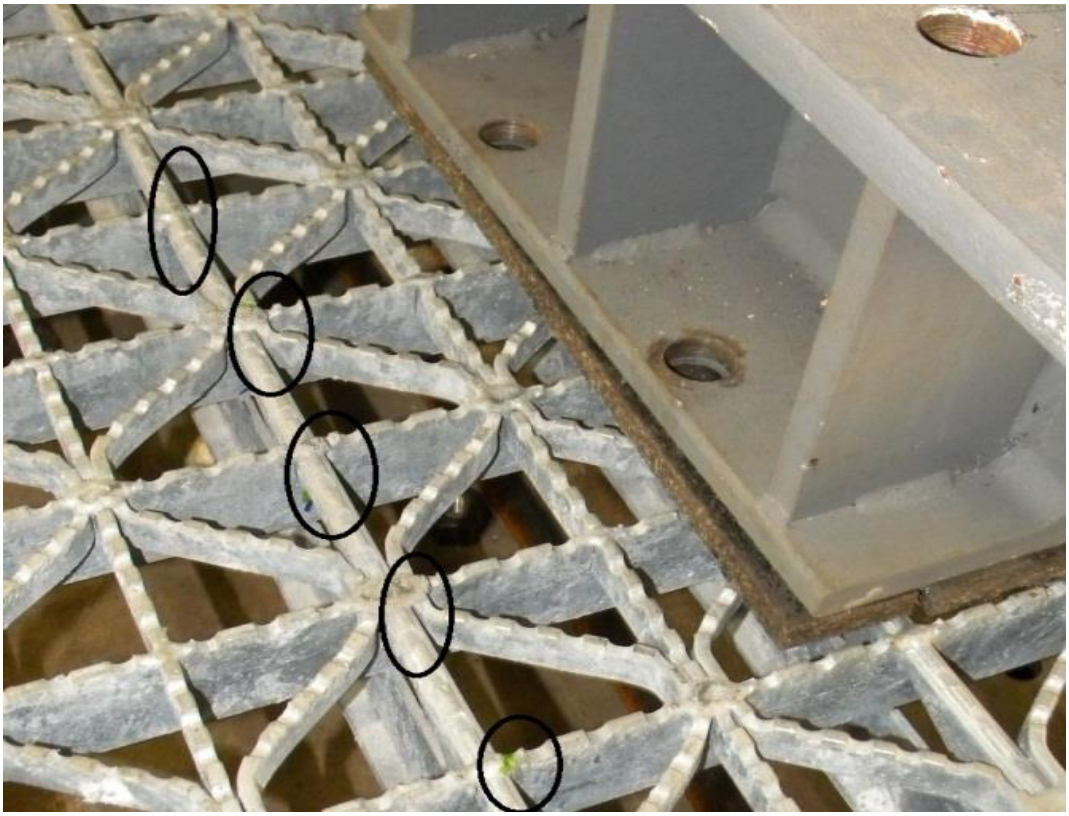

Figure 5.21: Cross bar cracks

Loss of stiffness is shown in Table 5.11 and Fig. 5.22. Deflections were measured at the outer main bar at midspan, on the north span of the test setup. N_{25} was used to plot the equivalent number of cycles versus midspan deflection in order to display loss of stiffness at a consistent stress range; the approximate 25 ksi stress range.

Measured stresses were used to calculate fatigue life of main and cross bars. Table 5.12 displays stress in the outer and inner main bar (see Fig. 5.18), and cross bar. Stresses for the inner main bar were interpolated from measured stresses on main bars on either side of the inner main bar (including the outer main bar). Once the outer main bar cracks, readings from strain gages on the outer main bars become unreliable and as a result, inner main bar stresses could no longer be interpolated. Therefore, stresses were chosen based on load

range and corresponding uncracked outer main bar stress, since this becomes the outer-most main bar after the outer main bar loses most of its stiffness due to significant cracking. While several cross bars cracked during testing, cross bar stress measurements come from a strain gage at midspan of the north span at the critical tensile stress location (i.e. 'C55.3' in the preceding section). Figure 5.23 shows fatigue life categorization for cracked components.

While strong and weak direction fatigue categorization were the goals of this test, strong direction fatigue is not typically reported to be of interest for in-service welded open grid bridge decks. The load scenario for this test created an artificially high negative moment over the center support in order to accelerate and induce cracking of main bars. While main bars remained intact, cross bar stress cycles were not sufficiently large to produce fatigue cracks by simply cycling the load in this particular load scenario. Once main bars began to crack, cross bars supporting the patch loads were subjected to higher stresses which eventually resulted in cracking of the welds in the weak direction. While cross bar fatigue life categorization from this test is consistent with fatigue tests in the proceeding section, the stresses produced in the experimental setup are not the same as those induced for in-service open grid decks. As described in section 5.2.1, a moving tire patch creates a higher net stress range in cross bars than that of a tire patch at a single location.

Table 5.11: Deflection vs. # of cycles until failure

N	N_{25}	Outer Main Bar Midspan Deflection (in/kip)
10	10	0.00414
100,000	100,000	0.00376
200,000	200,000	0.00412
300,000	300,000	0.00416
400,000	400,000	0.00416
500,000	500,000	0.00425
1,000,000	1,000,000	0.00404
1,050,000	1,204,800	0.00474
1,100,000	1,366,300	0.00598
1,200,000	1,466,300	0.00583
1,300,000	1,566,300	0.00809
1,350,000	1,616,300	0.01255

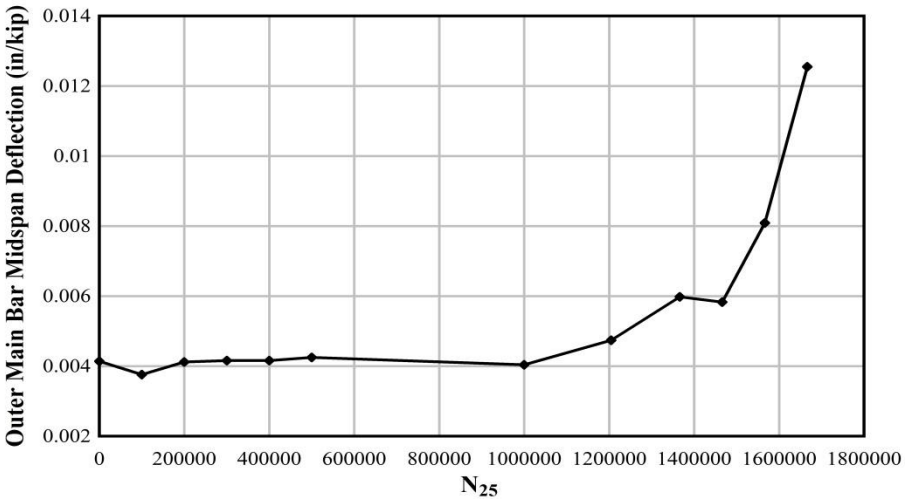

Figure 5.22: Midspan deflection vs. # of cycles until failure

Table 5.12: Stress and number of cycles until failure

N (Cumulative)	Load Range (kips)	Top of Outer Main Bar at Center Support		Top of Inner Main Bar at Center Support		Top Of Cross Bar at Midspan	
		Stress (ksi)	Cumulative N_{25}	Stress (ksi)	Cumulative N_{25}	Stress (ksi)	Cumulative N_{25}
100,000	20	23.7	85,221	17.5[a]	34,340	5.2	912
200,000	20	25.0	184,657	17.9[a]	70,949	5.6	2,064
300,000	20	25.4	288,946	18.0[a]	107,980	5.7	3,236
400,000	20	25.6	395,884	18.0[a]	145,417	5.7	4,440
500,000	20	25.0	495,723	17.8[a]	181,484	5.7	5,655
1,000,000	20	24.0	938,574	17.3[a]	347,443	5.9	12,209
1,030,000	33	39.0	1,052,163	30.7[a]	402,966	10.7	14,593
1,050,000	33	Cracked	Cracked	39.0[b]	478,692	11.6	16,574
1,086,000	33	Cracked	Cracked	39.0[b]	614,999	13.1	21,784
1,100,000	20	Cracked	Cracked	25.0[b]	628,976	8.9	22,423
1,200,000	20	Cracked	Cracked	25.0[b]	728,815	8.8	26,726
1,300,000	20	Cracked	Cracked	25.0[b]	828,653	Cracked	Cracked
1,350,000	20	Cracked	Cracked	Cracked	Cracked	Cracked	Cracked

[a] Stress linearly interpolated from adjacent main bars on either side of inner main bar

[b] Stress assumed to be outer main bar stress based on load range, after outer main bar is cracked

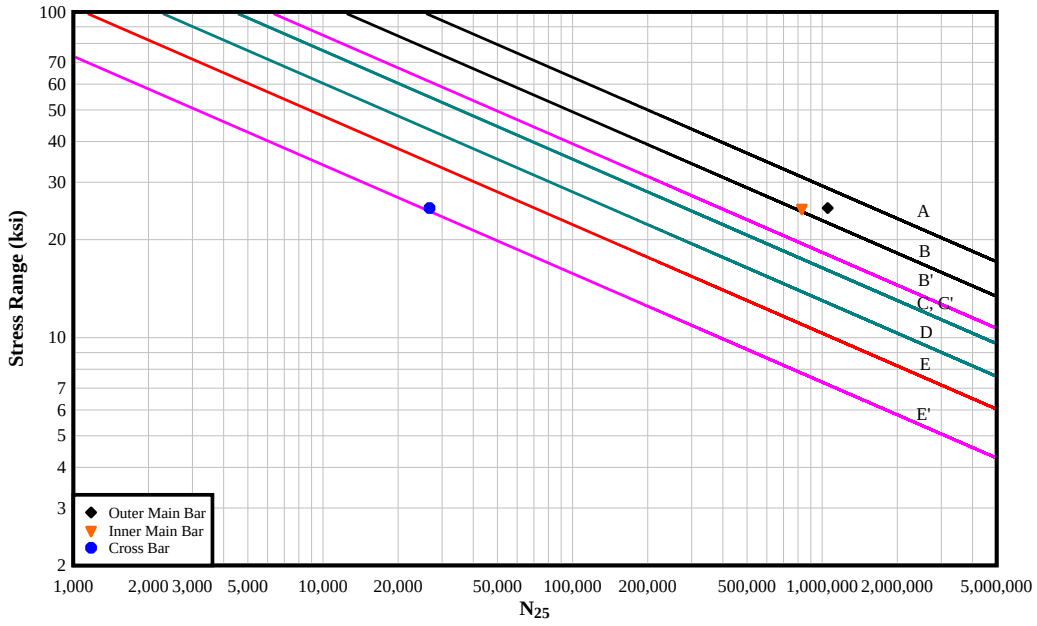

Figure 5.23: Stress range vs. number of cycles until crack initiation (infinite life thresholds are not shown)

5.2.4 Composite Action of Bolted Riveted Panels

Riveted open grid decks are bolted every 15 in. along the length of the main bars located at the free edge. Composite action of adjacent riveted open grid panels was investigated in order to determine what effect, if any, the bolt connection has on lowering stress in the free edge main bar. Figures 5.24 and 5.26 show section views of identical tests performed on specimens 37-R-L-5x1/4 and 37-R-5x1/4, respectively. Plan views of these test setups can be found in the Appendix. Transverse patch loads are placed at midspan at the free edge in tests 130/156. The patch load remains in the same location for tests 143/169, with the two panels bolted together. The transversely oriented patch load is placed over the center of the bolted connection at midspan in tests 145/171. Tests 128/154, 144/170 and 146/172 are similar to tests 130/156, 143/169 and 145/171, but parallel oriented tire patch is used. Figures 5.25 and 5.27 display strain from the bottom flange of main bars for a 10 kip patch load, with negative strain/stress representing tension measured at the mid-span strain gage locations (bottom of main bars). The ¾ in. gap between the main panel and the adjacent bolted panel is not shown in Figs. 5.25 and 5.27, y = 0 represents the centerline of M1 and M1*, the free edge main bars for each of the bolted panels.

For both the 37-R-L-5x1/4 and 37-R-5x1/4 panels, the bolted connection lowers the stress magnitude of the outermost main bar (M1). However, the magnitude of stress in adjacent main bars (i.e. M2-M5) is similar to that of an unbolted panel. If the bolted connection provided 100% composite action, strain for M1 and M1* would be the same for a patch load placed at the free edge of one panel (i.e. Test 143). Table 5.13 displays strains for composite action tests and their relative % composite action.

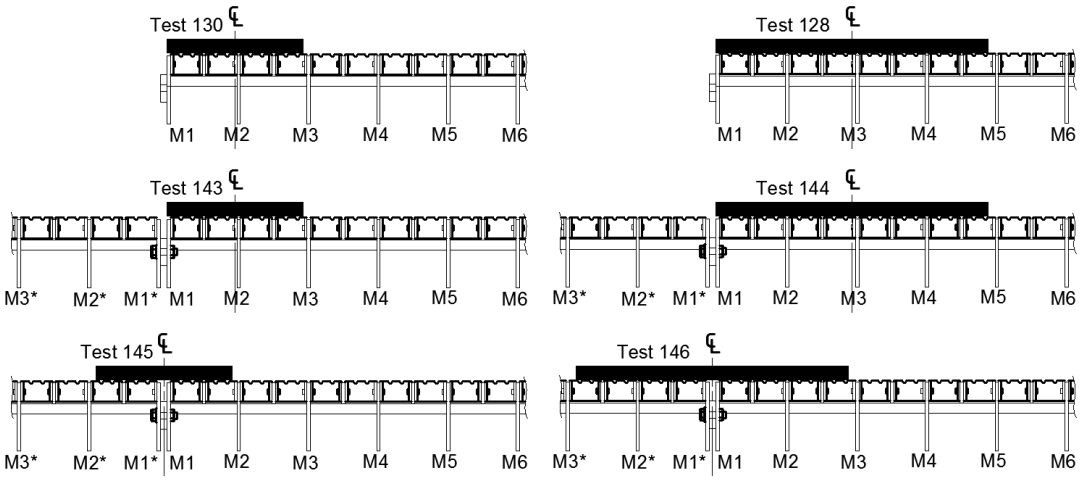

Figure 5.24: Transverse and parallel patch loads to examine composite action of 37-R-L-5x1/4 panel bolted connection

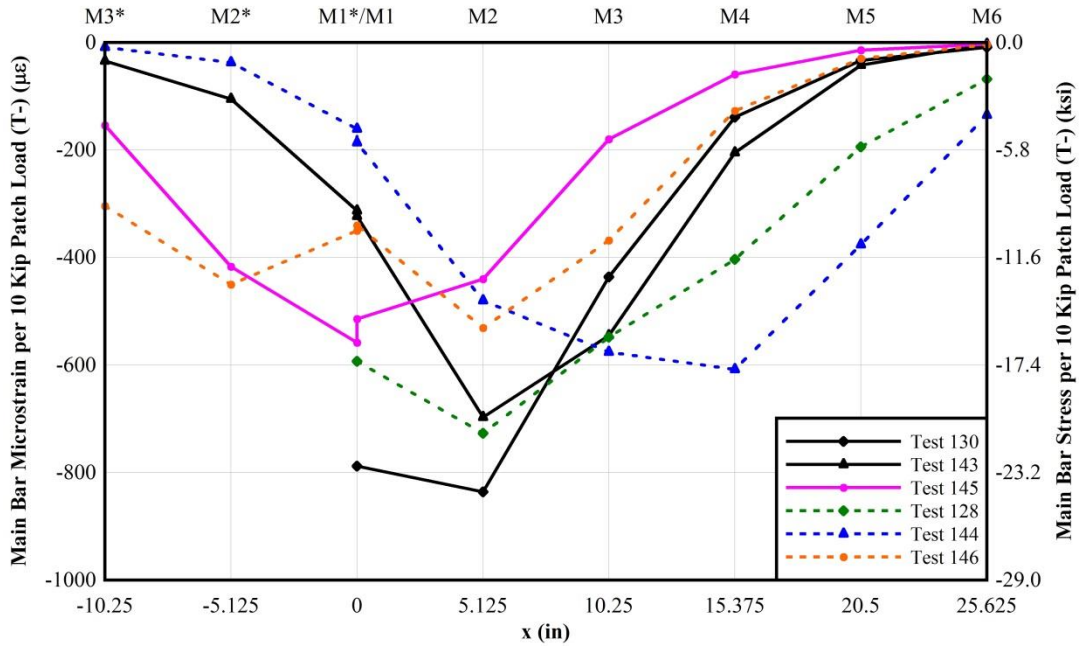

Figure 5.25: Load distribution for composite action tests of 37-R-L-5x¼ panels

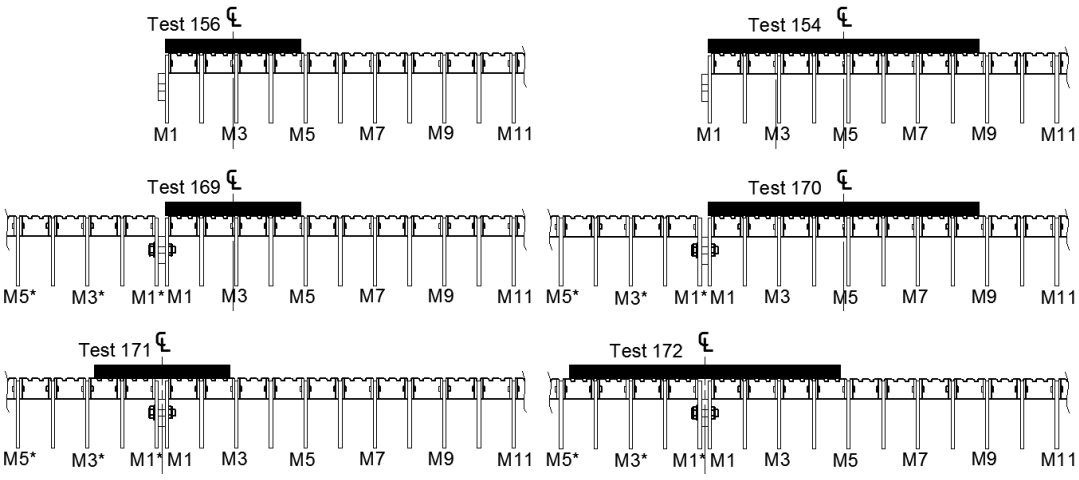

Figure 5.26: Transverse and parallel patch loads to examine composite action of 37-R-5x1/4 panel bolted connection

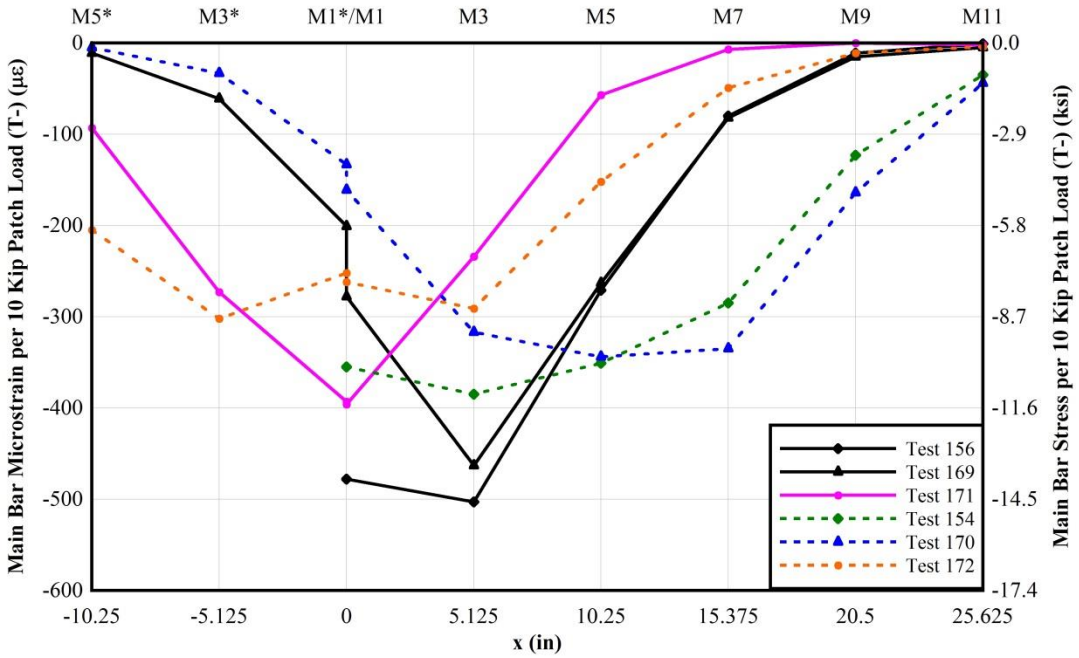

Figure 5.27: Load distribution for composite action tests of 37-R-5x¼ panels

Table 5.13: Composite action of 37-R-L-5x¼ and 37-R-5x¼ panels

Test #	Strain Gage Location/Strain (με)		% Difference	% Composite
	M45.1*	M45.1		
Test 143	-313	-323	3	97
Test 144	-161	-186	16	84
Test 169	-201	-278	38	62
Test 170	-133	-161	21	79

5.3 Subcomponent Fatigue Specimens

Cyclic fatigue tests were conducted on the subcomponent specimens described in Section 4.6. These specimens were monitored during the tests to observe when cracks initiated and the progression of crack propagation. Also, the location of crack formation was noted. Crack location was found to be dependent on the weld type. Table 5.14 displays N, the number of cycles applied when first cracking in each cross bar was observed. Also, the location of crack initiation in each cross bar is noted.

Each weld type had a consistent crack initiation location, designated by 'P', 'F', 'S', and 'N'. 'P' relates to a crack initiating from a puddle weld, as shown in Fig. 5.28. 'F' designates a crack initiating from a fillet weld as shown in Fig. 5.29. 'S' designates a crack initiating from a puddle weld that had weld run off into a notch that created a stress concentration, as shown in Fig. 5.30. 'N' designates a crack initiating from a serration along the top of the cross bar, as shown in Fig. 5.31. This was the only crack that did not initiate at a weld detail. Also, a greyed cell in Table 5.14 designates an uncracked cross bar. In proceeding tables and figures, the uncracked cross bars were conservatively assumed to be cracked at the highest number of cycles applied for that particular specimen.

Table 5.14: Number of cycles before cracking in welded open grid specimens, crack initiation location

Specimen #	Crossbar #	7.5DIAG2.5TYP1		7.5DIAG2.5TYP2		7.5DIAG2.5TYP3	
		N	Crack	N	Crack	N	Crack
Specimen 1	1	27,000	P	100,000	F	25,000	S
	2	50,000	P	125,000	F		
	3	27,000	P	125,000	F	25,000	S
Specimen 2	1	27,000	P	100,000	F	25,000	S
	2	50,000	P	125,000	F	40,000	P
	3	27,000	P	75,000	F	25,000	S
Specimen 3	1	100,000	P	73,000	F	265,000	S
	2	45,000	P	150,000	F	275,000	S
	3	130,000	P	73,000	F		
Specimen 4	1	45,000	P	150,000	F	125,000	S
	2	85,000	P	150,000	F	245,000	P&N
	3	35,000	P	150,000	F	245,000	N
Specimen #	Crossbar #	4.0RECT2.5TYP4		4.0RECT2.5TYP5		4.0RECT2.5TYP6	
		N	Crack	N	Crack	N	Crack
Specimen 1	1	35,000	P	400,000	F	400,000	N
	2	65,000	P	548,000	F	425,000	N
	3	111,000	P	550,000	F	450,000	N
Specimen 2	1	111,000	P	555,000	F		
	2	65,000	P	630,000	F	600,000	N
	3	35,000	P	630,000	F		
Specimen 3	1	32,000	P	95,000	F	520,000	N
	2	50,000	P	95,000	F	415,000	N
	3	50,000	P	122,000	F	520,000	N
Specimen 4	1	32,000	P	155,000	F	520,000	N
	2	32,000	P	140,000	F	470,000	N
	3	50,000	P	122,000	F	470,000	N

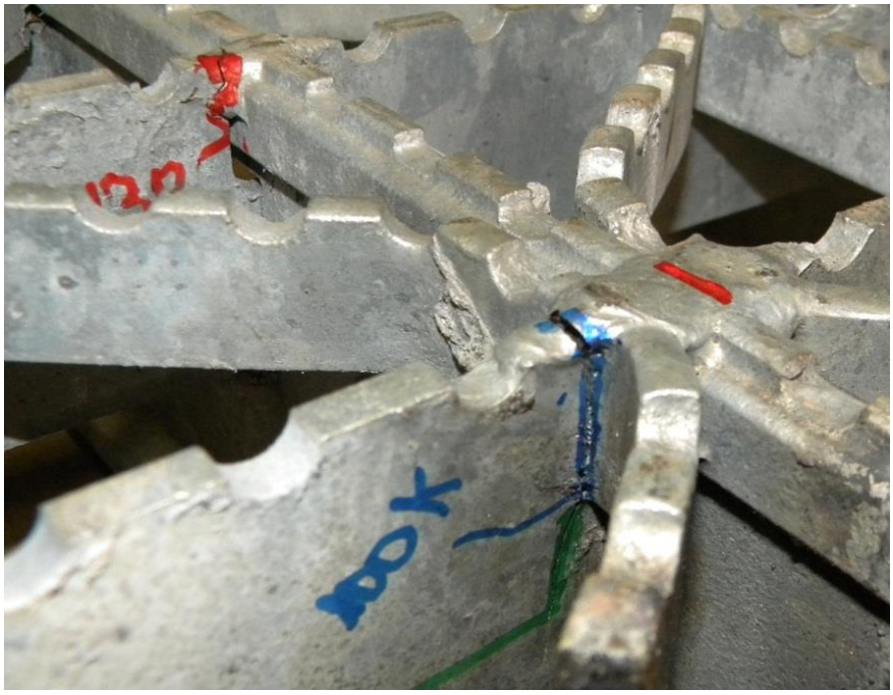

Figure 5.28: ‘P’ crack initiation from puddle weld

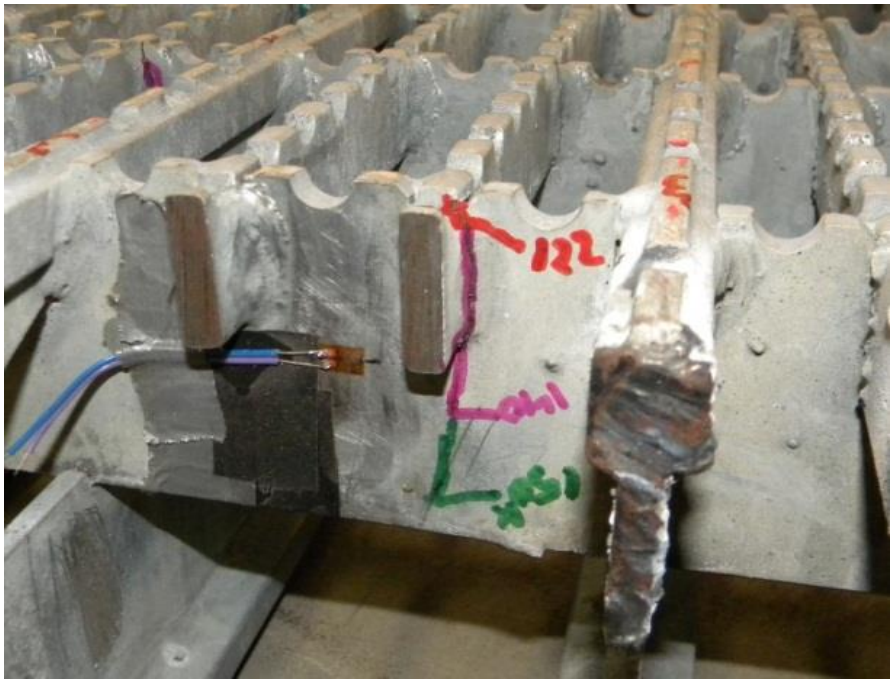

Figure 5.29: ‘F’ crack initiation from fillet weld

Figure 5.30: ‘S’ crack initiation from weld run off

Figure 5.31: ‘N’ crack initiation from serration punch-out

Two approaches were taken to categorize the performance of the different weld types. The first approach was to determine the neutral axis, y_b, of the cross bars based on engineering mechanics. Equation 5.2 was back-solved for y_b in order to determine the neutral axis of the section:

$$\sigma_i = \frac{M_i y_b}{I_i} \qquad [5.2]$$

where σ_i = stress at the bottom of the cross bar; M_i = applied moment from actuator load and span length; I_i = moment of inertia of the section. The moment of inertia (I_i) for each weld type was taken from weak direction stiffness tests. The bottom of the cross bar is continuous throughout the specimen, containing no welds or punch-outs, therefore strain gages mounted at this location are not prone to stress concentrations due to applied load. Table 5.15 shows y_b values determined from this approach.

Table 5.15: Theoretically determined y_b values

Specimen Type	Specimen 1 y_b (in)	Specimen 2 y_b (in)	Specimen 3 y_b (in)	Specimen 4 y_b (in)	Average y_b (in)
7.5DIAG2.5TYP1	1.25	1.35	1.24	1.16	1.25
7.5DIAG2.5TYP2	1.30	1.25	1.27	1.25	1.27
7.5DIAG2.5TYP3	1.38	1.41	1.28	1.30	1.34
4.0RECT2.5TYP4	1.35	1.37	1.46	1.43	1.40
4.0RECT2.5TYP5	1.38	1.11	1.28	1.23	1.25
4.0RECT2.5TYP6	1.16	1.13	1.16	1.11	1.14

Stresses were projected to the top of the cross bar at the weld intersection, where strain gages could not be mounted. Table 5.16 shows the number of cycles and stress range for all specimens tested. For both the 4.0RECT2.5TYP4 and 4.0RECT2.5TYP5 weld types, specimens 1 and 2 were subjected to cyclic testing at two different load ranges. As a

result, the numbers of cycles shown are normalized to the higher load range. Figures 5.32 and 5.33 display data points for Table 5.16.

Table 5.16: N_t values based on theoretically determined neutral axis

Specimen #	Crossbar #	7.5DIAG2.5TYP1		7.5DIAG2.5TYP2		7.5DIAG2.5TYP3	
		N_t	Stress Range	N_t	Stress Range	N_t	Stress Range
Specimen 1	1	27,000	18.51	100,000	17.55	25,000[b]	21.78
	2	50,000	18.51	125,000	17.55	40,000[a,b]	21.78
	3	27,000	18.51	125,000	17.55	25,000[b]	21.78
Specimen 2	1	27,000	17.01	100,000	18.18	25,000[b]	21.11
	2	50,000	17.01	125,000	18.18	40,000[b]	21.11
	3	27,000	17.01	75,000	18.18	25,000[b]	21.11
Specimen 3	1	100,000	13.61	73,000	16.44	265,000	18.78
	2	45,000	13.61	150,000	16.44	275,000	18.78
	3	130,000	13.61	73,000	16.44	275,000[a]	18.78
Specimen 4	1	45,000	12.59	150,000	16.69	125,000	18.41
	2	85,000	12.59	150,000	16.69	245,000	18.41
	3	35,000	12.59	150,000	16.69	245,000	18.41
Specimen #	Crossbar #	4.0RECT2.5TYP4		4.0RECT2.5TYP5		4.0RECT2.5TYP6	
		N_t	Stress Range	N_t	Stress Range	N_t	Stress Range
Specimen 1	1	14,000	15.06	54,000	20.51	400,000	23.87
	2	44,000	15.06	202,000	20.51	425,000	23.87
	3	90,000	15.06	204,000	20.51	450,000	23.87
Specimen 2	1	90,000	14.80	209,000	25.41	600,000[a]	24.40
	2	44,000	14.80	284,000	25.41	600,000	24.40
	3	14,000	14.80	284,000	25.41	600,000[a]	24.40
Specimen 3	1	32,000	13.58	95,000	22.28	520,000	23.95
	2	50,000	13.58	95,000	22.28	415,000	23.95
	3	50,000	13.58	122,000	22.28	520,000	23.95
Specimen 4	1	32,000	14.08	155,000	23.32	520,000	24.77
	2	32,000	14.08	140,000	23.32	470,000	24.77
	3	50,000	14.08	122,000	23.32	470,000	24.77

[a] No cracks, N conservatively set equal to highest # of cycles run

[b] Subjected to 2 million compression fatigue cycles before modified tension fatigue tests, points not shown on graph

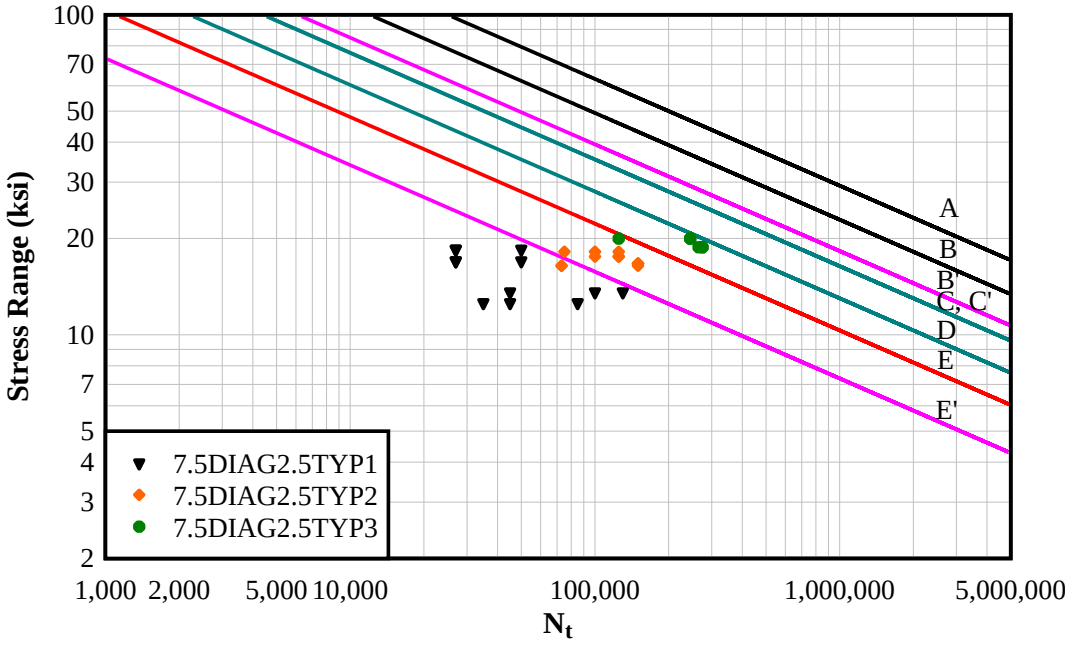

Figure 5.32: N_t for welded diagonal open grid specimens

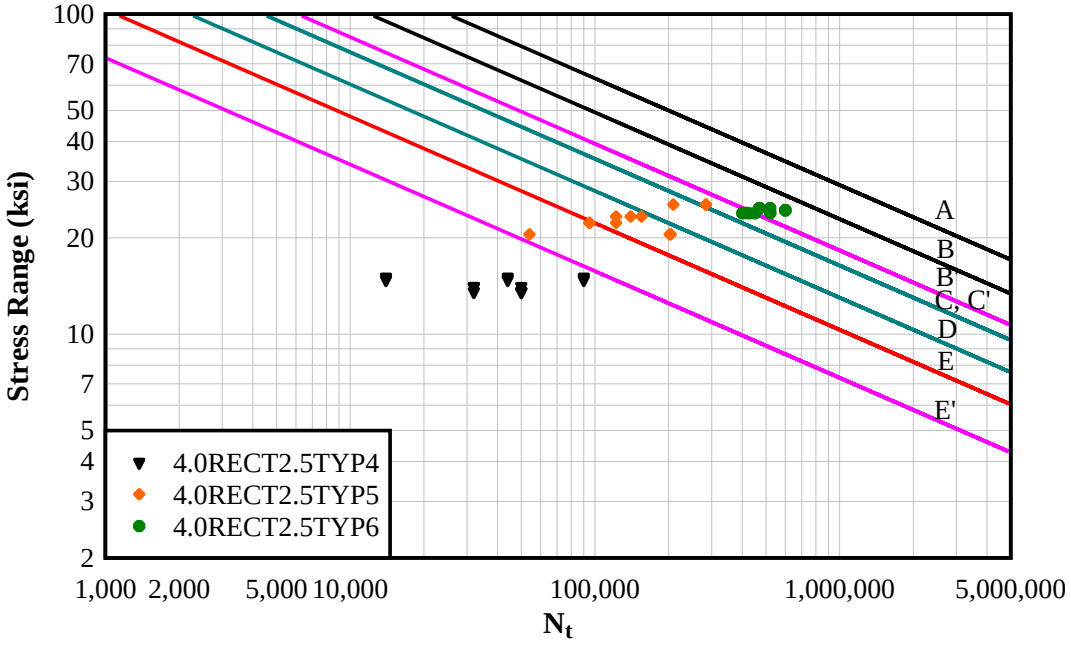

Figure 5.33: N_t for welded rectangular open grid specimens

Stresses were then normalized to a 20 ksi stress range in order to directly compare the fatigue life based on a constant stress range. AASHTO LRFD Bridge Design Specification Section 6.6.1.2.5 defines fatigue categories for details subject to load induced fatigue. Each category has a fatigue threshold where above a stress range amplitude, infinite life is assumed. Where fatigue life is finite, the number of cycles is inversely proportional to the cube of the stress range [AASHTO 2007]. N_i was normalized using the equation

$$N_{20} = N_i\left(\frac{SR_i^{\,3}}{SR_{20}^{\,3}}\right) \qquad [5.3]$$

where N_{20} is the equivalent number of cycles for a stress range of 20 ksi; N_i is the number of cycles before cracking for each specimen; SR_i is the measured stress range from testing; and SR_{20} is the 20 ksi stress range. Equation 5.3 is a form of the Palmgren-Miner linear damage hypothesis, which was developed to compare fatigue life of different stress ranges. The normalized number of cycles until first cracking in each cross bar, N_{20}, is shown as N_{20t} in Table 5.17. Figures 5.34 and 5.35 display the data from Table 5.17.

Table 5.17: N_{20t} values based on theoretically determined neutral axis

Specimen #	Crossbar #	7.5DIAG2.5TYP1	7.5DIAG2.5TYP2	7.5DIAG2.5TYP3
		N_{20t}	N_{20t}	N_{20t}
Specimen 1	1	21,415	67,620	See Table 5-19
	2	39,657	84,525	See Table 5-19
	3	21,415	84,525	See Table 5-19
Specimen 2	1	16,597	75,140	See Table 5-19
	2	30,735	93,925	See Table 5-19
	3	16,597	56,355	See Table 5-19
Specimen 3	1	31,536	40,544	219,473
	2	14,191	83,310	227,755
	3	40,997	40,544	227,755[a]
Specimen 4	1	16,885	87,195	97,425
	2	31,894	87,195	190,953
	3	13,133	87,195	190,953
Mean		24,587	74,006	192,386
Standard Deviation		9,919	18,634	49,512
95% Confidence Lower Bound		8,272	43,356	110,945
90% Confidence Lower Bound		11,876	50,126	128,933
Specimen #	Crossbar #	4.0RECT2.5TYP4	4.0RECT2.5TYP5	4.0RECT2.5TYP6
		N_{20t}	N_{20t}	N_{20t}
Specimen 1	1	6,136	58,640	679,920
	2	18,953	218,199	722,415
	3	38,604	220,355	764,910
Specimen 2	1	36,617	429,388	1,089,594[a]
	2	17,970	583,175	1,089,594
	3	5,809	583,175	1,089,594[a]
Specimen 3	1	10,026	131,271	892,528
	2	15,665	131,271	712,306
	3	15,665	168,580	892,528
Specimen 4	1	11,158	245,737	987,584
	2	11,158	221,956	892,624
	3	17,435	193,419	892,624
Mean		17,100	265,430	877,167
Standard Deviation		10,532	172,856	159,001
95% Confidence Lower Bound		0	0	615,633
90% Confidence Lower Bound		3,603	43,907	673,398

[a] No cracks, N conservatively equal to highest # of cycles ran

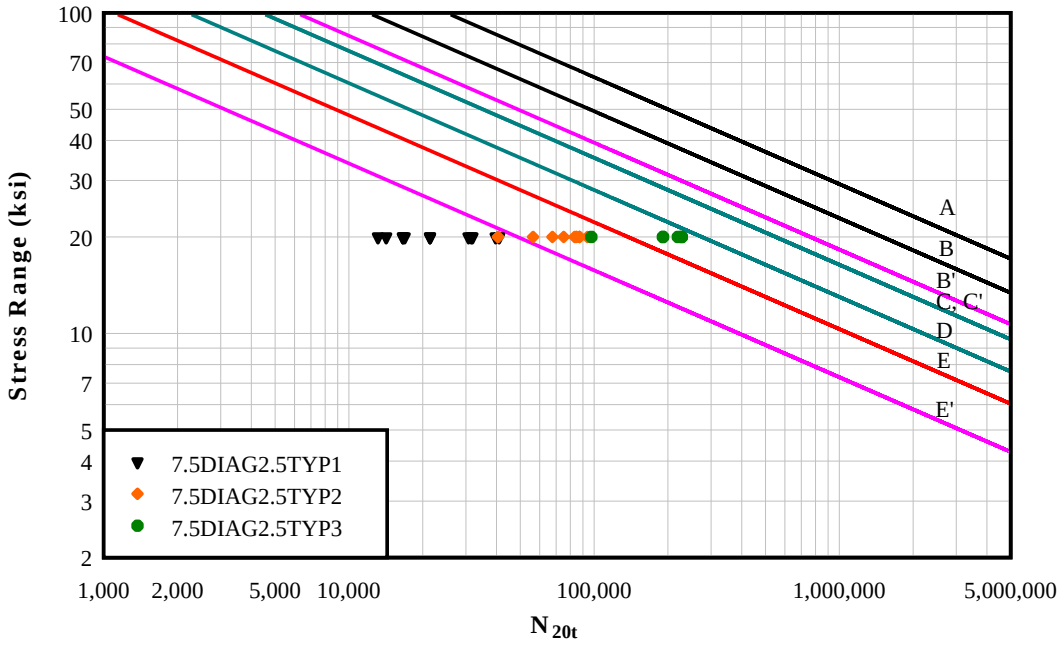

Figure 5.34: N_{20t} for welded diagonal open grid specimens

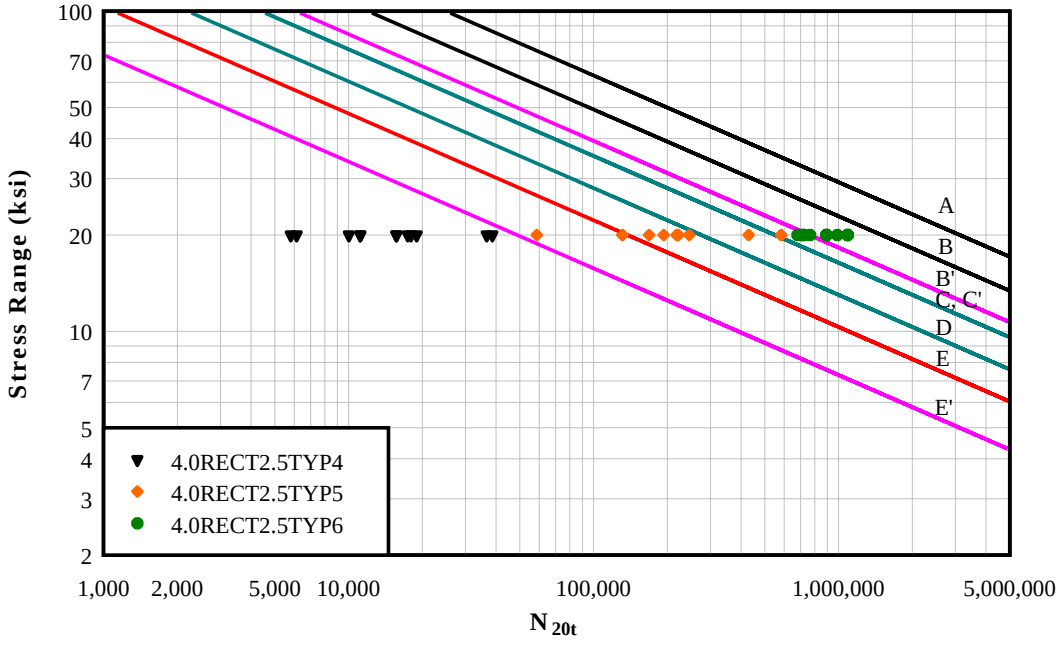

Figure 5.35: N_{20t} for rectangular diagonal open grid specimens

The second approach that was taken to categorize the performance of the different weld types was based on a constant applied moment for all specimens. Neutral axis location and stiffness was neglected in order to examine performance of each weld type based on a constant moment. Differences in stiffness between weld types will cause different weak-direction stresses in actual bridge deck spans under axle loading, but applying a constant moment allows for a direct fatigue life comparison of alternative weld types. Different loads were used to test each type of specimen; the applied moment could be normalized by manipulating Eqn. 5.3. Stress is directly proportional to moment; therefore Eqn. 5.3 can be modified to

$$N = N_i\left(\frac{M_i^3}{M^3}\right) \qquad [5.4]$$

where N=equivalent number of cycles for particular weld type; N_i= number of cycles for particular weld type; M_i=applied moment for particular weld type; M=applied moment for weld type to which N will be normalized. The welded diagonal and rectangular open grid specimens were compared separately, with both 7.5DIAG2.5TYP1 and 4.0RECT2.5TYP4 moments used for M. These two were chosen as a baseline for comparison because they represent weld details utilized in standard practice. In order to display N on AASHTO Figure C6.6.1.2.5-1 (AASHTO 2007), N was again normalized to 20 ksi based on theoretical stress ranges for specimens 7.5DIAG2.5TYP1 and 4.0RECT2.5TYP4, and is shown as N_{20M}. Table 5.18 shows the number of cycles based on the relative number of cycles for a constant applied moment on diagonal and rectangular open grid specimens. N for each specimen is shown graphically in Figs. 5.36 and 5.37.

Table 5.18: N_{20M} values relative to constant applied moment

Specimen #	Crossbar #	7.5DIAG2.5TYP1	7.5DIAG2.5TYP2	7.5DIAG2.5TYP3
		N_{20M}	N_{20M}	N_{20M}
Specimen 1	1	19,006	70,392	See Table 5-19
	2	35,196	87,989	See Table 5-19
	3	19,006	87,989	See Table 5-19
Specimen 2	1	19,006	70,392	See Table 5-19
	2	35,196	87,989	See Table 5-19
	3	19,006	52,794	See Table 5-19
Specimen 3	1	27,291	39,582	237,164
	2	12,281	81,334	246,113
	3	35,478	39,582	246,113[a]
Specimen 4	1	12,281	81,334	111,870
	2	23,197	81,334	219,265
	3	9,552	81,334	219,265
Mean		22,208	71,837	206,735
Standard Deviation		9,237	18,068	54,291
95% Confidence Lower Bound		7,014	42,118	117,435
90% Confidence Lower Bound		10,370	48,682	137,159
Specimen #	Crossbar #	4.0RECT2.5TYP4	4.0RECT2.5TYP5	4.0RECT2.5TYP6
		N_{20M}	N_{20M}	N_{20M}
Specimen 1	1	5,972	22,648	429,484
	2	18,460	84,254	456,327
	3	37,608	85,087	483,170
Specimen 2	1	37,608	87,168	644,226[a]
	2	18,460	118,388	644,226
	3	5,972	118,388	644,226[a]
Specimen 3	1	13,320	39,545	558,329
	2	20,813	39,545	445,590
	3	20,813	50,784	558,329
Specimen 4	1	13,320	64,521	558,329
	2	13,320	58,277	504,644
	3	20,813	50,784	504,644
Mean		18,874	68,282	514,307
Standard Deviation		10,176	30,713	65,936
95% Confidence Lower Bound		2,136	17,764	405,852
90% Confidence Lower Bound		5,833	28,922	429,807

[a] No cracks, N conservatively equal to highest # of cycles ran

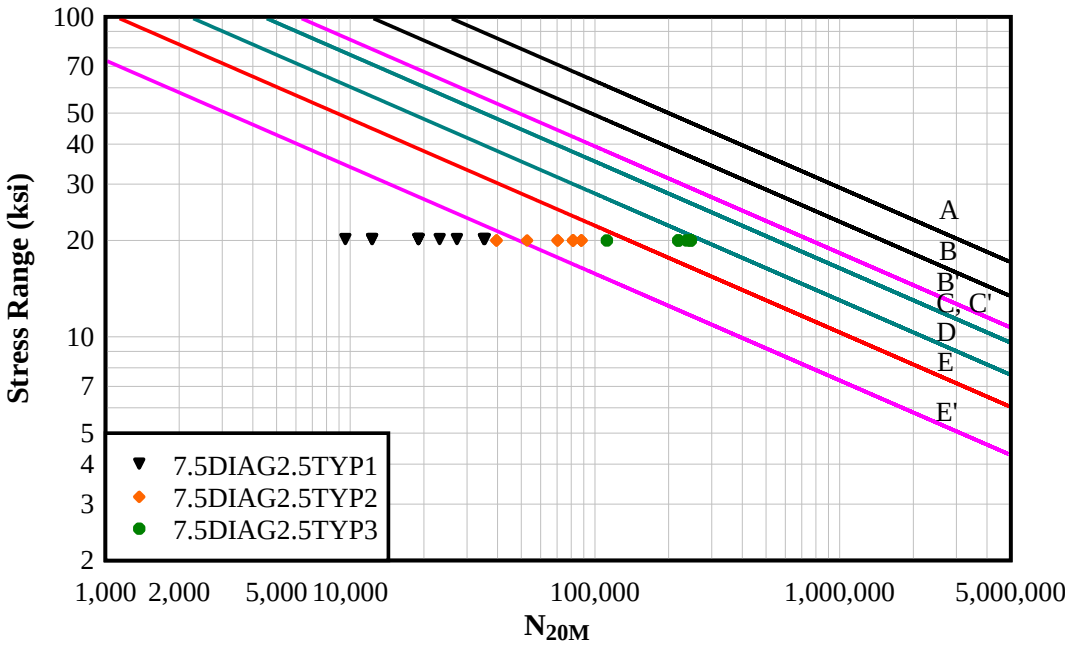

Figure 5.36: N_{20M} for welded diagonal open grid specimens

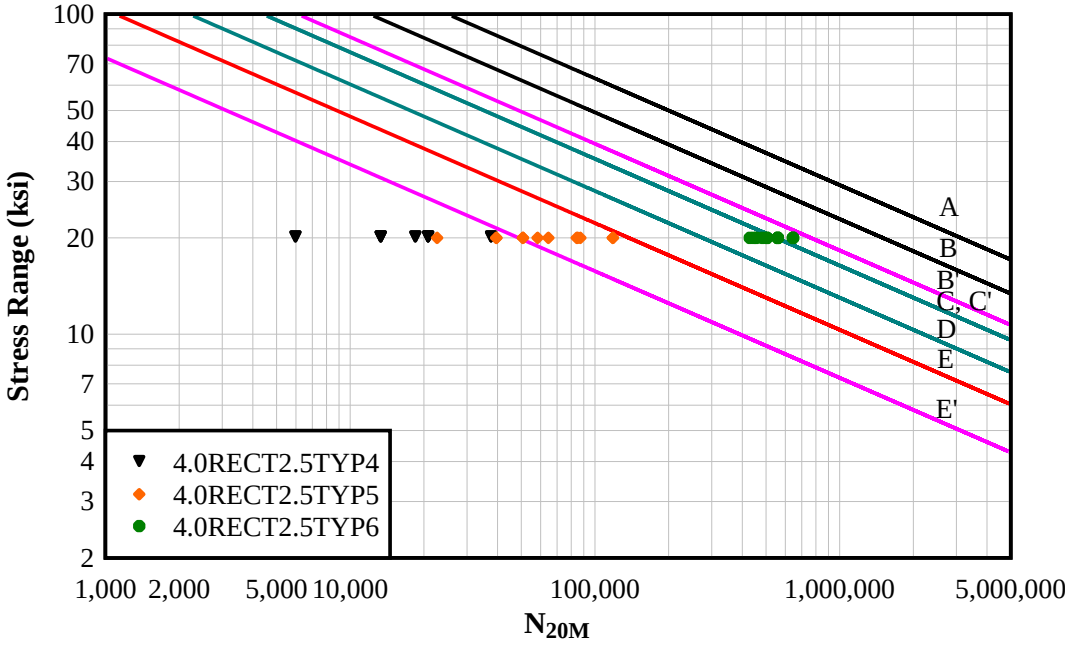

Figure 5.37: N_{20M} for welded rectangular open grid specimens

Table 5.19 displays the number of cycles until cracking for the two specimens initially subjected to 2 million cycles of compression (as discussed in Section 4.6). Specimen 1 and 2 of type 7.5DIAG2.5TYP3 exhibited a much lower fatigue life than specimens 3 and 4, which is due to residual tensile stresses induced by the welding process. When the specimens are loaded cyclically, the residual tensile stresses consume fatigue life and must be accounted for when designing open grid for fatigue. Therefore, a maximum residual stress based on results from fatigue specimens 1 and 2 of the 7.5DIAG2.5TYP3 open grid was calculated. The fatigue life consumed by positive moment fatigue was estimated by taking the average N_{20t} of specimens 3 and 4 of the 7.5DIAG2.5TYP3 open grid, which were subject to only negative moment fatigue, and subtracting the average N_{20t} of specimens 1 and 2. Using this approach, 155,000 cycles of N_{20t} negative moment fatigue life were consumed by 2 million cycles of positive moment fatigue at an average stress range of approximately 23.8 ksi. Using the Palmgren-Miner hypothesis, a residual stress range of 10.1 ksi would produce approximately 155,000 cycles of fatigue.

Table 5.19: Data for specimen 7.5DIAG2.5TYP3 after 2 million compression fatigue cycles

Specimen #	Crossbar #	7.5DIAG2.5TYP3	
		N_{20t}	N_{20M}
Specimen 1	1	32,276	50,034
	2	51,641[a]	80,055[a]
	3	32,276	50,034
Specimen 2	1	29,400	50,034
	2	47,040	80,055
	3	29,400	50,034

[a] No cracks, N conservatively equal to highest # of cycles run for particular specimen

6 COMPARISON BETWEEN EXPERIMENTAL AND ANALYTICAL RESULTS

The experimental results were compared with analytical predictions from a finite element analysis and analytical solutions that use orthotropic plate theory. The commercially available finite element analytical (FEA) software ABAQUS 6.8-2 was used to create the finite element model. The orthotropic plate model was derived from the general differential equation for bending and twisting moments of an orthotropic thin plate and was initially created for estimating moments and deflections in filled grid decks [Higgins 2003, 2004]. A uniformly thick plate using type S4R (4 node, reduced integration, conventional stress) shell elements (with bending stiffness only) was used, utilized with a thickness of 2.449 in., which produces stress output equal to the moment per unit width in kip-in/in. This plate thickness is achieved by manipulating the bending stress equation:

$$\sigma = \frac{Mc}{I} \qquad [6.1]$$

where M = Moment, c = distance from the neutral axis to extreme fiber; I = moment of inertia of the cross-section. If $c = \frac{t}{2}$ (for a uniformly thick plate), and $I = \frac{1}{12}bt^3$,

$$\sigma = \frac{M\left(\frac{t}{2}\right)}{\frac{1}{12}bt^3} \qquad [6.2]$$

If stress (σ) is set equal to Moment per unit width $\left(\frac{M}{b}\right)$ in the FEA model,

$$t = \sqrt{6} = 2.449in. \quad [6.3]$$

Solving Eqns. 6.4 to 6.6 for E_x, E_y and G using experimentally determined stiffness parameters for FEA model input allows for comparisons between full-scale system tests and the FEA model moments.

$$D_x = \frac{E_x t^3}{12(1 - v_x v_y)} \quad [6.4]$$

$$D_y = \frac{E_y t^3}{12(1 - v_x v_y)} \quad [6.5]$$

$$D_{xy} = \frac{G t^3}{12} \quad [6.6]$$

where E_x and E_y = the elastic modulus of elasticity in the x and y directions, respectively; G = the shear modulus; v_x and v_y = Poisson's ratio (set equal to zero); and t = plate thickness (Higgins 2004). Table 6.1 shows the stiffness parameters for the FEA model.

Table 6.1: Stiffness parameters for finite element analytical model

Specimen	E_x (k/in^2)	E_y (k/in^2)	G (k/in^2)
7.5DIAG2.5TYP1	17939	1878	88
7.5DIAG2.5TYP2	19109	1908	91
7.5DIAG2.5TYP3	19498	1963	86
4.0RECT2.5TYP4	42397	1746	79
4.0RECT2.5TYP5	36345	1250	86
4.0RECT2.5TYP6	42088	1757	94
37-R-L-5x1/4	18383	300	102
37-R-5x1/4	28249	64	125

A script was used to create the finite element model and report the results for strong- and weak-direction stresses (equal to strong- and weak-direction moments for the selected plate

thickness) and deflections along paths of interests. Parameters S22 and S11 represent output stress and moment in the strong and weak direction, respectively. The axes defined in the FEA model are different than the axes defined in the experimental results. The axis orientations are shown in Fig. 6.1.

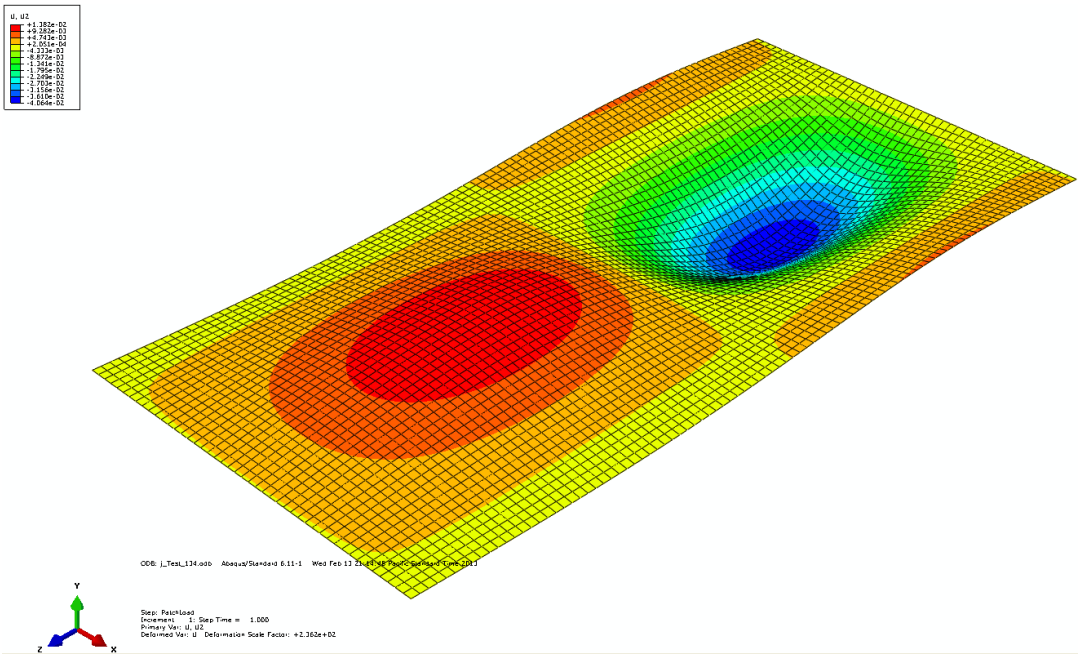

Figure 6.1: Isometric view of FEA model result for test 134

The x, y, and z axes in the FEA model represent weak direction, vertical displacement, and strong direction, respectively. All analyses involving the FEA model will be reported here using the previously defined axis orientations; with the x, y and z axes representing strong direction, weak direction, and vertical displacement, respectively.

In order to compare experimental load distribution test results with the FEA model, micro-strain measurements must be converted to moments in the decks. Main and cross bar strains were converted to moments using Eqn. 6.1. Substituting εE for σ, and solving for M, Eqn. 6.1 can be written as

$$M = \frac{\varepsilon EI_i}{c} = \frac{\varepsilon D_i}{c} \quad [6.7]$$

where M = moment at location of interest; ε = experimentally measured strain at location of interest; $D_i = D_x$ or D_y (k-in^2/in) (tabulated in Tables 5.1 and 5.4 for strong and weak directions, respectively); c = distance (in.) from neutral axis to location of strain gage (c can be determined using the neutral axis location, y_b, which is tabulated in Tables 5.2 and 5.5 for strong and weak directions, respectively).

Two FEA models were created to compare with the experimental data: a simply supported span loaded with a single patch, and a two-span continuous span loaded with either one or two patch loads. These two models allow FEA replication of the 177 load distribution tests shown in Appendix C (excluding eight tests measuring load transfer across riveted open grid connection detail). One boundary condition differs slightly between the FEA model and laboratory experiments. In the experimental tests where decks simply rest on roller supports, corner uplift of the open grid decks occurs at a distance sufficiently far from a patch load due to curvatures in the weak direction. Restricting this uplift at the supports increases stiffness, and also portrays field conditions more realistically, where welding of the open grid deck to the supports restricts movement in the vertical direction. In order to quantify the effects of corner uplift, the nodes restricting vertical translation in the FEA model were released where support nodes indicated tension. Releasing support nodes was an iterative process necessary to eliminate tension forces in the supports. A single iteration was performed to compare with Test 113 (configuration is shown in Appendix C) and the original FEA model. Figure 6.2 displays the difference in strong and weak direction moments for the original FEA model compared to the model with a single iteration of

released support nodes. A comparison with the original model shows a negligible difference between moments. Subsequent iterations would produce even smaller changes, and were not performed. After a single iteration, strong direction moments decrease at the free edge and increase at the center of the panel under the patch load, which correlates with experimental data (see Fig. 6.6).

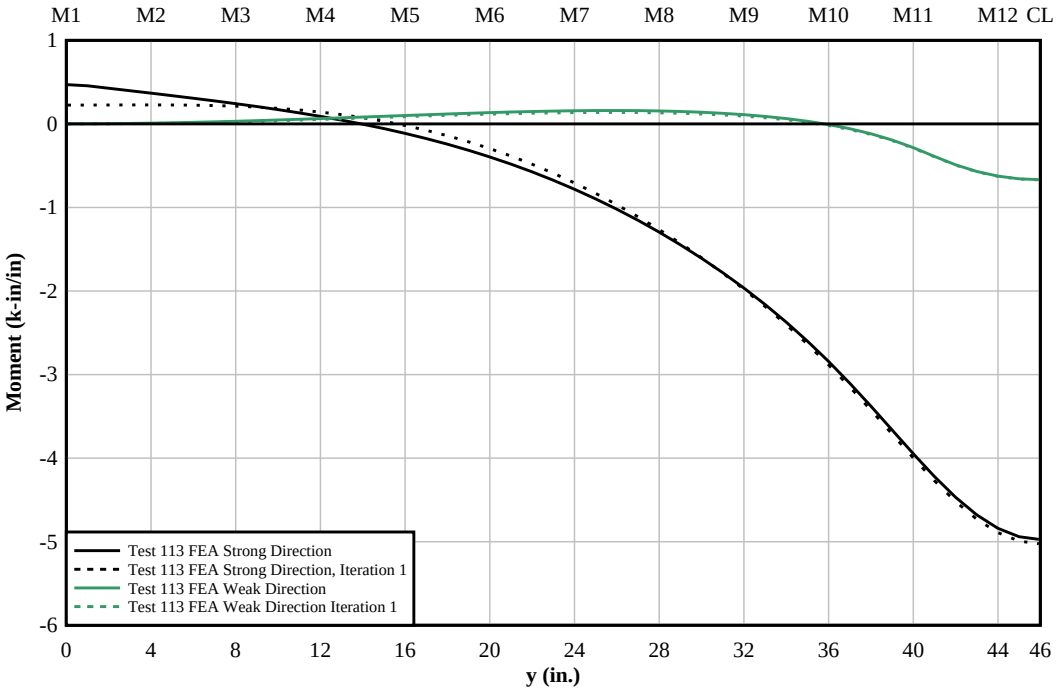

Figure 6.2: Changes in moments when accounting for uplift in FEA model

Figures 6.3 to 6.8 display comparisons between experimental and FEA results for similar patch load configurations for the four types of open grid decks. Results are shown for a patch load oriented transverse to traffic at three locations on one span of the two-span continuous configuration: free edge at midspan, centered at one-quarter of the width at midspan, and at the mid-point at midspan. Strong- and weak-direction moments are compared for the four specimens subjected to patch load tests.

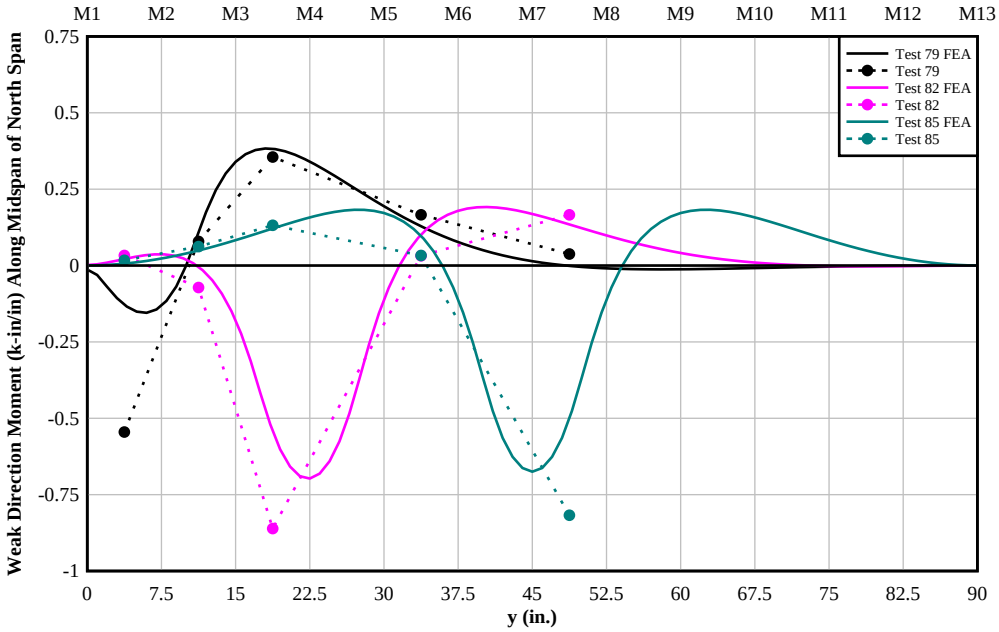

Figure 6.3: Weak-direction moment at midspan on north span for specimen 7.5DIAG2.5TYP1: edge, quarter-point and mid-point patch loading

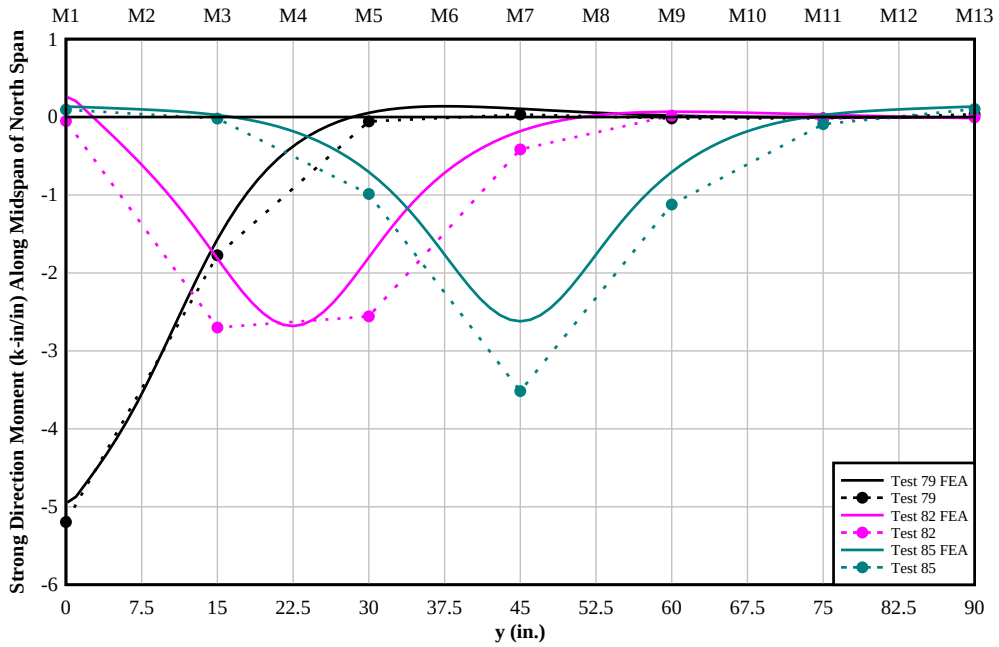

Figure 6.4: Strong-direction moment at midspan on north span for specimen 7.5DIAG2.5TYP1: edge, quarter-point and mid-point patch loading

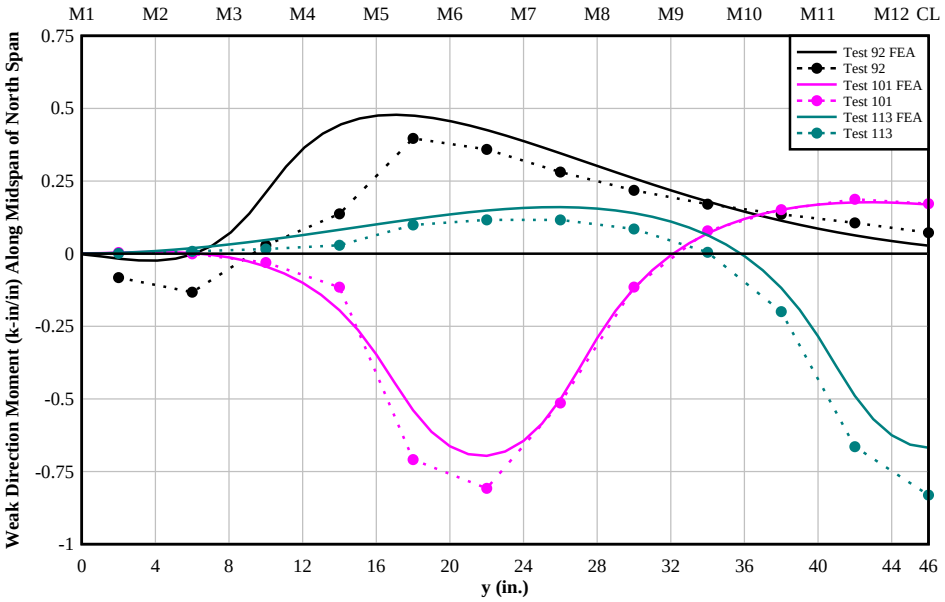

Figure 6.5: Weak-direction moment at midspan on north span for specimen 4.0RECT2.5TYP4: edge, quarter-point and mid-point patch loading

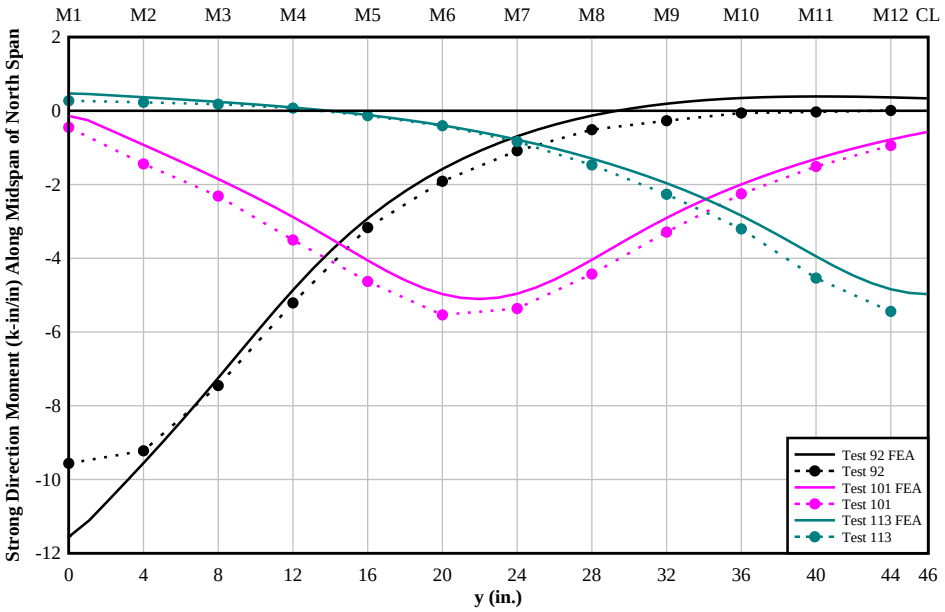

Figure 6.6: Strong-direction moment at midspan on north span for specimen 4.0RECT2.5TYP4: edge, quarter-point and mid-point patch loading

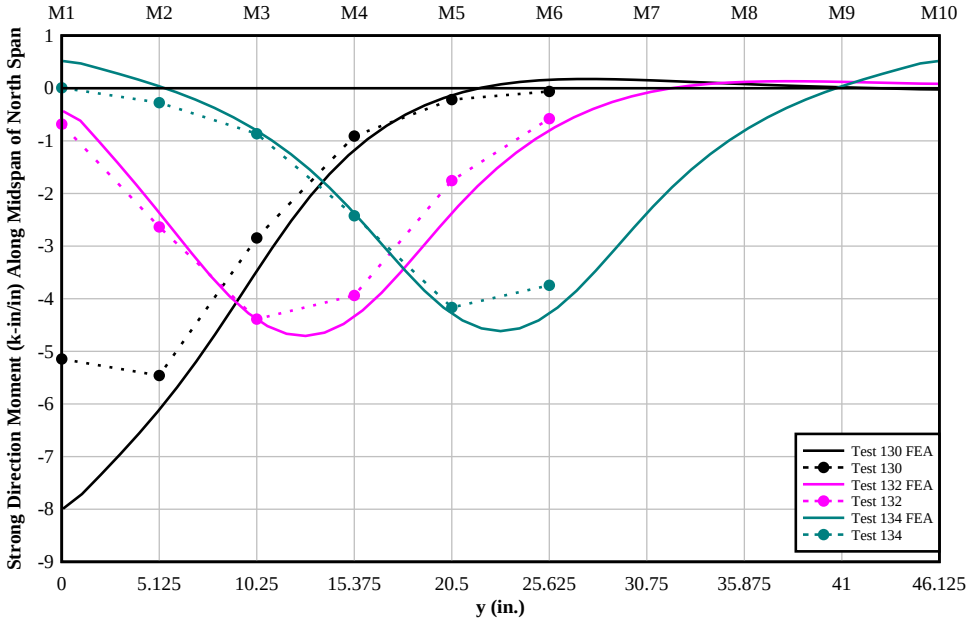

Figure 6.7: Strong-direction moment at midspan on north span for specimen 37-R-L-5x¼: edge, quarter-point and mid-point patch loading

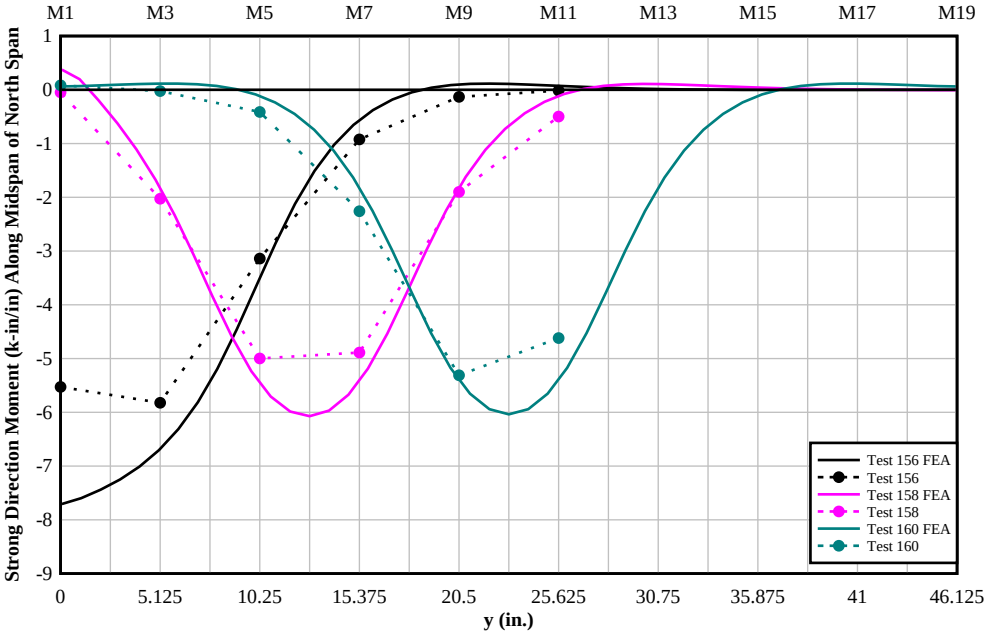

Figure 6.8: Strong-direction moment at midspan on north span for specimen 37-R-5x¼: edge, quarter-point and mid-point patch loading

Figures 6.3 to 6.8 show good correlation between experimental results and the FEA model results, therefore it is reasonable to develop design moment equations using the FEA model that can represent the wide range of orthotropic properties for different open grid bridge decks.

7 STRENGTH DESIGN MOMENTS FOR OPEN GRID DECKS

7.1 Previously Proposed Strength Design Equations

Strong- and weak-direction positive moment equations for strength design were developed by Higgins *et al.* [2010]. Design truck (32 kip axle) and tandem patch loads (25 kip axles) and configurations were incrementally marched across a simple span in the transverse and parallel directions, multiplied with a multiple presence factor (MPF) (1.0 for two vehicles and 1.2 for a single vehicle) to determine critical locations for maximum positive moments in the strong and weak direction. Maximum positive moments in the strong and weak direction were collected for a range of span lengths, stiffness parameters, and span configurations. The four factored strength moment (kip-in.) equations are expressed as:

$$M_{tr\_strong\_open}(L \le 84in.) = \frac{2.62D^{0.214}L^{0.468}}{\alpha^{0.231}}C \quad [7.1]$$

$$M_{tr\_weak\_open}(L \le 84in.) = \frac{0.405D^{-0.344}L^{0.655}}{\alpha^{0.187}}C \quad [7.2]$$

$$M_{pa\_strong\_open}(L \le 84in.) = \frac{1.59D^{0.12}L^{0.6}}{\alpha^{0.145}}C \quad [7.3]$$

$$M_{pa\_weak\_open}(L \le 84in.) = \frac{0.148D^{-0.437}L^{0.839}}{\alpha^{0.213}}C \quad [7.4]$$

where $\alpha = \frac{2D_{xy}}{\sqrt{D_x D_y}}$; $D = D_x/D_y$; L = span length (in.); and C is the continuity factor (1.0 for simply supported and 0.8 for continuous spans). The parameter α can be derived from Eqns. 3.1 and 3.6, where D_1 is set to zero [Turan 2011]. Included in these maximum

moment equations are: live load factor, γ (1.75); dynamic load allowance, IM (1.33); and MPF (1.0 for two vehicles and 1.2 for a single vehicle). The controlling conditions were for the design truck (32 kip axle) in a single lane (MPF = 1.2). The moment equations were calibrated over a range of α between 0.1 and 1.0 and D between 2.0 and 10, and varying L between 36 and 84 inches. After performing stiffness tests on the open grid specimens in this research, it was observed that the experimentally observed values for α and D were smaller than those used in the development of the Eqns. 7.1 to 7.4. As shown in Table 7.1, measured α ranged from 0.02 to 0.19, while measured D values ranged from 9.6 to 440. The effects of these values, below those used in the calibration on the above design moments are shown in Fig. 7.1. As seen in this figure, the moment values are highly nonlinear as α becomes smaller than 0.1 for a given span (shown set to L = 72 in. for this figure). This is because α is raised to a fractional power in the denominator of the strength moment equation. Therefore, because the experimentally observed values of α were much less than 0.1, the moment equations require calibration over the range of actual deck properties. To do this, additional finite element analyses were performed.

Table 7.1: Stiffness parameters for tested open grid specimens

Specimen	D_x (k-in^2/in)	D_y (k-in^2/in)	D_{xy} (k-in^2/in)	D	α
7.5DIAG2.5TYP1	21,971	2300	108	9.6	0.03
7.5DIAG2.5TYP2	23,403	2337	112	10.0	0.03
7.5DIAG2.5TYP3	23,880	2404	105	9.9	0.03
4.0RECT2.5TYP4	51,926	2139	97	24.3	0.02
4.0RECT2.5TYP5	44,513	1530	106	29.1	0.03
4.0RECT2.5TYP6	51,547	2151	116	24.0	0.02
37-R-L-5x1/4	22,514	367	125	61.3	0.09
37-R-5x1/4	34,597	79	153	440	0.19

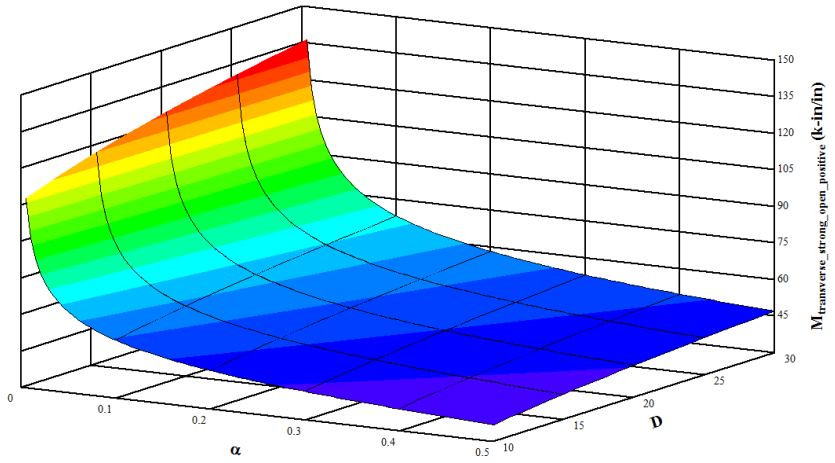

Figure 7.1: Sensitivity of strength design moment Eqn. 7.1 to parameters *D* and *α* for an example span of 72 in.

7.2 New Proposed Strength Design Equations

New equations were proposed using a larger range of '*D*' and '*α*'. Eight values of '*D*' (2.0, 5.0, 10, 20, 50, 100, 250, 500) and nineteen values of '*α*' (0.01, 0.02, 0.03, 0.04, 0.05, 0.06, 0.07, 0.08, 0.09, 0.1, 0.2, 0.3, 0.4, 0.5, 0.6, 0.7, 0.8, 0.9, 1.0) were used to develop new strength design moments. The five span lengths (36, 48, 60, 72, and 84 in.) remained the same as those in the initial calibration, representing a realistic range of span lengths typical for open grid decks. For a 16 kip patch load, the equations were calculated in kip-in./in. as:

$$M_{transverse\_strong\_positive\_strength} = \frac{0.618 D^{0.106} L^{0.905}}{\alpha^{0.101}} C \qquad [7.5]$$

$$M_{transverse\_weak\_positive\_strength} = \frac{0.346 D^{-0.383} L^{0.723}}{\alpha^{0.106}} \qquad [7.6]$$

$$M_{parallel\_strong\_positive\_strength} = \frac{0.385 D^{0.035} L^{1.002}}{\alpha^{0.067}} C \qquad [7.7]$$

$$M_{parallel\_weak\_positive\_strength} = \frac{0.120 D^{-0.486} L^{0.926}}{\alpha^{0.120}} \quad [7.8]$$

where all parameters are defined similar to those for Eqns. 7.1 to 7.4. While *C* is necessary for strong direction moment equations and is dependent on the number of spans, weak-direction cross bars do not have continuity effects. Thus, *C* should not be used for weak-direction moment design equations. In order to quantify the difference in weak-direction moment between simple and continuous spans, several FEA analyses were performed. It was determined that $C = 0.9$ is justified for weak-direction moment equations. However, *C* is omitted for weak-direction moment equations for conservatism. Figure 7.2 displays a plot of Eqn. 7.5 (with a fixed length $L = 72$ in.), which was calibrated with a range of *D* and α values that represent experimentally determined stiffness properties, as discussed in Section 7.1.

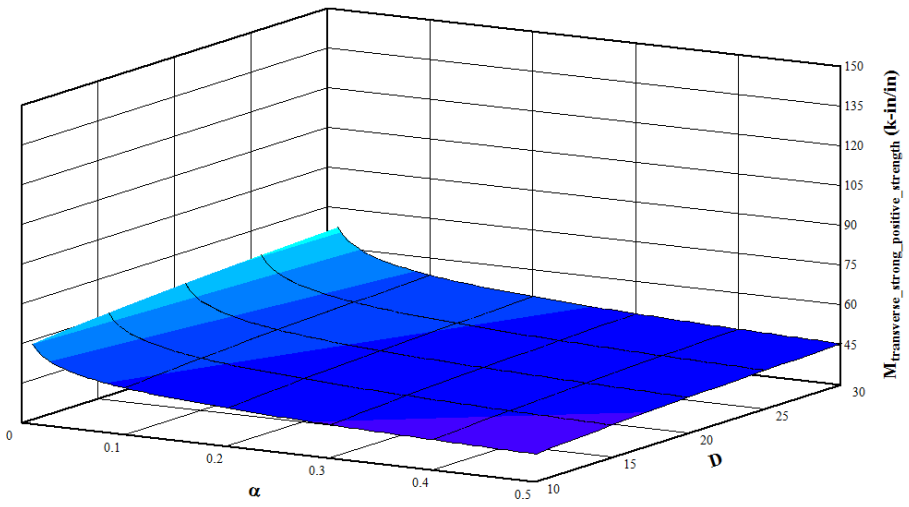

Figure 7.2: Plot of Eqn. 7.5 showing the effects of recalibration of moment equations to represent experimentally measured range of D and α

7.3 Comparison of Strength Design Moments with FEA Model and Laboratory Results

The proposed strength design moment equations (Eqns. 7.5 to 7.8) were compared with the FEA model and laboratory results. Firstly, strong-direction moment equations (Eqns. 7.5 and 7.7) were directly compared with FEA results. Table 7.2 shows the correlation between strength design moment equations and the FEA model results. The design moment equations and the FEA model correlate very well. The weak-direction moments in the highly orthotropic riveted open grid decks show higher percent differences, but this is due to the very low magnitude of the weak-direction moment.

Table 7.2: Positive moment correlation, strength design moment equations vs. FEA model results

		7.5DIAG2.5TYP1	4.0RECT2.5TYP4	37-R-L-5x1/4	37-R-5x1/4
$M_{transverse\_strong\_positive\_strength}$ (k-in/in)	Design Eqn.	36.3	49.8	32.4	37.0
	FEA	40.2	52.1	36.2	34.6
	% Diff.	11	5	12	-7
$M_{transverse\_weak\_positive\_strength}$ (k-in/in)	Design Eqn.	4.1	3.4	1.5	0.7
	FEA	3.7	3.0	1.3	0.4
	% Diff.	-9	-13	-13	-39
$M_{parallel\_strong\_positive\_strength}$ (k-in/in)	Design Eqn.	25.5	32.7	20.2	20.6
	FEA	27.5	33.8	19.7	19.3
	% Diff.	8	3	-2	-6
$M_{parallel\_weak\_positive\_strength}$ (k-in/in)	Design Eqn.	2.7	2.2	0.8	0.3
	FEA	2.4	1.8	0.5	0.1
	% Diff.	-13	-17	-37	-55

A comparison of the proposed design moment equations and experimental results is shown in Table 7.3 only for cases where strain gages were mounted at critical locations on main bars. The maximum weak-direction positive moment was measured for only specimen 4.0RECT2.5TYP4, where a strain gage was coincidentally located at the critical location. All other experimentally measured weak-direction moments were already shown to

correlate well with the FEA results because strain gages were not located at the maximum locations on cross bars. As shown in several figures in Chapter 6, strong-direction moments at the free edge could be greater in the FEA model than those measured in laboratory experiments. This is a conservative consequence of using smeared orthotropic plate properties in the FEA model. The transverse case is more sensitive than the parallel case because a transversely oriented tire patch has half the footprint of a parallel tire patch on the main bars. This can be seen in Table 7.3. The maximum strong-direction moments were seen to be larger at the free edge in the FEA model than the experimental measurements when the weak-direction stiffness decreases. Because the FEA overestimates the moment due to use of smeared properties, the resulting $M_{\text{transverse\_strong\_positive\_strength}}$ equation was corrected by dividing by a factor, λ=1.2, to better represent the experimentally observed moment magnitude. A comparison of results using this correction factor is shown in Table 7.4. As seen here, adjusting for the experimentally observed strong-direction moment produced closer estimates of the design moment. Weak-direction moments correlated well with the design equations; with some variability to be expected due to the large number of punch-outs in the cross bars and variance in the welded connections across the decks.

Table 7.3: Positive moment correlation, strength design moment equations vs. laboratory results

		7.5DIAG2.5TYP1	4.0RECT2.5TYP4	37-R-L-5x1/4	37-R-5x1/4
$M_{transverse\_strong\_positive\_strength}$ (k-in/in)	Design Eqn.	36.3	49.8	32.5	37.1
	Lab. Results	29.5	42.7	24.4	26.0
	% Diff.	-19	-14	-25	-30
$M_{transverse\_weak\_positive\_strength}$ (k-in/in)	Design Eqn.	NA	3.4	NA	NA
	Lab. Results	NA	3.7	NA	NA
	% Diff.	NA	8	NA	NA
$M_{parallel\_strong\_positive\_strength}$ (k-in/in)	Design Eqn.	25.5	32.7	20.3	20.6
	Lab. Results	22.5	31.1	21.2	20.8
	% Diff.	-12	-5	5	1
$M_{parallel\_weak\_positive\_strength}$ (k-in/in)	Design Eqn.	NA	2.2	NA	NA
	Lab. Results	NA	2.6	NA	NA
	% Diff.	NA	19	NA	NA

Table 7.4: Transverse orientation positive moment with correction factor, λ

		7.5DIAG2.5TYP1	4.0RECT2.5TYP4	37-R-L-5x1/4	37-R-5x1/4
$M_{transverse\_strong\_positive\_strength}/\lambda$ (k-in/in)	Design Eqn.	30.3	41.5	27.1	30.9
	Lab. Results	29.5	42.7	24.4	26.0
	% Diff.	-2	3	-10	-16

7.4 Maximum Allowable Span Lengths Based On Strength Design

Equations 7.5 to 7.8 were used to determine maximum allowable span lengths for the different open grid decks used in the experimental program. A yield stress of 50 ksi was assumed for all open grid deck elements. The respective orthogonal stiffness properties were used for the decks. Equation 6.1 was used to convert maximum moments to stresses, setting c equal to y_b or y_t, whichever was greater for each respective open grid deck. Maximum resulting stresses for BGFMA recommended maximum spans for $M_{transverse\_strong\_positive\_strength}/\lambda$ (the controlling strong direction moment) are shown in Table 7.5. These stresses are greater than the 50 ksi yield stress. This indicates that the present maximum spans would result in over-stress for the given AASHTO strength design truck load model.

Table 7.5: Resultant stresses for BGFMA recommended maximum span lengths

Specimen	D	α	Span Length L (in)	$M_{transverse\_strong\_positive\_strength}/\lambda$ (k-in/in)	$\sigma_{transverse\_strong\_positive\_strength}/\lambda$ (ksi)
7.5DIAG2.5TYP1	9.6	0.03	61	30.8	131
7.5DIAG2.5TYP2	10.0	0.03	61	31.0	114
7.5DIAG2.5TYP3	9.9	0.03	61	31.2	110
4.0RECT2.5TYP4	24.3	0.02	76	43.4	65
4.0RECT2.5TYP5	29.1	0.03	76	42.7	79
4.0RECT2.5TYP6	24.0	0.02	76	42.5	62
37-R-L-5x1/4	61.3	0.09	36	20.8	93
37-R-5x1/4	440	0.19	43	27.8	70

However, it is recognized that open grid decks do not exhibit strength issues in the field with the design typically being controlled by fatigue. Even if span lengths for the welded diagonal open grid decks are decreased to 36 in., the lower limit, yielding is still predicted. It is well known that the AASHTO models were developed considering superstructure elements such as girders rather than for deck elements. Therefore, for practical considerations and to reflect field experience it is clear that the AASHTO load model is overly conservative for deck designs. Firstly, the multiple presence factor (MPF = 1.2) can be eliminated. While MPF should be considered for the multi-lane supporting superstructure elements, the presence of multiple vehicles does not have an effect on open grid decks due to relatively short span lengths and negligible superposition of load effects from adjacent tire patches. A patch load produces relatively localized load effect because of low weak-direction stiffness; therefore additional stresses are not superimposed by adjacent patch loads. Also, more realistic truck axles should be represented by considering only the tandem axles (12.5 kip patch) as opposed to a single truck axle (16 kip patch) used for strength design. Recalling that the design moment equations were developed considering the maximum effect (truck or tandem) which was controlled by the truck in the present case, considering only the tandem axle we can further reduce the design moments

for strength by a factor of 0.78. By eliminating the multiple presence factor and considering axle weight from the design tandem, the strength design moment Eqns. 7.5 to 7.9 are multiplied by a cumulative reduction factor of 0.65.

Using these reductions the resulting stresses are shown in Table 7.6, while also modifying span lengths in order to limit resulting stresses to 50 ksi. The 7.5DIAG2.5TYP1 and 37-R-L-5x1/4 decks would still be limited by the yield stress at the lower span length limit. Maximum span lengths for 4.0RECT2.5TYP4 and 4.0RECT2.5TYP6 are controlled by the upper span length limit of 84 inches.

Table 7.6: Adjusted design moments and span lengths

Specimen	D	α	Span Length L (in)	$M_{transverse\_strong\_positive\_strength}/\lambda$ (k-in/in)	$\sigma_{transverse\_strong\_positive\_strength}/\lambda$ (ksi)
7.5DIAG2.5TYP1	9.6	0.03	36	12.4	53
7.5DIAG2.5TYP2	10.0	0.03	40	13.7	50
7.5DIAG2.5TYP3	9.9	0.03	41	14.1	50
4.0RECT2.5TYP4	24.3	0.02	84	31.0	46
4.0RECT2.5TYP5	29.1	0.03	73	26.9	50
4.0RECT2.5TYP6	24.0	0.02	84	30.4	44
37-R-L-5x1/4	61.3	0.09	36	13.5	60
37-R-5x1/4	440	0.19	48	20.1	50

While Table 7.6 gives more practical results for span lengths and strength limits, other strength design parameters can be modified. For example, the live load factor (LL = 1.75) is calibrated for a 75 year design life. While this may be appropriate for riveted open grid decks, which have exhibited service life upwards of 60 years according to Apperson *et al.* [2010], welded open grid decks typically have expected service lives of less than 20 years. As a result of this much shorter exposure period, a smaller live load factor could be considered for welded open grid decks. This was beyond the scope of this research.

8 FATIGUE DESIGN MOMENTS FOR WELDED OPEN GRID DECKS

8.1 Fatigue Design Moments for Open Grid Decks

This section addresses weak-direction fatigue design of open grid decks only. In order to design for fatigue, both negative bending and residual tensile stresses need to be accounted for in transversely oriented open grid decks. Also, negative bending stresses need to be accounted for in open grid decks oriented parallel to traffic. The following design equations account for AASHTO fatigue design factors, including live load (LL = 0.75), and impact (IM = 1.15) [AASHTO 2007].

8.1.1 Fatigue in Transversely Oriented Open Grid Decks

While Eqns. 7.5 to 7.8 may be sufficient for predicting positive moments for strength limit states of open grid decks, experimental testing revealed that fatigue is driven by negative moment (tension in the top of the open grid deck, at weld intersections) in the weak direction. As discussed in Section 5.2.1, and exemplified in Figs. 6.3 and 6.5, maximum negative moment in the weak direction is caused by patch loads at the free edge located at midspan. Analyses for transverse patch configurations were performed to determine the maximum negative moment over the same range of D, α and deck spans used for Eqns. 7.5 to 7.8. All relevant AASHTO fatigue design factors were applied to the negative moments collected in the analyses. The transverse weak direction negative moment for a 16 kip patch load was calculated as:

$$M_{transverse\_weak\_negative\_fatigue} = \frac{0.041 D^{-0.428} L^{0.811}}{\alpha^{0.220}} \qquad [8.1]$$

While Eqn. 8.1 accounts for maximum negative moment produced by a tire patch as it is located on the free edge of the open grid deck, it does not account for effects produced when the tire patch is located past the critical location when the patch load produces small negative moment effects. The relative magnitude of the secondary negative moment effect (shown in Figs. 5.9 and 5.14) is very small, and dependent on all three parameters (*D*, *L* and α). To fully account for the stress cycles of tire patches moving over the deck surface, several iterations of analyses would need to be performed for each of the 760 combinations of *D*, *L* and α.

In addition to the stress range cycles that need to be modeled, the residual tensile stresses at component intersections caused by the welding process must be accounted for when designing open grid bridge decks for fatigue (discussed in Section 5.3). Thus, maximum positive moments collected from strength design moments (adjusted for the fatigue limit state) can be used in conjunction with maximum negative moments (used in Eqn. 8.1) to determine the stress range, similar to those shown in Tables 5.8 and 5.9. As shown in Figs. 5.7 and 5.12, when the transverse tire patch reaches the critical location (producing maximum negative weak direction moment), maximum positive weak-direction moment is already achieved and remains constant as the tire patch moves past the center of the deck. Therefore, maximum positive weak direction moments used to develop Eqn. 7.6 (tire patch at the center of the deck) can be combined (after adjusting for the fatigue limit state) with maximum negative weak direction moments used to develop Eqn. 8.1.

Adjusting Eqn. 7.6 for fatigue limit state design factors, the design moment to account for residual stresses during positive bending for a 16 kip patch load is:

$$M_{transverse\_weak\_residual\_fatigue} = \frac{0.128 D^{-0.383} L^{0.723}}{\alpha^{0.106}} \quad [8.2]$$

The full tensile residual stress range may not be reached in every load condition and deck configuration. Thus, Eqn. 8.2 should be limited to a maximum resulting stress of 10.1 ksi in the top of the cross bar, the measured residual stress. Equations 8.1 and 8.2 must be combined to develop the design moment for negative moment and residual tensile effects.

8.1.2 Fatigue in Open Grid Decks Oriented Parallel to Traffic

In addition to transversely oriented open grid decks, fatigue must be considered for open grid decks oriented parallel to traffic. Negative moment in the weak direction will be highest as a tire patch runs along the free edge of the open grid deck. When multiplied by the applicable fatigue design factors, the design moment for fatigue for a 16 kip patch load is:

$$M_{parallel\_weak\_negative\_fatigue} = \frac{0.011 D^{-0.503} L^{1.047}}{\alpha^{0.186}} \quad [8.3]$$

Using design moment Eqns. 8.1 to 8.3, the fatigue life of welded open grid decks can be predicted for both transverse and parallel open grid deck orientations. Moments are converted to stress at the top of the cross bar (i.e. at the weld intersection) using Eqn. 6.1, where c = 2.5 (height of cross bar) - y_b (y_b can be found in Table 5.5 for each weld type). Fatigue life for all six welded specimens were considered at the maximum recommended span prescribed by the BGFMA (located in Appendix A).

8.2 Adjusting *N* to Account for Internal Redundancy of Open Grid Decks

The fatigue performance of the different weld types was established in Section 5.3. In Section 5.3, *N* values are defined as the number of cycles until "failure" taken as first visually observed crack in a cross bar. Five weld details per cross bar for diagonal specimens and ten weld details per cross bar for rectangular specimens were subjected to the same constant stress range in the subcomponent fatigue tests. Therefore, the probability of the worst weld detail being located at the location with the largest stress range is low. Further, a transverse tire patch will span over five cross bars, where the probability of the worst weld detail being located at the critical tensile location in one of the five cross bars is even lower.

Considering the high internally redundant nature of open grid decks, a system failure of multiple adjacent cross bars is necessary to define fatigue failure of the deck system. This requires cracking in all five cross bars to establish the weak-direction fatigue life of the open grid bridge deck. To establish the system fatigue life, a Monte Carlo simulation was conducted using the statistical data from the weak-direction fatigue tests described in Chapter 5. The fatigue life of five adjacent cross bars was simulated using the mean and standard deviation values of the number of cycles to failure (N_{20t}) from Table 5.17 for an individual cross bar. Simulations were performed for each of the six welded open grid deck specimens considered. A 95% probability lower bound was chosen for N_{20t}, and each weld type was placed in a fatigue category as defined in Section C6.6.1.2.5 of the AASHTO LRFD Bridge Design Specification. The *N* values developed by the Monte Carlo simulation are shown in Table 8.1 for a 20 ksi stress range, and were used for all

fatigue life predictions in the following sections. The value for *N* is the number of cycles required to initiate cracks in all five bars that the tire patch would effectively load.

Table 8.1: *N* for a 20 ksi stress range from Monte Carlo simulation

Specimen	Average	Standard Dev.	95% Confidence Lower Bound	Fatigue Category
7.5DIAG2.5TYP1	36,189	6,640	24,993	E'
7.5DIAG2.5TYP2	95,420	12,497	74,864	E'
7.5DIAG2.5TYP3	250,210	33,051	195,847	E
4.0RECT2.5TYP4	29,449	6,957	18,006	E'
4.0RECT2.5TYP5	465,169	113,734	278,092	E
4.0RECT2.5TYP6	1,061,814	105,030	889,056	B'

8.3 AASHTO LRFD Bridge Design Specification Fatigue Life Predictions

A fatigue truck from Section 3.6.1.4 of the AASHTO LRFD Bridge Design Specification 4th Edition [AASHTO 2007] was considered for fatigue design, using specified axle loads and specified fatigue live load and impact factors (live load factor, LL= 0.75; fatigue impact factor, IM = 1.15). The design truck consists of two 32 kip axles (16 kip patches) and one 8 kip steer axle (4 kip patch).

Since the design fatigue moment equations and fatigue stresses were based on a 16 kip patch, the Palmgren-Miner hypothesis can be used to determine an equivalent number of axles (i.e. fatigue cycles per truck) for the design truck, to avoid modifying the moment equations for patch loads other than 16 kips. In order to assume a full residual stress range of 10.1 ksi for every axle weight, Eqn. 8.2 must be checked for each individual axle. This can be done by multiplying the patch load weight (in kips) by 16. If the residual stress range is 10.1 ksi for all axle weights, then the Palmgren-Miner hypothesis can be used. The equivalent number of 32 kip axles for the design truck is calculated as

$$\#\,Axles = \left(\frac{16^3}{16^3}\right) + \left(\frac{16^3}{16^3}\right) + \left(\frac{4^3}{16^3}\right) = 2.016$$

Design moments and subsequent fatigue stress ranges (including residual stresses) are shown in Table 8.2 for transversely oriented open grid decks.

Table 8.2: Design fatigue life for BGFMA maximum recommended span lengths, open grid decks oriented transverse to traffic

Specimen	D	α	L (in)	$M_{trans.\_weak\_neg.\_fatigue}$ (k-in/in)	$\sigma_{trans.\_weak\_neg.\_fatigue}$ (ksi)	$\sigma_{trans.\_weak\_total\_fatigue}$ (ksi)	Fatigue Life for ADTT = 1,000 (years)
7.5DIAG2.5TYP1	9.6	0.03	61.2	0.95	15.3	25.4	0.02
7.5DIAG2.5TYP2	10.0	0.03	61.2	0.93	13.4	23.5	0.08
7.5DIAG2.5TYP3	9.9	0.03	61.2	0.95	12.7	22.8	0.23
4.0RECT2.5TYP4	24.3	0.02	75.6	0.84	14.5	24.6	0.02
4.0RECT2.5TYP5	29.1	0.03	75.6	0.72	19.1	29.2	0.20
4.0RECT2.5TYP6	24.0	0.02	75.6	0.81	14.4	24.5	0.78

Table 8.3 shows fatigue design moments for open grid decks oriented parallel to traffic, the resulting stress ranges and predicted fatigue life. As seen in these tables, the fatigue life for the decks is short for the AASHTO fatigue truck model with the wheel lines located such as to produce the largest possible stress ranges.

Table 8.3: Design fatigue life for BGFMA maximum recommended span lengths, open grid decks oriented parallel to traffic

Specimen	D	α	L (in)	$M_{pa.\_weak\_neg.\_fatigue}$ (k-in/in)	$\sigma_{pa.\_weak\_neg.\_fatigue}$ (ksi)	Fatigue Life for ADTT = 1,000 (years)
7.5DIAG2.5TYP1	9.6	0.03	61.2	0.50	8.1	0.74
7.5DIAG2.5TYP2	10.0	0.03	61.2	0.49	7.1	2.91
7.5DIAG2.5TYP3	9.9	0.03	61.2	0.50	6.7	9.03
4.0RECT2.5TYP4	24.3	0.02	75.6	0.43	7.4	0.79
4.0RECT2.5TYP5	29.1	0.03	75.6	0.37	9.7	5.53
4.0RECT2.5TYP6	24.0	0.02	75.6	0.42	7.4	28.51

8.4 Expected Fatigue Life Predictions

In order to predict a more realistic fatigue life for the open grid bridge deck specimens, axle load data were collected from a truck weigh-station on Interstate 5 located in Woodburn, Oregon. This is a major north-south corridor on the west coast in a state that routinely allows trucks to operate above the federal legal limits. The average truck had four 10 kip axles (5 kip patches) and one 10 kip steer axle (5 kip patch). The fatigue live load factor (LL = 0.75) used in Section 8.1 was neglected because actual service-level field data was used in this analysis. An impact factor (IM) of 1.33 (the same IM used for strength design) is used. The Palmgren-Miner hypothesis can be used for an equivalent number of cycles after ensuring $M_{\text{transverse\_weak\_residual\_fatigue}}$ produces a stress range of at least 10.1 ksi, the maximum residual stress, for every axle. The equivalent number of fatigue cycles from one truck with five 10 kip axles is equal to 0.56.

Because of the smaller number of equivalent axles (fatigue cycles) when using actual field data, Tables 8.4 and 8.5 show that the expected fatigue life increases from the predicted design fatigue life dictated by AASHTO [2007] (displayed in Tables 8.2 and 8.3) for transverse and parallel orientations of open grid decks, respectively. However, even these remain quite small.

Table 8.4: Expected fatigue life for maximum recommended span lengths, transversely oriented open grid decks

Deck Type	D	α	L (in)	$M_{trans.\_weak\_neg.\_fatigue}$ (k-in/in)	$\sigma_{trans.\_weak\_neg.\_fatigue}$ (ksi)	$\sigma_{trans.\_weak\_total\_fatigue}$ (ksi)	Fatigue Life for ADTT = 1,000 (years)
7.5DIAG2.5TYP1	9.6	0.03	61.2	0.95	15.3	25.4	0.09
7.5DIAG2.5TYP2	10.0	0.03	61.2	0.93	13.4	23.5	0.29
7.5DIAG2.5TYP3	9.9	0.03	61.2	0.95	12.7	22.8	0.83
4.0RECT2.5TYP4	24.3	0.02	75.6	0.84	14.5	24.6	0.08
4.0RECT2.5TYP5	29.1	0.03	75.6	0.72	19.1	29.2	0.73
4.0RECT2.5TYP6	24.0	0.02	75.6	0.81	14.4	24.5	2.83

Table 8.5: Expected fatigue life for maximum recommended span lengths, open grid decks oriented parallel to traffic

Specimen	D	α	L (in)	$M_{pa.\_weak\_neg.\_fatigue}$ (k-in/in)	$\sigma_{pa.\_weak\_neg.\_fatigue}$ (ksi)	Fatigue Life for ADTT = 1,000 (years)
7.5DIAG2.5TYP1	9.6	0.03	61.2	0.50	8.1	2.67
7.5DIAG2.5TYP2	10.0	0.03	61.2	0.49	7.1	10.53
7.5DIAG2.5TYP3	9.9	0.03	61.2	0.50	6.7	32.60
4.0RECT2.5TYP4	24.3	0.02	75.6	0.43	7.4	2.85
4.0RECT2.5TYP5	29.1	0.03	75.6	0.37	9.7	20.08
4.0RECT2.5TYP6	24.0	0.02	75.6	0.42	7.4	102.83

In order to increase the fatigue life for a given deck, one solution is to decrease the maximum allowable span length. Table 6.6.1.2.5-3 in the AASHTO LRFD Bridge Design Specification [AASHTO 2007] gives constant-amplitude fatigue thresholds for each detail category. If stress ranges are less than these thresholds, infinite life can be assumed. These thresholds cannot be achieved even at a span length L = 36 in., the lower bound at which Euler-Bernoulli beam behavior can be assumed.

Fatigue life in Tables 8.2 and 8.4 are for worst case loading scenarios, with wheel lines located such that the tire patches run transversely at midspan of the deck, thereby producing the largest weak-direction stress range. Shortening span lengths will not

dramatically increase the fatigue life. If the wheel lines do not place the tire patches at midspan of the deck, the weak-direction stress ranges will be reduced in both the strong and weak directions. This reduction in stress range will provide a longer life. Thus, ensuring that traffic wheel lines are not located at midspan of open grid bridge decks, particularly for transversely oriented open grid decks would be effective in increasing the fatigue life. This may not be as big of an issue for open grid decks that are oriented parallel to traffic, which are expected to have a much longer fatigue life. As seen in this analysis, it is expected that in-situ fatigue lives of open grid bridge decks would be highly variable. Given the relatively low fatigue resistance of the weak-direction welded connections and the sensitivity of the outcomes to the location of the wheel lines relative to supports, the same deck and span length could exhibit cracking within a year if the wheel lines are located in an adverse location or last much longer if the wheel line is close to a line of support. The reported excellent performance of riveted open grid decking may result from the relatively short span lengths that limit the stress range magnitudes in the decks.

9 CONCLUSIONS

Experimental tests were performed on a suite of eight different types of open grid bridge deck specimens. Tests included strong-direction, weak-direction, and twisting stiffness tests of all specimens to establish input parameters for analytical and finite element models. A two-span continuous deck test was used to assess system behavior and load distribution in the strong and weak directions, explore the use of an alternative concrete-filled connection of the deck superstructure, and quantify high-cycle fatigue response. Subcomponent tests were performed to characterize the weak-direction bending fatigue behavior, including alternative welded details at the cross-bar intersections. Experimental test data were correlated with finite element results that used an orthotropic plate formation to model the deck. The finite element models were then used to develop LRFD compatible design moment equations for strength and fatigue limit states. Based on the experimental, analytical, and design studies, key findings are summarized below.

Based on experimental stiffness tests:

- BGFMA section properties predictions for strong direction corresponded reasonably well with strong direction (D_x) experimental results.
- The industry practice of assuming 50% supplemental bar contribution was a conservative estimate of the actual stiffness contribution.
- For welded diagonal open grid decks, assuming 50% contribution from diagonal bars in the same manner as supplemental bars may not produce a conservative estimate of strong direction stiffness.
- The weak-direction (D_y) stiffness for welded decks was more strongly influenced by the weld details.

- Weak-direction stiffnesses for riveted open grid deck specimens were very small compared to welded open grid deck specimens.

Based on continuous span tests, and finite element modeling and analysis:

- Concrete infill over stringers eliminates welding of open grid deck to stringers as well as locked-in residual tensile stresses in the grid elements.
- Weak-direction fatigue was produced in the full-scale continuous span fatigue test; however stresses were not induced in the same manner as in in-service open grid decks.
- Strong, weak, and twisting stiffness parameters (experimentally determined) are required as inputs for analytical models.
- Stiffness parameters are also used to compute neutral axis locations for projecting stresses in grid components.
- Analytical expressions for strength and fatigue design moments were developed from finite element analysis models of orthotropic decks that compared well with experimental results.
- The design equations were developed over a range of stiffness values and span lengths for transverse- and parallel-to-traffic deck orientations.
- Strength design of decks is controlled by patch loads located at the free edge of the open grid deck.
- The strength design expressions use the tandem axle load magnitudes with impact and live load factors, but not the multiple presence factor.

- BGFMA span limits for strength design were compared with yielding of an individual main bar and showed that for most of the specimens considered the span limits should be reduced.

Conclusions based on weak-direction bending fatigue tests and analyses include:

- The industry standard detail of a puddle weld for diagonal and rectangular bar intersections (specimen types 7.5DIAG2.5TYP1 and 4.0RECT2.5TYP4) is categorized as AASHTO fatigue category E' (with 95% probability).
- With 95% probability, alternate weld types 7.5DIAG2.5TYP2, 7.5DIAG2.5TYP3, 4.0RECT2.5TYP5 and 4.0RECT2.5TYP6 are categorized as fatigue category E', E, E, and B', respectively.
- Crack initiation for specimens with Type 6 weld detail (for the four 4.0RECT2.5TYP6 fatigue specimens) was in the serration, as opposed to all other weld types where cracks initiated from the weld detail
- A longer fatigue life is expected for main bars oriented parallel to traffic because a single stress cycle per axle is unlikely to produce stress reversals.
- Fatigue design based on the LRFD design truck with prescribed factors resulted in very short service life predictions for the BGFMA recommended span lengths.
- Fatigue lives predicted using expected actual truck weight data were longer, but still relatively short.
- In-situ fatigue life of open grid decks oriented transverse to traffic are expected to be highly dependent on wheel line locations relative to the superstructure support members.

- To achieve infinite life, designers would need to reduce span lengths considerably or ensure wheel lines are located over beams or stringers.

Further research includes:

- Performing orthogonal stiffness tests for other welded open grid decks of various main bar spacing and cross bar sizes.
- Load distribution tests of other welded open grid decks to correlate with FEA model and proposed design moment equations.
- Acquiring more data to quantify residual stress effects (with respect to fatigue life) when subjecting welds in the weak direction to positive bending moment.
- Quantifying weak-direction bending fatigue life of an open grid deck oriented transvers to traffic based on wheel lines at different locations along the span length.

10 REFERENCES

American Association of State Highway and Transportation Officials (AASHTO-LRFD). (2007). *LRFD Bridge Design Specifications*, 4th edition with 2008 Interims, Washington, D.C.

Apperson, K. P., and C. C. Menzemer. *Heavy Duty Riveted Bridge Deck AASHTO H20 Loading and Fatigue Testing*. Rep., 2010. Heavy Movable Structures, Inc. 13th Biennial Symposium.

Baker, T. H. *Static and Fatigue Strength, Determination of Design Properties for Grid Bridge Decks Volume I*. Thesis. University of Pittsburgh, 1991.

Higgins, C., and H. Mitchell. "Behavior of Composite Bridge Decks With Alternative Shear Connectors." *Journal of Bridge Engineering* January/February 6.1 (2001): 17-22.

Higgins, C. "LRFD Orthotropic Plate Model for Live Load Moment in Filled Grid Decks." *Journal of Bridge Engineering* January/February 8.1 (2003): 20-28.

Higgins, C. "Orthotropic Plate Model for Estimating Deflections in Filled Grid Decks." *Journal of Bridge Engineering* November/December 9.6 (2004): 599-605.

Higgins, C., O. Tugrul Turan, R. Connor, and J. Liu. "Unified Approach for LRFD Live Load Moments in Bridge Decks." *Journal of Bridge Engineering* November/December 16.6 (2011): 804-11.

Higgins, C., and O. Tugrul Turan. *Estimating Live Loads on Open Grid Decks*. 2011. Oregon State University, Corvallis, OR.

Gilmore, G.R. "Steel-Grid Bridge Flooring." *Modern Steel Construction* (1987): 16-33

GangaRao, H. V.S., W. Seifert, and H. Kevork. "Behavior of Open Steel Grid Decks Under Static And Fatigue Loads." *Transportation Research Record No. 1180, Bridge Design and Testing* (1988): 94-100

Huang, H., M. J. Chajes, D. R. Mertz, H. W. Shenton, and V. N. Kaliakin. "Behavior of Open Steel Grid Decks for Bridges." *Journal of Constructional Steel Research* 58 (2002): 819-42

Timoshenko, S., and S. Woinowsky-Krieger. *Theory of Plates and Shells*. New York: McGraw-Hill, 1959. Print.

Turan, O. T., and C. C. Higgins. "Analytical Solutions to General Orthotropic Plates under Patch Loading." *Journal of Engineering Mechanics* 137.7 (2011): 504-08. Web.

APPENDECIES

APPENDIX A – BGFMA Recommended Design Spans for Various Welded Open Grid Decks

Obtained from http://www.bgfma.org/resources/pdf/DesignTables/OpenGrid.pdf

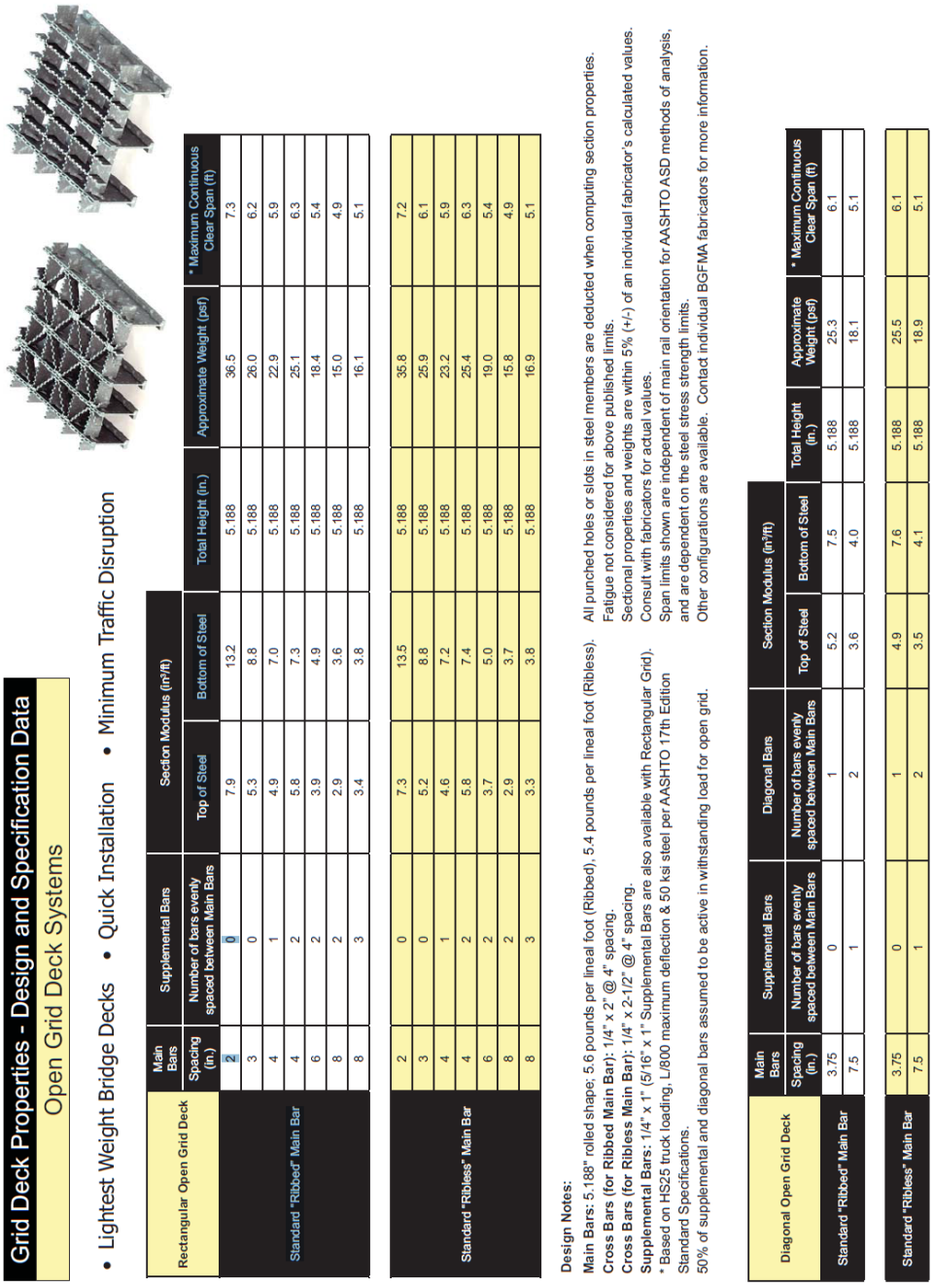

Grid Deck Properties - Design and Specification Data

Open Grid Deck Systems

• Lightest Weight Bridge Decks • Quick Installation • Minimum Traffic Disruption

Rectangular Open Grid Deck	Main Bars	Supplemental Bars	Section Modulus (in³/ft)		Total Height (in.)	Approximate Weight (psf)	* Maximum Continuous Clear Span (ft)
	Spacing (in.)	Number of bars evenly spaced between Main Bars	Top of Steel	Bottom of Steel			
Standard "Ribbed" Main Bar	2	0	7.9	13.2	5.188	36.5	7.3
	3	0	5.3	8.8	5.188	26.0	6.2
	4	1	4.9	7.0	5.188	22.9	5.9
	4	2	5.8	7.3	5.188	25.1	6.3
	6	2	3.9	4.9	5.188	18.4	5.4
	8	2	2.9	3.6	5.188	15.0	4.9
	8	3	3.4	3.8	5.188	16.1	5.1
Standard "Ribless" Main Bar	2	0	7.3	13.5	5.188	35.8	7.2
	3	0	5.2	8.8	5.188	25.9	6.1
	4	1	4.6	7.2	5.188	23.2	5.9
	4	2	5.8	7.4	5.188	25.4	6.3
	6	2	3.7	5.0	5.188	19.0	5.4
	8	2	2.9	3.7	5.188	15.8	4.9
	8	3	3.3	3.8	5.188	16.9	5.1

Design Notes:

Main Bars: 5.188" rolled shape; 5.6 pounds per lineal foot (Ribbed), 5.4 pounds per lineal foot (Ribless).
Cross Bars (for Ribbed Main Bar): 1/4" x 2" @ 4" spacing.
Cross Bars (for Ribless Main Bar): 1/4" x 2-1/2" @ 4" spacing.
Supplemental Bars: 1/4" x 1" (5/16" x 1" Supplemental Bars are also available with Rectangular Grid).
* Based on HS25 truck loading, L/800 maximum deflection & 50 ksi steel per AASHTO 17th Edition Standard Specifications.
50% of supplemental and diagonal bars assumed to be active in withstanding load for open grid.
All punched holes or slots in steel members are deducted when computing section properties.
Fatigue not considered for above published limits.
Sectional properties and weights are within 5% (+/-) of an individual fabricator's calculated values.
Consult with fabricators for actual values.
Span limits shown are independent of main rail orientation for AASHTO ASD methods of analysis, and are dependent on the steel stress strength limits.
Other configurations are available. Contact individual BGFMA fabricators for more information.

Diagonal Open Grid Deck	Main Bars	Supplemental Bars	Diagonal Bars	Section Modulus (in³/ft)		Total Height (in.)	Approximate Weight (psf)	* Maximum Continuous Clear Span (ft)
	Spacing (in.)	Number of bars evenly spaced between Main Bars	Number of bars evenly spaced between Main Bars	Top of Steel	Bottom of Steel			
Standard "Ribbed" Main Bar	3.75	0	1	5.2	7.5	5.188	25.3	6.1
	7.5	1	2	3.6	4.0	5.188	18.1	5.1
Standard "Ribless" Main Bar	3.75	0	1	4.9	7.6	5.188	25.5	6.1
	7.5	1	2	3.5	4.1	5.188	18.9	5.1

Figure A.1: BGFMA open grid deck design and specification data sheet

APPENDIX B – INSTRUMENTATION PLANS AND RESULTS FOR STIFFNESS TESTS

Table B.1 lists a naming convention for strain gages used in stiffness tests.

Figure B.1 shows plan views of the bottom of a welded diagonal open grid specimen used for strong- and weak-direction stiffness tests. The sensor configuration shown is typical for all open grid deck configurations.

Displacement sensors are labeled based on location with respect to the north arrow.

Displacement sensors beginning with 'N' and 'S' represent sensors that measure support displacements. Sensors beginning with 'D' measure midspan displacement. For all specimens, relative displacement sensor locations are consistent for D_x and D_y tests.

All strain and displacement values are based on a 10 kip load. Tensile strains are shown as negative values. Refer to Fig. 4.24 and Table 4.1 for actual load and span conditions and effective specimen widths for all D_x and D_y tests.

Strains for M5 and M7 in specimens 7.5DIAG2.5TYP2 and 4.0RECT2.5TYP6 are measured using N2A-06-20CBW-120 strain gages, as discussed in Section 4.4.

Table B.1: Strain gage naming convention

Gage	Location
M	Bottom/Top Rib of Main Bar (Depending on Symbol)
S	Bottom of Supplemental Bar
A	Bottom of Diagonal Bar
C	Bottom of Cross Bar
CR	Bottom of Crimp Bar

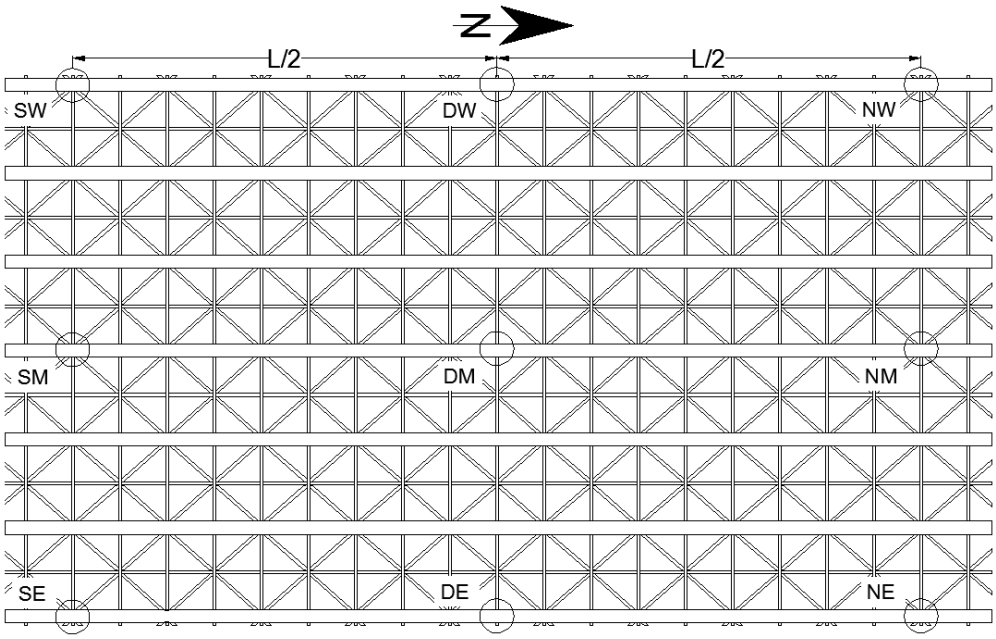

Figure B.1: Typical strong-direction (D_x) displacement sensor configuration

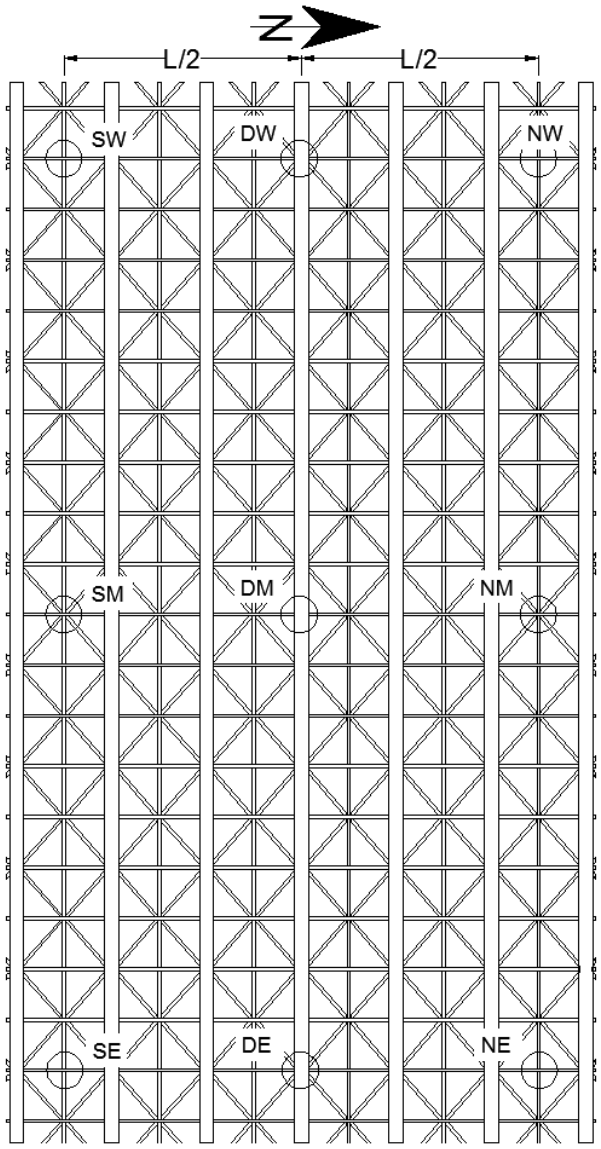

Figure B.2: Typical weak-direction (D_y) displacement sensor configuration

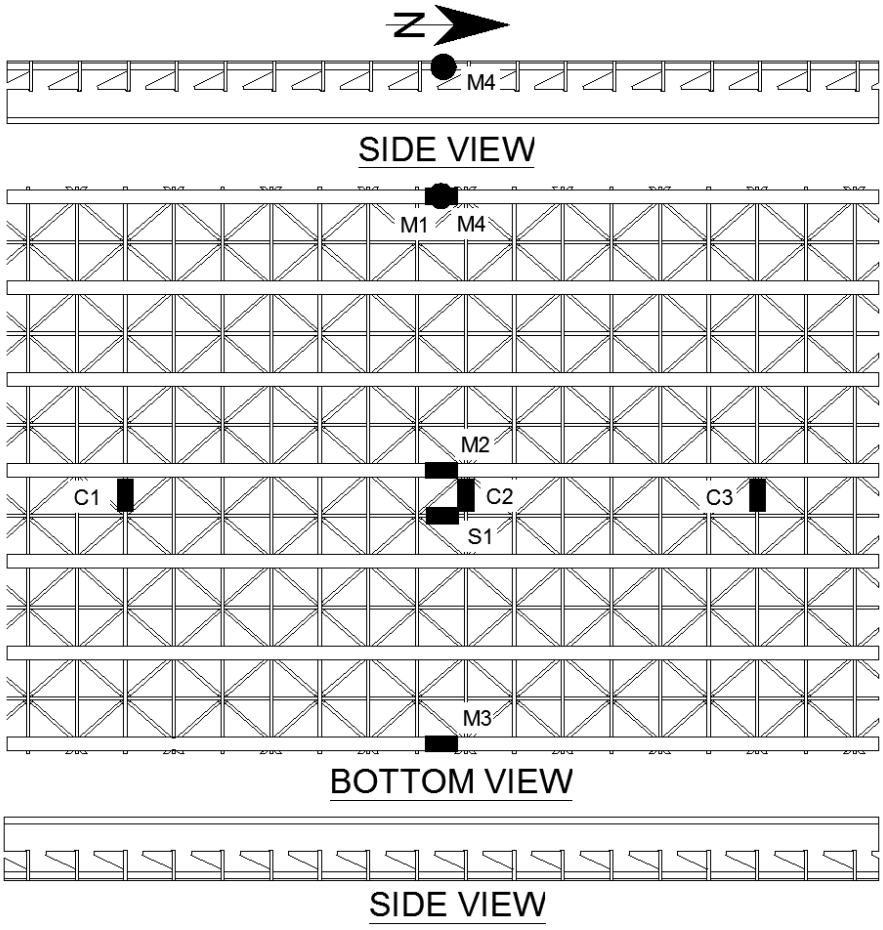

Figure B.3: 7.5DIAG2.5TYP1 D_x and D_y test strain gage plan

Table B.2: Strains and sisplacements for 7.5DIAG2.5TYP1 D_x and D_y tests

Displacement Sensor/ Strain Gage	Test	
	Dx	Dy
DW	-0.041	-0.061
DM	-0.041	-0.062
DE	-0.039	-0.068
M1	-218	NA
M2	-260	NA
M3	-236	NA
M4	301	NA
S1	143	NA
C1	NA	-623
C2	NA	-531
C3	NA	-503

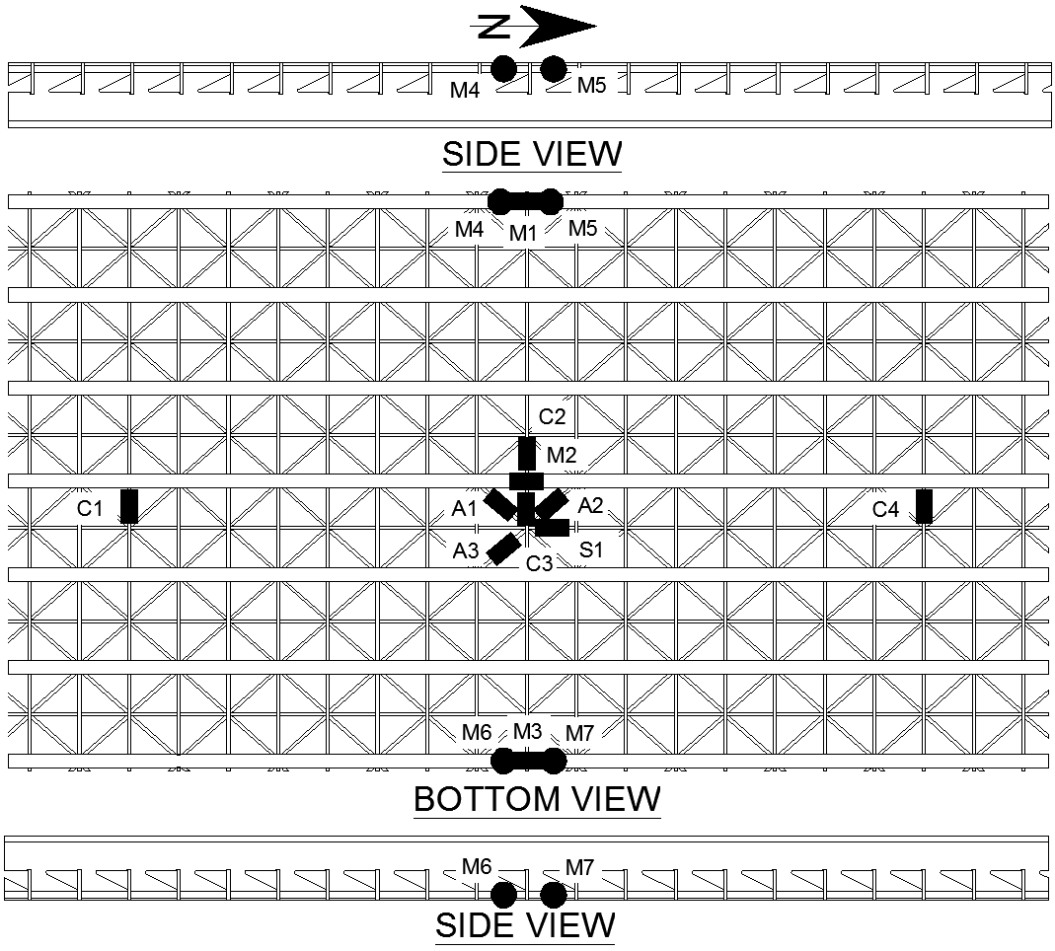

Figure B.4: 7.5DIAG2.5TYP2 D_x and D_y test strain gage plan

Table B.3: Strains and displacements for 7.5DIAG2.5TYP2 D_x and D_y tests

Displacement Sensor/ Strain Gage	Test	
	Dx	Dy
DW	-0.067	-0.051
DM	-0.067	-0.060
DE	NA	-0.051
M1	-301	NA
M2	-321	NA
M3	NA	NA
M4	370	NA
M5	331	NA
M6	316	NA
M7	313	NA
S1	190	NA
C1	NA	-443
C2	NA	-488
C3	NA	-524
C4	NA	-599
A1	11	-11
A2	-5	-45
A3	10	NA

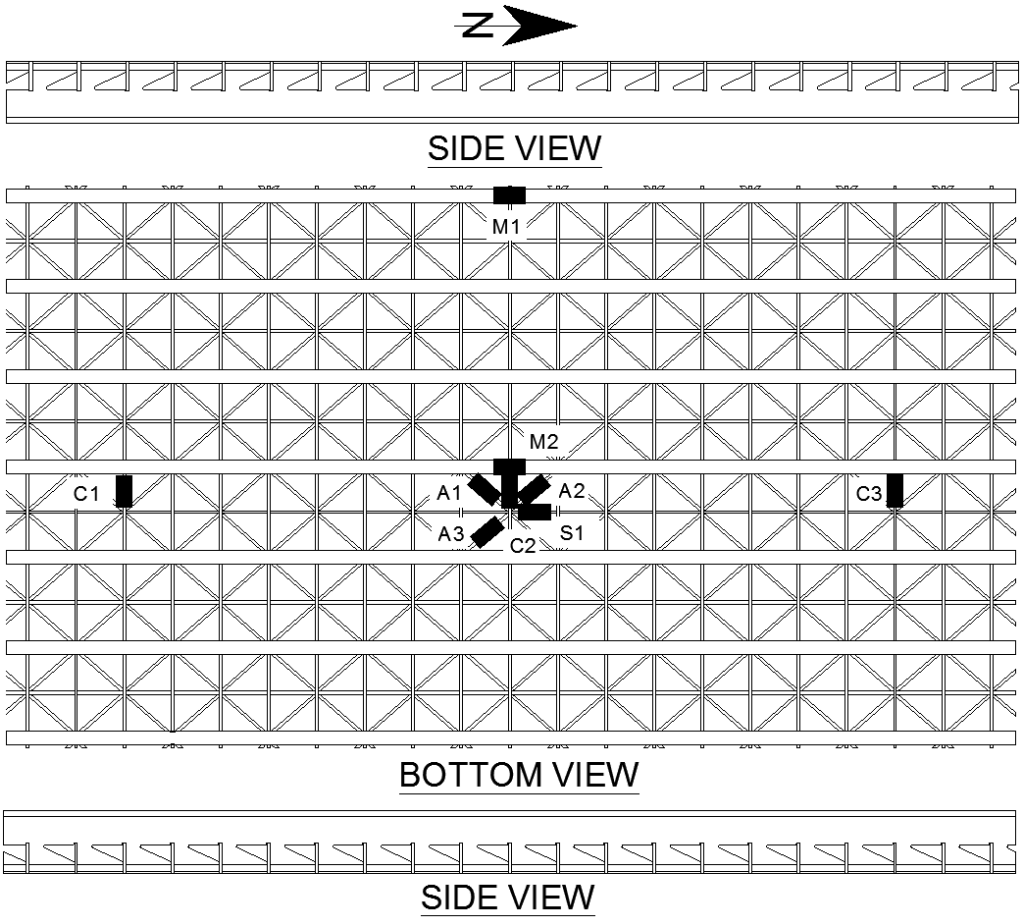

Figure B.5: 7.5DIAG2.5TYP3 D_x and D_y test strain gage plan

Table B.4: Strains and displacements for 7.5DIAG2.5TYP3 D_x and D_y tests

Displacement Sensor/ Strain Gage	Test	
	Dx	Dy
DW	-0.066	-0.050
DM	-0.064	-0.051
DE	-0.067	-0.053
M1	-309	NA
M2	-319	NA
S1	182	NA
C1	NA	-496
C2	NA	-522
C3	NA	-526
A1	7	NA
A2	5	-8
A3	-13	NA

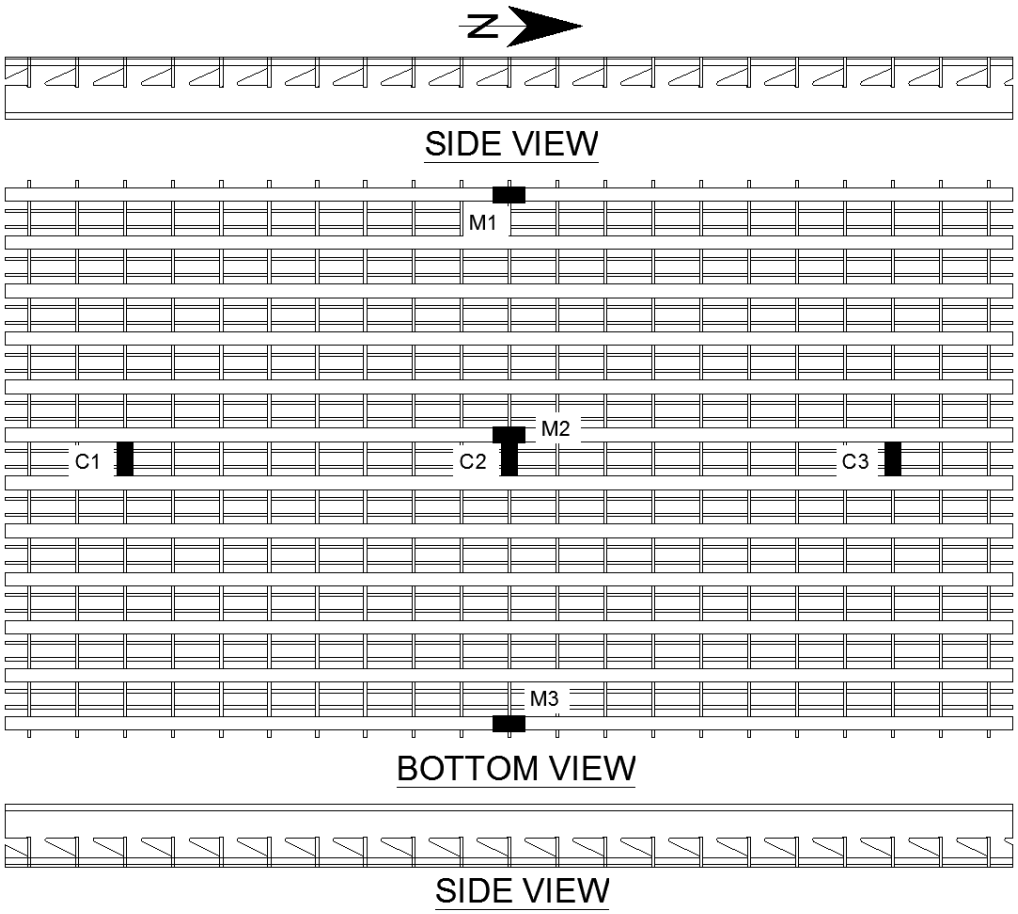

Figure B.6: 4.0RECT2.5TYP4 D_x and D_y test strain gage plan

Table B.5: Strains and displacements for 4.0RECT2.5TYP4 D_x and D_y tests

Displacement Sensor/ Strain Gage	Test	
	Dx	Dy
DW	-0.033	-0.083
DM	NA	-0.081
DE	-0.033	-0.087
M1	-175	NA
M2	-177	NA
M3	-146	NA
C1	NA	-671
C2	NA	-654
C3	NA	-619

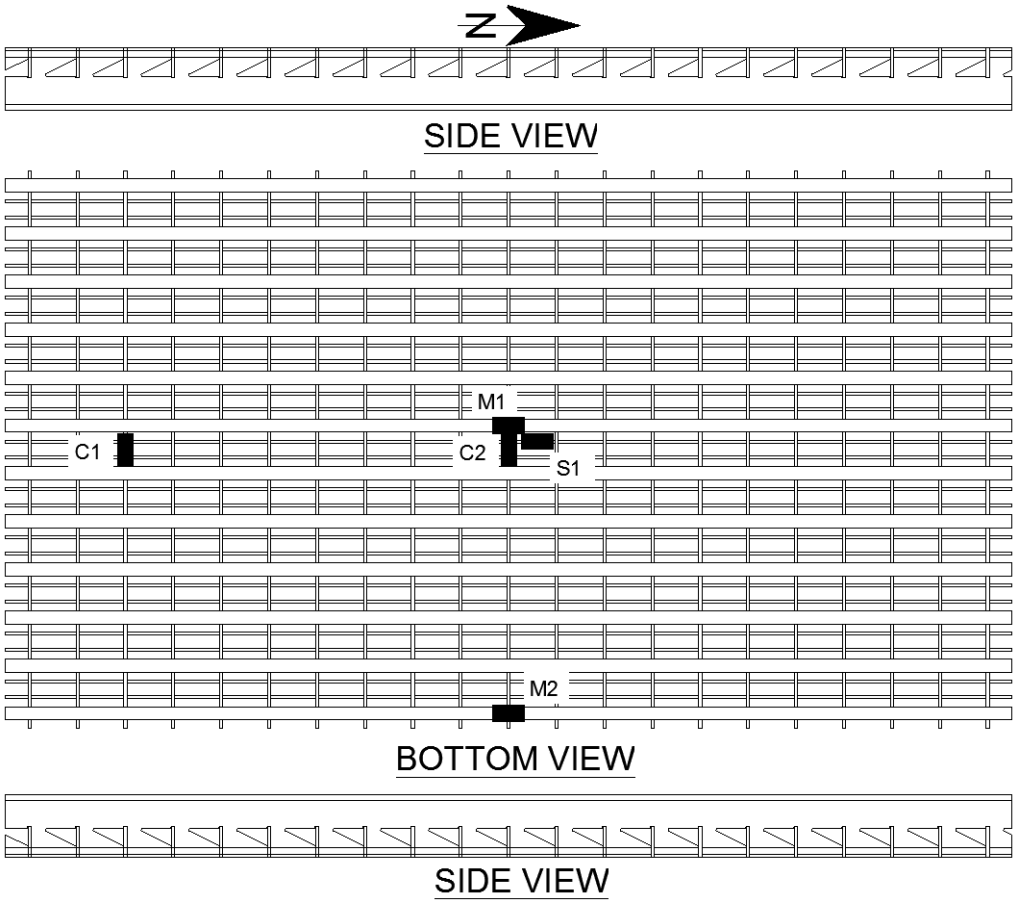

Figure B.7: 4.0RECT2.5TYP5 D_x and D_y test strain gage plan

Table B.6: Strains and displacements for 4.0RECT2.5TYP5 D_x and D_y tests

Displacement Sensor/ Strain Gage	Test	
	Dx	Dy
DW	-0.033	-0.105
DM	-0.039	-0.087
DE	-0.036	-0.117
M1	-187	NA
M2	-175	NA
S1	74	NA
C1	NA	-916
C2	NA	-637

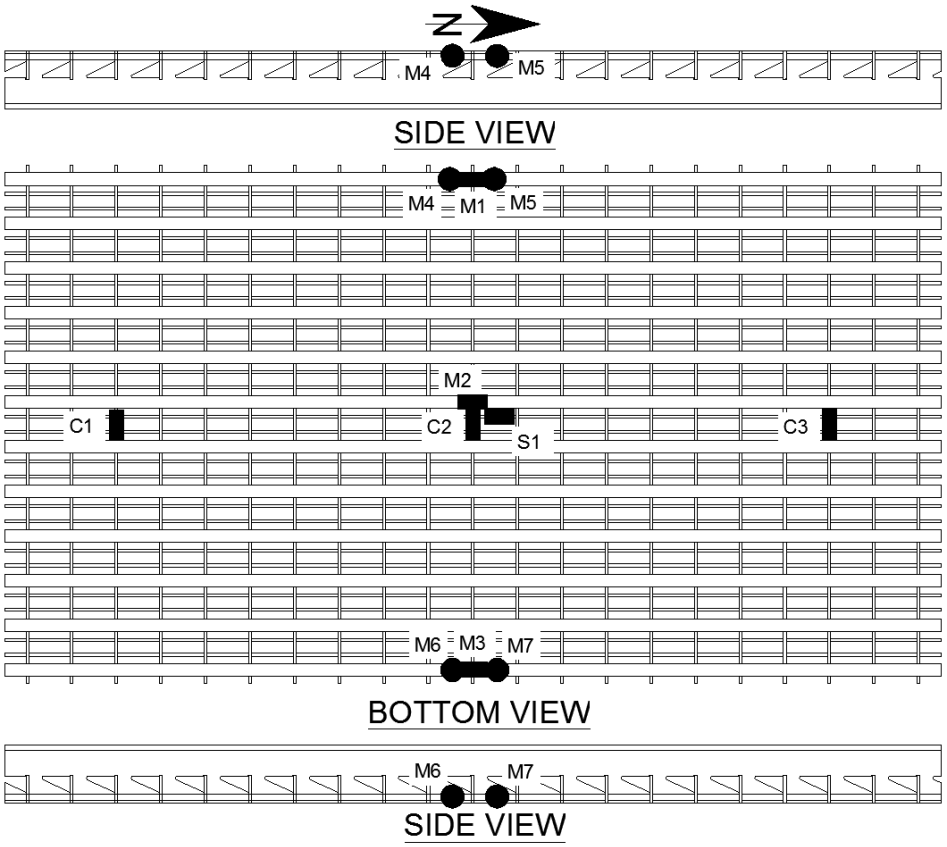

Figure B.8: 4.0RECT2.5TYP6 D_x and D_y test strain gage plan

Table B.7: Strains and displacements for 4.0RECT2.5TYP6 D_x and D_y tests

Displacement Sensor/ Strain Gage	Test	
	Dx	Dy
DW	-0.030	-0.084
DM	-0.034	-0.060
DE	-0.029	-0.079
M1	-163	NA
M2	-181	NA
M3	-173	NA
M4	160	NA
M5	163	NA
M6	172	NA
M7	135	NA
S1	74	NA
C1	NA	-678
C2	NA	-437
C3	NA	-660

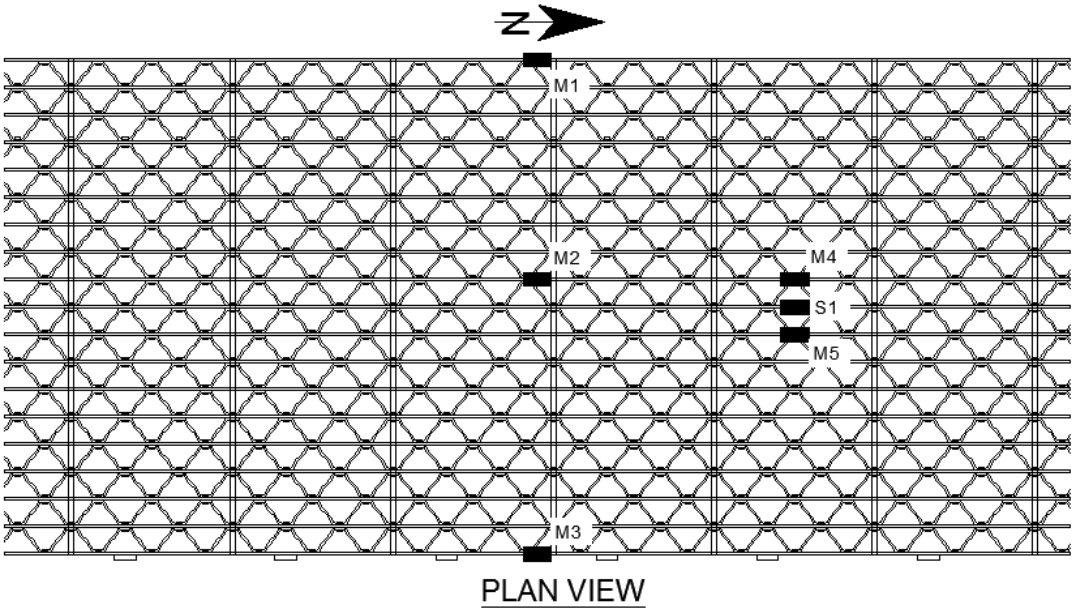

Figure B.9: 37-R-L-5x¼ D_x test strain gage plan

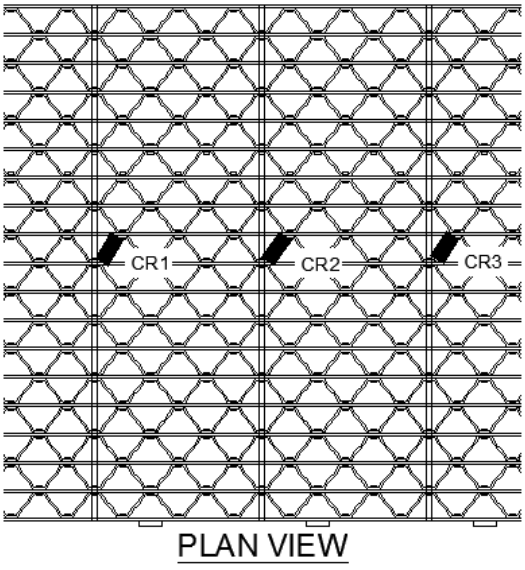

Figure B.10: 37-R-L-5x¼ D_y test strain gage plan

Table B.8: Strain and displacements for 37-R-L-5x¼ D_x and D_y tests

Displacement Sensor/ Strain Gage	Test	
	Dx	Dy
DW	-0.171	-0.663
DM	-0.171	-0.612
DE	-0.166	-0.578
M1	-710	NA
M2	-756	NA
M3	-661	NA
M4	-288	NA
M5	-322	NA
S1	75	NA
CR1	NA	-903
CR2	NA	-921
CR3	NA	-802

M4, M5, and S1 are located at the quarter-point of the simple span. The same panel was used for load distribution tests, therefore composite action of the supplemental bar was measured by these three strain gages during the strong-direction stiffness test.

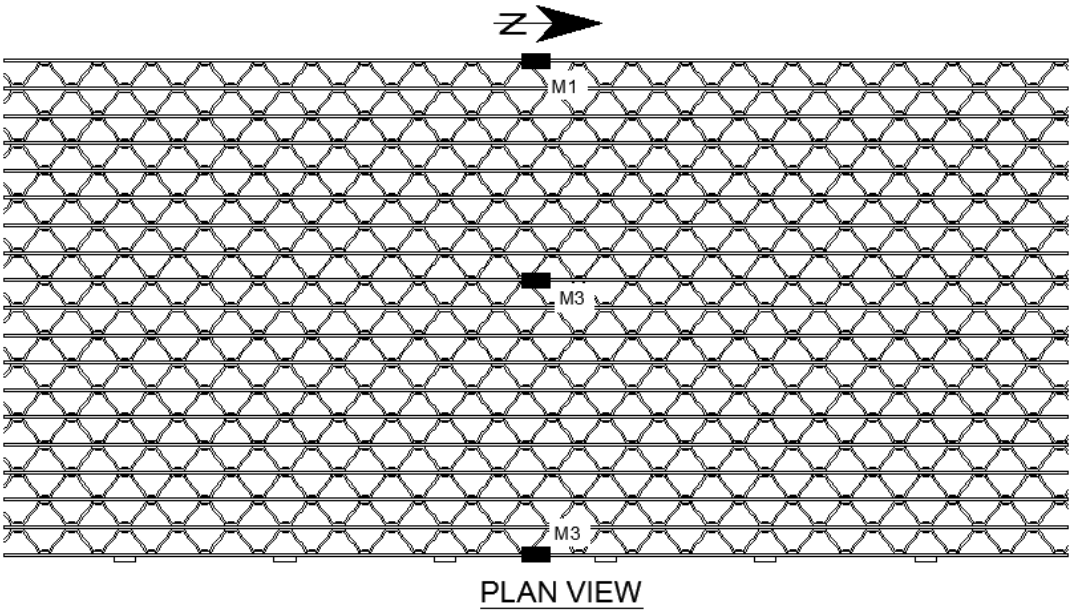

Figure B.11: 37-R-5x¼ D_x test strain gage plan

Table B.9: Strains and displacements for 37-R-L-5x¼ D_x and D_y tests

Displacement Sensor/ Strain Gage	Test	
	Dx	Dy
DW	-0.103	-3.061
DM	-0.111	-2.857
DE	-0.122	-2.855
M1	-414	NA
M2	-417	NA
M3	-369	NA

No strain gages were used in weak-direction stiffness tests for the 37-R-5x¼ open grid panel, so the tested panel is not shown.

APPENDIX C - INSTRUMENTATION PLANS AND RESULTS FOR LOAD DISTRIBUTION TESTS

For the origin of the coordinate system for all full size specimens subjected to load distribution tests, the x-axis (labeled 'X' in proceeding figures) is oriented in the strong direction and runs along the center of the outer main bar, and the y-axis (labeled 'Y') runs through the middle of the panel. For specimen 7.5DIAG2.5TYP1, the y-axis coincides with the midspan location for the 8 ft single span tests, and also the center support location for testing at the 4 ft, 5 ft, and 6 ft spans. The origin remains consistent for all figures and data related to specimen 7.5DIAG2.5TYP1. For all other panels, the y-axis runs along the center support.

The naming convention for strain gages is as follows: 'M' represents strain gages mounted on the bottom flange of the main bar. 'MT' represents gages that are mounted to the top rib of the main bar. 'C' represents strain gages that are mounted to the bottom of the cross bar. 'CR' represents strain gages mounted to the bottom of crimp bar on riveted panels. The first number represents span length and location along the span for which the strain gage is intended. For 'M' and 'MT' gages, the last number represents the main bar that the gage is mounted to. For 'C' gages, the last number represents the main bar that the gage is located above, in relation to the Y datum. For example, C85.8 is a strain gage mounted on the bottom of cross bar above main bar 8 (with respect to the Y datum) at midspan for the 8 ft simple span test configuration. M525.3 is a strain gage mounted on the bottom of main bar 3 at the quarter-point of the north span of the 5 ft 2-span continuous span configuration. For the riveted panels, an asterisk (*) following the sensor number represents a gage located on the adjacent bolted panel.

The naming convention for displacement sensors is as follows: Support displacement sensors are labeled ‘N’, ‘M’ and ‘S’ for north, middle and south supports, respectively. The number represents the main bar that the sensor is attached to, or the main bar that the sensor is located above, in relation to the Y datum. Displacement sensors labeled with a ‘D’ represent midspan displacements. For example, a sensor labeled N1 is a support displacement sensor located on the main bar labeled M1.

All strain gage data is shown as microstrain (με), positive and negative values representing compression and tensile strains, respectively. All displacements are shown in inches, with positive displacements representing uplift of open grid panels. If NA appears in any table cell, data was not collected for that particular test, or the strain gage/displacement sensor malfunctioned.

All displacement sensor and strain gage data are shown for 10 kip patch loads. If a particular test has two patch load locations listed, a tandem or axle load was used for a total actuator load of 20 kips.

For Tests 70 and 71, the elastomeric pads were not placed under the tire patch load beams. Thus, uniform pressure may not have been applied over the 10 x 20 in. contact area, and stress concentrations in individual grid components may have produced artificially and unreliably high strains.

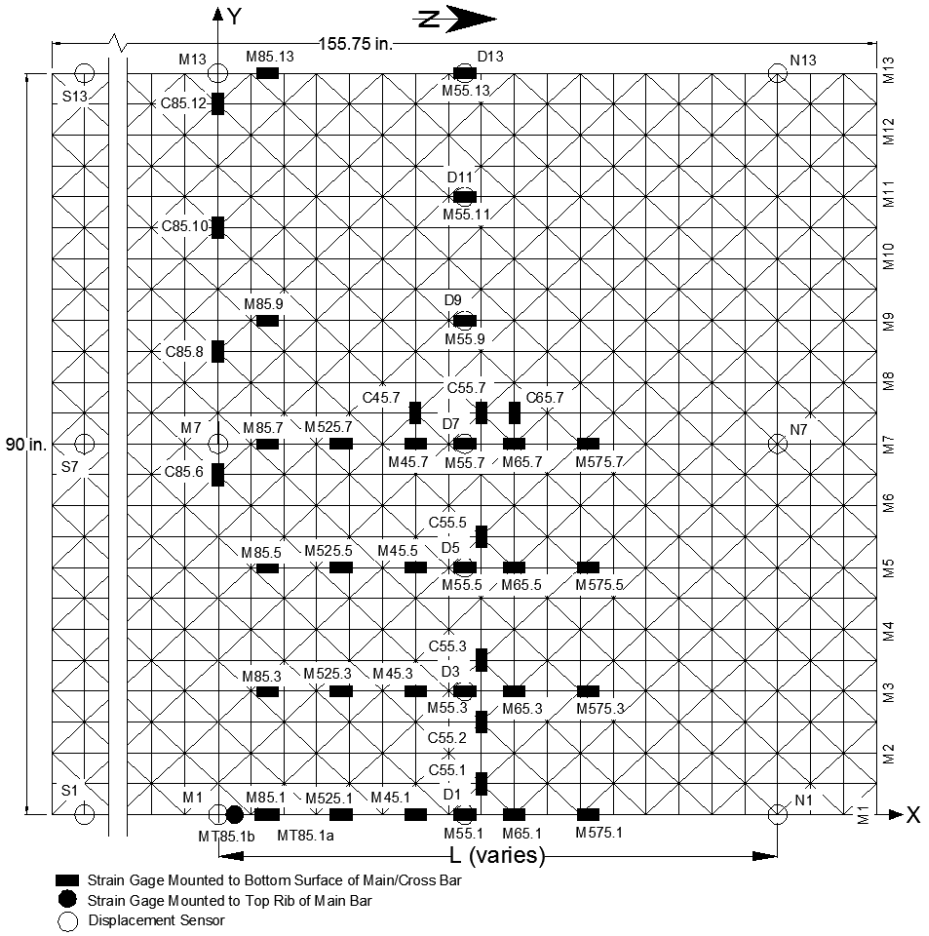

LEGEND					
Strain Gage	Location (x,y) (in.)	Strain Gage	Location (x,y) (in.)	Displacement Sensor	Location (x,y) (in.)
M85.1	(6, 0)	M55.11	(30, 75)	D1	(L/2, 0)
M85.3	(6, 15)	M55.13	(30, 90)	D3	(L/2, 15)
M85.5	(6, 30)	M65.1	(36, 0)	D5	(L/2, 30)
M85.7	(6, 45)	M65.3	(36, 15)	D7	(L/2, 45)
M85.9	(6, 60)	M65.5	(36, 30)	D9	(L/2, 60)
M85.13	(6, 90)	M65.7	(36, 45)	D11	(L/2, 75)
MT85.1a	(6, 0)	M575.1	(45, 0)	D13	(L/2, 90)
MT85.1b	(2, 0)	M575.3	(45, 15)	N1	(L, 0)
M525.1	(15, 0)	M575.5	(45, 30)	N7	(L, 45)
M525.3	(15, 15)	M575.7	(45, 45)	N13	(L, 90)
M525.5	(15, 30)	C85.6	(0, 41.25)	M1	(0, 0)
M525.7	(15, 45)	C85.8	(0, 56.25)	M7	(0, 45)
M45.1	(24, 0)	C85.10	(0, 71.25)	M13	(0, 90)
M45.3	(24, 15)	C85.12	(0, 86.25)	S1	(-L, 0)
M45.5	(24, 30)	C45.7	(24, 48.75)	S7	(-L, 45)
M45.7	(24, 45)	C55.1	(32, 3.75)	S13	(-L, 90)
M55.1	(30, 0)	C55.2	(32, 11.25)		
M55.3	(30, 15)	C55.3	(32, 18.75)		
M55.5	(30, 30)	C55.5	(32, 33.75)		
M55.7	(30, 45)	C55.7	(32, 48.75)		
M55.9	(30, 60)	C65.7	(36, 48.75)		

Figure C.1: Strain and displacement sensor plan for specimen 7.5DIAG2.5TYP1

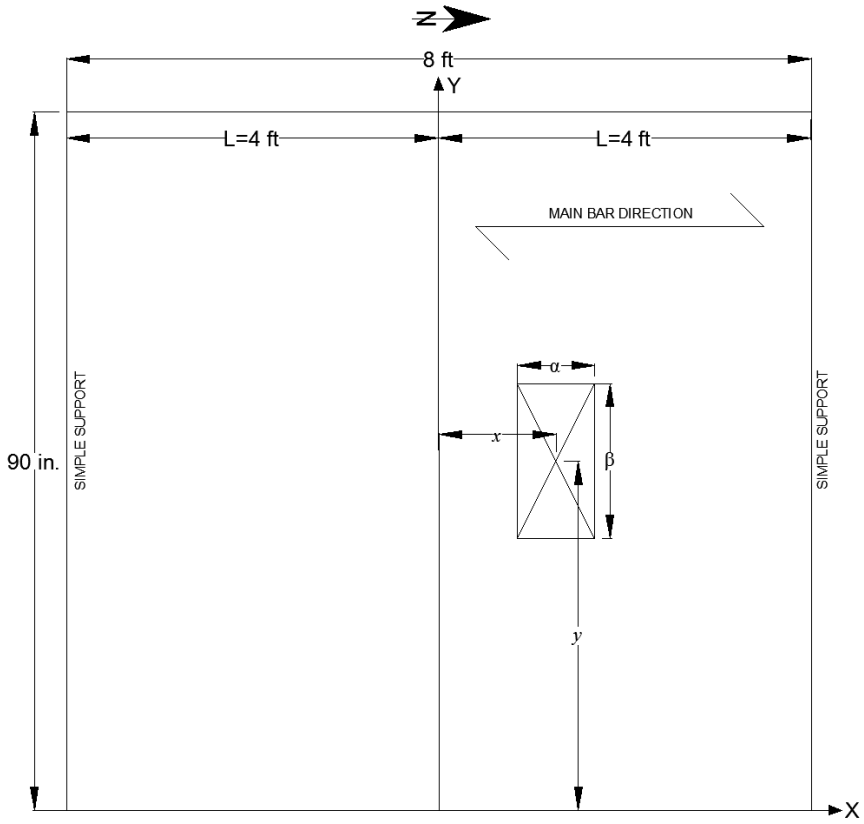

LEGEND		
Test #	Patch Location (x, y) (in.)	Patch Orientation (α, β) (in.)
1	(0, 45)	(10, 20)
2	(0, 45)	(20, 10)
3	(0, 22.5)	(10, 20)
4	(0, 22.5)	(20, 10)
5	(0, 9)	(10, 20)
6	(0, 4)	(20, 10)
7	(0, 67.5)	(10, 20)
8	(0, 67.5)	(20, 10)
9	(0, 81)	(10, 20)
10	(0, 86)	(20, 10)
11	(0, 9)	(10, 20)
	(0, 81)	(10, 20)

Figure C.2: Patch load plan for tests 1-11

Table C.1: Strain and displacement data for tests 1-11

Displacement Sensor/ Strain Gage	Test #										
	1	2	3	4	5	6	7	8	9	10	11
D1	-0.020	-0.018	-0.160	-0.156	-0.323	-0.367	0.014	0.015	0.024	0.033	-0.135
D3	-0.057	-0.059	-0.149	-0.145	-0.177	-0.188	-0.008	-0.007	0.005	0.015	-0.084
D5	-0.122	-0.121	-0.146	-0.143	-0.114	-0.100	-0.046	-0.037	-0.010	0.004	-0.062
D7	-0.152	-0.163	-0.088	-0.083	-0.046	-0.032	-0.094	-0.083	-0.044	-0.024	-0.047
D9	-0.119	-0.123	-0.042	-0.040	-0.011	-0.001	-0.156	-0.148	-0.116	-0.093	-0.064
D11	-0.062	-0.056	-0.006	-0.005	0.012	0.016	-0.155	-0.151	-0.191	-0.201	-0.090
D13	-0.009	-0.005	0.018	0.022	0.028	0.031	-0.124	-0.120	-0.272	-0.350	-0.113
M85.1	3	-8	-292	-282	-782	-867	41	41	40	43	-652
M85.3	-139	-139	-462	-484	-557	-603	-9	-4	28	46	-567
M85.5	-307	-302	-462	-363	-251	-188	-79	-67	-12	18	-256
M85.7	-492	-509	-203	-184	-79	-46	-213	-191	-88	-39	-177
M85.9	-314	-294	-78	-71	-9	12	-401	-435	-275	-180	-299
M85.13	6	12	42	41	40	36	-240	-250	-751	-930	-592
C85.6	-582	-828	23	25	160	194	69	81	127	168	291
C85.8	-223	-147	76	76	95	100	-223	-80	162	292	280
C85.10	31	36	44	43	32	27	-1006	-208	-947	307	-455
C85.12	13	13	6	6	2	0	14	-9	116	-674	-128

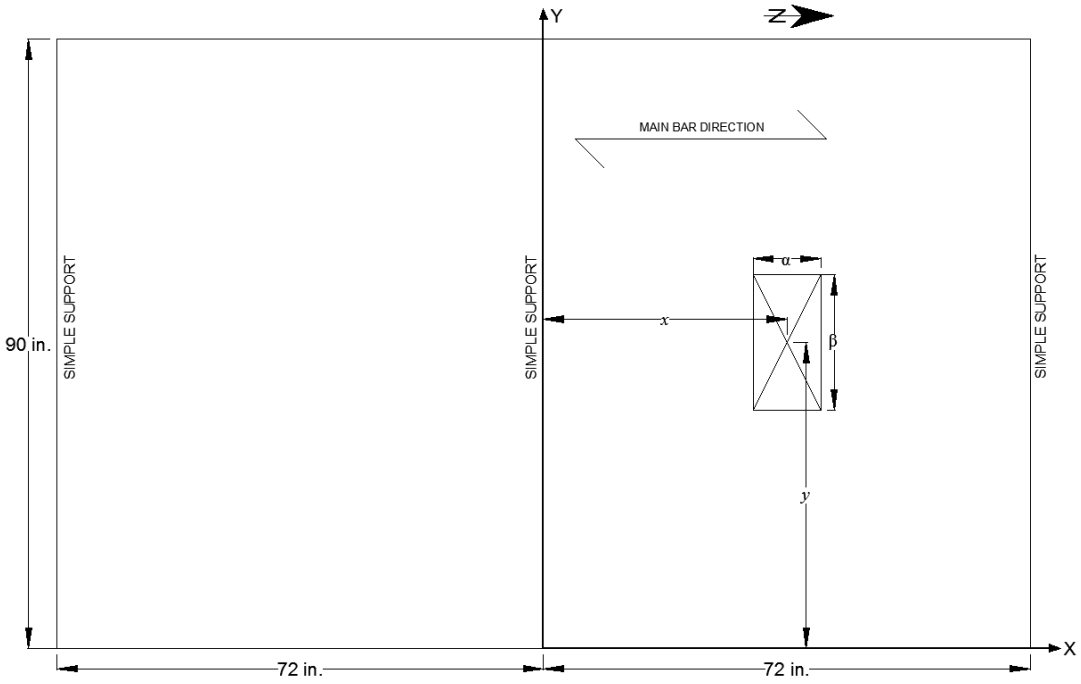

LEGEND					
Test #	Patch Location (x, y) (in.)	Patch Orientation (α, β) (in.)	Test #	Patch Location (x, y) (in.)	Patch Orientation (α, β) (in.)
12	(36, 45)	(10, 20)	29	(-36, 22.5)	(20, 10)
13	(36, 45)	(20, 10)	30	(-36, 9)	(10, 20)
14	(36, 22.5)	(10, 20)	31	(-36, 4)	(20, 10)
15	(36, 22.5)	(20, 10)	32	(-36, 9)	(10, 20)
16	(36, 9)	(10, 20)		(-36, 81)	(10, 20)
17	(36, 4)	(20, 10)	40	(36, 45)	(20, 10)
18	(36, 9)	(10, 20)		(-36, 45)	(20, 10)
	(36, 81)	(10, 20)	41	(36, 4)	(20, 10)
26	(-36, 45)	(10, 20)		(-36, 4)	(20, 10)
27	(-36, 45)	(20, 10)	42	(36, 86)	(20, 10)
28	(-36, 22.5)	(10, 20)		(-36, 86)	(20, 10)

Figure C.3: Patch load plan for tests 12-18, 26-32, 40-42

Table C.2: Strain and displacement data for tests 12-18

Displacement Sensor/ Strain Gage	Test #						
	12	13	14	15	16	17	18
D1	-0.004	-0.003	-0.138	-0.180	-0.001	-0.002	-0.138
D3	-0.019	-0.019	-0.085	-0.075	0.000	0.001	-0.078
D5	-0.059	-0.053	-0.044	-0.027	-0.002	0.001	-0.048
D7	-0.083	-0.085	-0.013	-0.001	-0.018	-0.001	-0.031
D9	-0.061	-0.060	-0.002	-0.001	-0.051	-0.029	-0.051
D11	-0.023	-0.021	-0.002	0.001	-0.096	-0.090	-0.087
D13	0.000	0.000	-0.004	0.002	-0.137	-0.175	-0.116
M85.1	-14	-11	-38	19	1	-13	25
M85.3	-34	-36	-16	-50	-2	-10	10
M85.5	-7	-15	-48	-73	-19	-12	-79
M85.7	48	58	-39	-30	-51	-37	-100
M85.9	-17	-20	-15	-13	-77	-78	-79
M85.13	-27	-27	4	-8	-60	-21	-57
M65.1	22	22	-585	-768	8	2	-599
M65.3	-65	-54	-522	-373	6	5	-504
M65.5	-244	-209	-170	-87	-4	1	-154
M65.7	-479	-447	-34	-11	-38	-10	-89
C65.7	-445	-510	86	86	124	137	218

Table C.3: Strain and displacement data for tests 26-32, 40-42

Displacement Sensor/ Strain Gage	Test #									
	26	27	28	29	30	31	32	40	41	42
D1	NA	NA	NA	NA	NA	NA	NA	0.000	-0.123	-0.003
D3	NA	NA	NA	NA	NA	NA	NA	-0.011	-0.041	0.005
D5	NA	NA	NA	NA	NA	NA	NA	-0.040	-0.005	0.007
D7	NA	NA	NA	NA	NA	NA	NA	-0.063	0.008	0.004
D9	NA	NA	NA	NA	NA	NA	NA	-0.041	0.006	-0.013
D11	NA	NA	NA	NA	NA	NA	NA	-0.008	0.002	-0.059
D13	NA	NA	NA	NA	NA	NA	NA	0.007	-0.001	-0.120
M85.1	-38	-35	53	130	-32	-5	81	4	540	5
M85.3	-37	-41	36	-4	-27	-4	39	20	211	9
M85.5	33	29	-26	-63	-29	-11	-54	124	12	5
M85.7	77	80	-42	-39	-40	-34	-90	259	-12	-5
M85.9	21	14	-27	-18	-20	-58	-51	127	-5	16
M85.13	-36	-34	-12	-12	26	104	64	6	1	473
M65.1	-23	-24	24	34	-25	-7	31	25	-607	11
M65.3	-2	-4	9	7	-15	-2	6	-15	-242	7
M65.5	11	10	-5	-12	-12	-10	-13	-151	-24	7
M65.7	14	13	-12	-19	-10	-17	-25	-399	8	15
C65.7	45	48	-43	-42	-40	-42	-86	-494	63	88

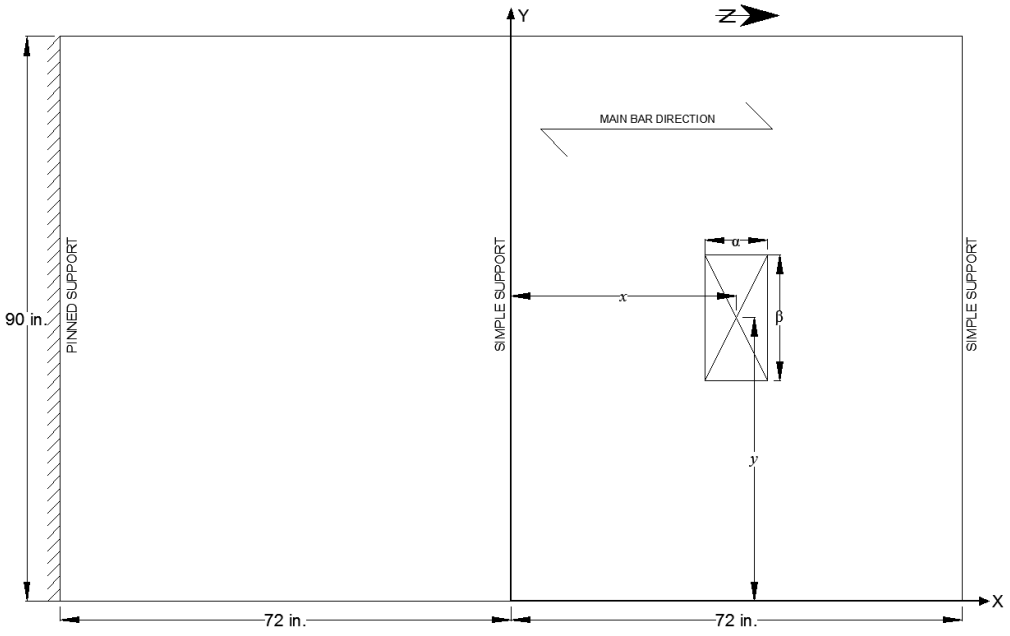

LEGEND		
Test #	Patch Location (x, y) (in.)	Patch Orientation (α, β) (in.)
19	(36, 45)	(10, 20)
20	(36, 45)	(20, 10)
21	(36, 22.5)	(10, 20)
22	(36, 22.5)	(20, 10)
23	(36, 9)	(10, 20)
24	(36, 4)	(20, 10)
25	(36, 9)	(10, 20)
	(36, 81)	(10, 20)

Figure C.4: Patch load plan for tests 19-25

Table C.4: Strain and displacement data for tests 19-25

Displacement Sensor/ Strain Gage	Test #						
	19	20	21	22	23	24	25
D1	-0.004	-0.003	-0.120	-0.156	-0.006	-0.005	-0.128
D3	-0.023	-0.023	-0.072	-0.059	-0.002	-0.002	-0.073
D5	-0.056	-0.053	-0.034	-0.018	0.001	-0.001	-0.038
D7	-0.078	-0.081	-0.013	0.001	-0.009	-0.003	-0.019
D9	-0.056	-0.057	-0.002	0.000	-0.037	-0.025	-0.039
D11	-0.018	-0.018	0.001	-0.002	-0.079	-0.074	-0.075
D13	0.002	0.000	0.001	0.000	-0.111	-0.143	-0.095
M85.1	-14	-17	106	174	-15	-23	71
M85.3	-25	-26	73	45	-12	-14	56
M85.5	25	19	-6	-31	-11	-5	-31
M85.7	80	89	-25	-22	-17	-9	-56
M85.9	13	9	-16	-15	3	-7	-20
M85.13	-7	-8	-10	-14	92	145	53
M65.1	21	19	-529	-680	-2	-3	-554
M65.3	-57	-49	-474	-345	1	3	-503
M65.5	-237	-203	-138	-62	1	5	-153
M65.7	-462	-434	-24	0	-15	6	-53
C65.7	-433	-513	89	86	114	125	204

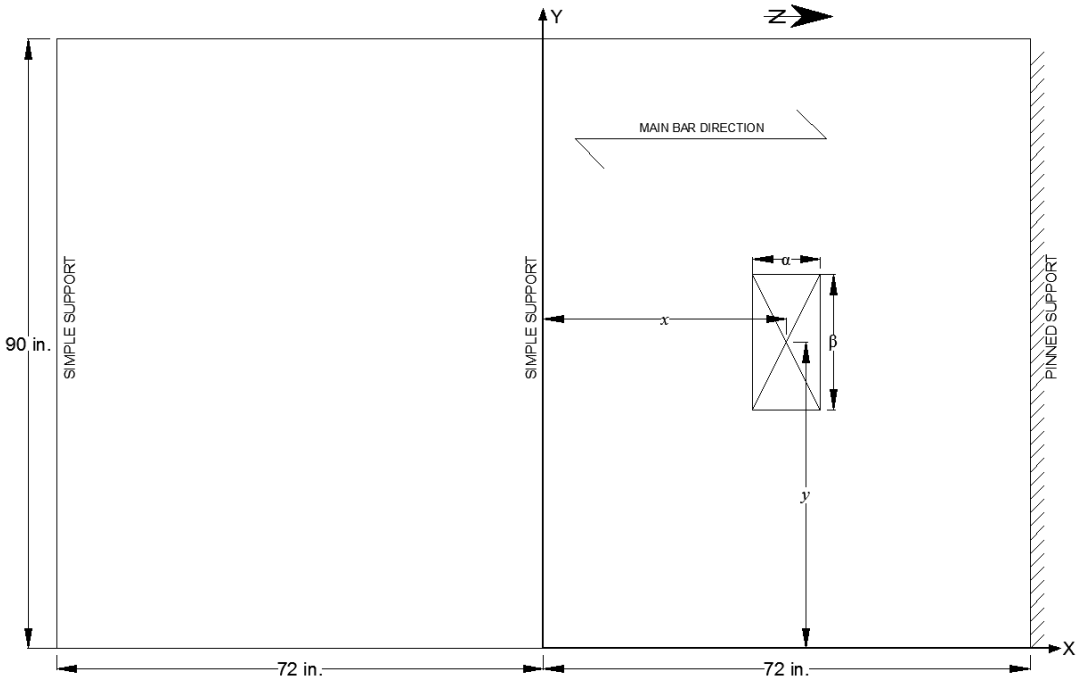

LEGEND		
Test #	Patch Location (x, y) (in.)	Patch Orientation (α, β) (in.)
33	(-36, 45)	(10, 20)
34	(-36, 45)	(20, 10)
35	(-36, 22.5)	(10, 20)
36	(-36, 22.5)	(20, 10)
37	(-36, 9)	(10, 20)
38	(-36, 4)	(20, 10)
39	(-36, 9)	(10, 20)
	(-36, 81)	(10, 20)

Figure C.5: Patch load plan for tests 33-39

Table C.5: Strain and displacement data for tests 33-39

Displacement Sensor/ Strain Gage	Test #						
	33	34	35	36	37	38	39
D1	NA	NA	NA	NA	NA	NA	NA
D3	NA	NA	NA	NA	NA	NA	NA
D5	NA	NA	NA	NA	NA	NA	NA
D7	NA	NA	NA	NA	NA	NA	NA
D9	NA	NA	NA	NA	NA	NA	NA
D11	NA	NA	NA	NA	NA	NA	NA
D13	NA	NA	NA	NA	NA	NA	NA
M85.1	-5	-6	217	328	-11	-23	208
M85.3	18	14	166	143	-13	-16	168
M85.5	95	92	56	17	-12	-10	54
M85.7	137	142	-2	-8	-11	-11	-6
M85.9	88	83	-4	-15	43	8	45
M85.13	-7	-8	-9	-18	177	282	163
M65.1	-5	-7	122	151	-8	-10	121
M65.3	20	20	65	71	-10	-11	59
M65.5	47	45	37	27	-9	-12	33
M65.7	58	57	15	1	6	-3	27
C65.7	30	33	-27	-21	-28	-29	-59

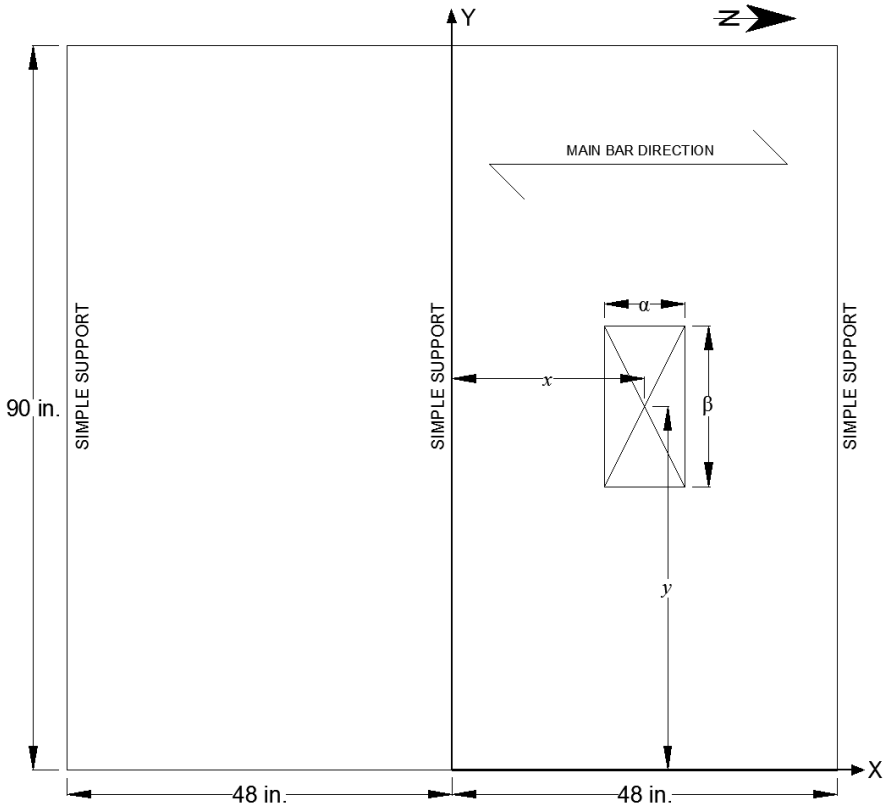

LEGEND		
Test #	Patch Location (x, y) (in.)	Patch Orientation (α, β) (in.)
43	(24, 45)	(10, 20)
44	(24, 45)	(20, 10)
45	(24, 9)	(10, 20)
46	(24, 4)	(20, 10)
47	(24, 81)	(10, 20)
48	(24, 86)	(20, 10)
49	(24, 9)	(10, 20)
	(24, 81)	(10, 20)
50	(24, 4)	(20, 10)
	(24, 52)	(20, 10)
51	(24, 52)	(20, 10)
61	(24 ,45)	(10, 20)
	(-24, 45)	(10, 20)
62	(24, 9)	(10, 20)
	(-24, 9)	(10, 20)

Figure C.6: Patch load plan for tests 43-51, 61, 62

Table C.6: Strain and displacement data for tests 43-51, 61, 62

Displacement Sensor/ Strain Gage	Test #										
	43	44	45	46	47	48	49	50	51	61	62
D1	-0.003	-0.002	-0.051	-0.071	-0.003	-0.002	-0.051	-0.075	-0.003	0.002	-0.040
D3	-0.004	0.000	-0.034	-0.027	0.001	0.003	-0.041	-0.023	-0.002	-0.001	-0.027
D5	-0.019	-0.016	-0.011	0.000	0.001	0.001	-0.014	-0.005	-0.018	-0.013	-0.008
D7	-0.037	-0.039	-0.001	-0.001	-0.002	0.001	-0.005	-0.029	-0.036	-0.029	0.001
D9	-0.022	-0.021	0.000	0.000	-0.007	0.004	-0.007	-0.038	-0.022	-0.023	0.002
D11	-0.005	-0.002	-0.001	0.000	-0.033	-0.025	-0.031	-0.010	-0.004	-0.005	0.005
D13	0.002	0.003	-0.004	-0.004	-0.040	-0.059	-0.045	0.005	0.002	0.003	0.004
M85.1	5	4	-82	-73	0	1	-58	-72	5	6	107
M85.3	-20	-18	-45	-82	0	3	-36	-83	-20	-10	142
M85.5	-16	-22	-55	-40	-4	4	-69	-56	-16	75	-7
M85.7	-4	-1	-17	-6	-18	-5	-43	-62	-4	144	-9
M85.9	-61	-66	0	6	-52	-36	-52	-50	-61	34	-5
M85.13	6	6	13	14	-129	-147	-84	24	6	16	-2
M45.1	17	15	-411	-582	2	4	-378	-574	17	10	-261
M45.3	-19	-15	-359	-211	4	6	-391	-224	-19	-3	-282
M45.5	-152	-125	-85	-30	1	6	-90	-91	-152	-98	-49
M45.7	-397	-357	-10	3	-11	1	-24	-233	-396	-315	-4
C45.7	-439	-459	41	33	66	70	93	-359	-437	-425	38

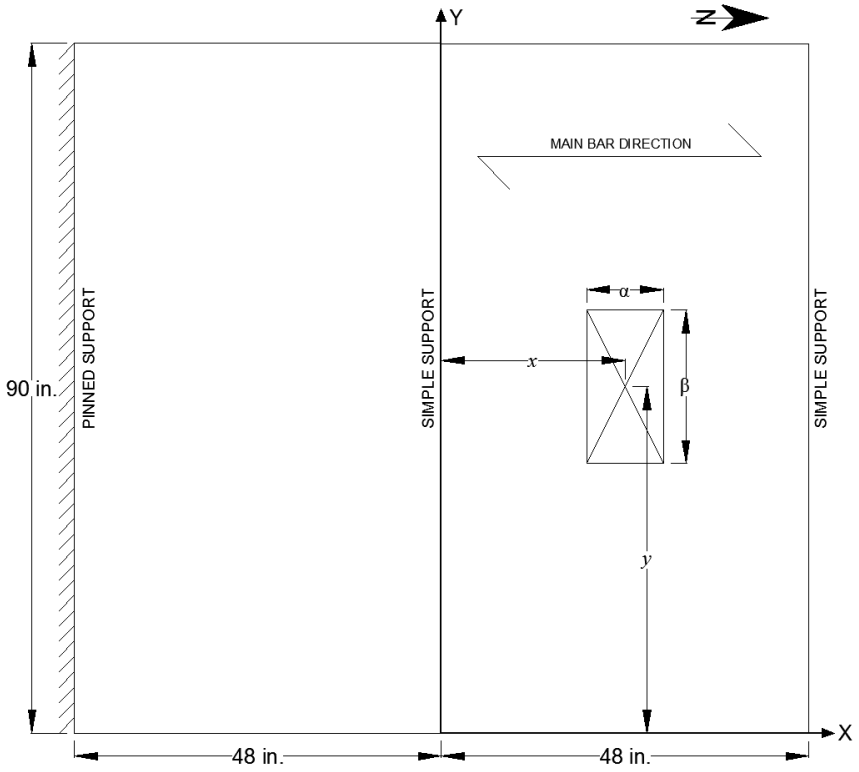

LEGEND		
Test #	Patch Location (x, y) (in.)	Patch Orientation (α, β) (in.)
52	(24, 45)	(10, 20)
53	(24, 45)	(20, 10)
54	(24, 9)	(10, 20)
55	(24, 4)	(20, 10)
56	(24, 81)	(10, 20)
57	(24, 86)	(20, 10)
58	(24, 9)	(10, 20)
	(24, 81)	(10, 20)
59	(24, 4)	(20, 10)
	(24, 52)	(20, 10)
60	(24, 52)	(20, 10)

Figure C.7: Patch load plan for tests 52-60

Table C.7: Strain and displacement data for tests 52-60

Displacement Sensor/ Strain Gage	Test #								
	52	53	54	55	56	57	58	59	60
D1	-0.002	-0.001	-0.044	-0.061	-0.004	-0.003	-0.051	-0.062	-0.003
D3	-0.001	-0.002	-0.028	-0.017	0.000	0.001	-0.024	-0.013	0.001
D5	-0.017	-0.016	-0.007	0.001	0.000	0.000	-0.005	0.002	-0.006
D7	-0.037	-0.036	-0.003	0.001	-0.003	-0.001	-0.004	-0.028	-0.030
D9	-0.017	-0.018	0.002	0.001	-0.009	0.001	-0.007	-0.033	-0.033
D11	-0.002	-0.002	0.001	0.000	-0.031	-0.024	-0.030	-0.005	-0.008
D13	0.003	-0.001	0.001	0.004	-0.035	-0.050	-0.031	0.010	0.006
M85.1	3	4	-24	0	-4	-6	-12	-44	1
M85.3	-15	-11	40	12	-2	-1	23	26	-11
M85.5	-4	-13	-29	-11	-1	2	-44	-20	-16
M85.7	2	9	-14	2	-9	1	-27	-45	-15
M85.9	-32	-35	-7	-1	-15	-13	-26	-29	-17
M85.13	8	9	-3	-10	14	24	1	7	9
M45.1	16	14	-361	-498	-1	-2	-399	-512	9
M45.3	-17	-12	-331	-183	0	2	-305	-198	-4
M45.5	-154	-121	-62	-10	2	5	-58	-63	-51
M45.7	-385	-343	-4	8	-4	6	-12	-223	-251
C45.7	-406	-434	39	33	54	54	92	-374	-421

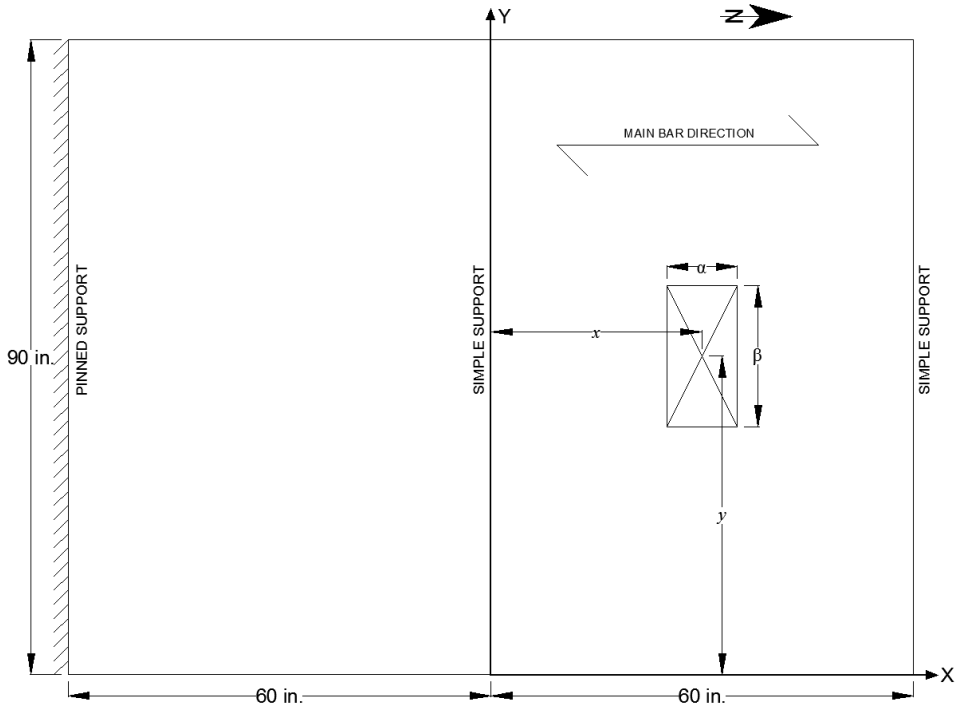

LEGEND		
Test #	Patch Location (x, y) (in.)	Patch Orientation (α, β) (in.)
63	(30, 45)	(10, 20)
64	(30, 45)	(20, 10)
65	(30, 9)	(10, 20)
66	(30, 4)	(20, 10)
67	(30, 81)	(10, 20)
68	(30, 86)	(20, 10)
69	(30, 9)	(10, 20)
	(30, 81)	(10, 20)
70	(30, 4)	(20, 10)
	(30, 52)	(20, 10)
71	(30, 9)	(20, 10)
	(30, 57)	(20, 10)

Figure C.8: Patch load plan for tests 63-71

Table C.8: Strain and displacement data for tests 63-71

Displacement Sensor/ Strain Gage	Test #								
	63	64	65	66	67	68	69	70	71
D1	-0.003	-0.003	-0.084	-0.108	-0.003	-0.005	-0.070	-0.079	-0.117
D3	-0.010	-0.010	-0.047	-0.038	0.000	-0.005	-0.051	-0.045	-0.038
D5	-0.033	-0.032	-0.018	-0.007	0.002	-0.018	-0.022	-0.036	-0.023
D7	-0.053	-0.054	-0.002	-0.001	-0.003	-0.046	-0.007	-0.048	-0.051
D9	-0.032	-0.032	0.000	0.001	-0.020	-0.047	-0.013	-0.053	-0.044
D11	-0.009	-0.007	0.001	0.000	-0.053	-0.014	-0.044	-0.021	-0.010
D13	0.001	-0.002	0.001	-0.002	-0.073	0.001	-0.082	-0.002	-0.007
M85.1	-9	-4	54	105	-9	-4	-9	22	60
M85.3	-35	-29	34	4	-6	-26	40	20	-11
M85.5	-7	-10	-26	-31	-8	-33	-47	-30	-56
M85.7	34	44	-21	-13	-15	12	-49	-38	-21
M85.9	-1	-7	-11	-5	-14	24	-30	7	-10
M85.13	3	4	-7	-7	57	10	71	4	12
M525.1	3	7	-163	-219	-5	2	-153	-147	-224
M525.3	-40	-34	-121	-120	-2	-22	-136	-132	151
M525.5	NA	NA	NA	NA	NA	NA	NA	NA	NA
M525.7	-124	-130	-18	-5	-16	-136	-43	-142	-157
M55.1	15	18	-502	-635	-3	11	-380	-521	-616
M55.3	-40	-33	-383	-242	2	-15	-460	-421	-260
M55.5	-193	-171	-92	-31	2	-90	-137	-233	-141
M55.7	-429	-393	-13	6	-11	-311	-33	-313	-319
M55.9	-190	-161	0	4	-87	-294	-70	-369	-267
M55.11	-36	-26	1	3	-398	-72	-349	-119	-63
M55.13	23	22	-1	-1	-473	32	-576	22	34
M575.1	15	16	-270	-370	0	11	-216	-195	-393
M575.3	-31	-27	-165	-164	2	-11	-168	-176	-183
M575.5	-119	-129	-73	-26	3	-78	-109	-175	-123
M575.7	-149	-160	-9	5	-7	-164	-22	-150	-141
C55.1	12	11	-252	-266	-1	7	-160	126	-111
C55.2	36	36	-244	68	3	24	-345	178	136
C55.3	68	66	-97	213	8	52	-349	-744	324
C55.5	-104	-45	124	123	35	63	158	207	210
C55.7	-439	-444	58	49	89	-502	165	-638	-426

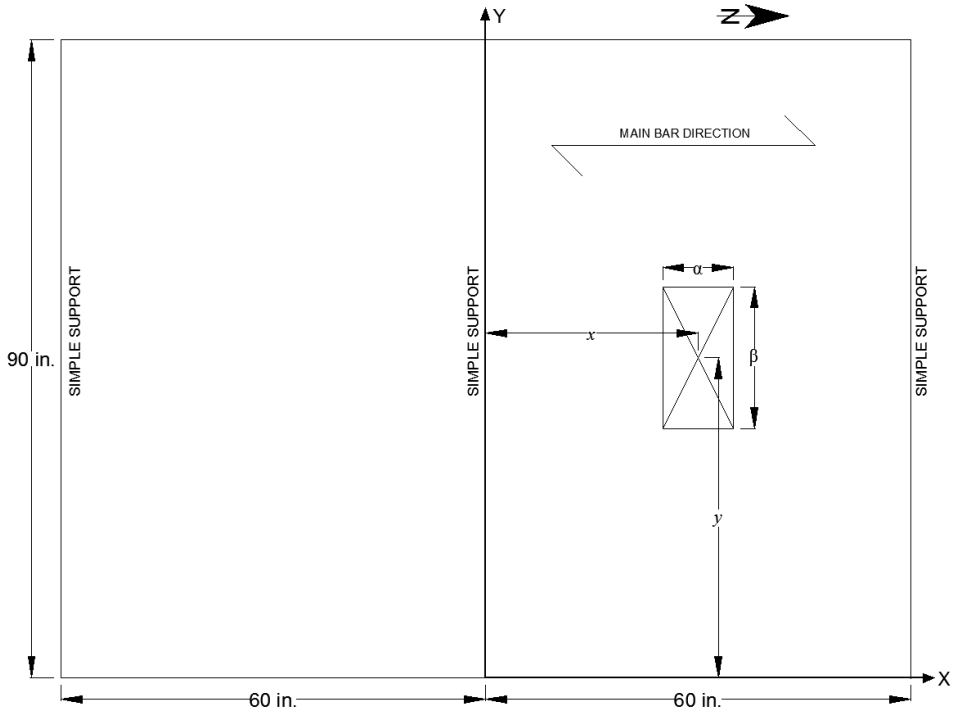

LEGEND		
Test #	Patch Location	Patch Orientation
	(x, y) (in.)	(α, β) (in.)
72	(30, 45)	(10, 20)
	(-18, 45)	(10, 20)
73	(30, 9)	(10, 20)
	(-18, 9)	(10, 20)
74	(24, 9)	(10, 20)
	(-24, 57)	(10, 20)

Figure C.9: Patch load plan for tests 72-74

Table C.9: Strain and displacement data for tests 72-74

Displacement Sensor/ Strain Gage	Test #		
	72	73	74
D1	-0.003	-0.053	-0.045
D3	-0.005	-0.031	-0.028
D5	-0.022	-0.014	-0.014
D7	-0.034	0.000	-0.003
D9	-0.021	0.000	-0.001
D11	0.001	0.002	0.000
D13	0.006	-0.002	0.010
M85.1	13	258	243
M85.3	7	212	192
M85.5	87	4	4
M85.7	153	-21	-21
M85.9	106	-8	-9
M85.13	20	-1	-1
M525.1	15	17	-31
M525.3	7	-4	-71
M525.5	NA	NA	NA
M525.7	15	-18	-17
M55.1	23	-321	-261
M55.3	-10	-322	-247
M55.5	-122	-64	-63
M55.7	-315	-10	-10
M55.9	-146	-4	-3
M55.11	-10	-1	0
M55.13	28	3	1
M575.1	19	-186	-135
M575.3	-16	-125	-84
M575.5	-91	-53	-46
M575.7	-106	-6	-7
C55.1	9	-198	-58
C55.2	34	-279	-116
C55.3	60	-177	-61
C55.5	-84	83	70
C55.7	-470	34	31

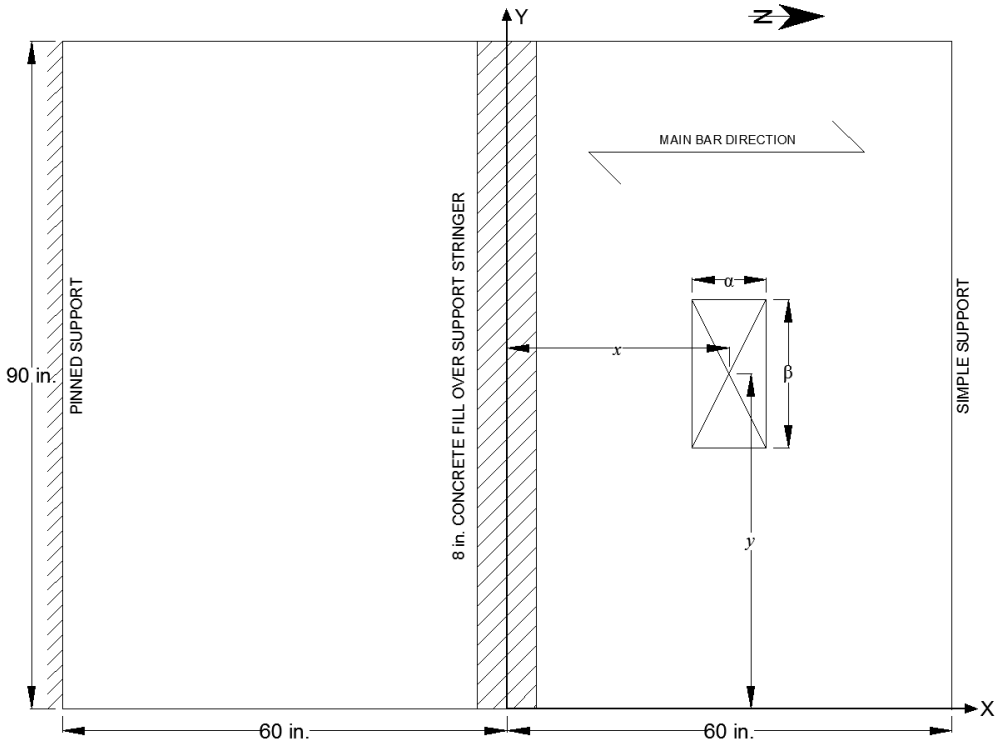

LEGEND		
Test #	Patch Location (x, y) (in.)	Patch Orientation (α, β) (in.)
75	(30, 45)	(10, 20)
76	(30, 45)	(20, 10)
77	(30, 9)	(10, 20)
78	(30, 4)	(20, 10)

Figure C.10: Patch load plan for tests 75-78

Table C.10: Strain and displacement data for tests 75-78

Displacement Sensor/ Strain Gage	Test #			
	75	76	77	78
D1	-0.003	-0.003	-0.060	-0.091
D3	-0.010	-0.007	-0.038	-0.030
D5	-0.028	-0.027	-0.013	-0.006
D7	-0.046	-0.048	-0.003	-0.001
D9	-0.025	-0.024	-0.001	-0.002
D11	-0.006	-0.004	0.002	0.002
D13	0.002	0.005	-0.002	0.004
M85.1	-38	-32	143	267
M85.3	-33	-35	136	57
M85.5	NA	NA	NA	NA
M85.7	NA	NA	NA	NA
M85.9	40	28	-17	-11
M85.13	-22	-20	-8	-5
M525.1	-16	-14	-100	-166
M525.3	-39	-37	-57	-77
M525.5	NA	NA	NA	NA
M525.7	-52	-58	-20	-12
M55.1	4	2	-450	-590
M55.3	-39	-33	-357	-198
M55.5	-177	-149	-80	-23
M55.7	-391	-362	-11	0
M55.9	-150	-133	-2	-1
M55.11	-33	-29	-2	-1
M55.13	9	7	-1	1
M575.1	10	9	-244	-317
M575.3	-34	-27	-146	-137
M575.5	-117	-114	-62	-19
M575.7	-146	-152	-7	5
C55.1	12	11	-222	-230
C55.2	38	35	-254	112
C55.3	72	71	-92	211
C55.5	-107	-21	115	100
C55.7	-375	-358	46	28

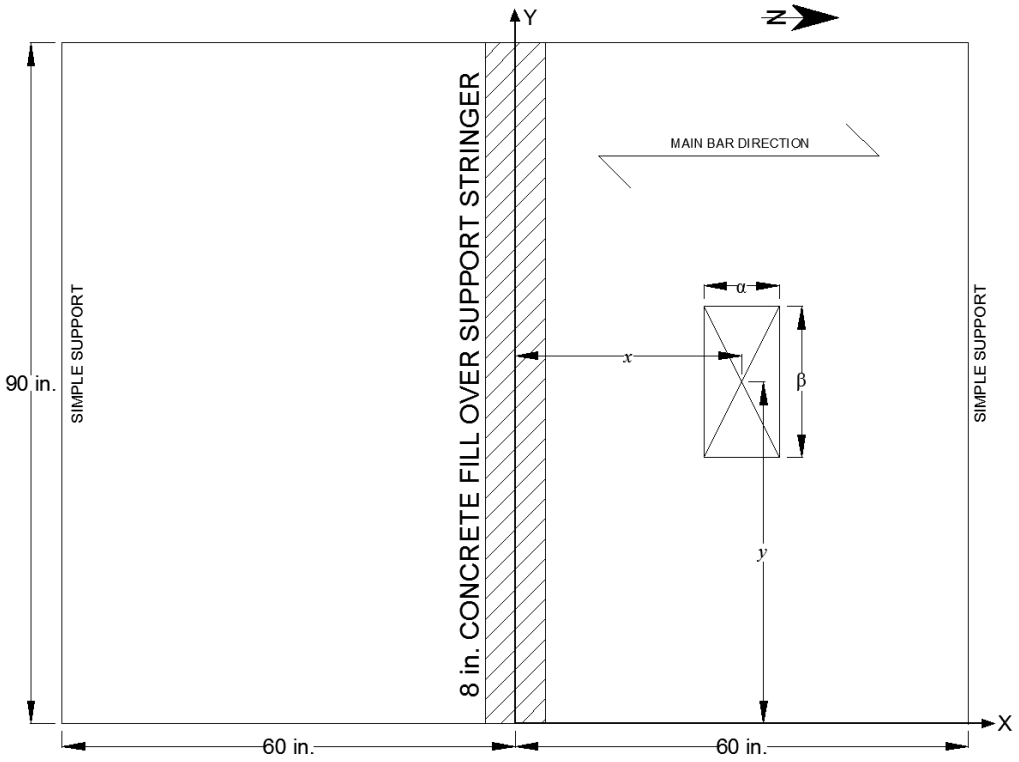

LEGEND		
Test #	Patch Location (x, y) (in.)	Patch Orientation (α, β) (in.)
79	(30, 4)	(20, 10)
	(-30, 4)	(20, 10)
80	(30, 7.5)	(20, 10)
	(-30, 7.5)	(20, 10)
81	(30, 15)	(20, 10)
	(-30, 15)	(20, 10)
82	(30, 22.5)	(20, 10)
	(-30, 22.5)	(20, 10)
83	(30, 30)	(20, 10)
	(-30, 30)	(20, 10)
84	(30, 37.5)	(20, 10)
	(-30, 37.5)	(20, 10)
85	(30, 45)	(20, 10)
	(-30, 45)	(20, 10)

Figure C.11: Patch load plan for tests 79-85

Table C.11: Strain and displacement data for tests 79-85

Displacement Sensor/ Strain Gage	Test #						
	79	80	81	82	83	84	85
D1	-0.081	-0.060	-0.025	-0.014	-0.004	-0.004	-0.007
D3	-0.023	-0.030	-0.036	-0.035	-0.020	-0.008	-0.005
D5	-0.002	-0.007	-0.018	-0.034	-0.043	-0.032	-0.022
D7	-0.001	-0.001	-0.003	-0.009	-0.020	-0.031	-0.044
D9	0.000	0.000	0.000	-0.002	-0.004	-0.010	-0.021
D11	0.000	0.000	-0.002	-0.001	-0.002	-0.003	-0.004
D13	-0.001	0.007	0.000	0.001	0.002	0.003	0.004
M85.1	446	318	109	3	-30	-28	-19
M85.3	191	247	320	247	124	34	0
M85.5	NA	NA	NA	NA	NA	NA	NA
M85.7	NA	NA	NA	NA	NA	NA	NA
M85.9	-14	-17	-16	-14	-3	44	132
M85.13	-1	-2	-2	-3	-4	-7	-13
M525.1	15	9	9	1	-1	-4	-4
M525.3	13	19	27	2	-7	3	2
M525.5	NA	NA	NA	NA	NA	NA	NA
M525.7	-6	-7	0	-3	-5	14	32
M55.1	-464	-314	-88	-4	23	18	8
M55.3	-158	-224	-314	-241	-112	-30	-2
M55.5	-5	-28	-102	-228	-327	-210	-88
M55.7	3	2	-3	-37	-105	-228	-314
M55.9	-2	0	3	2	-7	-29	-100
M55.11	-1	-3	-4	-2	0	1	-8
M55.13	3	1	-1	0	-1	3	9
M575.1	-294	-232	-95	-18	19	22	14
M575.3	-126	-135	-134	-139	-100	-40	-7
M575.5	-10	-34	-89	-138	-142	-130	-83
M575.7	9	2	-11	-49	-105	-143	-136
C55.1	-289	-304	-48	17	28	17	9
C55.2	42	-306	-402	-38	57	54	33
C55.3	188	82	-411	-457	-12	83	70
C55.5	88	99	106	17	-385	-403	17
C55.7	20	30	53	88	106	17	-434

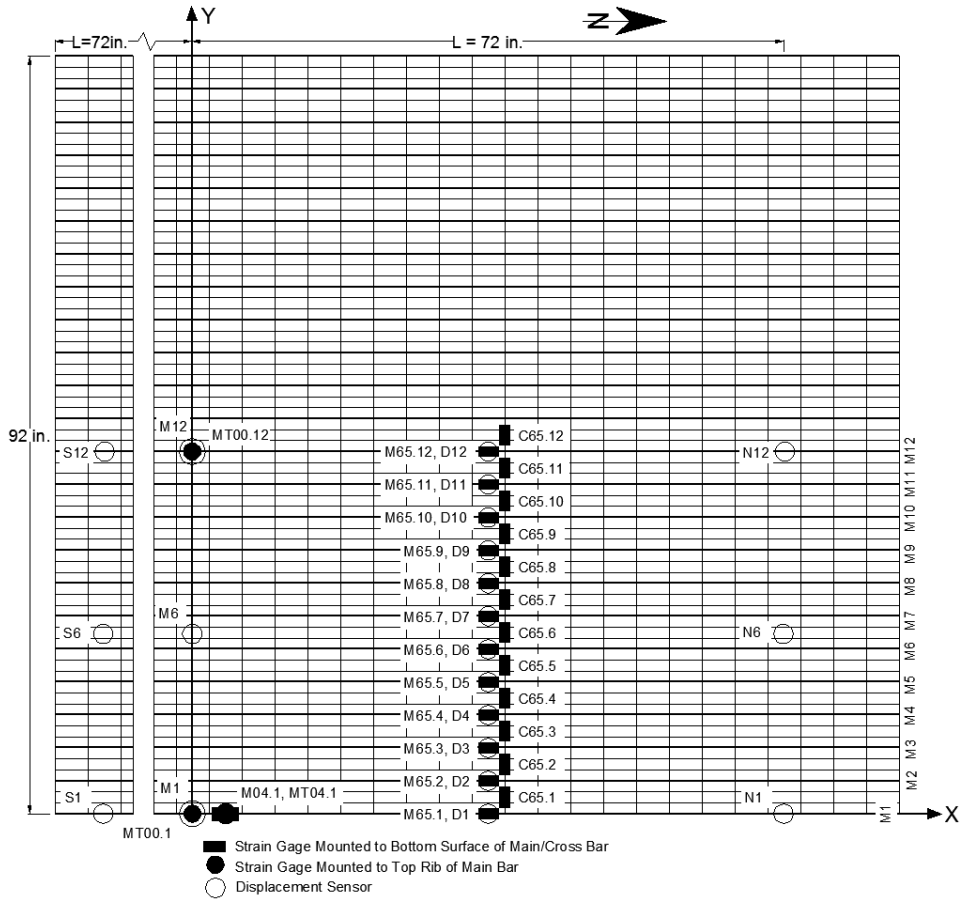

LEGEND					
Strain Gage	Location (x,y) (in.)	Strain Gage	Location (x,y) (in.)	Displacement Sensor	Location (x,y) (in.)
M65.1	(36, 0)	C65.6	(38, 22)	D1	(36, 0)
M65.2	(36, 4)	C65.7	(38, 26)	D2	(36, 4)
M65.3	(36, 8)	C65.8	(38, 30)	D3	(36, 8)
M65.4	(36, 12)	C65.9	(38, 34)	D4	(36, 12)
M65.5	(36, 16)	C65.10	(38, 38)	D5	(36, 16)
M65.6	(36, 20)	C65.11	(38, 42)	D6	(36, 20)
M65.7	(36, 24)	C65.12	(38, 46)	D7	(36, 24)
M65.8	(36, 28)			D8	(36, 28)
M65.9	(36, 32)			D9	(36, 32)
M65.10	(36, 36)			D10	(36, 36)
M65.11	(36, 40)			D11	(36, 40)
M65.12	(36, 44)			D12	(36, 44)
M04.1	(4, 0)			N1	(72, 0)
MT04.1	(4, 0)			N6	(72, 22)
MT00.1	(0, 0)			N12	(72, 44)
MT00.12	(0, 44)			M1	(0, 0)
C65.1	(38, 2)			M6	(0, 22)
C65.2	(38, 6)			M12	(0, 44)
C65.3	(38, 10)			S1	(-72, 0)
C65.4	(38, 14)			S6	(-72, 22)
C65.5	(38, 18)			S12	(-72, 44)

Figure C.12: Strain and displ. sensor plan for specimen 4.0RECT2.5TYP4

For tests 86-117, the north support is located at x = 72 in., the middle support is located at x = 0 in., and the south support is located at x = -72 in.

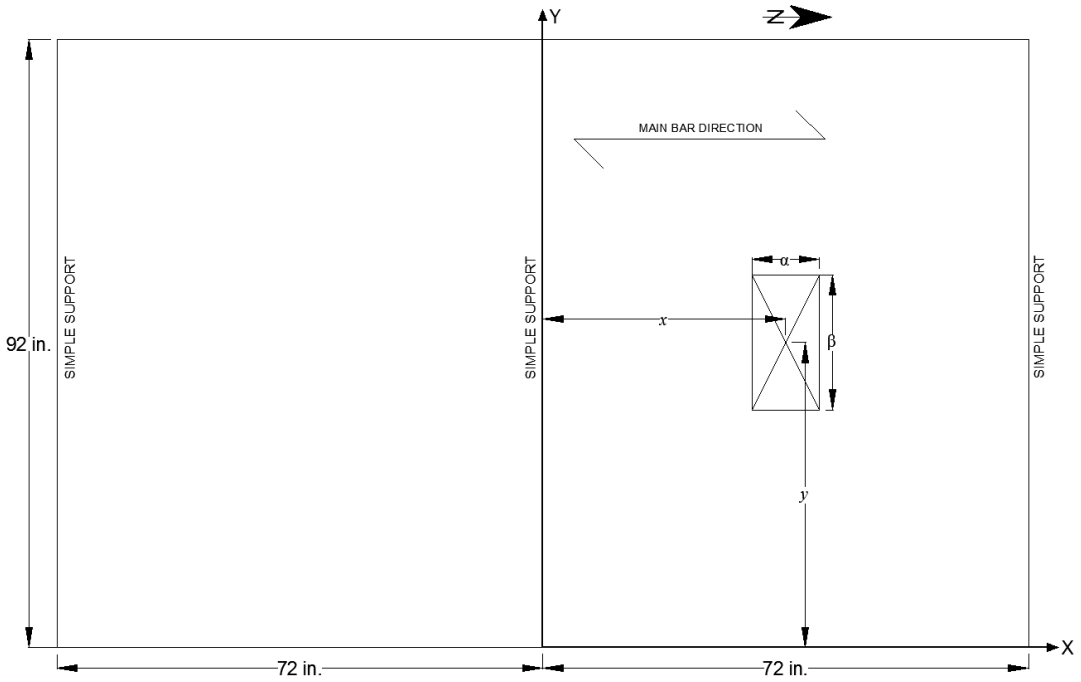

LEGEND		
Test #	Patch Location (x, y) (in.)	Patch Orientation (α, β) (in.)
86	(36, 9)	(10, 20)
87	(36, 23)	(10, 20)
88	(36, 46)	(10, 20)

Figure C.13: Patch load plan for tests 86-88

Table C.12: Strain and displacement data for tests 86-88

Displacement Sensor/ Strain Gage	Test #		
	86	87	88
D1	-0.088	-0.021	0.006
D2	-0.077	-0.023	0.001
D3	-0.071	-0.032	-0.003
D4	-0.061	-0.042	-0.005
D5	-0.054	-0.048	-0.004
D6	-0.041	-0.051	-0.008
D7	-0.030	-0.057	-0.016
D8	-0.020	-0.045	-0.026
D9	-0.015	-0.041	-0.033
D10	-0.004	-0.032	-0.042
D11	-0.002	-0.026	-0.048
D12	-0.002	-0.015	-0.048
M65.1	-397	-59	16
M65.2	-400	-111	8
M65.3	-366	-160	0
M65.4	-332	-223	-10
M65.5	-280	-272	-23
M65.6	-204	-295	-41
M65.7	-132	-287	-68
M65.8	-79	-267	-106
M65.9	-48	-211	-159
M65.10	-24	-144	-218
M65.11	-12	-97	-272
M65.12	0	-64	-289
C65.1	-23	3	1
C65.2	-25	-2	6
C65.3	-43	-32	11
C65.4	-60	-101	16
C65.5	-93	-286	52
C65.6	53	-293	54
C65.7	86	-269	46
C65.8	85	-195	13
C65.9	76	-11	-123
C65.10	60	61	-241
C65.11	47	86	-322
C65.12	29	82	-327
M04.1	-2	-74	9
MT04.1	0	65	-6
MT00.1	-62	62	-3
MT00.12	11	11	-35

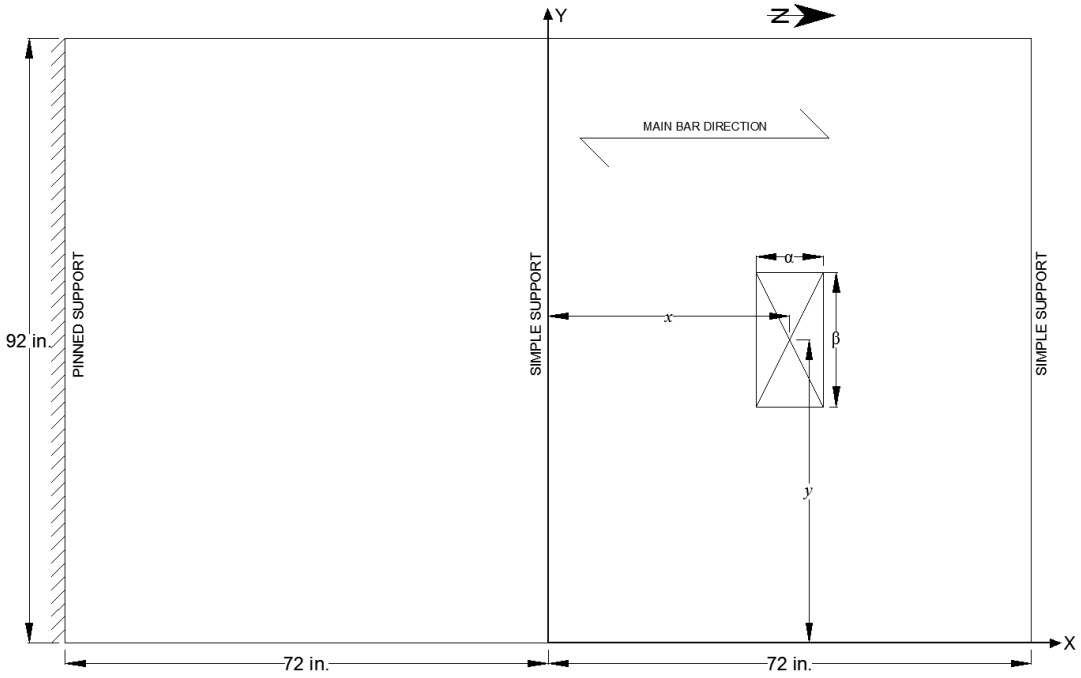

LEGEND					
Test #	Patch Location (x, y) (in.)	Patch Orientation (α, β) (in.)	Test #	Patch Location (x, y) (in.)	Patch Orientation (α, β) (in.)
89	(36, 9)	(10, 20)	102	(36, 24)	(20, 10)
90	(36, 23)	(10, 20)	103	(36, 26)	(20, 10)
91	(36, 46)	(10, 20)	104	(36, 28)	(20, 10)
92	(36, 4)	(20, 10)	105	(36, 30)	(20, 10)
93	(36, 6)	(20, 10)	106	(36, 32)	(20, 10)
94	(36, 8)	(20, 10)	107	(36, 34)	(20, 10)
95	(36, 10)	(20, 10)	108	(36, 36)	(20, 10)
96	(36, 12)	(20, 10)	109	(36, 38)	(20, 10)
97	(36, 14)	(20, 10)	110	(36, 40)	(20, 10)
98	(36, 16)	(20, 10)	111	(36, 42)	(20, 10)
99	(36, 18)	(20, 10)	112	(36, 44)	(20, 10)
100	(36, 20)	(20, 10)	113	(36, 46)	(20, 10)
101	(36, 22)	(20, 10)			

Figure C.14: Patch load plan for tests 89-113

Table C.13: Strain and displacement data for tests 89-101

Displacement Sensor/	Test #												
Strain Gage	89	90	91	92	93	94	95	96	97	98	99	100	101
D1	-0.071	-0.015	0.004	-0.100	-0.086	-0.074	-0.061	-0.050	-0.038	-0.029	-0.024	-0.014	-0.008
D2	-0.062	-0.016	-0.002	-0.082	-0.072	-0.065	-0.059	-0.048	-0.039	-0.032	-0.026	-0.020	-0.013
D3	-0.056	-0.025	-0.003	-0.068	-0.063	-0.060	-0.057	-0.053	-0.048	-0.042	-0.034	-0.030	-0.023
D4	-0.054	-0.037	-0.001	-0.049	-0.052	-0.051	-0.053	-0.054	-0.051	-0.047	-0.044	-0.039	-0.034
D5	-0.046	-0.043	-0.004	-0.038	-0.041	-0.046	-0.049	-0.051	-0.052	-0.050	-0.049	-0.047	-0.044
D6	-0.037	-0.047	-0.010	-0.021	-0.031	-0.032	-0.039	-0.041	-0.046	-0.045	-0.049	-0.050	-0.047
D7	-0.028	-0.048	-0.016	-0.010	-0.022	-0.024	-0.031	-0.033	-0.039	-0.043	-0.049	-0.049	-0.050
D8	-0.018	-0.040	-0.023	-0.005	-0.012	-0.012	-0.021	-0.022	-0.026	-0.029	-0.034	-0.038	-0.041
D9	-0.012	-0.034	-0.028	-0.008	-0.008	-0.006	-0.014	-0.013	-0.019	-0.023	-0.023	-0.027	-0.034
D10	-0.008	-0.030	-0.041	0.002	0.001	-0.003	-0.006	-0.010	-0.012	-0.016	-0.020	-0.022	-0.025
D11	-0.002	-0.021	-0.045	0.003	0.002	-0.001	-0.005	-0.006	-0.009	-0.010	-0.012	-0.015	-0.016
D12	-0.003	-0.015	-0.046	0.001	0.002	-0.002	-0.001	-0.001	0.000	-0.006	-0.006	-0.009	-0.010
M65.1	-325	-35	15	-464	-375	-315	-240	-185	-140	-100	-68	-43	-22
M65.2	-337	-86	10	-448	-391	-351	-293	-240	-196	-155	-124	-94	-70
M65.3	-317	-133	3	-362	-350	-341	-318	-289	-249	-210	-173	-140	-112
M65.4	-298	-200	-6	-253	-278	-289	-306	-308	-293	-269	-240	-203	-170
M65.5	-258	-246	-20	-154	-185	-200	-242	-263	-280	-285	-277	-258	-225
M65.6	-192	-269	-40	-93	-120	-136	-175	-197	-231	-251	-276	-281	-269
M65.7	-121	-267	-66	-53	-71	-84	-115	-135	-167	-186	-219	-248	-260
M65.8	-76	-245	-106	-25	-40	-49	-77	-92	-117	-132	-163	-189	-215
M65.9	-45	-194	-160	-13	-19	-27	-46	-59	-79	-90	-115	-135	-160
M65.10	-24	-131	-221	-3	-7	-13	-24	-33	-48	-57	-75	-91	-109
M65.11	-11	-87	-269	-2	-1	-4	-11	-16	-26	-34	-48	-60	-73
M65.12	-3	-56	-277	0	2	1	-3	-6	-13	-17	-28	-35	-46
C65.1	-21	2	2	-47	-49	-43	-27	-14	-8	-3	0	1	2
C65.2	-26	-2	7	-76	-98	-122	-107	-76	-45	-26	-14	-6	0
C65.3	-46	-32	11	16	-78	-118	-154	-169	-142	-99	-63	-34	-18
C65.4	-66	-101	19	79	22	-20	-111	-161	-181	-192	-160	-107	-66
C65.5	-103	-283	61	228	152	99	-24	-132	-312	-413	-478	-494	-408
C65.6	63	-288	68	206	167	139	81	25	-71	-160	-324	-427	-465
C65.7	104	-261	55	162	147	133	111	86	41	-2	-80	-172	-296
C65.8	108	-188	15	125	122	118	114	103	87	66	36	-4	-66
C65.9	104	-4	-136	98	102	104	108	108	105	98	88	72	45
C65.10	90	68	-262	78	82	86	94	99	104	102	104	99	87
C65.11	76	97	-329	61	65	70	82	90	95	99	107	111	108
C65.12	55	92	-305	42	45	50	57	65	73	80	88	97	99
M04.1	125	-17	1	188	-248	58	56	37	13	0	-6	-12	-10
MT04.1	-93	11	-3	-159	-131	-104	-71	-47	-25	-11	0	5	4
MT00.1	-165	5	2	-265	-221	-181	-128	-90	-56	-30	-12	-2	-1
MT00.12	8	-3	-61	15	12	11	10	9	7	8	5	2	-2

Table C.14: Strain and displacement data for tests 102-113

Displacement Sensor/	Test #											
Strain Gage	102	103	104	105	106	107	108	109	110	111	112	113
D1	-0.003	-0.001	0.004	0.001	0.000	0.000	-0.002	-0.004	0.003	0.004	0.002	0.002
D2	-0.006	-0.003	0.000	0.005	0.003	0.004	0.002	0.002	0.000	-0.003	-0.002	-0.002
D3	-0.016	-0.015	-0.009	-0.006	-0.004	-0.003	0.000	0.002	0.001	-0.002	-0.005	-0.006
D4	-0.027	-0.024	-0.020	-0.015	-0.012	-0.010	-0.009	-0.005	0.000	-0.001	-0.006	-0.007
D5	-0.039	-0.036	-0.029	-0.024	-0.019	-0.018	-0.015	-0.010	-0.007	-0.004	-0.002	-0.004
D6	-0.046	-0.044	-0.037	-0.033	-0.028	-0.025	-0.020	-0.015	-0.009	-0.006	-0.003	-0.003
D7	-0.050	-0.050	-0.048	-0.043	-0.035	-0.032	-0.032	-0.025	-0.019	-0.015	-0.011	-0.009
D8	-0.043	-0.044	-0.047	-0.043	-0.041	-0.041	-0.038	-0.029	-0.025	-0.026	-0.020	-0.017
D9	-0.040	-0.044	-0.045	-0.046	-0.046	-0.046	-0.049	-0.039	-0.034	-0.031	-0.029	-0.028
D10	-0.031	-0.035	-0.043	-0.045	-0.049	-0.050	-0.054	-0.049	-0.050	-0.044	-0.041	-0.035
D11	-0.024	-0.026	-0.033	-0.033	-0.040	-0.041	-0.049	-0.050	-0.051	-0.049	-0.047	-0.043
D12	-0.016	-0.020	-0.022	-0.023	-0.031	-0.034	-0.042	-0.042	-0.045	-0.050	-0.050	-0.047
M65.1	-4	8	26	25	25	23	22	20	18	17	14	13
M65.2	-44	-30	-8	-1	4	6	7	10	10	11	12	11
M65.3	-85	-64	-41	-33	-20	-14	-6	-2	2	6	6	9
M65.4	-133	-110	-86	-67	-50	-39	-28	-16	-9	-2	2	4
M65.5	-193	-166	-133	-111	-85	-72	-53	-40	-26	-19	-10	-6
M65.6	-255	-229	-190	-165	-132	-115	-92	-72	-54	-40	-28	-20
M65.7	-282	-272	-248	-222	-184	-162	-135	-110	-85	-69	-55	-41
M65.8	-257	-270	-282	-272	-250	-225	-193	-160	-129	-108	-86	-71
M65.9	-194	-224	-260	-276	-285	-273	-260	-223	-188	-159	-130	-110
M65.10	-136	-160	-192	-223	-253	-267	-279	-263	-245	-214	-182	-155
M65.11	-93	-112	-138	-163	-193	-224	-257	-269	-281	-269	-250	-220
M65.12	-62	-74	-92	-110	-134	-160	-189	-218	-249	-272	-278	-264
C65.1	3	4	5	4	3	4	4	3	3	1	2	1
C65.2	6	7	12	11	11	11	10	9	9	6	5	5
C65.3	-1	5	14	16	17	18	19	16	14	14	11	9
C65.4	-28	-11	8	14	20	22	25	24	21	20	18	17
C65.5	-258	-163	-53	-13	28	46	64	67	65	66	62	57
C65.6	-489	-399	-218	-122	-32	7	43	58	66	70	69	67
C65.7	-436	-445	-413	-343	-187	-106	-27	11	41	55	62	67
C65.8	-157	-286	-417	-419	-407	-321	-191	-98	-24	12	39	49
C65.9	7	-61	-160	-301	-434	-436	-454	-343	-205	-106	-34	3
C65.10	74	43	-1	-76	-181	-322	-434	-440	-443	-331	-199	-115
C65.11	106	95	75	41	-10	-86	-193	-353	-480	-507	-485	-382
C65.12	103	102	98	86	68	39	-5	-85	-181	-357	-481	-478
M04.1	-15	-8	-2	-5	-5	-8	-7	-4	-3	3	5	5
MT04.1	6	4	2	2	2	5	4	2	-1	-5	-6	-7
MT00.1	8	8	6	7	8	10	8	7	4	-1	-2	-1
MT00.12	-5	-11	-18	-22	-31	-39	-49	-58	-66	-71	-72	-67

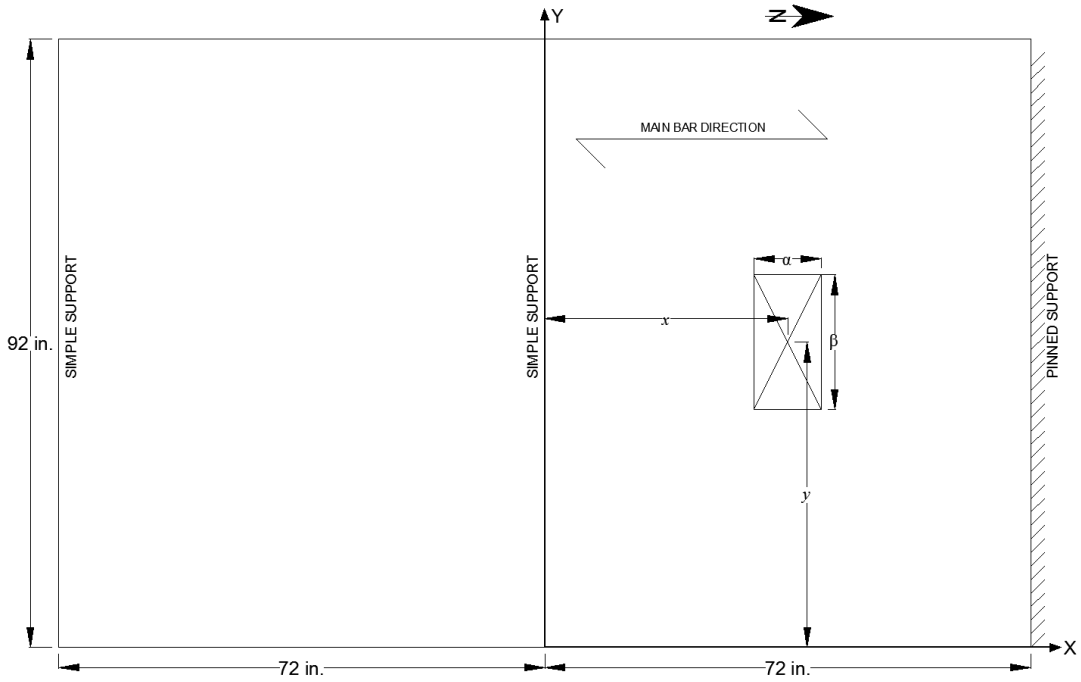

LEGEND		
Test #	Patch Location (x, y) (in.)	Patch Orientation (α, β) (in.)
114	(-36, 9)	(10, 20)
115	(-36, 4))	(20, 10)
116	(-36, 46)	(10, 20)
117	(-36, 46)	(20, 10)

Figure C.15: Patch load plan for tests 114-117

Table C.15: Strain and displacement data for tests 114-117

Displacement Sensor/ Strain Gage	Test #			
	114	115	116	117
D1	NA	NA	NA	NA
D2	NA	NA	NA	NA
D3	NA	NA	NA	NA
D4	NA	NA	NA	NA
D5	NA	NA	NA	NA
D6	NA	NA	NA	NA
D7	NA	NA	NA	NA
D8	NA	NA	NA	NA
D9	NA	NA	NA	NA
D10	NA	NA	NA	NA
D11	NA	NA	NA	NA
D12	NA	NA	NA	NA
M65.1	61	85	-12	-12
M65.2	57	80	-6	-8
M65.3	50	65	0	-1
M65.4	41	52	9	5
M65.5	36	39	10	9
M65.6	31	28	14	14
M65.7	25	18	18	17
M65.8	17	8	22	22
M65.9	11	0	26	25
M65.10	6	-7	29	30
M65.11	0	-8	37	37
M65.12	-3	-11	40	41
C65.1	-1	-5	0	0
C65.2	0	-5	-2	-2
C65.3	0	-9	-4	-3
C65.4	0	-13	-4	-3
C65.5	-4	-35	-6	-6
C65.6	-9	-40	-3	-2
C65.7	-11	-39	1	4
C65.8	-16	-35	7	10
C65.9	-16	-29	12	15
C65.10	-18	-23	18	21
C65.11	-15	-15	23	25
C65.12	-12	-8	23	22
M04.1	231	293	-6	-7
MT04.1	-140	-262	6	8
MT00.1	-143	-280	4	3
MT00.12	6	6	-65	-71

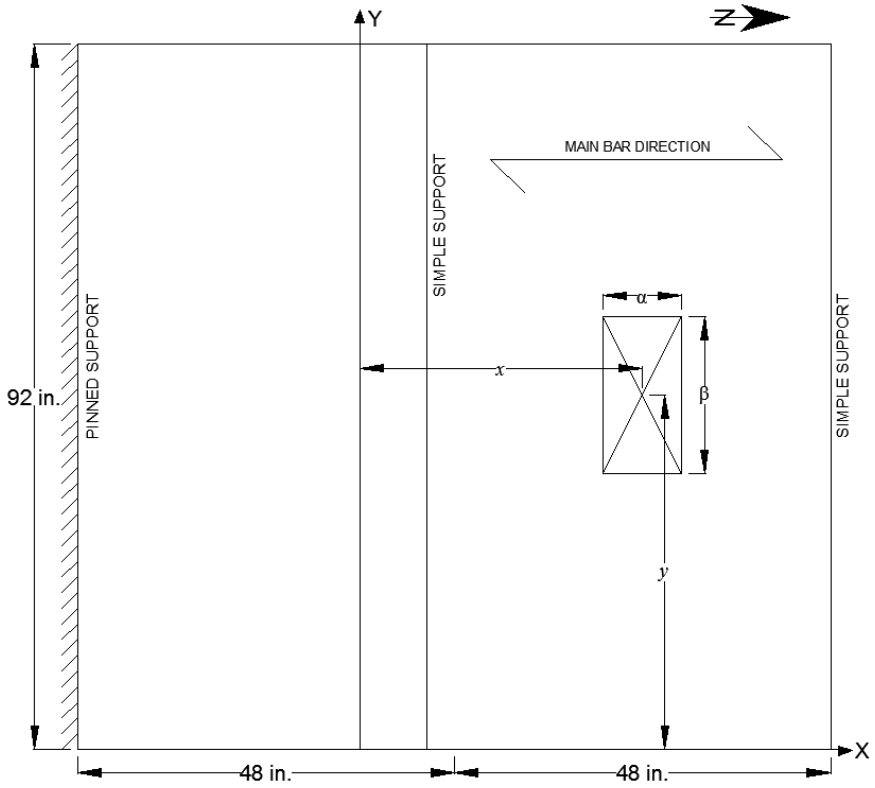

LEGEND		
Test #	Patch Location (x, y) (in.)	Patch Orientation (α, β) (in.)
118	(36, 9)	(10, 20)
119	(36, 4))	(20, 10)
120	(36, 46)	(10, 20)
121	(36, 44)	(20, 10)
122	(36, 46)	(20, 10)

Figure C.16: Patch load plan for tests 118-122

For tests 118-122, a 4’ span length was chosen. The supports were moved in order to keep the 6’ span midspan strain gages at midspan for the 4’ span lengths as well. The north simple support was moved from x = 72 in to x = 60 in. The middle simple support was moved from x = 0 in to x = 12 in. The south pinned support was moved from x = -72 in. to x = -36 in. X-coordinates for north, middle, and south support displacement sensors move accordingly.

Table C.16: Strain and displacement data for tests 118-122

Displacement Sensor/ Strain Gage	Test #				
	118	119	120	121	122
D1	0.000	-0.052	-0.004	0.010	-0.001
D2	-0.020	-0.035	-0.002	0.000	0.000
D3	-0.020	-0.026	0.000	0.000	0.001
D4	-0.018	-0.013	0.000	-0.001	0.000
D5	-0.020	-0.006	0.000	0.000	0.000
D6	-0.008	0.003	-0.002	0.000	0.000
D7	-0.010	0.003	-0.003	-0.001	0.001
D8	-0.003	0.003	-0.007	-0.006	-0.003
D9	0.002	0.002	-0.014	-0.014	-0.007
D10	0.004	0.000	-0.015	-0.012	-0.011
D11	0.005	0.001	-0.019	-0.020	-0.018
D12	0.004	0.000	-0.025	-0.027	-0.025
M65.1	-194	-356	8	6	6
M65.2	-228	-321	5	6	5
M65.3	-234	-236	3	5	3
M65.4	-234	-147	1	5	6
M65.5	-210	-69	-4	1	1
M65.6	-152	-27	-14	-5	-2
M65.7	-88	-6	-32	-17	-10
M65.8	-52	3	-67	-39	-29
M65.9	-30	4	-119	-81	-63
M65.10	-14	5	-185	-129	-107
M65.11	-5	3	-230	-193	-169
M65.12	1	2	-230	-229	-217
C65.1	-20	-33	1	-1	0
C65.2	-24	-30	3	2	2
C65.3	-49	41	6	3	4
C65.4	-77	74	10	9	7
C65.5	-149	168	47	36	31
C65.6	32	125	61	52	47
C65.7	76	77	76	68	62
C65.8	78	50	58	72	75
C65.9	71	29	-91	39	64
C65.10	58	19	-218	-97	-27
C65.11	50	13	-260	-363	-271
C65.12	33	9	-209	-373	-364
M04.1	129	209	2	4	5
MT04.1	-85	-178	0	-3	-3
MT00.1	-72	-152	1	0	-1
MT00.12	7	5	-46	-50	-49

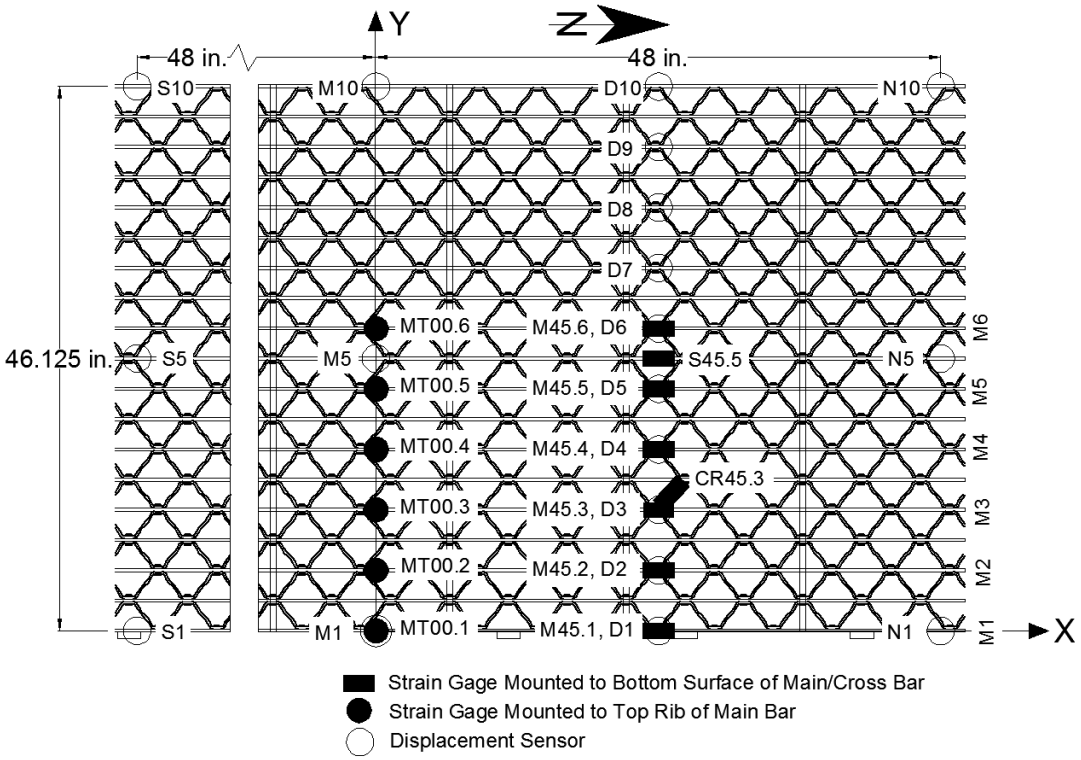

LEGEND			
Strain Gage	Location (x,y) (in.)	Displacement Sensor	Location (x,y) (in.)
MT00.1	(0, 0)	D1	(24, 0)
MT00.2	(0, 5.125)	D2	(24, 5.125)
MT00.3	(0, 10.25)	D3	(24, 10.25)
MT00.4	(0, 15.375)	D4	(24, 15.375)
MT00.5	(0, 20.5)	D5	(24, 20.5)
MT00.6	(0, 25.625)	D6	(24, 25.625)
M45.1	(24, 0)	D7	(24, 30.75)
M45.2	(24, 5.125)	D8	(24, 35.875)
M45.3	(24, 10.25)	D9	(24, 41)
M45.4	(24, 15.375)	D10	(24, 46.125)
M45.5	(24, 20.5)	N1	(48, 0)
M45.6	(24, 25.625)	N5	(48, 23.0625)
S45.5	(24, 23.0625)	N10	(48, 46.125)
CR45.3	(25.17 , 11.66)	M1	(0, 0)
		M5	(0, 23.0625)
		M10	(0, 46.125)
		S1	(-48, 0)
		S5	(-48, 23.0625)
		S10	(-48, 46.125)

Figure C.17: Strain and displ. sensor plan for specimen 37-R-L-5x¼ for tests 123-142

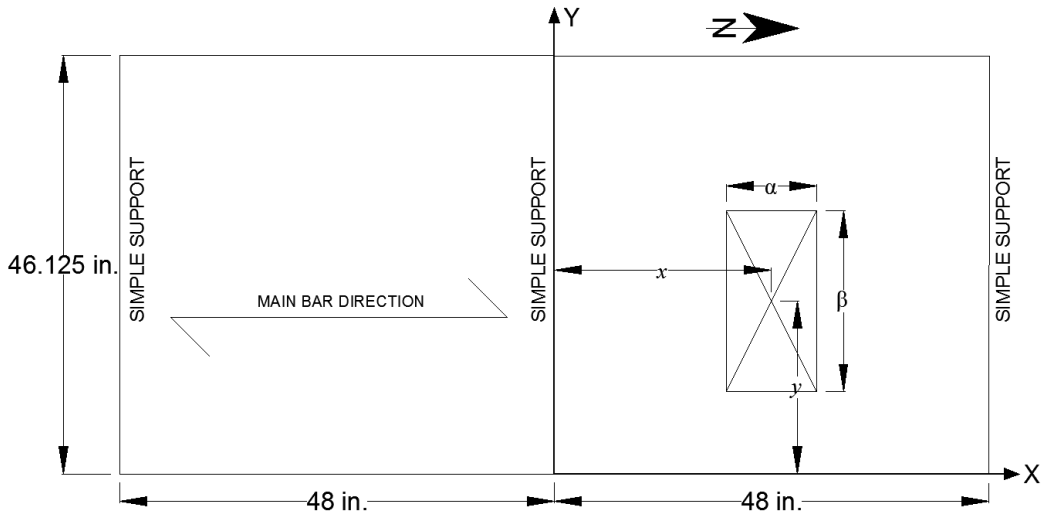

LEGEND		
Test #	Patch Location (x, y) (in.)	Patch Orientation (α, β) (in.)
123	(24, 23.0625)	(10, 20)
124	(24, 23.0625)	(20, 10)
125	(24, 9.625))	(10, 20)
126	(24, 4.625)	(20, 10)

Figure C.18: Patch load plan for tests 123-126

Table C.17: Strain and displacement data for tests 123-126

Displacement Sensor/ Strain Gage	Test #			
	123	124	125	126
D1	-0.007	-0.005	-0.048	-0.067
D2	-0.010	-0.007	-0.050	-0.064
D3	-0.021	-0.015	-0.046	-0.044
D4	-0.034	-0.031	-0.036	-0.022
D5	-0.043	-0.049	-0.022	-0.008
D6	-0.038	-0.043	-0.010	0.001
D7	-0.027	-0.024	-0.003	0.000
D8	-0.013	-0.007	0.001	0.000
D9	-0.007	-0.001	-0.001	0.001
D10	-0.006	0.005	-0.003	0.000
MT00.1	85	76	-10	-114
MT00.2	74	79	-119	-243
MT00.3	29	54	-23	1
MT00.4	-122	-28	-5	85
MT00.5	-198	-336	-15	82
MT00.6	-132	-190	16	54
M45.1	-40	-28	-617	-858
M45.2	-117	-84	-772	-963
M45.3	-263	-194	-650	-587
M45.4	-534	-437	-515	-238
M45.5	-642	-694	-319	-101
M45.6	-607	-605	-133	-46
S45.5	26	-5	40	15
CR45.3	-10	-99	112	-65

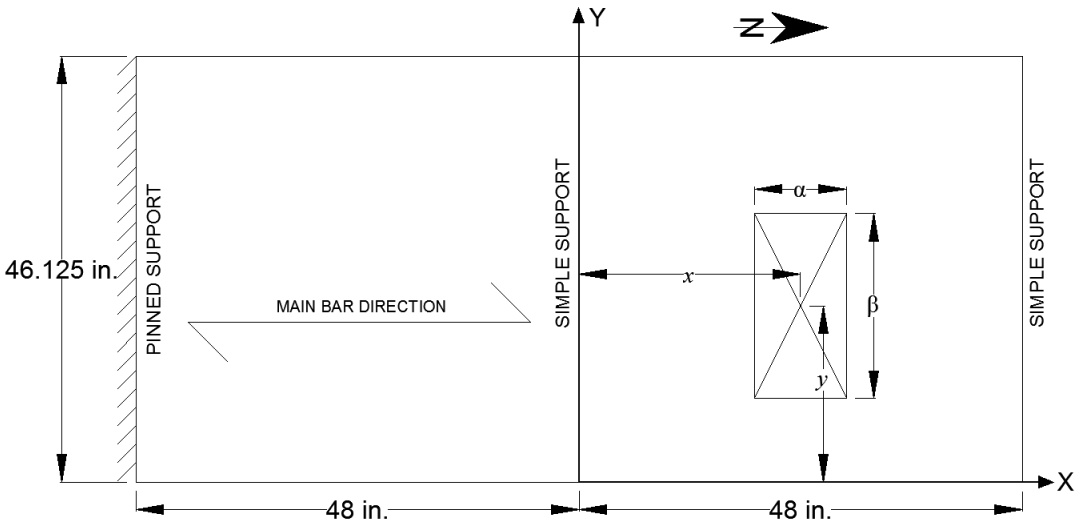

LEGEND		
Test #	Patch Location (x, y) (in.)	Patch Orientation (α, β) (in.)
127	(24, 23.0625)	(10, 20)
128	(24, 9.625))	(10, 20)
129	(24, 36.5)	(10, 20)
130	(24, 4.625)	(20, 10)
131	(24, 7.6875)	(20, 10)
132	(24, 12.8125)	(20, 10)
133	(24, 17.9375)	(20, 10)
134	(24, 23.0625)	(20, 10)
135	(24, 28.1875)	(20, 10)
136	(24, 33.3125)	(20, 10)
137	(24, 38.4375)	(20, 10)
138	(24, 41.5)	(20, 10)

Figure C.19: Patch load plan for tests 127-138

Table C.18: Strain and displacement data for tests 127-138

Displacement Sensor/ Strain Gage	Test #											
	127	128	129	130	131	132	133	134	135	136	137	138
D1	-0.004	-0.044	-0.003	-0.058	-0.035	-0.014	-0.004	-0.002	-0.004	-0.004	-0.004	-0.003
D2	-0.008	-0.044	0.001	-0.053	-0.051	-0.033	-0.013	-0.004	0.000	0.001	0.001	0.001
D3	-0.020	-0.037	0.001	-0.032	-0.044	-0.047	-0.031	-0.013	-0.002	-0.001	0.001	0.002
D4	-0.036	-0.024	-0.002	-0.012	-0.022	-0.039	-0.044	-0.028	-0.009	-0.003	-0.001	0.000
D5	-0.041	-0.013	-0.006	-0.004	-0.007	-0.021	-0.041	-0.046	-0.025	-0.012	-0.002	0.002
D6	-0.031	-0.004	-0.019	0.002	0.001	-0.003	-0.018	-0.038	-0.044	-0.027	-0.010	-0.004
D7	-0.026	-0.001	-0.035	0.001	0.002	0.000	0.000	-0.021	-0.043	-0.050	-0.035	-0.014
D8	-0.007	0.005	-0.043	0.004	0.005	0.007	0.005	-0.003	-0.025	-0.048	-0.049	-0.039
D9	-0.003	0.002	-0.038	0.003	0.001	0.002	0.002	-0.001	-0.011	-0.022	-0.046	-0.051
D10	0.000	0.003	-0.036	0.002	-0.004	0.002	0.000	0.004	0.004	-0.004	-0.025	-0.055
MT00.1	29	-257	15	-404	-149	10	28	26	25	15	13	15
MT00.2	-8	-315	23	-419	-378	-205	-27	18	24	24	18	17
MT00.3	-44	-55	5	18	-104	-115	-45	-5	7	7	5	4
MT00.4	-108	-75	5	-8	-70	-145	-158	-69	-6	5	6	6
MT00.5	-139	-26	-8	4	-7	-55	-152	-169	-77	-14	5	7
MT00.6	-89	-6	-35	5	6	-4	-48	-123	-128	-58	-4	7
M45.1	-3	-593	-3	-788	-400	-104	-10	1	-1	-4	-3	-1
M45.2	-89	-727	-2	-836	-736	-404	-129	-42	-10	-2	-1	0
M45.3	-260	-548	-4	-436	-643	-672	-346	-133	-31	-5	-2	-4
M45.4	-587	-403	-19	-139	-313	-604	-688	-372	-110	-28	-9	-4
M45.5	-631	-194	-75	-33	-90	-269	-591	-638	-307	-107	-30	-16
M45.6	-495	-68	-242	-9	-20	-89	-280	-574	-599	-324	-107	-52
S45.5	2	23	30	-55	13	31	57	-6	54	42	15	6
CR45.3	22	89	-25	-96	178	350	67	-94	-69	-36	-15	-12

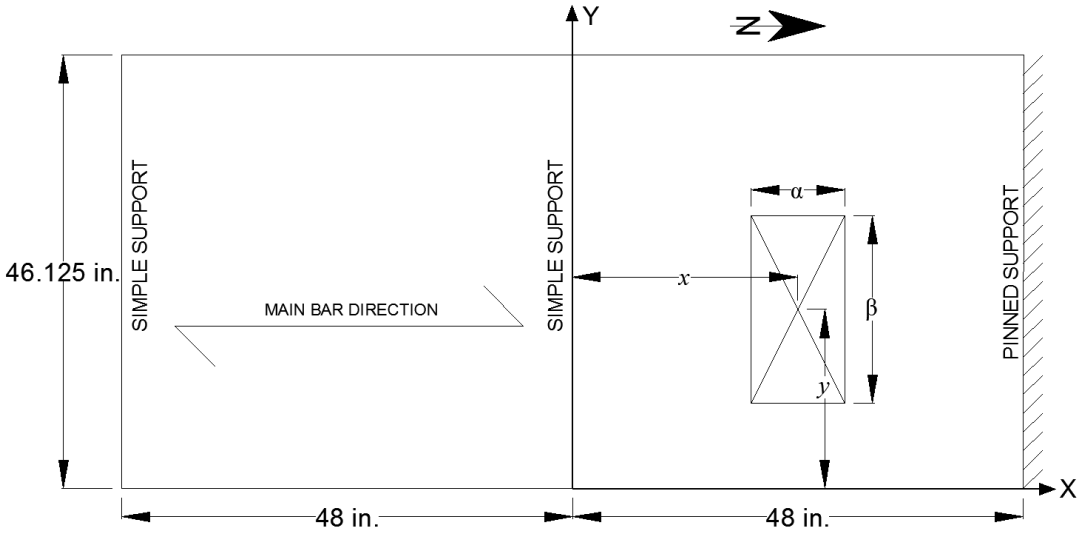

LEGEND		
Test #	Patch Location (x, y) (in.)	Patch Orientation (α, β) (in.)
139	(-24, 23.0625)	(10, 20)
140	(-24, 23.0625)	(20, 10)
141	(-24, 9.625))	(10, 20)
142	(-24, 4.625)	(20, 10)

Figure C.20: Patch load plan for tests 139-142

Table C.19: Strain and displacement data for tests 139-142

Displacement Sensor/ Strain Gage	Test #			
	139	140	141	142
MT00.1	-2	4	-229	-421
MT00.2	-14	6	-277	-385
MT00.3	-23	-14	-79	-63
MT00.4	-102	-92	-111	-31
MT00.5	-61	-74	-24	0
MT00.6	-101	-130	0	2
M45.1	4	-5	122	188
M45.2	31	19	128	162
M45.3	54	41	123	119
M45.4	68	67	81	63
M45.5	105	119	60	28
M45.6	100	109	33	8
S45.5	-24	-27	-11	-3
CR45.3	-2	-5	-6	28

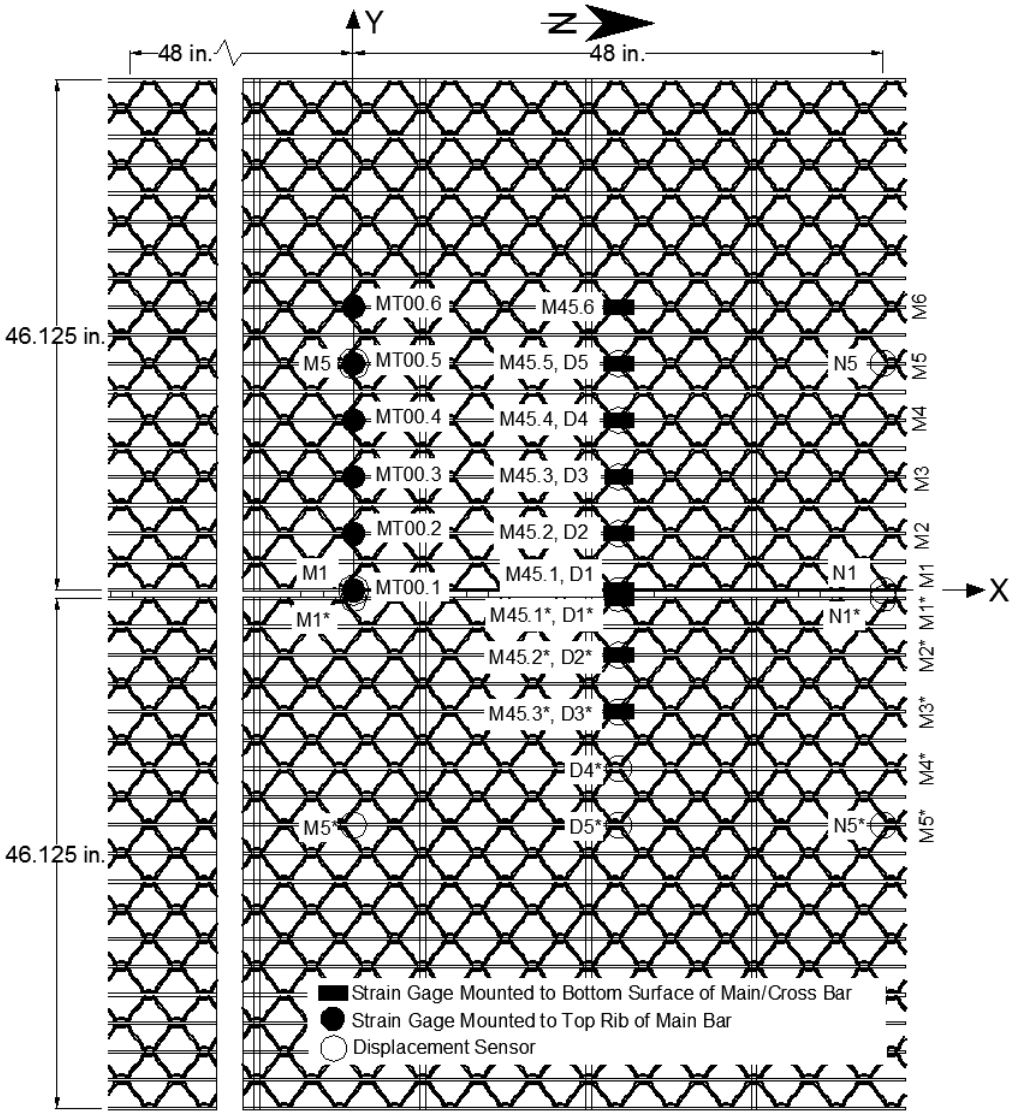

LEGEND							
Strain Gage	Location (x,y) (in.)	Strain Gage	Location (x,y) (in.)	Displ. Sensor	Location (x,y) (in.)	Displ. Sensor	Location (x,y) (in.)
MT00.1	(0, 0)	M45.3	(24, 10.25)	D1	(24, 0)	D5*	(24, -21.25)
MT00.2	(0, 5.125)	M45.4	(24, 15.375)	D2	(24, 5.125)	N1	(48, 0)
MT00.3	(0, 10.25)	M45.5	(24, 20.5)	D3	(24, 10.25)	N5	(48, 20.5)
MT00.4	(0, 15.375)	M45.6	(24, 25.625)	D4	(24, 15.375)	N1*	(48, -0.75))
MT00.5	(0, 20.5)	M45.1*	(24, -0.75)	D5	(24, 20.5)	N5*	(48, -21.25)
MT00.6	(0, 25.625)	M45.2*	(24, -5.875)	D1*	(24, -0.75)	M1	(0, 0)
M45.1	(24, 0)	M45.3*	(24, -11)	D2*	(24, -5.875)	M5	(0, 20.5)
M45.2	(24, 5.125)			D3*	(24, -11)	M1*	(0, -0.75)
				D4*	(24, -16.125)	M5*	(0, -21.25)

Figure C.21: Strain and displ. sensor plan for specimen 37-R-L-5x¼ for tests 143-146

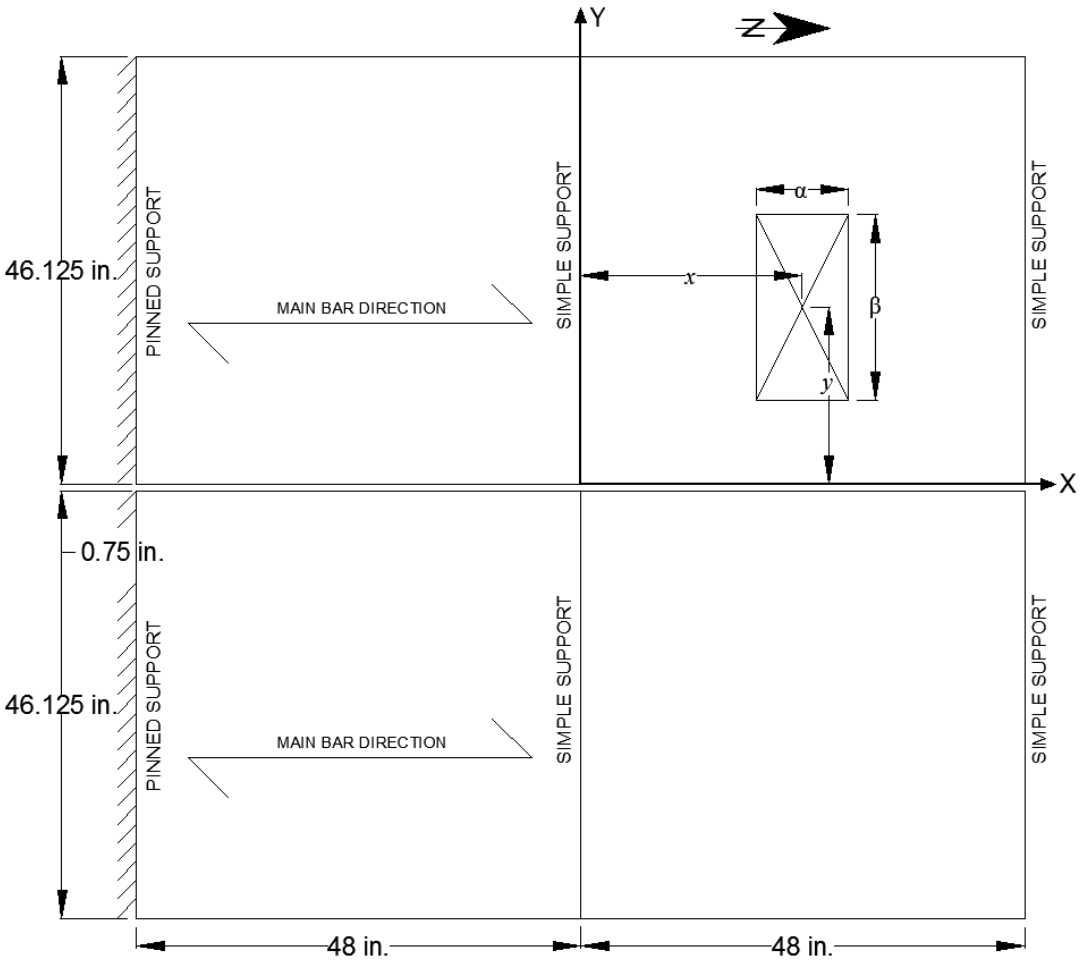

LEGEND		
Test #	Patch Location (x, y) (in.)	Patch Orientation (α, β) (in.)
143	(24, 4.625)	(20, 10)
144	(24, 9.625)	(10, 20)
145	(24, -0.375)	(20, 10)
146	(24, -0.375)	(10, 20)

Figure C.22: Patch load plan for tests 143-146

Table C.20: Strain and displacement data for tests 143-146

Displacement Sensor/ Strain Gage	Test #			
	143	144	145	146
D5*	-0.004	-0.004	-0.004	-0.007
D4*	0.001	0.000	-0.001	-0.008
D3*	0.003	0.001	-0.009	-0.016
D2*	-0.004	-0.002	-0.027	-0.022
D1*	-0.013	-0.007	-0.039	-0.025
D1	-0.033	-0.016	-0.045	-0.028
D2	-0.046	-0.027	-0.027	-0.033
D3	-0.043	-0.038	-0.013	-0.020
D4	-0.016	-0.038	-0.004	-0.010
D5	-0.001	-0.026	-0.003	0.007
MT00.1	-217	-96	-329	-172
MT00.2	-396	-239	-216	-230
MT00.3	-95	-86	-18	-50
MT00.4	-32	-103	6	-15
MT00.5	0	-52	6	4
MT00.6	4	-26	5	4
M45.1	-323	-186	-514	-340
M45.2	-697	-480	-440	-531
M45.3	-545	-576	-180	-368
M45.4	-205	-608	-59	-127
M45.5	-42	-376	-14	-30
M45.6	-3	-135	-3	-4
M45.1*	-313	-161	-558	-350
M45.2*	-105	-37	-417	-450
M45.3*	-34	-9	-154	-304

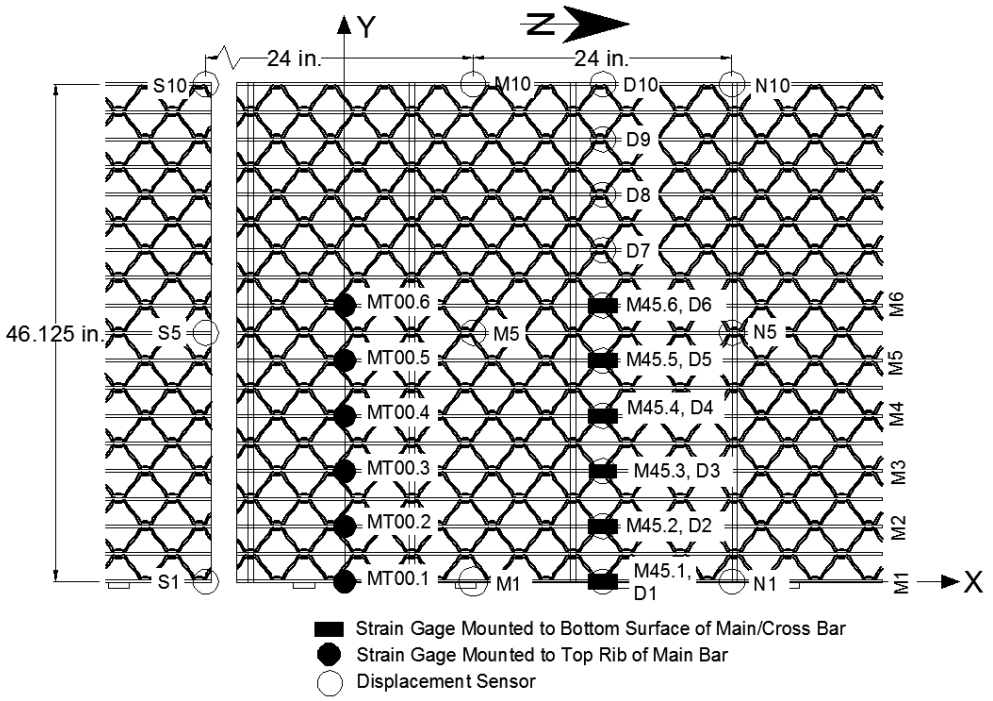

LEGEND			
Strain Gage	Location (x,y) (in.)	Displacement Sensor	Location (x,y) (in.)
MT00.1	(0, 0)	D1	(24, 0)
MT00.2	(0, 5.125)	D2	(24, 5.125)
MT00.3	(0, 10.25)	D3	(24, 10.25)
MT00.4	(0, 15.375)	D4	(24, 15.375)
MT00.5	(0, 20.5)	D5	(24, 20.5)
MT00.6	(0, 25.625)	D6	(24, 25.625)
M45.1	(24, 0)	D7	(24, 30.75)
M45.2	(24, 5.125)	D8	(24, 35.875)
M45.3	(24, 10.25)	D9	(24, 41)
M45.4	(24, 15.375)	D10	(24, 46.125)
M45.5	(24, 20.5)	N1	(36, 0)
M45.6	(24, 25.625)	N5	(36, 23.0625)
		N10	(36, 46.125)
		M1	(12, 0)
		M5	(12, 23.0625)
		M10	(12, 46.125)
		S1	(-12, 0)
		S5	(-12, 23.0625)
		S10	(-12, 46.125)

Figure C.23: Strain and displ. sensor plan for specimen 37-R-L-5x¼ for tests 147, 148

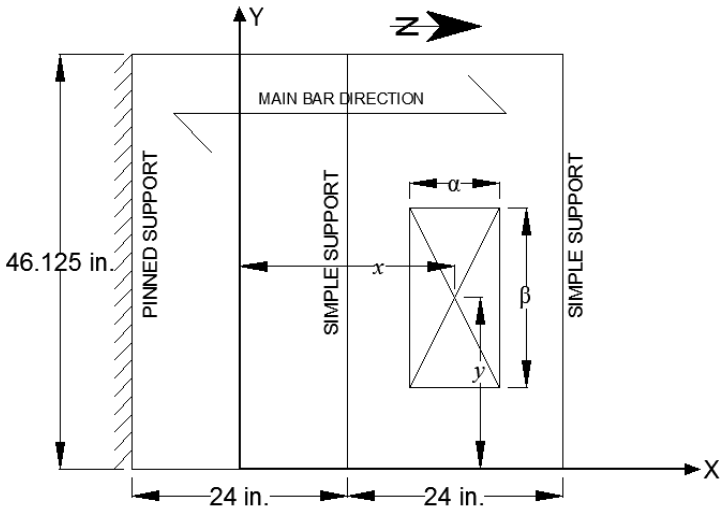

LEGEND		
Test #	Patch Location (x, y) (in.)	Patch Orientation (α, β) (in.)
147	(24, 23.0625)	(10, 20)
148	(24, 23.0625)	(20, 10)

Figure C.24: Patch load plan for tests 147, 148

Table C.21: Strain and displacement data for tests 147, 148

Displacement Sensor/ Strain Gage	Test #	
	147	148
D1	-0.006	0.000
D2	-0.003	0.005
D3	-0.006	0.004
D4	-0.010	-0.006
D5	-0.007	-0.010
D6	-0.009	-0.010
D7	NA	NA
D8	NA	NA
D9	0.001	0.001
D10	NA	NA
MT00.1	25	17
MT00.2	23	18
MT00.3	5	8
MT00.4	-2	4
MT00.5	-6	-15
MT00.6	-8	-11
M45.1	-8	-2
M45.2	-30	-16
M45.3	-81	-44
M45.4	-235	-158
M45.5	-342	-363
M45.6	-345	-316

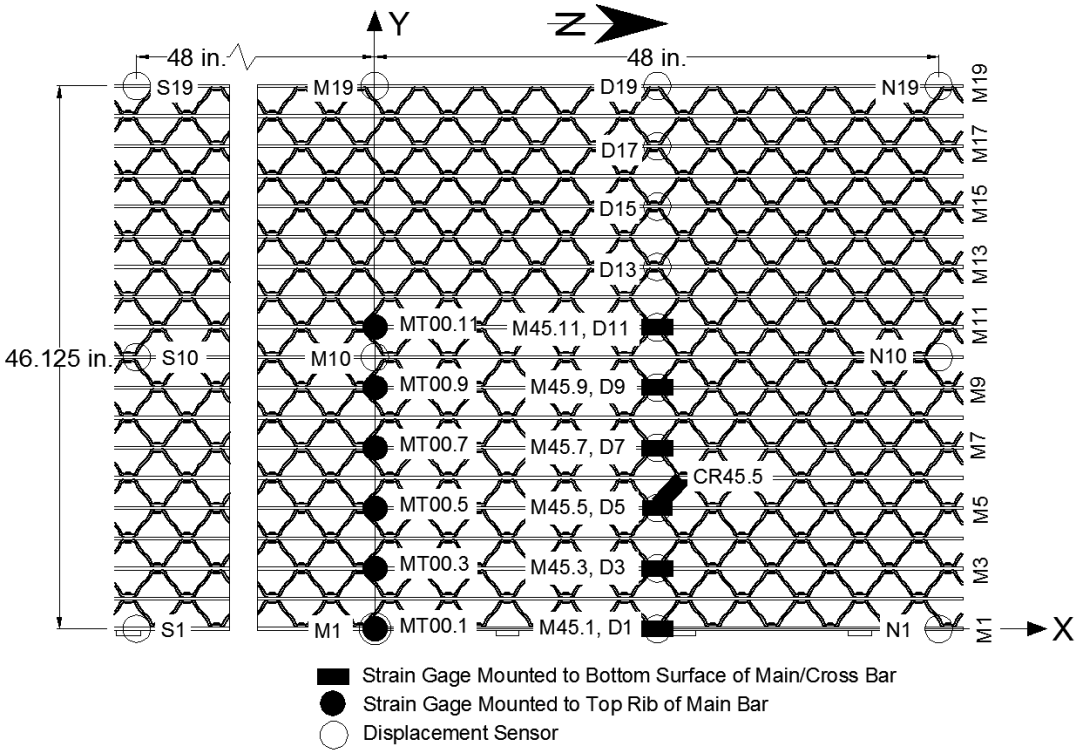

LEGEND			
Strain Gage	Location (x,y) (in.)	Displacement Sensor	Location (x,y) (in.)
MT00.1	(0, 0)	D1	(24, 0)
MT00.3	(0, 5.125)	D3	(24, 5.125)
MT00.5	(0, 10.25)	D5	(24, 10.25)
MT00.7	(0, 15.375)	D7	(24, 15.375)
MT00.9	(0, 20.5)	D9	(24, 20.5)
MT00.11	(0, 25.625)	D11	(24, 25.625)
M45.1	(24, 0)	D13	(24, 30.75)
M45.3	(24, 5.125)	D15	(24, 35.875)
M45.5	(24, 10.25)	D17	(24, 41)
M45.7	(24, 15.375)	D19	(24, 46.125)
M45.9	(24, 20.5)	N1	(48, 0)
M45.11	(24, 25.625)	N10	(48, 23.0625)
CR45.5	(25.17 , 11.66)	N19	(48, 46.125)
		M1	(0, 0)
		M10	(0, 23.0625)
		M19	(0, 46.125)
		S1	(-48, 0)
		S10	(-48, 23.0625)
		S19	(-48, 46.125)

Figure C.25: Strain and displ. sensor plan for specimen 37-R-5x¼ for tests 149-168

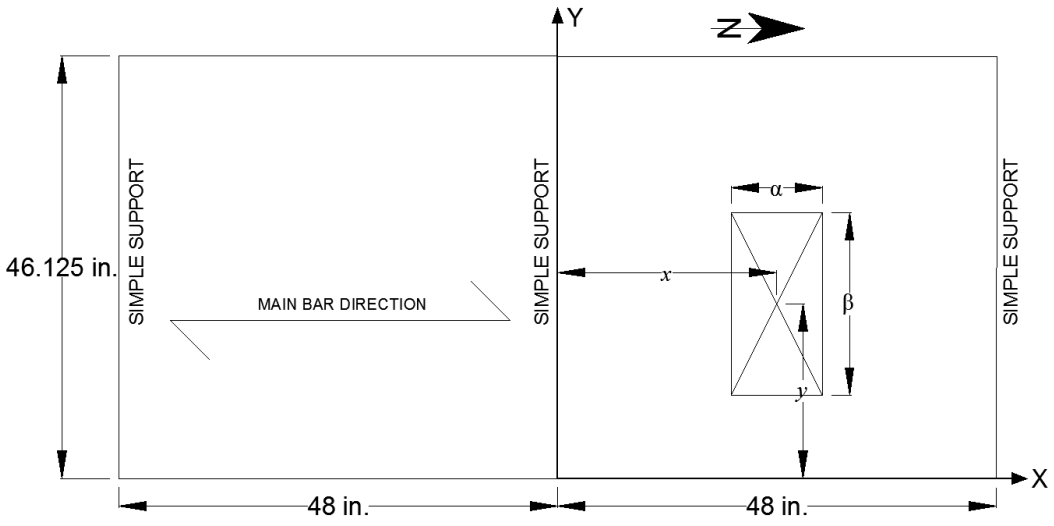

LEGEND		
Test #	Patch Location (x, y) (in.)	Patch Orientation (α, β) (in.)
149	(24, 23.0625)	(10, 20)
150	(24, 23.0625)	(20, 10)
151	(24, 9.625))	(10, 20)
152	(24, 4.625)	(20, 10)

Figure C.26: Patch load plan for tests 149-152

Table C.22: Strain and displacement data for tests 149-152

Displacement Sensor/ Strain Gage	Test #			
	149	150	151	152
D1	NA	NA	NA	NA
D3	0.000	0.001	-0.029	-0.043
D5	NA	NA	NA	NA
D7	NA	NA	NA	NA
D9	-0.027	-0.033	-0.015	0.001
D11	-0.032	-0.038	-0.006	-0.001
D13	-0.024	-0.024	-0.002	-0.001
D15	-0.006	-0.002	0.001	0.000
D17	-0.001	0.000	0.000	0.001
D19	0.000	-0.001	0.000	0.000
MT00.1	40	32	103	111
MT00.3	54	61	-88	-273
MT00.5	20	27	-25	6
MT00.7	-21	11	-26	31
MT00.9	-36	-63	16	23
MT00.11	-18	-39	22	13
M45.1	2	2	-344	-523
M45.3	-41	-20	-419	-600
M45.5	-136	-64	-420	-335
M45.7	-345	-213	-371	-106
M45.9	-431	-485	-185	-27
M45.11	-382	-448	-61	-8
CR45.5	28	106	-136	114

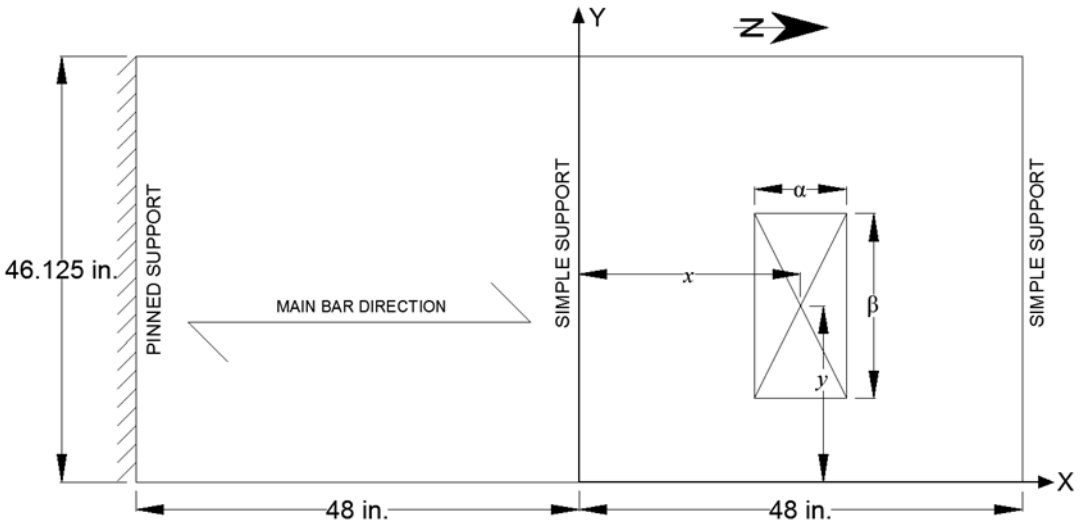

LEGEND		
Test #	Patch Location (x, y) (in.)	Patch Orientation (α, β) (in.)
153	(24, 23.0625)	(10, 20)
154	(24, 9.625))	(10, 20)
155	(24, 36.5)	(10, 20)
156	(24, 4.625)	(20, 10)
157	(24, 7.6875)	(20, 10)
158	(24, 12.8125)	(20, 10)
159	(24, 17.9375)	(20, 10)
160	(24, 23.0625)	(20, 10)
161	(24, 28.1875)	(20, 10)
162	(24, 33.3125)	(20, 10)
163	(24, 38.4375)	(20, 10)
164	(24, 41.5)	(20, 10)

Figure C.27: Patch load plan for tests 153-164

Table C 23: Strain and displacement data for tests 153-164

Displacement Sensor/ Strain Gage	Test #											
	153	154	155	156	157	158	159	160	161	162	163	164
D1	NA	NA	NA	-0.043	-0.023	-0.002	-0.001	-0.005	-0.002	-0.004	-0.003	-0.004
D3	0.000	-0.027	0.000	-0.038	-0.031	-0.014	0.000	-0.002	0.001	0.001	0.001	0.000
D5	NA	NA	NA	-0.026	-0.031	-0.033	-0.017	-0.002	0.001	0.001	0.002	0.001
D7	NA	NA	NA	-0.004	-0.012	-0.033	-0.037	-0.014	-0.004	0.002	0.002	-0.001
D9	-0.025	-0.005	0.004	0.001	0.002	-0.015	-0.030	-0.032	-0.010	0.000	0.005	0.001
D11	-0.025	-0.002	-0.011	0.000	0.003	-0.004	-0.016	-0.038	-0.030	-0.011	0.001	0.001
D13	-0.018	0.001	-0.020	0.000	0.003	-0.001	-0.004	-0.019	-0.036	-0.029	-0.015	-0.006
D15	-0.005	0.002	-0.021	-0.001	0.002	0.002	0.000	0.000	-0.015	-0.032	-0.026	-0.017
D17	0.000	0.002	-0.024	-0.001	0.002	0.000	-0.001	0.000	0.000	-0.018	-0.032	-0.037
D19	-0.001	-0.001	-0.028	0.000	0.002	-0.001	-0.001	0.004	0.000	-0.007	-0.023	-0.045
MT00.1	19	-170	12	-282	-60	34	26	18	17	14	7	0
MT00.3	14	-186	18	-296	-283	-52	10	21	21	20	9	3
MT00.5	-15	-68	8	-55	-91	-101	-38	13	11	10	4	2
MT00.7	-58	-43	9	1	-14	-95	-105	-30	7	8	6	2
MT00.9	-65	-6	7	8	9	-18	-68	-92	-20	7	7	5
MT00.11	-52	6	-18	6	8	6	-20	-74	-87	-19	6	6
M45.1	11	-355	-4	-478	-237	-4	16	7	1	-7	-6	-1
M45.3	-18	-385	-4	-503	-463	-175	-39	-2	-1	-4	-2	0
M45.5	-117	-351	-7	-271	-386	-432	-200	-36	-10	-5	-2	0
M45.7	-342	-285	-23	-80	-174	-422	-476	-195	-49	-11	-3	3
M45.9	-403	-123	-54	-11	-37	-164	-377	-459	-172	-45	-6	1
M45.11	-334	-35	-180	-1	-9	-43	-149	-399	-429	-170	-44	-7
CR45.5	15	-115	19	90	-113	-269	-39	97	52	18	9	10

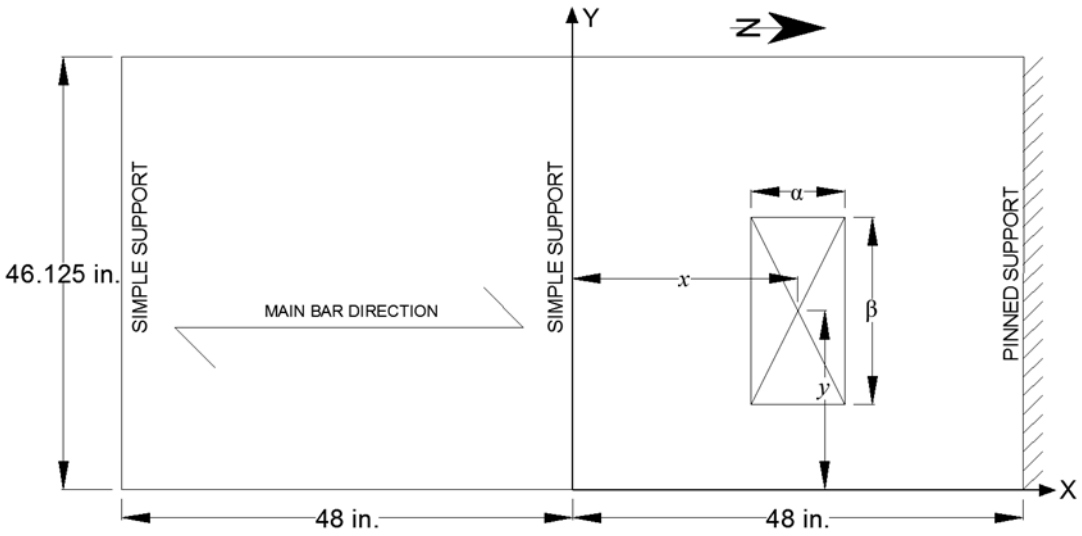

LEGEND		
Test #	Patch Location (x, y) (in.)	Patch Orientation (α, β) (in.)
165	(-24, 23.0625)	(10, 20)
166	(-24, 23.0625)	(20, 10)
167	(-24, 9.625))	(10, 20)
168	(-24, 4.625)	(20, 10)

Figure C.28: Patch load plan for tests 165-168

Table C.24: Strain and displacement data for tests 165-168

Displacement Sensor/ Strain Gage	Test #			
	165	166	167	168
MT00.1	13	20	-32	-48
MT00.3	3	19	-292	-475
MT00.5	-12	2	-49	-47
MT00.7	-75	-42	-69	-4
MT00.9	-75	-119	-12	3
MT00.11	-78	-112	-4	1
M45.1	-5	-11	89	131
M45.3	10	1	42	52
M45.5	32	19	76	83
M45.7	52	49	60	45
M45.9	68	76	35	6
M45.11	60	76	8	-5
CR45.5	2	-11	23	14

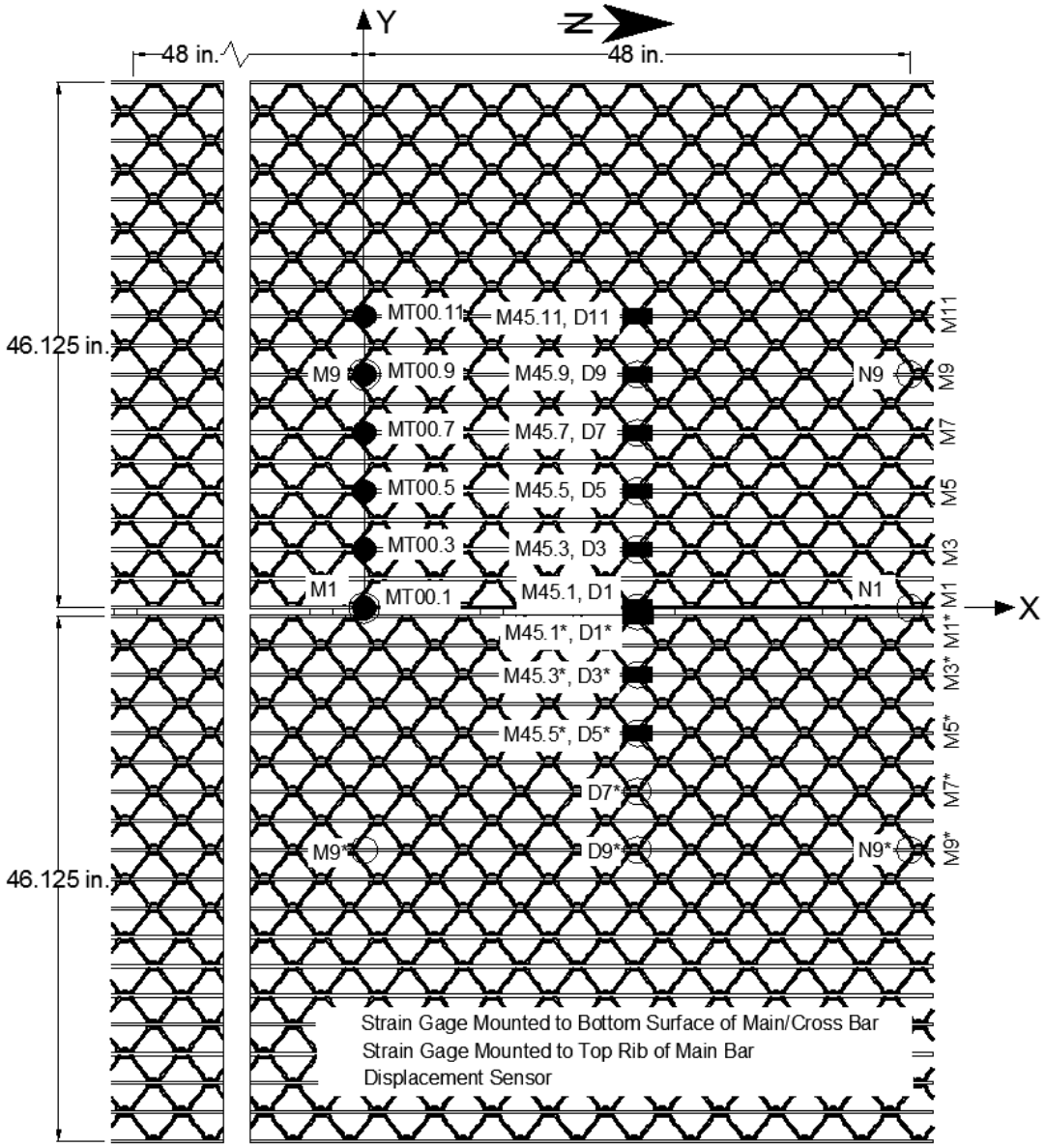

LEGEND							
Strain Gage	Location (x,y) (in.)	Strain Gage	Location (x,y) (in.)	Displ. Sensor	Location (x,y) (in.)	Displ. Sensor	Location (x,y) (in.)
MT00.1	(0, 0)	M45.5	(24, 10.25)	D1	(24, 0)	D7*	(24, -16.125)
MT00.3	(0, 5.125)	M45.7	(24, 15.375)	D3	(24, 5.125)	D9*	(24, -21.25)
MT00.5	(0, 10.25)	M45.9	(24, 20.5)	D5	(24, 10.25)	N1	(48, 0)
MT00.7	(0, 15.375)	M45.11	(24, 25.625)	D7	(24, 15.375)	M1	(0, 0)
MT00.9	(0, 20.5)	M45.1*	(24, -0.75)	D9	(24, 20.5)	N9	(48, 20.5)
MT00.11	(0, 25.625)	M45.3*	(24, -5.875)	D1*	(24, -0.75)	M9	(0, 20.5)
M45.1	(24, 0)	M45.5*	(24, -11)	D3*	(24, -5.875)	N9*	(48, -21.25)
M45.3	(24, 5.125)			D5*	(24, -11)	M9*	(0, -21.25)

Figure C.29: Strain and displ. sensor plan for specimen 37-R-5x¼ for tests 169-172

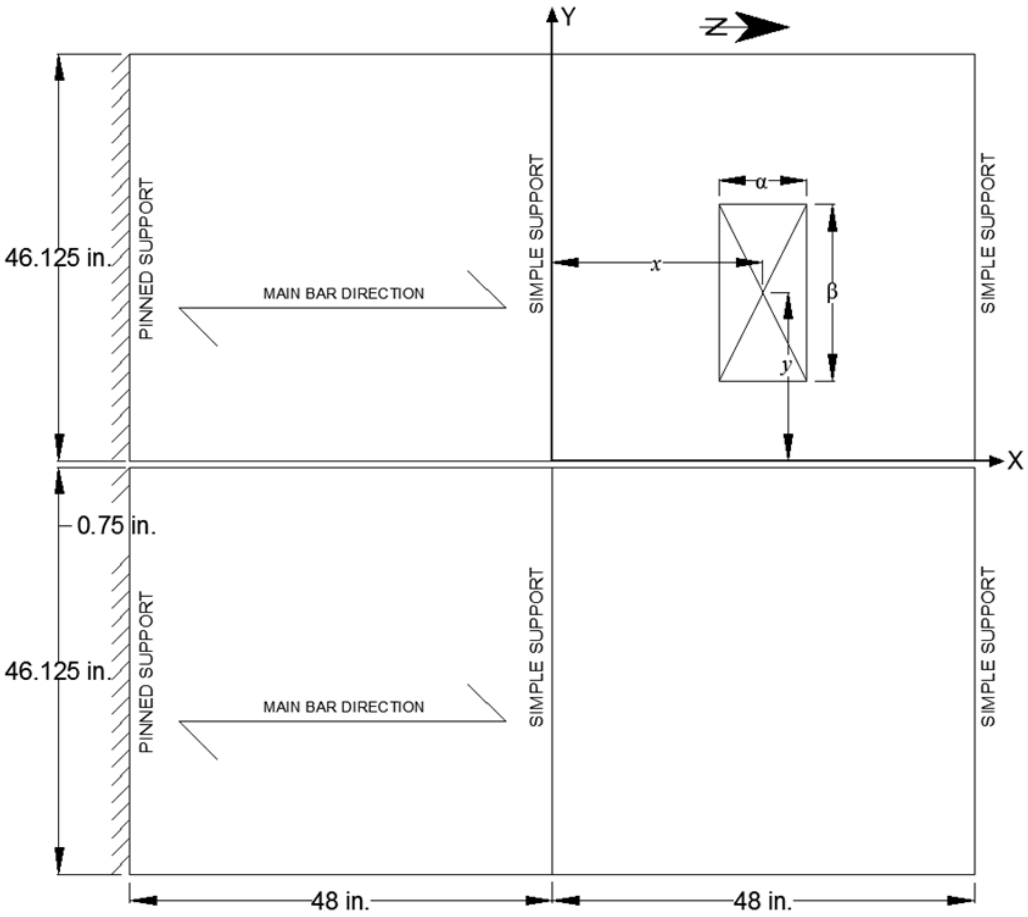

LEGEND		
Test #	Patch Location	Patch Orientation
	(x, y) (in.)	(α, β) (in.)
169	(24, 4.625)	(20, 10)
170	(24, 9.625)	(10, 20)
171	(24, -0.375)	(20, 10)
172	(24, -0.375)	(10, 20)

Figure C.30: Patch load plan for tests 169-172

Table C.25: Strain and displacement data for tests 169-172

Displacement Sensor/ Strain Gage	Test #			
	169	170	171	172
D9*	-0.004	-0.004	-0.004	-0.007
D7*	0.001	0.000	-0.001	-0.008
D5*	0.003	0.001	-0.009	-0.016
D3*	-0.004	-0.002	-0.027	-0.022
D1*	-0.013	-0.007	-0.039	-0.025
D1	-0.033	-0.016	-0.045	-0.028
D3	-0.046	-0.027	-0.027	-0.033
D5	-0.043	-0.038	-0.013	-0.020
D7	-0.016	-0.038	-0.004	-0.010
D9	-0.001	-0.026	-0.003	0.007
MT00.1	-201	-61	-231	-131
MT00.3	-280	-161	-124	-140
MT00.5	-38	-52	2	-15
MT00.7	4	-45	6	5
MT00.9	10	-21	5	8
MT00.11	7	5	4	6
M45.1	-278	-161	-396	-262
M45.3	-463	-317	-234	-291
M45.5	-263	-344	-57	-152
M45.7	-82	-335	-7	-49
M45.9	-15	-164	0	-11
M45.11	-5	-44	-2	-4
M45.1*	-201	-133	-393	-252
M45.3*	-61	-33	-273	-302
M45.5*	-11	-5	-93	-205

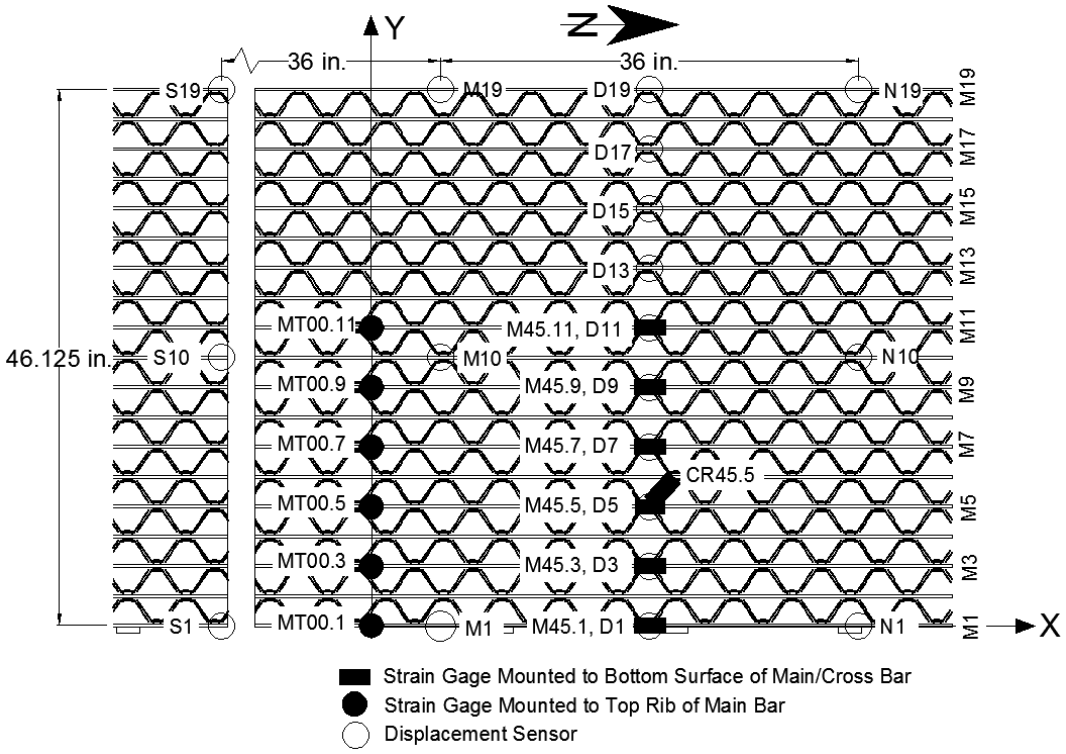

LEGEND			
Strain Gage	Location (x,y) (in.)	Displ. Sensor	Location (x,y) (in.)
MT00.1	(0, 0)	D1	(24, 0)
MT00.3	(0, 5.125)	D3	(24, 5.125)
MT00.5	(0, 10.25)	D5	(24, 10.25)
MT00.7	(0, 15.375)	D7	(24, 15.375)
MT00.9	(0, 20.5)	D9	(24, 20.5)
MT00.11	(0, 25.625)	D11	(24, 25.625)
M45.1	(24, 0)	D13	(24, 30.75)
M45.3	(24, 5.125)	D15	(24, 35.875)
M45.5	(24, 10.25)	D17	(24, 41)
M45.7	(24, 15.375)	D19	(24, 46.125)
M45.9	(24, 20.5)	N1	(42, 0)
M45.11	(24, 25.625)	N10	(42, 23.0625)
CR45.5	(25.17 , 11.66)	N19	(42, 46.125)
		M1	(6, 0)
		M10	(6, 23.0625)
		M19	(6 46.125)
		S1	(-30, 0)
		S10	(-30, 23.0625)
		S19	(-30, 46.125)

Figure C.31: Strain and displ. sensor plan for specimen 37-R-5x¼ for tests

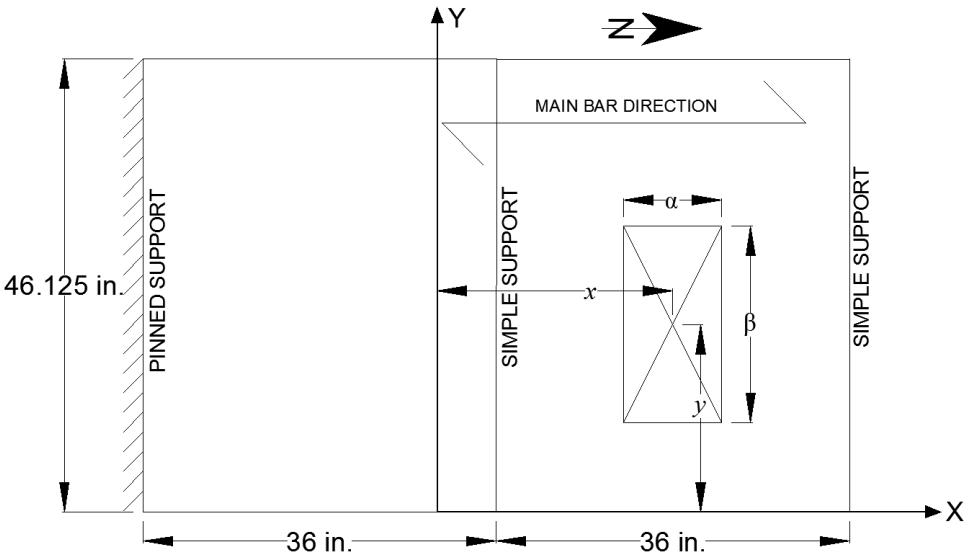

LEGEND		
Test #	Patch Location (x, y) (in.)	Patch Orientation (α, β) (in.)
173	(24, 23.0625)	(10, 20)
174	(24, 23.0625)	(20, 10)
175	(24, 9.625)	(10, 20)
176	(24, 4.625)	(20, 10)
177	(24, 12.8125)	(10, 20)

Figure C.32: Patch load plan for tests 173-177

Table C.26: Strain and displacement data for tests 173-177

Displacement Sensor/ Strain Gage	Test #				
	173	174	175	176	177
D1	-0.003	-0.003	-0.006	-0.017	-0.003
D3	0.000	-0.001	-0.013	-0.015	-0.007
D5	0.001	0.001	-0.011	-0.006	-0.017
D7	-0.007	-0.002	-0.013	0.001	-0.020
D9	-0.010	-0.012	-0.006	0.002	-0.007
D11	-0.007	-0.010	0.002	0.003	0.002
D13	-0.008	-0.003	0.000	0.003	0.001
D15	0.000	0.001	-0.001	0.002	0.001
D17	-0.001	-0.001	-0.001	0.002	0.000
D19	-0.003	-0.001	-0.001	0.002	0.000
MT00.1	17	11	-54	-174	18
MT00.3	15	12	-80	-157	-42
MT00.5	2	4	-36	-25	-53
MT00.7	-22	-15	-38	4	-52
MT00.9	-42	-58	-16	6	-14
MT00.11	-42	-57	5	6	6
M45.1	-1	2	-168	-385	10
M45.3	-12	0	-237	-373	-107
M45.5	-45	-12	-259	-159	-319
M45.7	-176	-107	-294	-36	-339
M45.9	-289	-331	-123	-5	-99
M45.11	-293	-314	-23	-3	-14
CR45.5	34	62	-99	81	-190

APPENDIX D – CRACK MAPS FOR FULL-SYSTEM FATIGUE TEST

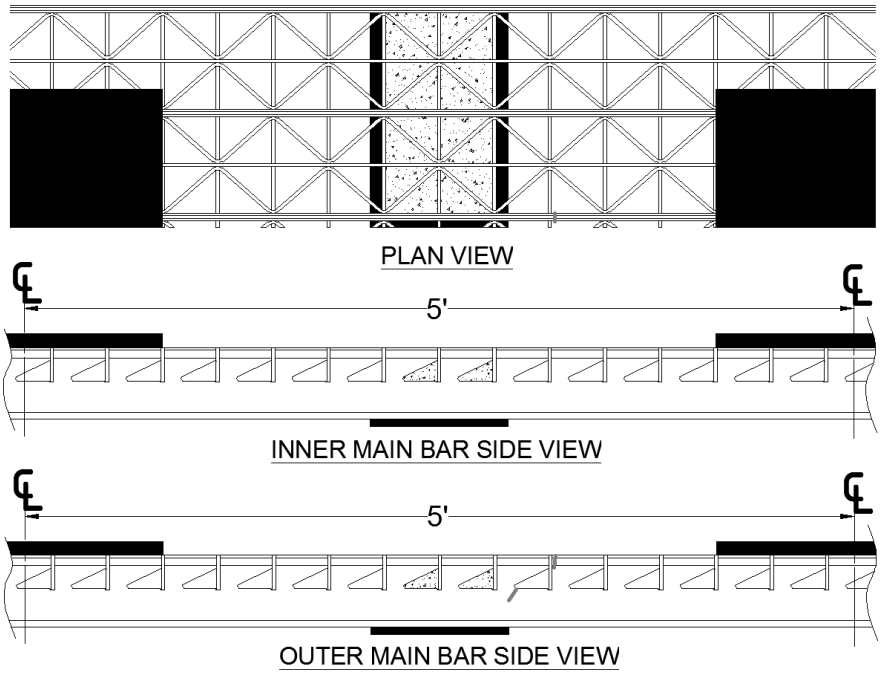

Figure D.1: 7.5DIAG2.5TYP1 fatigue at 1,030,000 cycles

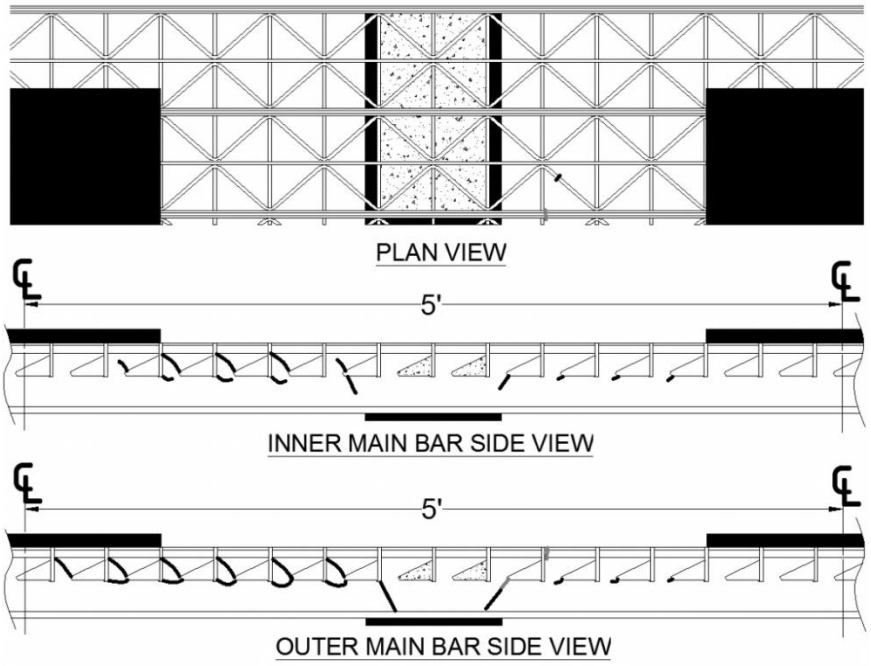

Figure D.2: 7.5DIAG2.5TYP1 fatigue at 1,086,000 cycles

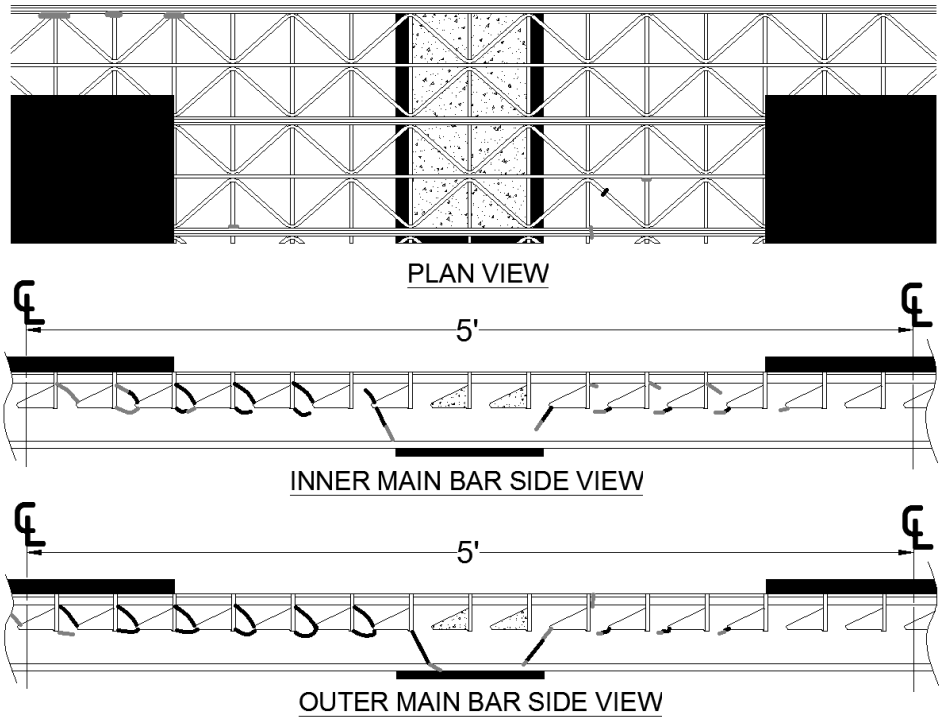

Figure D.3: 7.5DIAG2.5TYP1 fatigue at 1,200,000 cycles

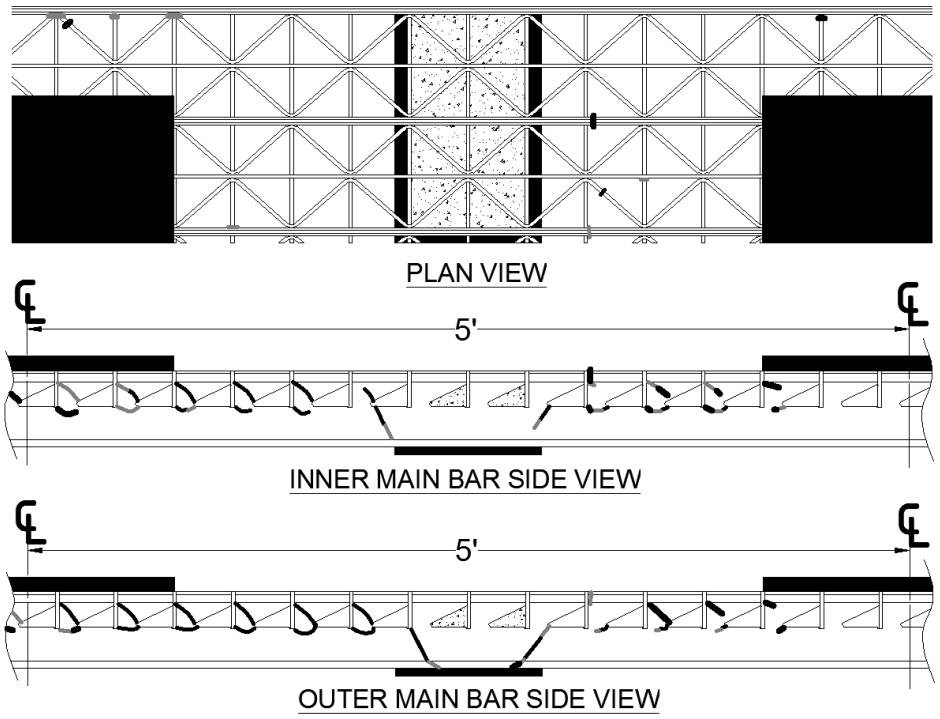

Figure D.4: 7.5DIAG2.5TYP1 fatigue at 1,300,000 cycles

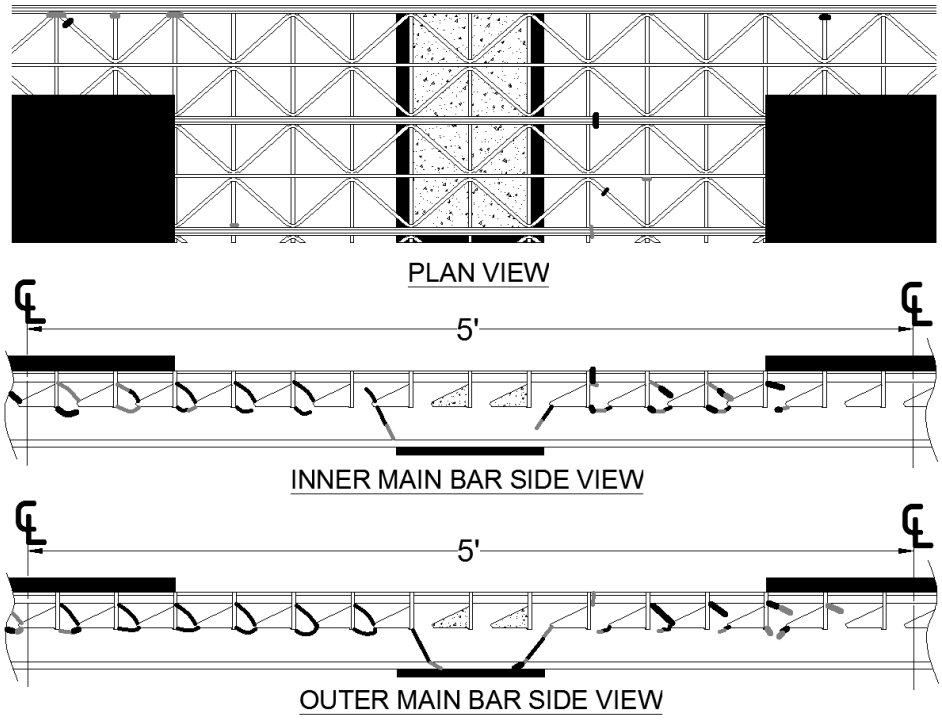

Figure D.5: 7.5DIAG2.5TYP1 fatigue at 1,350,000 cycles